# THÈSE

En vue de l'obtention du

# DOCTORAT DE L'UNIVERSITÉ DE TOULOUSE

**Délivré par :**

Institut National Polytechnique de Toulouse (INP Toulouse)

**Discipline ou spécialité :**

Electromagnétisme et Systèmes Haute Fréquence

---

**Présentée et soutenue par :**

M. JUAN ANTONIO DURAN VENEGAS
le lundi 5 décembre 2016

**Titre :**

## Reconfigurable Metasurfaces for Beam Scanning Planar Antennas

---

**Ecole doctorale :**
Génie Electrique, Electronique, Télécommunications (GEET)

**Unité de recherche :**
Laboratoire Plasma et Conversion d'Energie (LAPLACE)
**Directeur(s) de Thèse :**
M. GAETAN PRIGENT
M. CEDRIC MARTEL

**Rapporteurs :**
M. CHRISTIAN PERSON, TELECOM BRETAGNE CAMPUS DE BREST
M. FRANCISCO MEDINA, UNIVERSITE DE SEVILLE

**Membre(s) du jury :**
M. CHRISTIAN PERSON, TELECOM BRETAGNE CAMPUS DE BREST, Président
M. CEDRIC MARTEL, ONERA TOULOUSE, Membre
M. ERWAN FOURN, INSA DE RENNES, Membre
M. GAETAN PRIGENT, INP TOULOUSE, Membre
M. OLIVIER PASCAL, UNIVERSITE TOULOUSE 3, Membre

# Abstract

This thesis introduces original works on the development of low profile antennas for on-the-move Ku band SATCOM applications. The antennas presented in this thesis allow the communication with GEO satellites from a moving platform, whether it is terrestrial, marine or airborne. Hence, one of its main characteristics is the ability to steer its main beam towards the satellite.

The thesis focuses on the study of a radiating linear antenna that constitutes the basic element of the full antenna and that is capable of steering the beam within one plane. The radiating linear antenna here proposed is a linear series array. The proposed architecture dissociates the phasing from the radiation of the line, which differentiates it from a leaky wave antenna. For that, the transmission line controlling the phase is shielded from the rest of the structure.

The phase control is based on periodic Composite Right-/Left-Handed (CRLH) cells, which are implemented on a Coplanar Waveguide (CPW) and are reconfigured with varactor diodes. The characterization of the discontinuities -series capacitor and shunt inductor- is investigated in detail. A statistical characterization method of these discontinuities is proposed.

An energy extraction device is proposed as a means of redirecting a portion of the energy, away from the line and towards the radiating element. The energy extraction device has a direct connection to the CRLH line and utilizes a capacitance to adjust the quantity of energy extracted.

The series array here presented is compatible with different types of radiating elements. As an example, a linearly polarized and a dual polarized patch antennas are proposed. Finally, the integration of all investigated antenna components (phase reconfigurable CRLH line, energy extraction device and the radiating elements) is addressed as well as the biasing of the diodes.

# Résumé

Cette thèse apporte une contribution originale dans le développement d'antennes faibles épaisseurs pour les applications SATCOM on-the-move en bande Ku. Les antennes étudiées permettent de communiquer avec les satellites géostationnaires à partir d'une plateforme mobile aérienne, marine ou terrestre (avion, bateau, train...). Elles doivent, par conséquent, dépointer le faisceau dans diverses directions pour maintenir la communication avec le satellite.

Les travaux de thèse portent principalement sur l'étude d'une ligne rayonnante qui constitue la brique élémentaire de l'antenne et qui permet de dépointer le faisceau dans un plan.

La ligne proposée est un réseau linéaire en série. Une architecture judicieuse de la ligne permet de dissocier la ligne de transmission reconfigurable en phase et les éléments rayonnants. Pour ce faire, un blindage de la ligne de transmission est réalisé.

Le contrôle de la phase est effectué à l'aide de cellules à métamatériaux CRLH (Composite Right Left Hand) intégrées sur un guide d'onde co-planaire et reconfigurables par des diodes varactors. La caractérisation des discontinuités (capacités séries et inductances parallèles) est investiguée en détail. Une méthode de caractérisation basée sur des modèles statistiques est proposée.

Une méthode de prélèvement d'énergie est proposée pour diriger l'onde électromagnétique vers l'élément rayonnant. Le mécanisme de prélèvement fait intervenir une connexion directe entre la ligne de phase et la ligne de prélèvement et dispose d'une capacité série permettant d'ajuster la quantité d'énergie à prélever pour chaque élément rayonnant du réseau.

Le concept de ligne rayonnante proposé est compatible avec divers types d'antennes à polarisation circulaire ou linéaire. Dans cette thèse, nous proposons le design d'une antenne patch.

Enfin, la cointégration des divers éléments de l'antenne est abordée : ligne de transmission CRLH reconfigurable, lignes de prélèvement, éléments rayonnants, ainsi que le pilotage des diodes.

# Acknowledgements

Merci d'abord à Cédric pour avoir proposé le sujet et pour avoir déposé sa confiance en moi. Merci beaucoup à Olivier et Gaëtan pour avoir accepté cette aventure et merci aux trois pour m'avoir montré le chemin à suivre et les rouages du travail de recherche.

Je remercie Francisco Medina, Christian Person et Erwan Fourn pour avoir accepté de rapporter et examiner cette thèse et pour leur retour sur le manuscrit et travaux de thèse. Je remercie Christian Person pour avoir accepté de présider le jury. Je remercie aussi Jérôme Lorenzo pour être présent pendant la soutenance.

Je voudrais remercier au Laboratoire LAPLACE pour son support, spécialement à Olivier Piggaglio pour son grand soutien pendant la réalisation et mesure de circuits.

Aussi pour sa rapidité et disponibilité sur fortes contraintes de temps, merci beaucoup à Benjamin Gabard et Sylvain Bollioli, avec qui j'ai aussi partagé pas mal des repas pendant mes trois ans à l'ONERA.

Merci à David Colin, du laboratoire LAAS pour le soudage des bondwires des cellules CRLH.

Merci au Département d'Electromagnétisme et Radar de l'ONERA Toulouse pour être si accueillant et pour leur aide dans les plans scientifique et administrative, vous êtes trop nombreux pour vous nommer un par un. Mais je serais en faute si je ne mentionne mes conversations scientifiques inspiratrices avec Florian Mahiddini et Benjamin Alzaix, las muchas veces que Corinne ha tenido paciencia con mis ordres de mission, envoie de documents, etc et bien sûr, j'avoue que rien n'aurait pas été la même chose sans le saltimbanquisme et les petit guillous.

Benjamin mérite une deuxième mention pour le support technique LaTeX.

Gracias a mis padres y mi hermano que me apoyaron desde la decisión de cambiar de rumbo hasta el momento de hacer de público en los ensayos.

Quiero agradecer a todos aquellos que considero cruciales en la sucesión de eventos que me condujeron a la tesis (Gabriel, Fuensanta, Enrique, Cecilio, Carlos Camacho, Kasia y Cédric) y a todos aquellos que me dieron confianza en mí mismo y seguridad en mis decisiones, especialmente Francisco, Jorge, Gonzalo y Salvador (que ha sido testigo de primera fila de este viaje desde el principio de los principios).

Final thanks to my partner in crime, Kasia, who shared with me this adventure day by day, from the day we decided to start applying for PhD up to the present day.

# Contents

# Part I

# Introduction

# Introduction

## Context

Since the coming of the Information Age, the need for communication has steadily increased with time. While in the 1990s mainstream internet communication was primarily reserved to human-to-human communication, nowadays they represent the medium for business transactions, social networks and most of the state and private bureaucracy. No longer can data telecommunication be restrained to static posts in buildings, thus, new generations of cellular communications and spatial variety in WiFi access points flourished in the recent years. Yet it remains challenging to provide access to long distance transportation vehicles, such as transoceanic flights or convoys passing through remote areas like the desert, the jungle or non populated regions.

Where the terrestrial infrastructure is poor or inexistent, satellite communications offer a marginally cheap alternative. Indeed, they can provide for the populated and unpopulated regions for the same cost with no geographic boundaries, as long as there is a Line-of-Sight (LoS) link between the satellite and the receiver. Several solutions exist, such as the Iridium network in Medium Earth Orbit (MEO) or the Artemis and Inmarsat communications satellites in Geostationary Orbits (GEO). Moreover, renewed efforts from the European Space Agency (ESA) and the French Space Agency (CNES) have been made to create a new, cheaper generation of GEO communications satellites, Neosat. Neosat is the next generation of communications platform, which will have their first prototypes developed by Airbus Defence & Space (Eurostar Neo) and Thales Alenia Space (Spacebus Neo) and launch in 2019 for in-orbit demonstration [1].

GEO communications are very well suited for receiver *on the move*. The inhabited regions of the Earth are covered almost in their totality by GEO satellites, loosing coverage only in the poles, where commercial flights do not transit. The steering required by the antenna is typically much smaller than for MEO satellites. An Iridium satellite crosses over the sky for a static user at a rate of $206 arcsec/s$ while a plane flying at $870 kmh$ —cruise speed of the *Airbus* A320— tracks a GEO satellite at a speed of $1.38 arcsec/s$, hence the preference for GEO over MEO communication as a first step in the development of beam steerable antennas for satcom.

However, GEO communications involve communications at distances well over $35000 km$ and need to go through several layers of the atmosphere, including the ionosphere that introduces polarization rotation. Additionally, the available transmission power in a satellite bus is restrained and the transmission EIRP at downlink might be low. For these reasons, ground receiving antennas must invariably feature very high gains and different types of polarization.

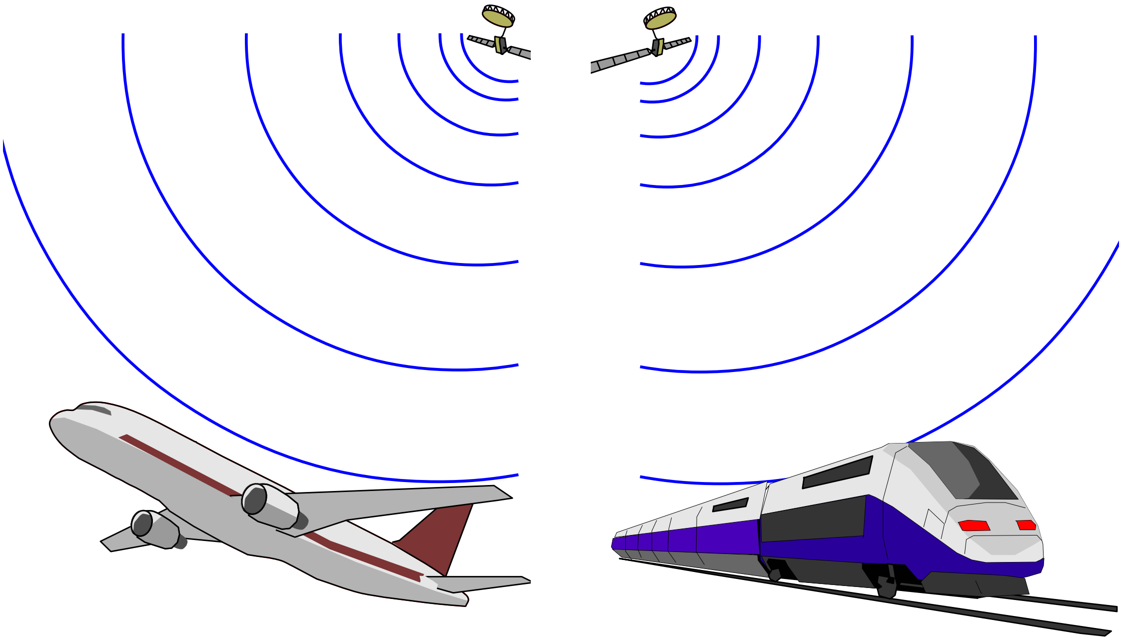

**Fig. 1:** GEO satellite communications *on the move*

For applications *on the move*, the requirements extend to the dimensions and aerodynamics of the antenna and its tracking speed.

Some commercial solutions have appeared during the lasts years, such as *mTenna*$^{TM}$ [2] or the jast-viasat antenna [3]. This thesis aims to find an alternative solution from scratch to the problem of beam steering with high gain, low profile solutions. It is worth noting that traditional corporate antenna arrays already present a surface-like antenna capable of achieving such results but the beam-forming network is usually bulky. The antenna is usually not the only element in the communications subsystem and there is a clear interest in further reducing its size while keeping the expected performances of GEO communications.

## In This Thesis

This thesis studies the theory behind a radiating line that could be used as the building block of an electrically beam steerable radiating metasurface suitable for satcom *on-the-move*.

Based on Composite Right-/Left-Handed (CRLH) metamaterial, a series array is constructed whose inner structure can be reconfigured through the biasing of varactor diodes.

The change in the CRLH line behavior introduced by the biasing of the varactor is reflected as a change in the scan angle of the radiating line. Since a single line is studied, the scan of the beam achieved by the line is constraint to one plane.

Throughout the thesis, the study and design of the radiating line is performed under the assumption that the line is one building block of a radiating metasurface. While the main objective of this thesis remains the study of the single line, a secondary objective is its suitability for two-dimensional steering.

The hypothesis presented in this thesis are supported by proofs of concept using circuit and full-wave simulations and experimental measurements.

## Document Organization

The present report is organized as follows. Chapter 1 defines the context and objectives of the works undertaken for the thesis. In that chapter, the strategic choices taken to design a beam steering method for satcom antennas are described and justified. To support those choices as well as the objectives, a *state of the art* both in satcom antennas at large and the particular technology utilized during the thesis is included.

The final architecture of the radiating line is based on a series array fed by tunable, metamaterial transmission lines. Chapter 2 describes the design process of such a line and the works carried out to realize it. At the end of the chapter, a novel design procedure is proposed for the synthesis of reconfigurable lines.

The lines described in chapter 2 are not readily suitable for being used as a series beam forming network, chapter 3 focuses on the modifications incorporated to the transmission line to probe energy in a controlled fashion and how to divert it into a radiating element. Both chapters 2 and 3 include the experimental validation of some of its key components.

Finally, chapter 4 deals with the integration of the feed line and the radiating element. The proof of concept is detailed in this chapter as well as a road-map for the validation and implementation of a fully working Ku band receiving antenna.

# Part II

# Research Works

# State of the Art and Objectives

## Contents

## Objectives

This chapter sets the bases for the rest of the report. Due to the long distance and low power transmission involved in GEO communications, the demand of high gain is fairly important. The design of the antenna becomes even more challenging if the antenna has electrical steering capabilities. In this chapter, a thorough study of the requirements for GEO communications is laid out. Additionally, the study of the *state of the art* in beam steering and antenna reconfigurability sets a context of the possible technology that could allow electrical beam steering in a high-gain planar antenna. A brief state of the art in coplanar waveguide metamaterial lines is also included since that will be revealed to be the technology of choice.

Finally, this chapter sets the strategy and methodology adopted in this thesis. A description of the strategic choices leading to an electrically controlled metasurface with steering capabilities is made.

# 1 Antenna Requirements for GEO Satellite Communication Receivers and *State of the Art* in current solutions

GEO satellites orbit the Earth at 35,786km, which implies link distances that can reach over 40,000 km and free space losses of almost 210dB at Ku band. The on-board transmitter has tight restrictions on the transmission power and the board antenna that can be used, resulting in minimal EIRP values in the downlink budget. Most of the technologies that makes the downlink communication possible need to reside in the ground receiver. In particular, antennas with gain over 30dB are required. These very directive antennas need to have their bore-sight continuously pointing to the satellite, which increases the challenge of the design, whether it is achieved through electrical or mechanical means or a combination of both.

Most of user GEO communications are built on L and Ka band, where the communication is divided in channels, or colors, defined by a frequency and a polarization —RHCP/LHCP or V/H plus skew—. This works focuses on Ku band antennas with different polarizations, with the ultimate objective of achieving a dual polarized antenna. Since the antenna will jump from beam to beam as the receiver moves around the surface of Earth, a large bandwidth would also be required in a fully working antenna.

For mobiles on the ground such a train, where the antenna remains leveled at all times, a beam steering ranging from ±60° from the zenith is sufficient for most applications. Aircraft antennas need to be able to point in a much wider range since the carrier may change its attitude on flight. Still, ±60° may be enough if more than one antenna is utilized in different parts of the plane.

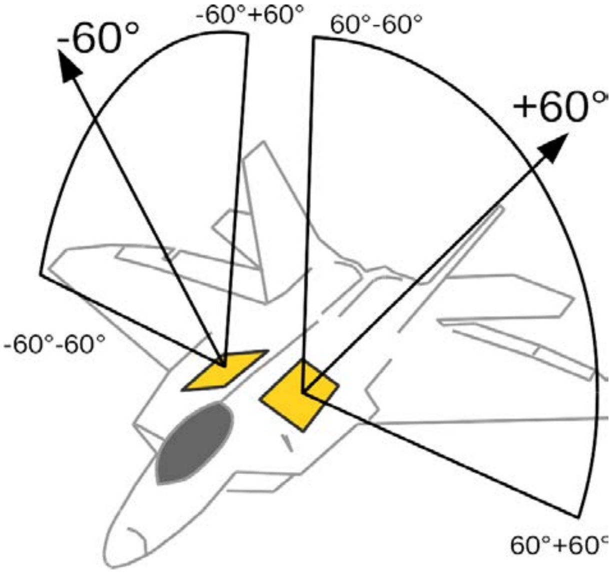

**Fig. 1.1:** caption

In this section, a *state of the art* in the current solutions for GEO communications is presented. Next the principles of leaky wave antennas (frequency scanning) and reconfigurable materials are explained. The purpose is to have a clear understanding of the requirements and technological and physical limits of beam steering.

| **Satellite** | **Operator** | **Band** | **Channels** | **EIRP**[1] | **Pol.** | **Ref** |
|---|---|---|---|---|---|---|
| Yamal 300K | Gazprom | C | 11x72MHz | 45dBW | Linear | [4] |
| | | Ku | 11x72MHz | 44dBW | Linear | |
| Intelsat 701 | Intelsat | C | 42x36MHz | 26dBW | Circular | [5] |
| | | Ku | 20x36MHz | 41dBW | Linear | |
| NSS-7 | SES | C | 50 channels | 39dBW | Circular | [6] |
| | | Ku | 40 channels | 44dBW | Linear | |
| Star One C2 | Star One | C | 28x36MHz | 37dBW | Linear | [7] |
| | | Ku | 12x36MHz<br>2x72MHz | 46dBW | Linear | |
| Light Squared | SLight Squared | L | 1.5-1.7GHz | - | Linear | [8] |

**Table 1.1:** Summary of some important communication geostationary satellites[1]End of coverage, approximative values

| Parameter | Value |
|---|---|
| Gain | >30dB |
| Polarization | Circular or dual linear |
| Azimuthal Steering | $0-360°$ |
| Elevation Steering | $0-60°$ |
| Bandwidth | Large |
| Height | Low |

**Table 1.2:** Generic satcom "on-the-move" antenna requirements

## 1.1 Mechanically steered antennas

The most popular option for ground based antennas in satellite communications is the parabolic reflector. Parabolic reflectors have the drawback of having a static boresight direction and need to be steered mechanically in order to track the relative position of the satellite as the Viasat Aero Mobile Terminal 5230 antenna shown in fig 1.2a.

An example of a satcom antenna with a low profile is the LOCOMO antenna (LOw cost and COmpact Ka-band MObile satcom terminal) [9]. The LOCOMO antenna is a switchable LHCP/RHCP, high directivity —up to 38dB—, planar antenna that can change its pointing direction mechanically while remaining compact in size (fig 1.3a).

An example of a very compact steerable antenna operating in Ka-band can be seen in fig 1.3b [10, 11], where a pillbox transition incorporates a quasi-optical reflector that illuminates a corporate network. By changing the position of the feed along a direction, the antenna can steer the beam in one plane.

Other examples of mechanically steered antennas are the *Honeywell Jetwave Fuselage* (fig 1.2d) and the Honeywell JetWave Tail antenna (fig 1.2c) operating in Ka-band. The *Fuselage* antenna allows up to 50Mbps of data transmission bit rate and is almost 23cm high. The *Tail* antenna is a steered reflector with up to 33Mbps of data transmission bit rate and almost 35cm of height.

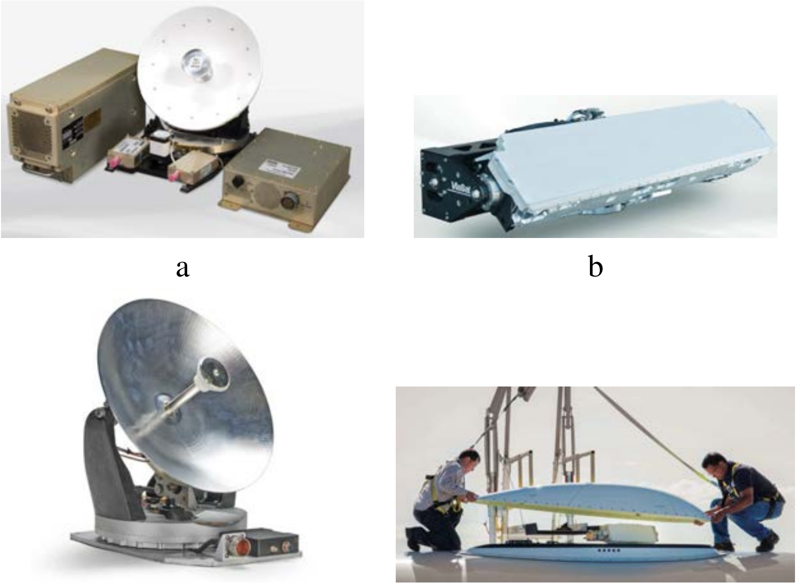

a b

c d

**Fig. 1.2:** Mechanically steered antennas. a) Viasat aero mobile antenna 5230 [12]. b) Viasat aero mobile antenna 5320[13]. Honeywell JetWave c) tail mounted and d) fuselage mounted antenna

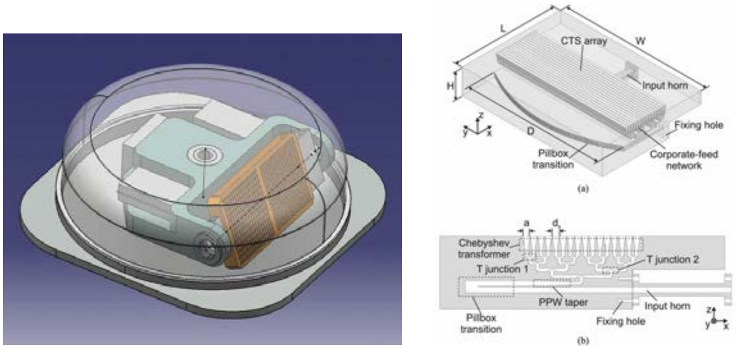

a b

**Fig. 1.3:** Mechanically steered antennas. a) LOCOMO antenna [9]. b) Ka-band pillbox antenna [10]

Other solutions, like the ESA-Jast project [3] make use of electrical reconfigurability for elevation and polarization steering while the azimuthal steering is done by mechanical means. The Jast antenna —currently belonging to ViaSat— makes use of a scalable structure of hexagonal tiles. The ViaSat-Jast antenna can steer up to 70° away from broadside and 360° in azimuth. This antenna has more than $20dBi$ of gain and less than 70mm of height [14].

Mechanically steered antennas offer a reliable and readily available solution, however they are subject to limitations. The servo that controls the antenna as well as the rotary joints that transmit the movement have lifetimes considerably shorter than solid state electronics and the tracking speed is limited by those same systems. Electronic beam steering may be a more durable, lighter and more compact solution than mechanically steered antennas.

## 1.2 Planar Array

Commercial aricraft antenna is often an industrial secret, therefore not always available to the general public. Other than mechanically steered antennas, the antenna arrays are the preferred choice for on-aircraft beam steerable antennas. Some examples of the published on-board systems that can be found in large aircrafts are the *CMC Electronics' CMA-2012*, installed in the *Boeing 747* airplanes and *Airbus A380* [15] with a gain of 12 to 17dBiC and the *CMA-2200SB* [16], seen in fig 1.5, that operates with the *Inmarsat* satellite communications service and ensures a minimum gain of 6 to 8dBiC over 90% of the specified *Inmarsat* hemisphere.

In the domain of antenna arrays, on-spacecraft communications arrays have seen great improvements lately. By breaking the periodicity of the array, extra degrees of freedom can be used to boost the gain and reduce the secondary lobe level. The aperiodicity can be achieved by switching of any number of elements in an array —*thinned arrays*— or by using truly aperiodic array patterns —*sparse arrays*— [17]. A non-uniform array can improve the effective illumination of the equivalent aperture by congregating more elements in the center and can affect the grating lobes by changing the distance between elements from element to element (fig 1.4) [18, 19, 17, 20].

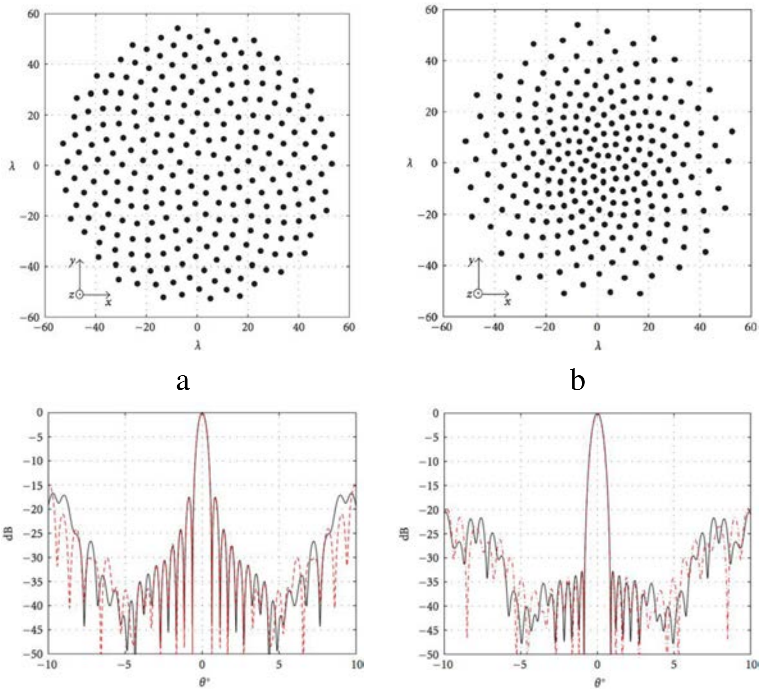

a

b

c

d

**Fig. 1.4:** Distribution of 250 elements in the uniform sunflower array (a) and radiation pattern (c). Distribution of 250 elements in the tappered sunflower array (b) and radiation pattern (d) [17]

## 1.3 Leaky Wave Antennas

Besides antenna arrays, the preferred architecture for electrical beam steering is the leaky wave antenna. Leaky wave antennas naturally present frequency beam scanning techniques

**Fig. 1.5:** *CMC Electronics' CMA-2200SB* Antenna [16]

and a considerable effort has been made in the literature to translate this feature into single frequency electrical beam steering.

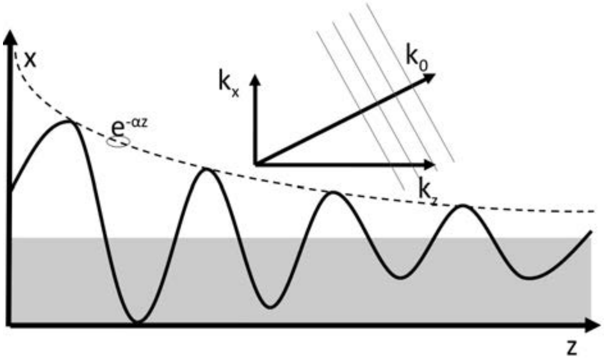

**Fig. 1.6:** Leaky wave. As the wave propagates in the $z$ direction, some power leaks out, thus creating an $x$ component to the wavenumber vector and introducing an attenuation/leakage component in the $z$ direction

A leaky wave antenna is a guiding structure that leaks out energy as it propagates within the antenna. Assuming that the leaky wave is uni-dimensional and lies on the $z$-axis, as seen in fig 1.6, its bore-sight depends on the guided wavelength inside the antenna in the following way

$$\theta_0 = \cos^{-1} \frac{\lambda_0}{\lambda_g} \tag{1.1}$$

from equation 1.1 it can be seen that only those modes whose phase velocity is larger than the speed of light in vacuum —known as *fast waves*— radiate. Otherwise, if $v_p < c$, then $\lambda_g < \lambda_0$ and the argument of the *arccosinus* is larger than one and the mode travelling in the line is purely guided [21, 22, 23, 24].

*Fabry-Pérot Antennas*

Leaky wave antennas can be implemented through different procedures. One of the most usual ways is the Fabry-Pérot (FP) cavity or antenna. In a FP antenna, the energy is trapped between a ground plane and a partially reflecting surface (PRS) [25]. While the ground plane bounces the energy back into the cavity, the PRS reflects only part of the energy and the rest of it is radiated outside. Highly reflective PRS are desired since the FP antenna will have an illumination extended over a larger surface, hence increasing the directivity.

The boresight of the antenna depends on multiple parameters, namely, the height and permittivity of the substrate or the phase of the reflection coefficients of the ground plane and PRS.

By changing the electrical properties of the PRS, the direction of radiation can be modified. In [26], a PRS is created with parallel strips coupled electrically. The coupling between the lines is tuned with varactors, changing the reflection coefficient and the boresight of the antenna.

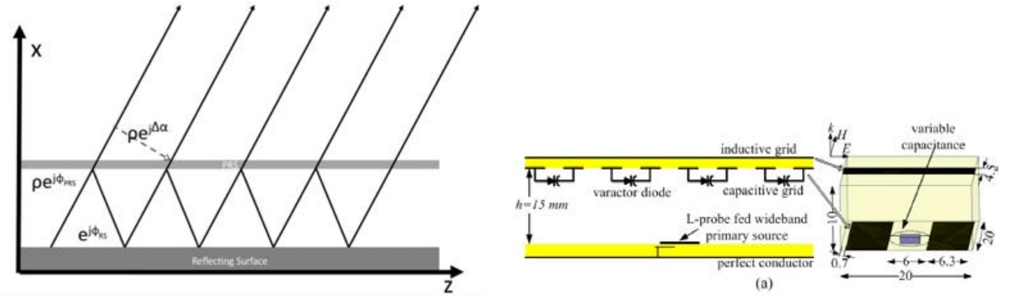

**Fig. 1.7:** a) Profile of a Fabry-Pérot antenna. b) A varactor loaded capacitive grid can change its coupling and the reflection coefficient of a PRS electronically [26]

The antenna in fig 1.7b successfully steers up to ±10° the radiation beam in one plane [26]; Problems derived from the tolerance of the diodes result in degraded maximum steer angle and directivity.

It is possible to modify the FP antenna in [26] to steer the beam over two planes to cover a whole hemisphere. However, as FP antennas usually present asymmetry in the propagation modes within the excitation and the performances for different planes may be different. Some technical difficulties also arise from the locally controllable grid, because the number of diodes grows quadratically as the antenna grows in size. Thereby, the calibration and control of the diodes becomes very complex for large antennas. Moreover, the solution is based on a cavity, which naturally limits the bandwidth of the antenna. Although they present some drawbacks, the results presented are encouraging and the solid state devices are a much safer approach to solving the steering problem than reconfigurable bulky materials.

Fabry-Pérot antennas offer another possibility for reconfiguration. The ground plane can be substituted with an Artificial Magnetic Conductor (AMC), like the mushroom surface [27], thus changing the reflection phase on the ground plane. This is implemented in the leaky wave antennas in [28] (fig 1.8). Using the Electronic Band Gap (EBG) properties of metasurfaces, the propagation conditions within the FP antenna are switched between three different states:

- Purely guiding structure - *slow wave* condition.
- Leaky wave configuration - *fast wave* condition.
- Non propagative configuration - electronic band gap.

In the last section of [28], a centrally fed FP cavity is modified so the propagation is forbidden in all but one azimuthal direction. This modification over the original FP antenna breaks the revolution symmetry of the radiation pattern and achieves azimuthal beam steering. The reflection coefficient of the reflective surface can be configured to be modified electronically.

Although simple, this approach presents some practical problems. [28, 29] shows that the azimuthal steering is not achieved over a continuum of directions but rather at discrete directions. To fully cover the whole space, the azimuthal scanning can be divided into axis created either through a forbidden direction of propagation [28] or through distinct arms [30].

Another problem comes from the reflections on the walls of the cavity. If any energy bounces off the end of the line, it will come back generating secondary lobes. This can be easily prevented with matching networks in linear antennas but it is more difficult to do for 2D FP cavities, often requiring the use of absorbers.

The last main drawback of the structure is that, since only one azimuthal direction can be used at a time to radiate, most of the surface of the antenna is not illuminated, except for radiation in the broadside. This means that the area needed to obtain a certain gain will be roughly $N_d$ bigger than the illuminated region, where $N_d$ is the number of azimuthal directions of radiation. Additionally, since most of the power is radiated in a narrow surface, the transverse beam width will be fan-like, as predicted by Fourier analyses.

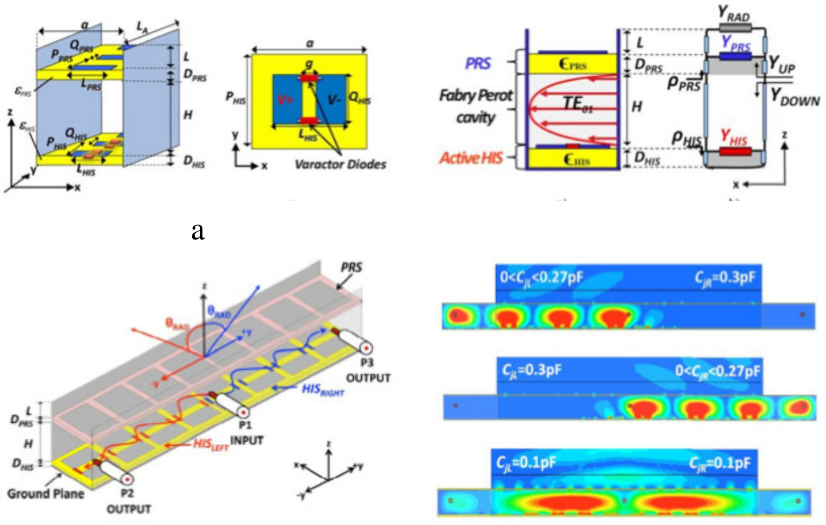

a

b c

**Fig. 1.8:** a) Detailed depiction of the configurable FP cavity cell in [28] , b) one dimension reconfigurable FP antenna and its c) forward, backwards and broadside operation [30]. Broadside radiation is created when the whole AMC operates in the EBG state

*Metamaterial Linear Leaky Wave Antennas*

Leaky wave antennas are also implemented with Composite-Right/Left Handed (CRLH) technology [31]. CRLH lines are composed of cells featuring series capacitors and shunt inductors in addition to the traditional series inductor and shunt capacitor of a traditional line (fig 1.9a). By convention, the series capacitor and shunt inductor are called the left-handed components and are denoted $C_L$ and $L_L$, whereas the traditional components are called right-handed components $C_R$ and $L_R$.

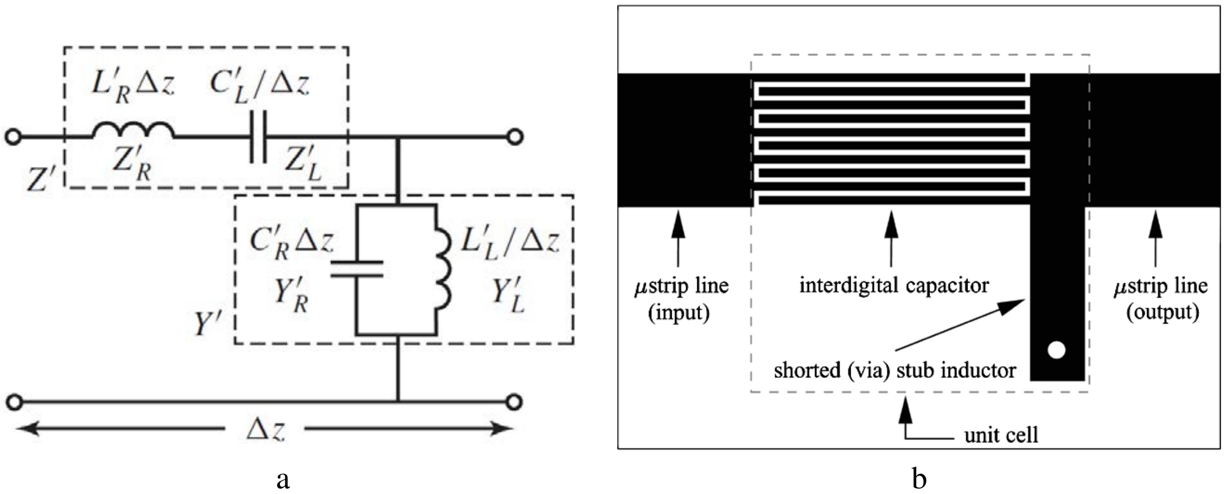

**Fig. 1.9:** CRLH cell. a) Equivalent circuit [31] and b) microstrip realization [32].

A deeper analysis of the CRLH structure will be presented in Chapter 2. Since there is abundant literature on CRLH and metamaterial structures, this section focuses on the description of the *state of the art* in electronically steerable CRLH leaky wave antennas.

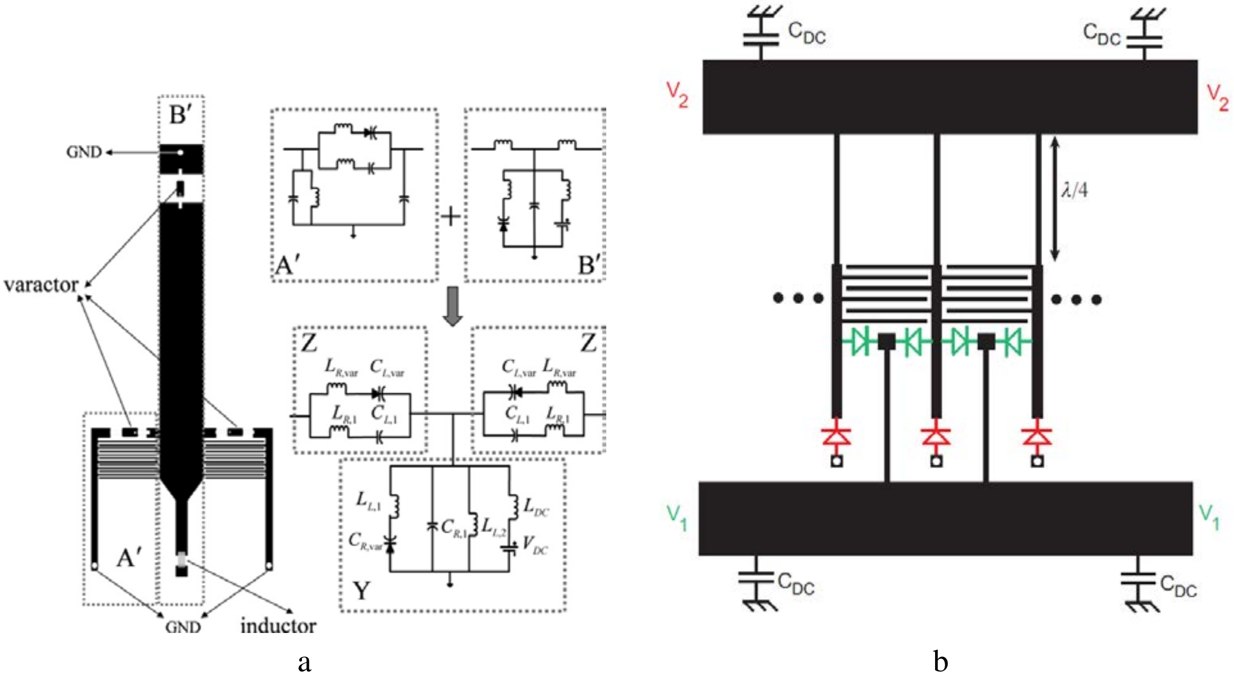

**Fig. 1.10:** a) One-way reconfigurable microstrip CRLH cell [33] and b) two-way reconfigurable microstrip CRLH cell [34]

Some first attempts to create electronically steerable leaky wave antennas can be found in [35, 36]. These antennas could switch the direction of radiation in discrete values. Lim *et al.* [33, 37, 38] improved on the switched antennas by creating an electronically controlled leaky wave that could scan continuously in the range of ±40°. The antenna, described in [33], created the CRLH line with interdigital capacitors and stubs. Both of which are loaded with varactor diodes as shown in fig 1.10a.

The biasing of the diodes effectively modifies the equivalent circuit, which allows the electronic control of the left handed capacitor and inductor, consequently modifying the propagation constant of the line and the scan angle. Lin's design places the varactor diode so one single biasing circuit can control the three diodes in a cell at the same time. This geometry greatly reduces the complexity of the biasing but comes with a trade-off.

The varactors modifies both the propagation constant and the Bloch impedance of the line but, since both the series and shunt varactors are polarized with the same current, there is only one degree of freedom to the control of the characteristics of the line. This could lead to mismatch and loss of power. A modification of this cell [34] can be seen in fig 1.10b. There, the independent control of the series and shunt diodes give two degrees of freedom that allows to tune both the propagation constant and the characteristic impedance of the CRLH line separately.

Some results of the electronically steerable microstrip CRLH antenna are shown in fig 1.11. One phenomenon that can be appreciated is that the highest gain is obtained for broadside radiation and then rapidly falls, asymmetrically, as the scan angle increases. This is not surprising, the CRLH leaky wave antenna can be seen as an array. Thereby, the unit cell acts as a radiating element, whose maximum of radiation is in the direction of broadside. As the antenna steers, shifting its array factor, the main lobe will be attenuated by the modulation of the radiation pattern of the unit cell, while the secondary lobes occupy more central positions, having its influence increased. The asymmetry in the maximum gain versus scanning angle diagram, as argued in [33] comes from the fact that the varactor diodes have bigger losses for lower biasing voltages, this is the case for forward scan, where the bias voltage is smaller than 3.5V for this case.

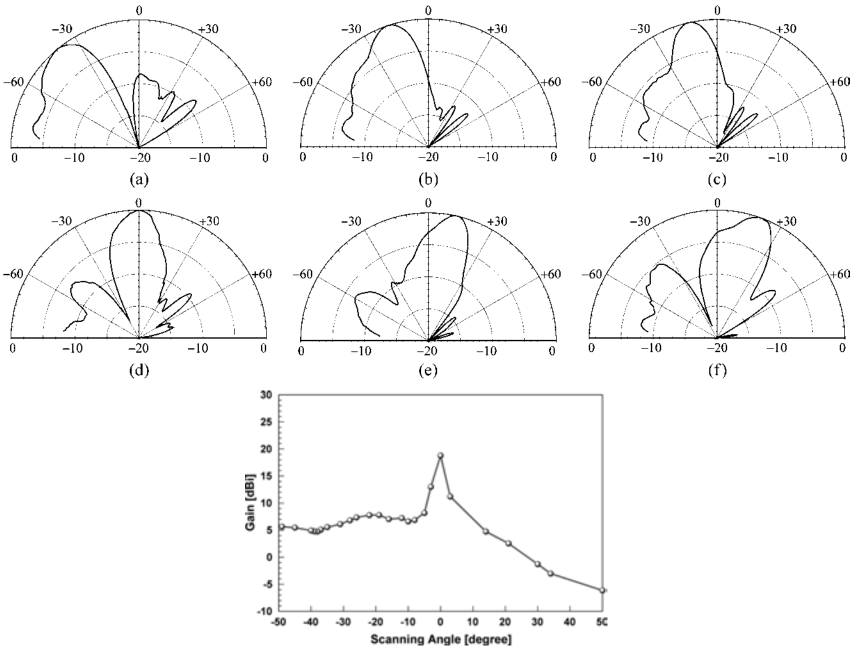

**Fig. 1.11:** Radiation pattern of an electronically beam steerable antenna [33]

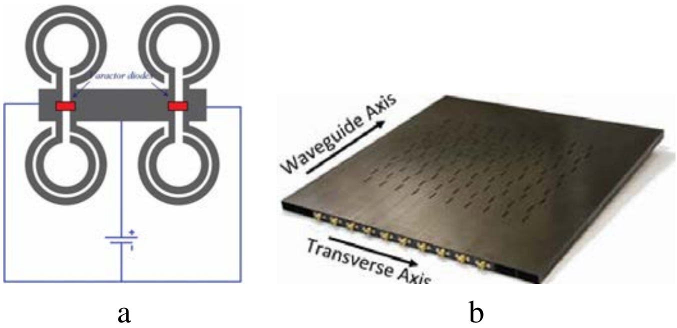

**Fig. 1.12:** a) Varactor diode loaded Split-Ring Resonator (SRR) cell [39]. b) Slotted Waveguide Antenna Stiffened Structure (SWASS) [40]

One last type of electronically controlled CRLH leaky wave antenna worth mentioning is the slotted waveguide published in [40, 41]. This is an example of a non-microstrip based technology. In this case, a rectangular waveguide is modified with a central conductor (fig 1.12a), creating a coaxial like structure. The structure is based on unit cells with varactor loaded series gaps and shunt lines, to create a CRLH equivalent circuit. A series of slots have been etched on the top wall of the waveguide, as in a traditional leaky wave. The propagation constant of the line, hence its scan angle, is controlled by the varactor diodes (fig 1.12b). For further information, an overview of some CRLH leaky wave antennas can be found in [42].

Metasurface based antennas have also being researched in the industry. Two relevant examples are the fully electric *mTenna* antenna (fig 1.13a) and the hybrid electrical-mechanically steered ViaSat antenna (fig 1.13b) covered in the first section. The *mTenna* makes use of metamaterial technology to create a certain scattering pattern to steer the beam in a certain direction. In order to do that, a liquid crystal based cellular surface is electronically controlled. The detailed function remains confidential and no concrete specifications in terms of gain and steer have been found in the commercial website.

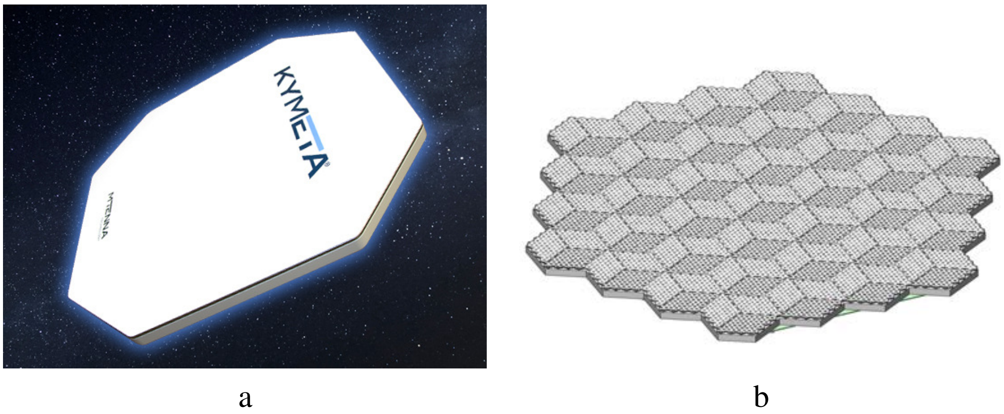

**Fig. 1.13:** a) Kymeta antenna [2]. b) ViaSat's Jast atnenna [3]

## 1.4 Reconfiguration Technologies

Some of the efforts in antenna reconfiguration have been invested into reconfiguring the substrate itself. This is possible using the special properties of materials like ferrites, plasmas or liquid crystals. These materials can change their permittivity or permeability through the application of electromagnetic static fields, opening a wide field of applications.

Ghaffar and Shamin [43] demonstrate the beam steering of a two element phased array where the phase shifter is based on ferrites working in the partially magnetized state. The shifter is built by loading a rectangular waveguide with a ferrite and changing its magnetic permeability through a compact biasing winding. The phase shifter works in Ku band and can achieve phase shifts of up to 180° (fig 1.14b). A prototype was integrated in a two patch antenna array, achieving beam steers of up to 30° (fig 1.14c).

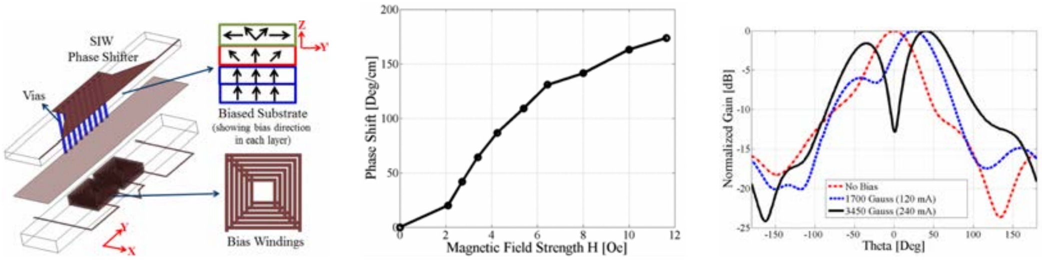

a b c

**Fig. 1.14:** Ferrite based phase shifter. a) Diagram of the shifter. The shifter is created within a rectangular waveguide, the access to the SIW waveguide are connected to a microstrip line. The bias windings polarize the ferrite and control the phase shift. b)Phase shift versus magnetic field strength for one shifter. c) Steering created by a two patch array phased with the phasor in (a) [43]

Iskander *et al.* [44] improve the phased array design by integrating the ferroelectric phase shifters in a continuous array, this smooths transitions and reduces insertion loss between components. Through simulations they demonstrated optimal designs in the structure (fig 1.15) and argued that inserting gaps in the ferroelectric layer where the radiating element is placed improves radiation efficiency and reduces the impact of manufacturing tolerances.

For further information, other phase ferrite based shifting techniques can be found in [45, 46], or for Ferrite loaded EBG-Mushroom structures, in [44, 47]. Also a good review of the concept and applications of magneto-dielectrics can be found in [48]. An example of ferrite-loaded leaky wave antenna can be found in [49]. In general, magnetic permeability control can help achieve phase shifting in Ku band for low profile antenna arrays. However promising, the magnetic permeability control still suffers from high losses, temperature gradients and complicated biasing structures. At this stage, the technology does not seem robust enough for mass production and low cost beam steering technology.

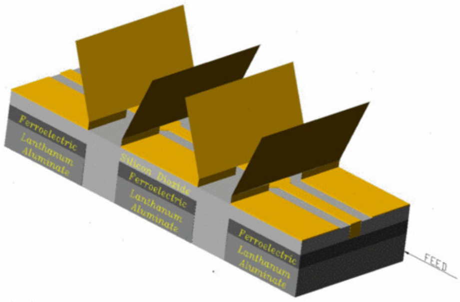

**Fig. 1.15:** CTS array with ferrite based steering [44]

There exist also materials whose electric permittivity can be controlled. Plasmas are ionized gases whose electric permittivity can take on negative values for a certain range of frequencies. If plasmas are contained and controlled, they can be used for electric reconfiguration of antennas. This is what Kallel *et al.* present in [50], where the permittivity profile of the plasma is modified by varying the low frequency power injected into the plasma. The plasma acts as the dielectric in a slab waveguide (fig 1.16) and the RF wave that propagates through the guide refracts into space in different angles depending on the working point of the plasma.

Although the plasma does steer the radiated wavefront, it remains an emerging technology, difficult to manage and to reproduce at big scale.

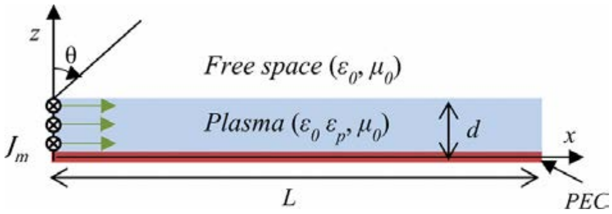

**Fig. 1.16:** Reconfigurable leaky wave antenna with a plasma as dielectric [50]

Liquid crystals (LC) offer an alternative to plasmas in permittivity reconfiguration. LCs are composed of rod like molecules that can be reoriented with strong DC electric fields [51]. By creating anisotropy, the effective electric permittivity seen by a field inside the LC in a given direction can be controlled. LC can be used, as in the case of ferrites, to manufacture phase shifters [52], for phased arrays or they can be used to modify the substrate of a line [53]. By changing the propagation constant of a microstrip line, the beam of a LWA can be steered. Also, it can be used to feed an array of patches, acting as an integrated set of phase shifters.

The use of tunable dielectrics materials open a wide range of possibilities for beam steering, the limit of which remains to be seen. Nevertheless, the knowledge of this type of technologies is limited since they are still in their first stages of development. None of these approaches will be used in this thesis. Solid state devices and SMD components, e.g. diodes, MEMS or transistors, have been intensely used for a long time, still offering a lot of potential in reconfiguration techniques by carefully choosing the structure that hosts them. The use of SMD components can help explore optimal meta-structures for beam steering that could eventually be extrapolated to ferrite or plasma based technologies, once they are developed.

## 2 Our Proposed Antenna Solution and Originality of this Work

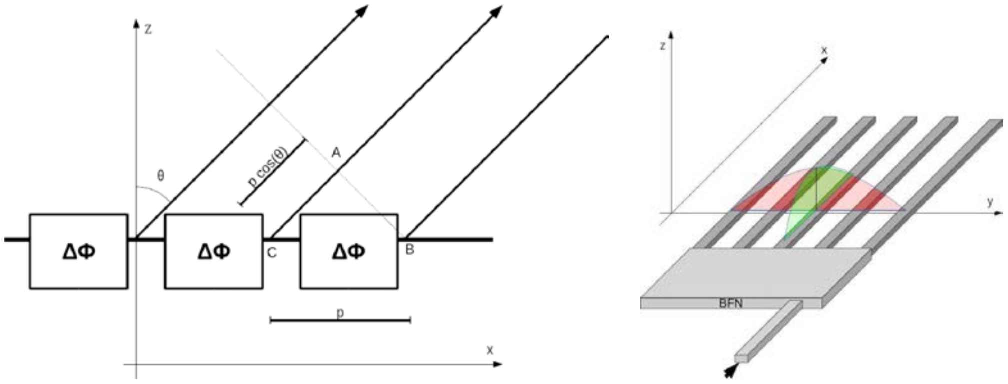

a b

**Fig. 1.17:** a)Series linear array. b)Double linear array

The antenna proposed here is inspired by the CRLH leaky wave antenna. The traditional CRLH line is electrically modified with varactor diodes similarly to [34] to later utilize it as the feed of a series, linear array. By controlling the *per-unit-length* phase shift of the CRLH, the relative phase of the radiating elements of the array can also be controlled, thus defining the direction of radiation within a plane.

In order to create a two-plane beam steering (2D beam steering), a set of CRLH-based linear arrays are used as radiating elements of a second, transverse linear array. While the CRLH array is used to point in one plane (XZ in fig 1.17), the relative phase between the excitation of each of the CRLH lines controls the pointing in the transverse plane (YZ in fig 1.17). A similar structure is proposed in [54], where the antenna scans in frequency on the positive semi-space.

Whereas the antenna in [54] is based on leaky wave radiation, the structure here proposed is not. Moreover, the lines are shielded to prevent unwanted radiation and be able to control the quantity and polarization of radiation per element. Consequently, a method for coupling energy from the CRLH line out to a radiating element is also introduced. This coupling mechanism can be tuned to divert a particular amount of energy out to a radiating element of arbitrary polarization.

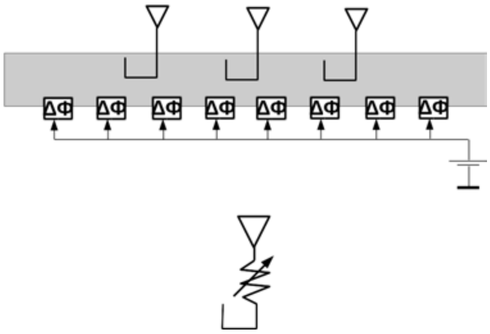

**Fig. 1.18:** The energy is diverted out of the line into radiating elements in a controlled fashion

Due to their relatively low complexity compared to material reconfiguration, the technology of choice is varactor diodes to modify the equivalent circuit of the CRLH cell. Because of the choice of varactors, the coplanar waveguide (CPW) is utilized as the host technology for the CRLH implementation. CPW lines are suitable for connecting Surface Mounted Devices (SMD) or integrated components since the signal and ground planes are in the same level. CPW characteristics, such as impedance, depend strongly on geometrical ratios of its topology, this makes it a very wideband technology and a perfect candidate for this project since the Ku-band designs created in Ku band will be easier to transpose to Ka-band and lower frequency demonstrators will be more significant than a microstrip based technology.

*Originality of this Work*

As mentioned before, a similar structure is proposed in [54], yet the scanning is done in frequency and the design does not include the complexity of electrical reconfiguration.

Regarding the CRLH line, varactor based reconfigurable lines have been presented before in the literature [34]; however, these CRLH were used as leaky wave structures instead of the feed of a linear array. Even if some attempts have been made to analyze a leaky wave antenna as an array [55], their use as an independent beamforming network constitutes a novelty.

Additionally, the line is built on CPW technology instead of microstrip. In order to accurately design a CPW CRLH line, new characterization mechanisms are proposed for the series gap and the shunt stub and a design procedure that focuses on reconfigurability is also proposed.

One last axis of originality in this work comes from the radiation. The energy probing mechanism designed to extract energy out of a shielded CPW line resembles some directional couplers [56, 57], from where part of the inspiration came; nevertheless, the control of impedance is added to the coupling and it is used as a feed of a radiating element.

Summarizing, the originality of the proposed work comes from:

*Originality of this work*

- Use of varactor diodes integrated in a CRLH line as a beamforming network for a linear array (chapter 2)
- The shielding and, especially, probing a CPW line with a novel mechanism that controls the amount of energy drained from the line (chapter 3)
- The reconfiguration oriented design methodology for a CPW CRLH line (chapter 2)
- The characterization methods for the discontinuities utilized in the CPW CRLH line (chapter 2)

# 3 State of the Art CRLH and Co-Planar Waveguide

The advent of metamaterials has caused a revolution in the scientific panorama for more than a decade already. An extensive analysis of CRLH lines can be found in [31] as well as an overview of the early, microstrip based, metamaterials. For Split-Ring Resonator (SRR) based lines, [58] can be consulted and chapter 2 includes a summary of the concepts required for the synthesis of CRLH lines. Since the work presented in the remainder of this text focuses on CPW based CRLH, which is a subdomain of metamaterials that traditionally receives less attention than microstrip, it will be the focus of this *state of the art*.

## 3.1 State of the Art of Composite-Right/Left Handed Metamaterials in CPW

CRLH lines can be etched into CPW planes in a fashion similar to microstrip. Gaps can be etched in the central strip and printed connections to the ground can be placed to create the desired layout [59, 60, 61], as seen in fig 1.19a. The series gap acts as left handed capacitor while the shunt strip behaves as an inductor. Should these not be sufficient, they can be enhanced as shown in fig 1.19b.

A wide variety of topologies can be used to create the *left-handed* contributions of the CRLH. Stronger capacitors can be created by lengthening the capacitor into a distributed component as is the interdigital capacitor [62, 63] (fig 1.19c). Analogously, meander lines produce strong inductors [64] that can be used to create antennas since their layout forces wide CPW side gaps. This is one of the many dualities found in CRLH and metamaterials. As the series gap is the dual circuit of the shunt plate inductor in 1.19a, the interdigital capacitor in 1.19c is the dual circuit of the meander line in 1.19d.

One of the main advantages of CPW for the purpose of this thesis is the suitability of CPW to incorporate external components, as Surface Mounted Device (SMD). This is evident in fig 1.20a [65] and 1.20b [66], where SMD components smoothly connect strip sections and ground plane without the need of via holes or extra printed levels. SMD components can be fixed capacitors and inductors, as in fig 1.20a, to generate the *left-handed* contribution in a controlled manner. SMD can also modify the coupling between elements of the circuit to change the properties of the line in real time. For instance, fig 1.20b shows a set of SRR loading a line whose electrical coupling between the ends of the split ring is modified via external varactors. This way, the resonance frequency of the ring can be modified by means of the diode.

SRR have been presented in metamaterial design since its inception. They are particularly suitable for CPW since they can be etched in the back of the circuit and the magnetic field generated by the CPW line will pass through the ring transversely, creating the coupling required to simulate a series capacitor. It can also be etched in the ground plane, creating a mono-layer structure [67]. Several examples can be found in [68, 69, 70, 71]

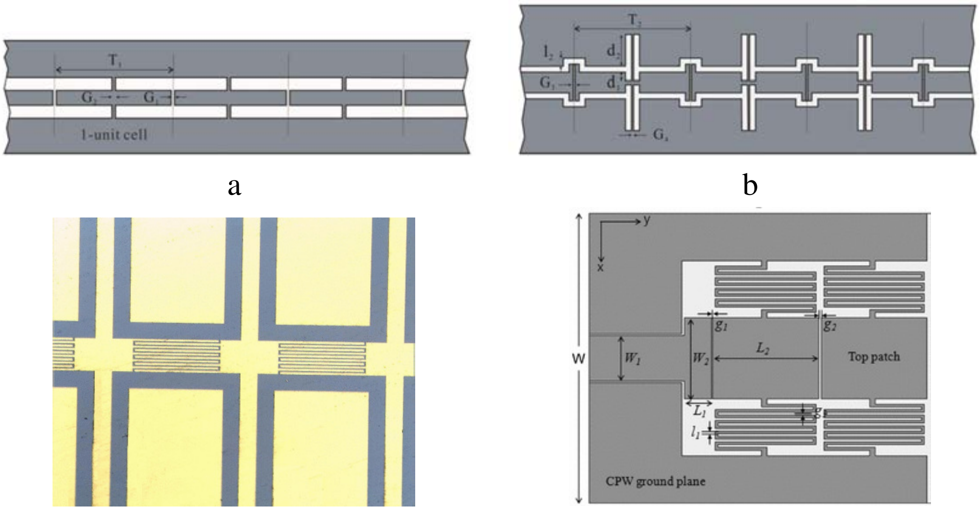

a b c d

Fig. 1.19: CPW based CRLH circuits. a)[60] b) [59] c) [63] d) [64]

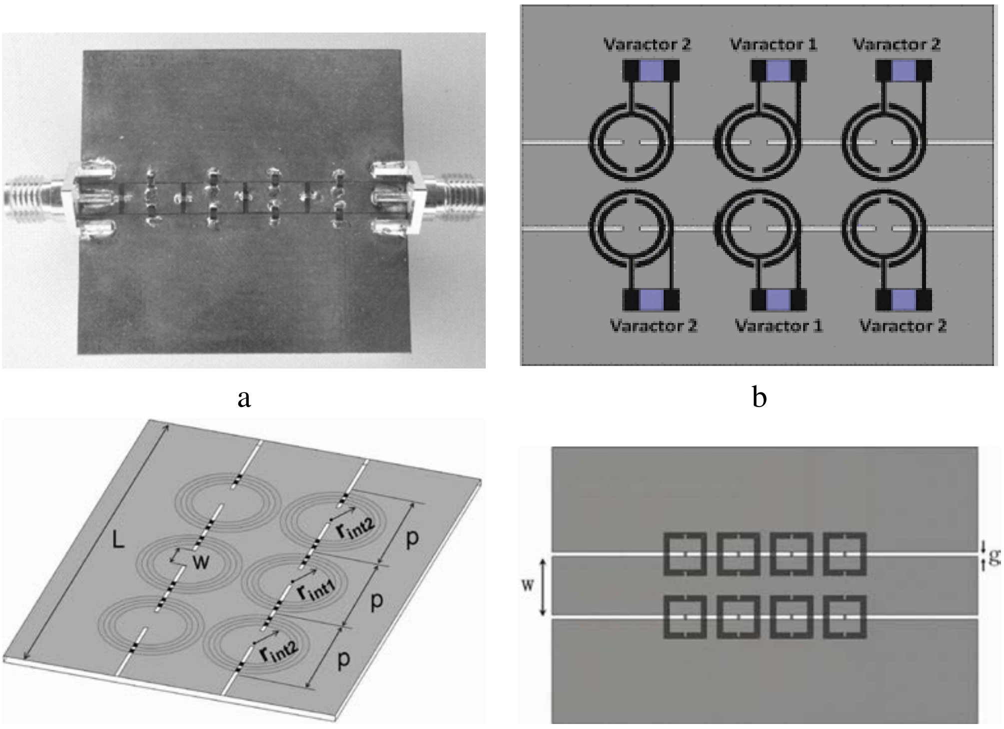

a b c d

**Fig. 1.20:** CPW based CRLH circuits. a)SMD based CRLH line [65]. b) CRLH line with tunable SRR [66].c)CRLH line created with SRR loading [69]. d) [71]

## 3.2 State-of-the-Art on Coplanar Waveguide Discontinuity Characterization

The presence of a discontinuity in a transmission line triggers the apparition of reflected waves and the storage of reactive energy in its vicinity. The intensity and type of the excited modes depends on the geometry of the discontinuity and the modes propagating through the line.

The exact solution of the Maxwell equations for the discontinuity can be extremely difficult to derive. Moreover, when the analysis is focused on the dominant mode, an exact solution may not be required. The higher order modes will act as a perturbation in the propagation of the dominant mode, causing phase shift and impedance transformation. For the case of an sole discontinuity in a mono-modal guide, the problem can be reduced to the characterization of an equivalent circuit plugged in the middle of a transmission line [72]. In that case, a lossless discontinuity can be represented as a LC network.

This characterization is only valid for discontinuities separated a distance long enough to exhaust any higher order modes that may be generated. General conventions usually establish this distance to be larger than about $\lambda/10$ to $\lambda/8$; however, it depends on the discontinuity and the host guide. If some error is assumed, the models can be applied to separations smaller than that but some post-optimization of the circuit for accuracy (full wave simulation) can be expected.

In order to define the value of these equivalent lumped elements, a full resolution of the Maxwell equations could be attempted but it is usually difficult, if not impossible. Variational methods can be used in these situations [72], full-wave electromagnetic simulation or measures. The most straightforward method would be to measure or simulate the transmission parameters at the ends of the access lines and de-embed the circuit using the model for the transmission line.

In 1976 Houdar proposed some intuitive circuit models for a selection of CPW discontinuities [73]. A more precise analysis of some of these models came in 1988 by Simmons and Ponchak [74], where they measured the equivalent circuit of a series gap, a step discontinuity, a bent and an open circuit. It was chiefly an attempt to define models for the discontinuities so they could be exploited in a real circuit.

The magnitude of the parameters in an equivalent circuit of a CPW discontinuity can be also characterized based on numerical simulations. Naghed and Wolff [75] create a three dimensional Finite Difference method that solves a coplanar structure with a gap in the middle. The equivalent capacitances coupling the structure are then evaluated from the charge distribution on the conductors. This method can only evaluate equivalent electrostatic capacitances, therefore only valid for TEM modes propagating through the CPW. This method is able to calculate equivalent capacitances for a very wide range of structures and well suited for discontinuities in which the capacitive effect is dominant.

A wider approach was taken by Dib and Katehi [76], where they use the Space Domain Integral Equation (SDIE) and the method of moments (MoM) to characterize stub like discontinuities and asymmetric CPW discontinuities. An equivalent numerical method that can be used for any type of planar structure can be found in [59].

There are models that also consider the effect of the thickness in the conductor [77, 78, 79] or the effect of non rectangular edges in the conductor print [80]. However this effect is negligible for etching precision much wider than the metallization thickness.

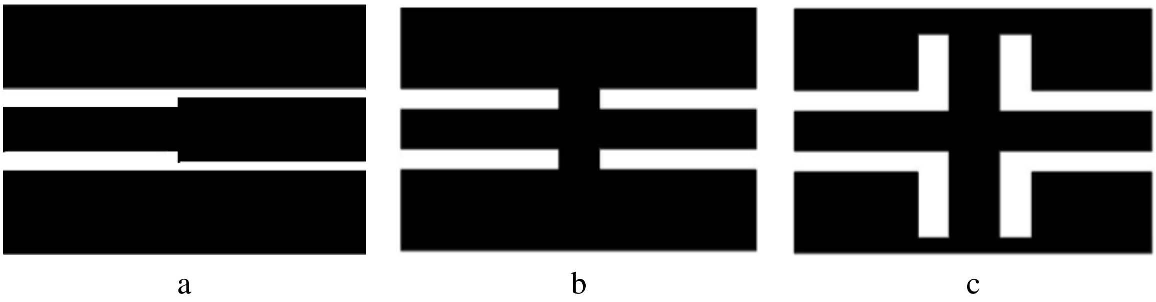

**Fig. 1.21:** Some CPW discontinuities: a) step discontinuity, b) shunt inductor, c) shunt stub

One of the most studied discontinuities is the step in the strip width (fig 1.21a). Many techniques have been attempted to model it, each of them valid for different application ranges [81]. Because of its simplicity, elaborated methods, such as mode matching [82, 83, 84] can be studied. In the mode matching technique [85], the full spectrum of modes —propagating and evanescent— to the left and to the right of the discontinuity are calculated and they are matched at the plane of the discontinuity through the boundary conditions [82].

Another attempt to characterize the step discontinuity comes from Sinclair and Nightingale [81], where they use the conformal transformation —commonly used to analyze the CPW line— to extract an analytical model of the step. This technique was also utilized by Getsinger [86] to analyze the series gap (fig 1.23a) and will be further explained in the next subsection.

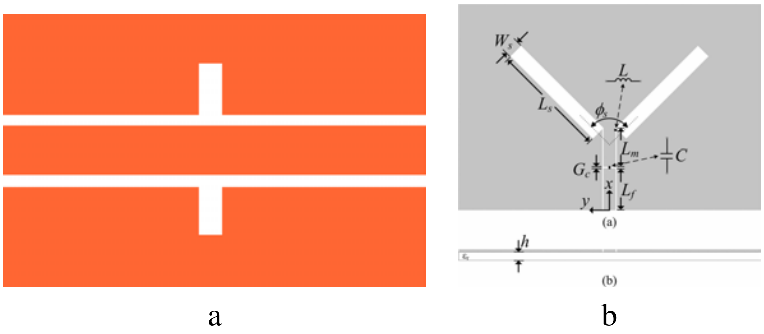

**Fig. 1.22:** CPW fed slot antennas: a) In a line. b) Circularly polarized [87]

A study on some radiating discontinuities can be found in [88], where a rigorous dispersive characterization of radiating slotline stubs is presented. This type of structure creates an asymmetry in the magnetic currents that can be exploited as CPW fed antennas (fig 1.22a). [87] utilizes the slot-line stub to create a compact, circularly polarized CPW antenna (fig 1.22b).

Finally, some alternative techniques involve the use of artificial neural networks (ANN) [89]. In this type of methodology, as it could be the case of the use of genetic algorithms, there is no previous electromagnetic analysis of the system and ANN are tuned to be able to predict the value of a discontinuity based on the knowledge of previous simulations.

### *The series gap*

The series gap is, by far, the most studied two port discontinuity of the CPW line. It is very useful for the design of filters and its geometrical simplicity makes it a prefered target as the first step for the theoretical study of CPW discontinuities. It will be shown in this section that, however simple, the analysis of the CPW series gap is far from straightforward.

Throughout the years, different strategies for analyzing the series gap discontinuity in the CPW line have risen with different accuracies and applicability domains [90, 75, 91, 92, 93, 94, 95], while their approaches differ, all agree on the circuit model that better represents the gap (fig 1.23).

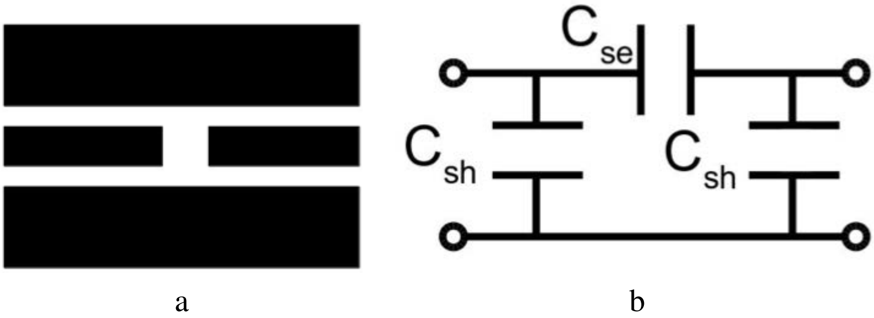

**Fig. 1.23:** Series gap and its equivalent circuit representation

W. J. Getsinger proposed one of the earliest analysis in 1983, based on the inductance of a thin wire and its transposition into a capacitance by means of the Babinet's principle. The dual of a circuit can be obtained by changing all of its inductors by capacitors and vice-versa. The complementary of a planar surface can be found by interchanging the PEC and dielectric surface, i.e. substituting the surface by its dual. [86] explains the relations between a TEM excited planar circuit and its complementary and maintains that the equivalent circuit of the complementary of a planar geometry is the dual of the original geometry. Although the model is accurate for a wide range of geometries and frequencies, it does not predict the value of the shunt capacitor $C_{sh}$ (fig 1.23).

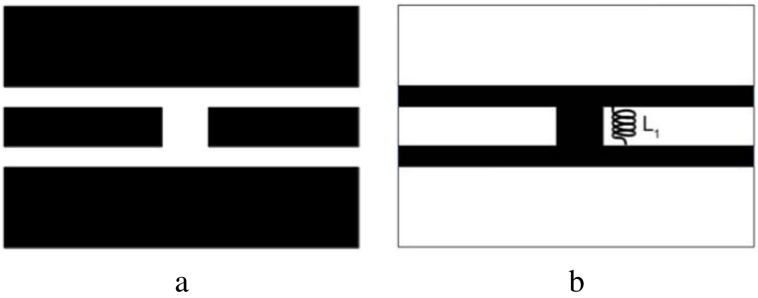

**Fig. 1.24:** Series gap and its dual circuit

In 1995 Gevorgian *et al.* [95] used a conformal mapping approach that leads to an accurate electromagnetic analysis of the problem. Under the assumptions of infinitely thick homogeneous substrate and zero thickness strips, Gevorgian argues that the fringing fields producing the series and shunt capacitors Cse and Csh (fig 1.23) are a consequence of the extra charge accumulated on the strips of the CPW. Under the assumption that those charges extend far beyond the gap, Getsinger extends the line to a sufficient large distance and places magnetic walls in the accesses of the line. Then, derived closed expressions for the series and shunt capacitances based on conformal mapping techniques —Schwzartz-Christoffel and Hilberg transformation—, akin to those used in the analysis of the CPW line [95].

Nevertheless, Gevorgian assumes infinitely thick substrate and uniformly charged conditions. It can be argued that, in the absence of a ground plane printed in the back of the substrate and for substrate heights much larger than the slot width, the infinitely thick substrate condition is true. However, as it will be discussed in Chapter 2, the uniformly charged condition may not hold true for increased frequencies.

Other analysis have also been performed [90], mostly for filter applications, based on observations [74, 96], numerical analysis [75, 93, 97], or Neural Networks [89] yet no universal model has preponderant validity over the rest. Still, readily available models only exist for the most basic discontinuities and not for a wide range of circuits, as is the case for microstrip. A good summary of models and analysis for the most common CPW discontinuities models can be found in [90].

## 4 Commercial Varactor Diodes

A brief description of the use and modeling of varactor diodes as tunable capacitors is described here. For a more complete description of the theory behind varactors, please refer to appendix D or to the references [98, 99].

A varactor diode is basically the union of a donor doped semiconductor $N$ and another semiconductor highly doped with acceptors $P^+$. When the excess of electrons in the $N$ region meet the excess of holes of the $P$ region, a depletion region is created around the junction. This depletion region is a non conductive zone between two conductive materials, creating a capacitor. When the diode is reversed biased (fig 1.25), the size of the depletion region can be controlled with the biasing voltage, which an be seen as a capacitance controlled by voltage.

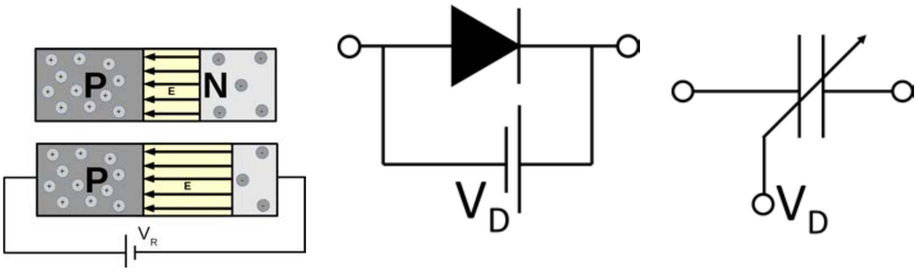

a b c

**Fig. 1.25:** a)PN junction. b) Reverse biased diode c) Equivalent circuit

A diode as described here is commercially available as *bondable chip diode*; however, it requires precise soldering techniques to mount it in a circuit. A common way to integrate the diode in a CPW line is to use Surface Mounted Device (SMD) packaging (fig 1.25). This type of packaging allows to solder the diode into a printed circuit with conventional soldering equipment but introduces parasitic effects that make the varactor deviate from the operation described before.

The most important parasitic effects of the packaging can be seen in fig 1.26. The packaging capacitance is added in parallel to the capacitance of the junction, but reduces the dynamic

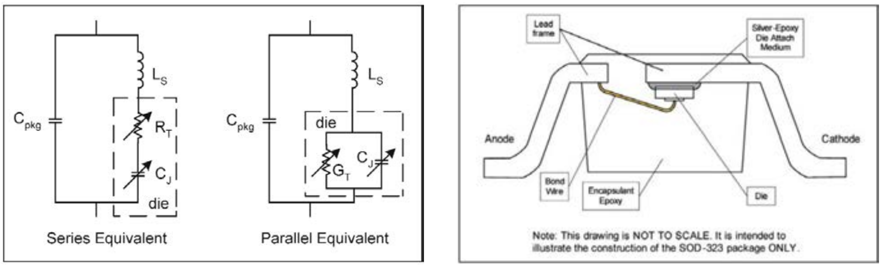

a b

**Fig. 1.26:** a) Equivalent circuit of a single bond chip diode mounted in a generic package b) Cross section of a single bond chip diode mounted in a generic package

| Diode | $R_T(\ )$ | $L_S(nH)$ | $C_{pkg}(pF)$ | Dynamic Range (pF) $(C_j)$ |
|---|---|---|---|---|
| SMV1405-079LF | 0.8 | 0.7 | 0.29 | 0.63-2.67 |
| SMV1408-079LF | 0.6 | 0.7 | 0.21 | 0.95-4.08 |
| SMV1413-079LF | 0.35 | 0.7 | 0.3 | 1.77-9.24 |
| SMV1430-079LF | 3.15 | 0.7 | 0.13 | 0.31-1.24 |
| SMV1493-240 | 0.5 | 0.5 | 0 | 7.1-28.7 |
| SMV1494-240 | 0.5 | 0.5 | 0 | 14.7-57.8 |

**Table 1.3:** Summary of diode characteristics

range of the total capacitance of the varicap. The series inductance is more problematic since it introduces a resonance that can cancel the overall reactance of the varactor at high frequencies. As the matter of a fact, most varactor diodes will not perform adequately in Ku band when they are mounted in their packaged form. Fig 1.27 shows the variation from the operation as a bondable die at different frequencies. In this report, the die capacitance will be taken as a reference and only in lower frequency bands (L, C) will a SMD mounted device be used. For higher frequencies (Ku), diodes directly mounted on the CPW line will be required.

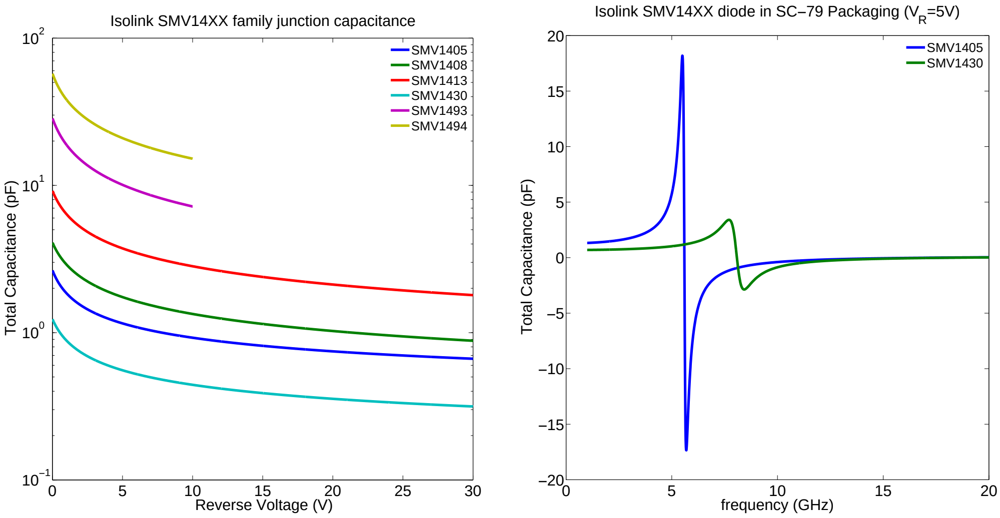

a b

**Fig. 1.27:** SMV family junction a) capacitances and b) self resonance

# Objectives of the Thesis

The objectives of this thesis are to define a technology that enables electrical beam steering for receiving *satcom* antennas *on the move*. To do that high-gain, low profile, dual polarized, wide-band antennas in Ku band are required.

Because of the time constraints imposed in a PhD and the high ambition of such requirements, the wide-band parameter will be waived. Possible techniques to widen the band will be presented in the *Way-Forward* section.

Due to schedule and budgetary constraints, a full system is not an objective of this thesis. Proof of concept will be presented in terms of full-wave simulations and demonstrators for the most critical parts of one-dimensional scanning. As explained in this chapter, the scanning in the transverse plane can be easily done with traditional beam forming techniques.

Although the concepts developed hereafter will be proven through simulations, a road-map for experimental validation will also be presented detailing how to verify such concepts.

Because of the viability of the available manufacturing processes, prototype validation will be done in L band (2GHz) and full-wave simulations will be presented both in L and Ku band.

Table 1.4 summarizes the generic satcom specifications that will be used as the reference horizon for the technology studied in this thesis. Since the objective is not to develop a full antenna, there will be not a final product that fulfills the specifications one by one; rather, this thesis defines a technology that could be used to achieve such specifications.

| Parameter | Value | Parameter | Value |
|---|---|---|---|
| Gain | >30dB | Height | Low |
| Polarization | Circular/Dual | Reconfiguration | Varactor based |
| Azimuthal Steering | $0-360°$ | Elevation Steering | $0-60°$ |
| Bandwidth | Narrow | Steering | full-electrical |

**Table 1.4:** General specifications to use as reference

*Objectives of the thesis*

- Study and propose a novel low profile architecture of a one plane scan radiating line that could be used as the building block of a SATCOM on-the-move full steerable antenna.

*Proposed Methodology*

- Select a planar technology for the radiating line.
- Integrate varactors on CRLH metamaterial cells to control the phase of the line and, ultimately, the scanning direction.
- Release the bandwidth constraint as a first step.
- Dissociate the phase control of the line from the radiating elements.
- Carry out some experimental validations.
- Propose a design methodology based on circuit design and statistical models to reduce the full-wave simulation time.

# Conclusion

In this section, the requirements for a GEO satcom ground antenna *on-the-move* have been investigated. It has been complemented with a *state of the art* of beam steerable satcom ground antennas. Once the limits of the existing technologies have been understood, the objectives for this thesis have been defined and an antenna architecture has been proposed.

The proposed antenna will be studied throughout this report and consists of a CRLH transmission line that acts as a beam forming network for a linear array. The method for steering used is the incorporation of SMD varactors, chiefly for that reason CPW was chosen as the base manufacturing technology. The *state of the art* of CPW and varactor technology has also been included in the report because of its relevance.

In the next chapter, the beam forming network will be designed. As explained before, the beam steering is done with a varactor-controlled transmission line that creates phase profile required to feed the radiating elements. Chapter 2 deals solely with a single line that creates steering in a single plane. The radiating element is discussed in chapter 3 and its integration into the CRLH line in chapter 4. The extension to full space beam steering will be dealt with in the *Way Forward* section of chapter 4.

# Phase-Reconfigurable Coplanar CRLH Transmission Lines

# 2

## Contents

## Objectives

This chapter describes the methodology and tools required for the development of the reconfigurable transmission lines that will be used as feed lines for the steered array. The delay lines are based on CRLH transmission lines, hence this chapter begins in section 1 with a description of the characteristics and design of such lines. The design of CRLH lines requires accurate models of the discontinuities that constitute them, in this case series gap capacitors and shunt stubs are the preferred choice. These discontinuities are studied in section 2. Finally, a design procedure is proposed in section 3 along with some examples.

## 1 Coplanar Composite-Right/Left Handed Transmission Lines

During the past two decades there has been an increasing number of publications on the so-called metamaterials. Although there are some detractors of the metamaterial that insist that they do not bring any novelty to the design of microwave structures [100], the analysis and design of metamaterials is undoubtedly a powerful tool for the design of microwave structures.

The use of the theory of metamaterials allows the synthesis of electromagnetic behavior in a wide range of frequencies, only limited by the available manufacturing technology. Some of the behaviors achieved by metamaterials are exotic surface impedances —such as PMC-like surfaces [27]—, anisotropic materials [101] or the popular invisibility cloaking for radiofrequencies [102].

One of the earliest definitions of metamaterial can be found in [31]:

> "Artificial effectively homogeneous electromagnetic structures with unusual properties not readily available in nature."

By *effectively homogeneous structure* is understood any lattice, periodic or non periodic whose average cell size $p$ is much smaller than the guided wavelength. In effectively homogeneous structures, the spatial variation is so small that the electromagnetic wave can only react to the structure as a whole and not to its rapid spatial variations. Much like how radio-frequencies react to rain or fog, an artificial structure can be built so its structural cell size is so small that its electromagnetic behavior can be characterized in terms of homogeneous constitutive parameters $\epsilon$ and $\mu$. This can be applied to any dimensions from one-dimensional (linear) metamaterial [103, 104] to two-dimension (metasurfaces) [105], three-dimensions (bulky metamaterials) [106] or even four-dimensional (spacetime metamaterials) [107]. However, this chapter will be restricted to linear metamaterials.

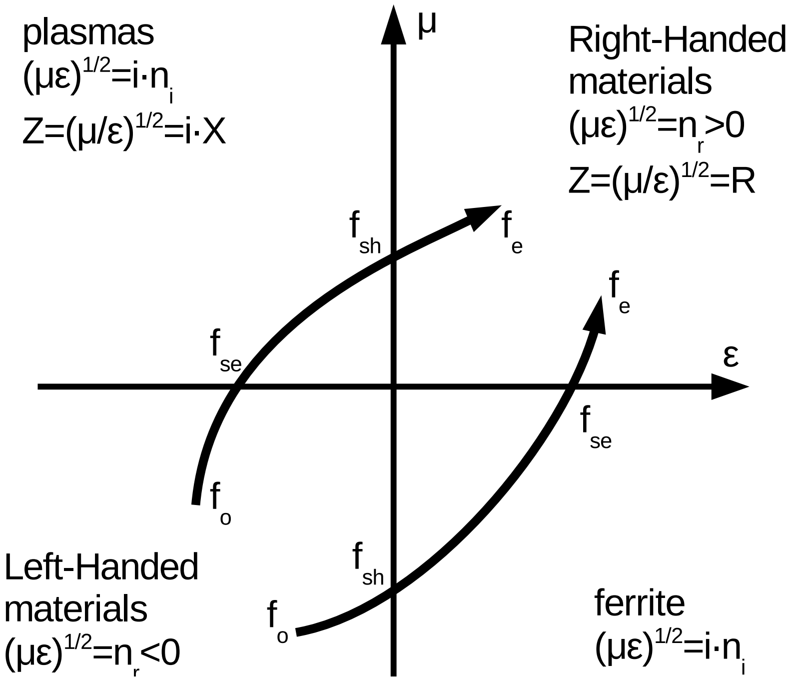

**Fig. 2.1:** $\mu - \epsilon$ diagram. Traditional materials are plotted in the first quadrant ($\mu, \epsilon > 0$) and left-handed materials in the third quadrant ($\mu, \epsilon < 0$). A CRLH line typically moves up-right in this diagram as the frequency increases.

While in nature there are materials with negative $\epsilon$ and $\mu$, such as plasmas and ferrites respectively, no materials have been found yet with simultaneously negative $\epsilon$ and $\mu$. Prior to the advent of metamaterials, Veselago [108] speculated that materials with negative $\epsilon$ and $\mu$ would allow transmission of electromagnetic waves with the peculiar characteristic of having a negative refraction index $n = \sqrt{\epsilon\mu}$. These materials are known as *Left-Handed* (LH) materials, as opposed to the traditional, *Right-Handed* materials. Fig 2.1 shows all the possible combinations of values and sign for $\epsilon$ and $\mu$. The constitutive parameters in any feasible metamaterial show dispersion and grow monotonically with frequency [31]. As shown in fig 2.1, when $\epsilon$ and $\mu$ evolve from the LH region to the RH region, a given CRLH structure almost inevitably passes through a region of imaginary refraction index where propagation is not allowed, called the band-gap. The only exception is when both $\epsilon$ and $\mu$ change sign at the same frequency, in that case, waves propagate in zero $n$ conditions and the structure is known as balanced. A material presenting zero $n$ propagation could be utilized to feed a linear array where all its elements are excited in phase.

One of the most popular linear metamaterials is the CRLH line. The CRLH line is based on the principle that an infinitesimally small slice of a LH loaded transmission line would have an equivalent circuit dual to that of a RH loaded. By periodically introducing capacitors $C_L$ and shunt inductors $L_L$ in a line, a combination of LH and RH behavior can be synthesized. While the series capacitor and shunt inductor generate the LH behavior, the host transmission line inserts right handed parasite shunt capacitors $C_R$ and series inductors $L_R$ that account for the RH behavior.

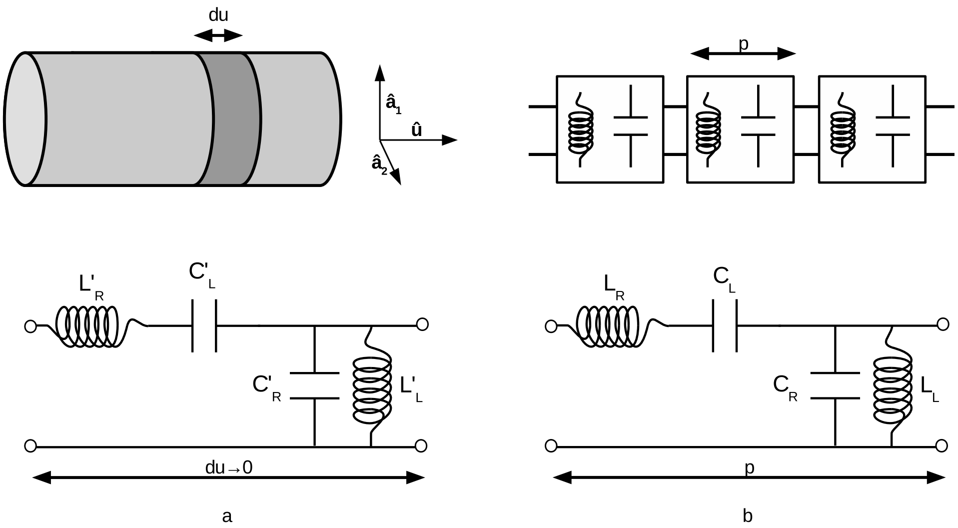

**Fig. 2.2:** A periodic structure can be understood as a cascading of bi-ports. Each of the bi-ports of the ladder can be characterized by any of their equivalent matrices, however transmission matrices are more efficient for its analysis

Fig 2.2 shows the per-unit-length values —which appear primed in equations 2.1-2.3— of an hypothetical infinitesimally small slice of transmission line. A real structure, however, has a footprint of size $p$ and whole values of inductance and capacity —not primed–. Applying the telegraphist equation for the cell, an effective propagation constant can be defined as

$$_{eff} = \sqrt{Z\ Y} = \sqrt{ZY}\frac{1}{p} \tag{2.1}$$

$$Z = \quad L_R - \frac{1}{C_L} \quad = \quad L_R - \frac{1}{C_L}\ \frac{1}{p} \tag{2.2}$$

$$Y = \quad C_R - \frac{1}{L_L} \quad = \quad C_R - \frac{1}{L_L}\ \frac{1}{p} \tag{2.3}$$

The series and shunt resonances frequencies $_{se}$ and $_{sh}$ can be defined as the frequencies in which $Z$ and $Y$ change sign respectively:

$$_{se} = \frac{1}{\sqrt{C_L L_R}} \tag{2.4}$$

$$_{sh} = \frac{1}{\sqrt{C_R L_L}} \tag{2.5}$$

These are important because they mark the transitions from left handed to right handed bands.

From eq. (2.1) it can be inferred that for a metamaterial line to have a LH propagation band it is sufficient to incorporate a $C_L$ and a $L_L$ contribution. This could be achieved directly by inserting series capacitors and shunt inductors in a line [103] or indirectly, with resonators [104] or corrugated surfaces [109]. To avoid Bragg resonances, the size of the cell needs to be much smaller than the wavelength, as a rule of thumb this is commonly accepted to be $p < \lambda_g/4$. Moreover, when the line is used as a feed for a phased array, it is convenient to think in terms of the phase shift per cell $\Delta\phi = \beta_g p$ rather than physical size, $p$. Consequently, the homogeneity condition can be written in one of these forms:

$$p < \lambda_g/4 \tag{2.6}$$

$$\Delta\phi < \quad /2 \tag{2.7}$$

Note that the electrical size is equivalent to the phase shift introduced by that TL of the same length as the cell. The actual phase shift introduced by the CRLH cell is

$$\Delta\phi_{eff} = \beta_{eff} p = Im \quad \sqrt{Z\ Y}\ p \quad .$$

Metamaterials, as quasi-homogeneous structures, do not require periodicity. However, there is a well developed theory of periodic structures. Additionally, the most suitable structure for the feed of an uniformly distributed array is a periodic structure. Therefore, in the next section, a summary of the theory of guiding periodic structures will be presented.

## 1.1 Periodic structures

An infinitely long periodic structure can be analyzed as a cascade of bi-ports like the one in fig 2.3. Each of the bi-ports can be analyzed as an independent structure as long as the cells that conform the ladder are connected through transmission lines long enough to exhaust high order modes, preventing inter-cell coupling. The bi-ports, identical to each other, can be characterized by any of their equivalent matrices,*e.g.* Z, Y or H; however, the ABCD matrix is more convenient for the analysis of periodic structures. For instance, the ABCD matrix of a bi-port.

$$\begin{matrix} V_i \\ I_i \end{matrix} = \begin{matrix} A & B \\ C & D \end{matrix} \cdot \begin{matrix} V_{i+1} \\ I_{i+1} \end{matrix} \tag{2.8}$$

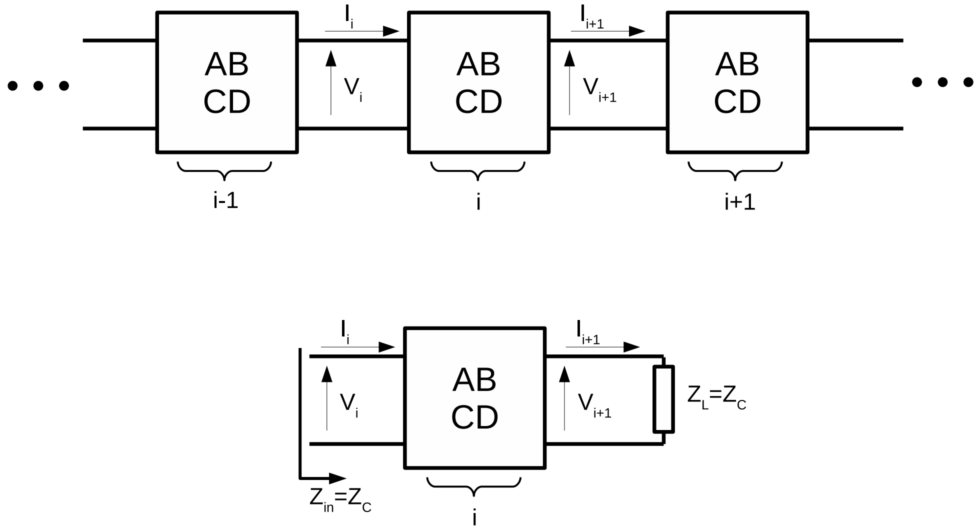

**Fig. 2.3:** Periodic cell. The cascading of a cell periodically can be described in terms of the unitary cell.

in such a structure, a propagating wave should verify the following relation

$$V_{i+1} = V_i \cdot e^{-j \quad p} \tag{2.9}$$

$$I_{i+1} = I_i \cdot e^{-j \quad p} \tag{2.10}$$

or

$$\begin{matrix} V_i \\ I_i \end{matrix} = \begin{matrix} e^{j \quad p} & 0 \\ 0 & e^{j \quad p} \end{matrix} \cdot \begin{matrix} V_{i+1} \\ I_{i+1} \end{matrix} \tag{2.11}$$

where $\quad = \alpha + j\beta$ plays the role of propagation constant. Combining eq. (2.8) and (2.11), the non-trivial solution to this equation system is

$$\begin{matrix} A - e^{-j \quad p} & B \\ C & D - e^{-j \quad p} \end{matrix} = 0 \tag{2.12}$$

which can be expressed as

$$\cosh \quad p \ = \cosh \ \alpha p + j\beta p \ = \frac{A+D}{2} \tag{2.13}$$

in terms of the Z parameters as

$$\cosh \quad p \ = \frac{Z_{11}+Z_{22}}{2Z_{12}} \tag{2.14}$$

To better understand the meaning of this equation, the complex variable $a + jb = \cosh \quad p$ can be defined, and the cosh can be expanded into real and imaginary parts

$$a + jb = \cosh \quad p \ = \cosh \ \alpha p \ \cos \ \beta p \ + j \sinh \ \alpha p \ \sin \ \beta p \ = \frac{Z_{11}+Z_{22}}{2Z_{12}} \tag{2.15}$$

For a loss-less structure, $\{Z_{ij}\} = 0$, and thus $b = 0$, which can only be achieved through either $\alpha = 0$ or $\beta = m$ . On the other hand, $a$ can take on any value. The following cases can be considered

$$\begin{array}{llll} i & a < -1 & \alpha > 0 & \beta = \pm \\ ii & -1 < a < 1 & \alpha = 0 & |\beta| < \\ iii & a = 1 & \alpha = 0 & \beta = 0 \\ iv & a > 1 & \alpha > 0 & \beta = 0 \end{array} \tag{2.16}$$

Cases ii and iii have $\alpha = 0$ and are propagative. The fact that $\beta = 0$ in case ii means that the fields at the connections between cells is always in phase but, unlike for the standing wave case, the energy propagates with a velocity $v_g$. In cases i and iv the propagation is forbidden in the line. Case iv is commonly known as the band-gap and in CRLH lines occurs at the frequencies where one of the two constitutive parameters $\epsilon$ or $\mu$ changed from negative to positive but the other one did not, resulting in an imaginary effective refractive index. In lines where $a > 1$ for a band, there is a discontinuity in the imaginary part of the propagation constant.

The power propagating through a periodic line is described by the real part of the Poynting vector [72],

$$\frac{1}{2} Re\{S\} = (W_e + W_m) \frac{v_g}{p} \tag{2.17}$$

where $W_e$ and $W_m$ are the stored electric and magnetic energy respectively and

$$v_g = \ \frac{d\beta}{d} \ ^{-1} \tag{2.18}$$

Therefore, only for continuous $\beta$ functions, $v_g$ is defined and propagation of energy is allowed in the line. In the case of CRLH lines, $\beta = 0$ is propagative when case iv is avoided by forcing case iii to occur only at one single frequency. Such structures are usually called balanced structures and satisfy the following condition:

$$ {}_{se} = \ {}_{sh} \tag{2.19}$$

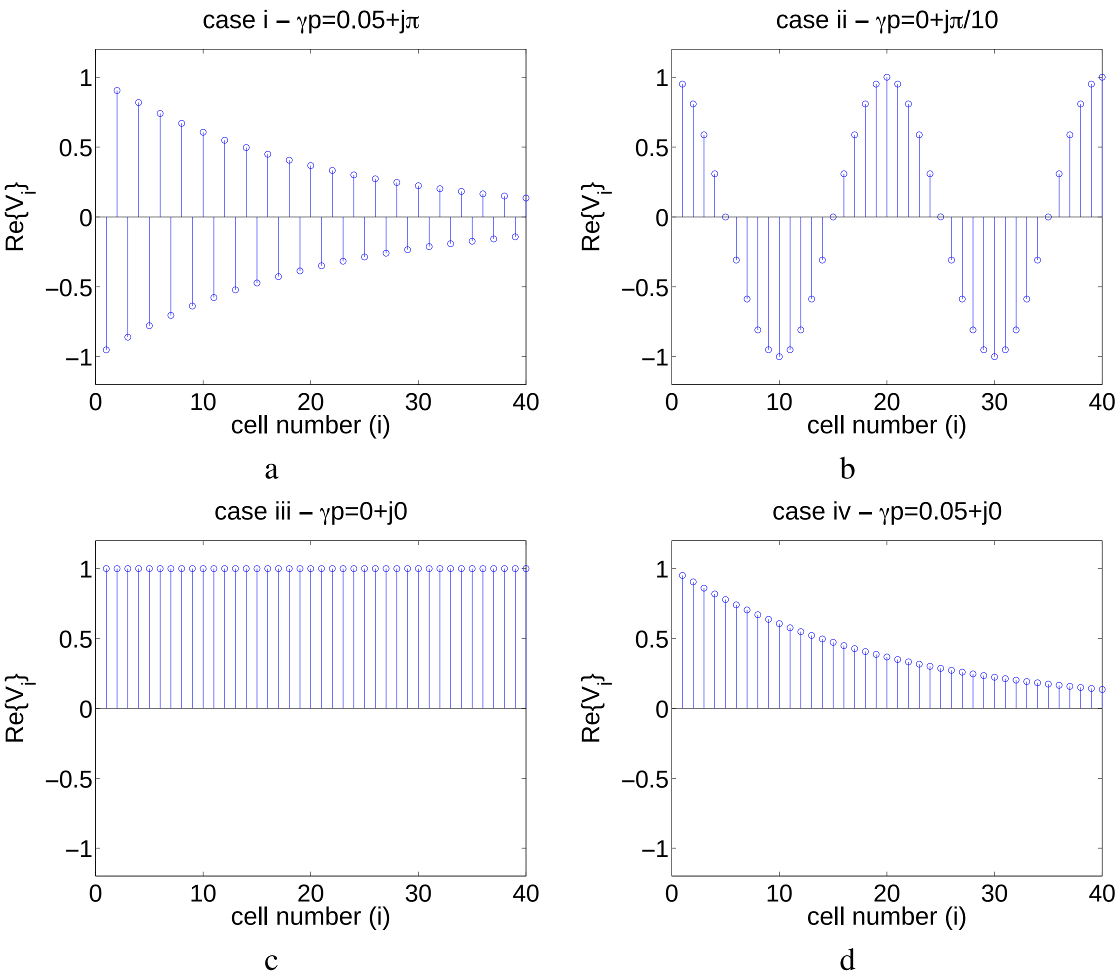

a b c d

**Fig. 2.4:** Voltage at the junction of the cells in a periodic structure for different cases

Since the *cosinus* is an even function, there is no way to distinguish whether its argument, $\beta$, is positive or negative. For the CLRH line, the $\beta$ function is composed of reactance functions, as seen in eq. (2.1). After Foster's reactance theorem [110, 111], reactances grow monotonically with frequency and so $\frac{d\beta}{d} > 0$. This rule may not apply when the capacities and inductances in the model show dispersion, especially the LH ones. However, for small bandwidths it can be used as a rule of thumb to distinguish between the LH and the RH bands.

Another parameter of interest for the propagation of waves in periodic media is the characteristic impedance. Since there is not an uniform $E/H$ ratio, a true characteristic impedance of the artificial transmission line cannot be defined. Nevertheless, there are parameters that mimic the behavior of a characteristic impedance if some precautions are taken. For instance, the characteristic impedance of a periodic cell, also called the Bloch impedance is defined as the impedance that is seen at the input of the cell when the cell is loaded with that same input impedance,

$$Z_{in}|_{Z_L=Z_c} = Z_c \tag{2.20}$$

$Z_c$ is equivalent to the characteristic impedance of a transmission line. Indeed, when the periodic line is loaded with $Z_c$, the ratio $V/I$ or $E/H$ is conserved along the line. This is also the case in a infinitely long periodic line. Nevertheless, the value of $Z_c$ depends on the point of the cell at which the impedance is considered. To understand this, a cell could be imagined to be composed of a discontinuity with two transmission line accesses of impedance $Z_w$ and propagation constant $_w$ (Fig 2.5).

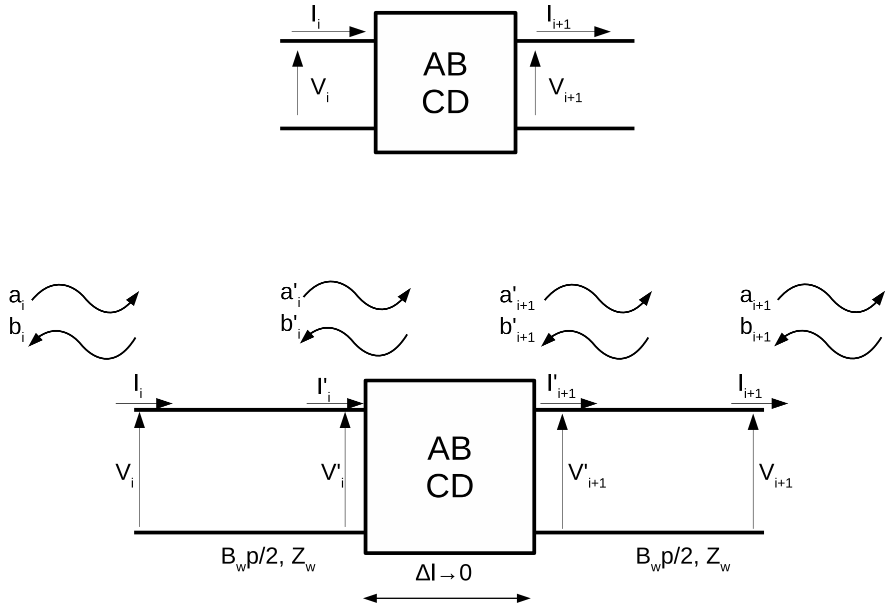

**Fig. 2.5:** Periodic cell as a bi-port accessed by transmission lines

The impedance, as measured at two different points $Z_{c,1} = Z_c(x_1)$ and $Z_{c,2} = Z_c(x_2)$ are related by the following equation

$$Z_{c,1} = Z_w \frac{Z_{c,2} + Z_w \tanh[\ (x_2 - x_1)]}{Z_w + Z_{c,2} \tanh[\ (x_2 - x_1)]} \tag{2.21}$$

therefore it will only be equivalent to the characteristic impedance if it is measured always at the same point for each cell. Keeping that in mind, and using eq. (2.20), the characteristic impedance can be calculated as

$$Z_c^+ = \frac{Z_{11} - Z_{22}}{2} \pm \quad \frac{Z_{11} + Z_{22}}{2}^{\ 2} - Z_{12}^2 \ ^{1/2} \tag{2.22}$$

For the backwards propagating wave, with propagation constant $^{-} = -$ , the characteristic impedance is

$$Z_c^- = \frac{Z_{22} - Z_{11}}{2} \quad \frac{Z_{11} + Z_{22}}{2}^{\ 2} - Z_{12}^2 \ ^{1/2} \tag{2.23}$$

For a symmetric network, $Z_{22} = Z_{11}$ and the forward and backwards propagation constants can be described as

$$Z_c^{\pm} = \pm \sqrt{Z_{11}^2 - Z_{12}^2} \tag{2.24}$$

Finally, the characteristic/Bloch impedance can be calculated with the $ABCD$ parameters

$$Z_B = \frac{(A-D) + \sqrt{(D-A)^2 + 4BC}}{2C} \tag{2.25}$$

The characteristic impedance is important because it relates to the power transmission. If the line is not loaded with $Z_c$, undesired reflections will appear along the line. It is also important to ensure that the mismatch at the input of the line is minimum, otherwise there will be no energy injected into the line.

It can be shown [72] that the input reflection coefficient of the total N cell line is

$$_{in} = {}_{L}e^{j2\beta_{eff}pN} \tag{2.26}$$

where $\beta_{eff} = \{\ \}$ is the effective propagation constant and $_{L}$ is the reflection coefficient at the end of the structure

$$_{L} = \frac{Z_L - Z_C^+}{Z_L + Z_C^+} \tag{2.27}$$

This conclusion has two major implications. Firstly, there will be mismatching at the input of the structure whenever the end is not loaded with $Z_c$. This can be avoided with an input matching network. Secondly, some power will travel backwards, radiating a second *primary* lobe through the periodic structure. Since the cells considered are reciprocal and symmetric, this radiation will be symmetrically opposite to the main one and would look like a secondary lobe.

When the mismatch is small, the line could be just matched at the ends through matching networks and the secondary effects are negligible. If the mismatch is too big, the power never reaches the end of the line. Consequently, the array does not radiate the energy with the required efficiency and sidelobes might appear.

## 1.2 CRLH Realizations based on periodic structures

A CRLH line can be created by periodically inserting *LH* components in a transmission line. The *host* transmission line naturally imposes a *RH* contribution to complete the CRLH structure.

There are several strategies to generate *LH* components within the line. Some modify the electrical or magnetic behavior of the substrate (as in SRR) but it can be created directly as series capacitors and shunt inductors. Fig 2.7 shows a CPW CRLH cell, where the series capacitor is a gap in the central strip and a shorted stub generates the shunt inductor. As long as the cell is small with respect to the guided wavelength, the behavior is that of a CRLH line.

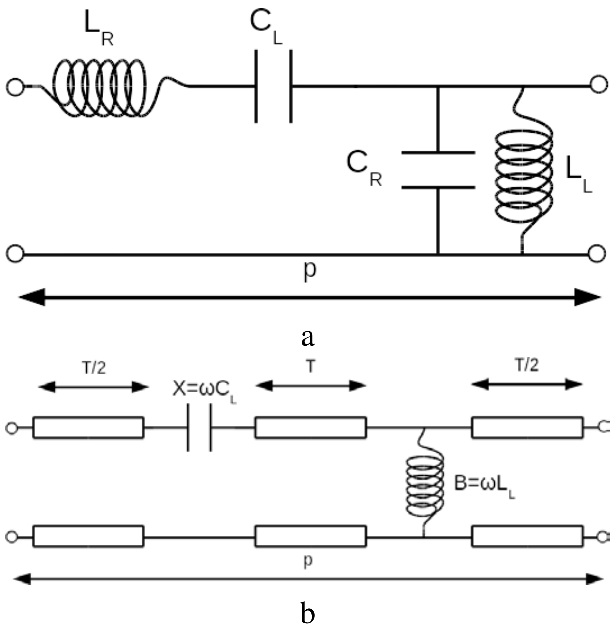

**Fig. 2.6:** CRLH periodic cell equivalent circuits. a) Compact model, b) model for small discontinuities

When the cell is much smaller than the wavelength, it can be analyzed as the series circuit in fig 2.6a. In that case, the equivalent circuit elements can be derived from equations (2.2) and (2.3). However, for cell sizes closer to the homogeneity limit and circuit elements spatially narrow, the model in fig 2.6b can better describe the behavior of the cell. The design equations for this type of cell model can be found in [59].

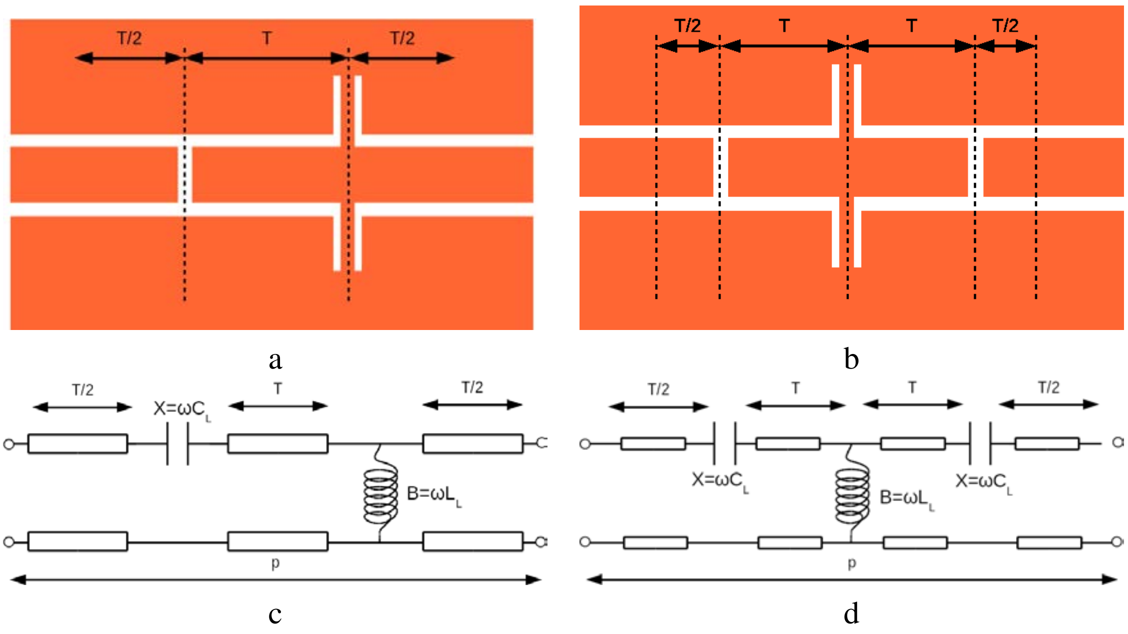

**Fig. 2.7:** Different cell types. a) Traditional CRLH cell adapted to coplanar waveguide and c) equivalent circuit. b) Cell with two LH capacitors and one LH inductor and d) equivalent circuit.

The architecture of the cell can be enriched [112] with discontinuities to create different and more complex behaviors. When two capacitors are included in series in the line, the value of each can be twice the value of the capacitor in the conventional cell. This is helpful when the range of values that can be synthesized is limited by technology. However, in [112] the scanning range is halved —augmenting the scanning dispersion $\frac{\beta}{}$— because the distance between discontinuities is kept as more discontinuities are inserted.

Here, a modification to that structure is proposed in fig 2.7b. The difference with [112] is that the overall dimension of the double capacitor plus inductor (or viceversa) remains much smaller than the wavelength. This is achievable with discontinuities of small dimensions and allows to use larger values of capacitance while keeping similar beam squint properties as the traditional CRLH line. Additionally, the layout of that cell creates regions that are electrically insulated in DC, which is very convenient for the biasing of varactors. More on the biasing of varactors will be discussed in the next chapter.

So far, the theory behind CRLH lines has been lied out. In order to synthesize CRLH lines, a reliable model of the LH discontinuities in CPW is necessary. Hence, an effort remains to be made in order to generate accurate models for series capacitors —*e.g.* gaps in the line— and shunt inductors —*e.g.* shorted stubs—.

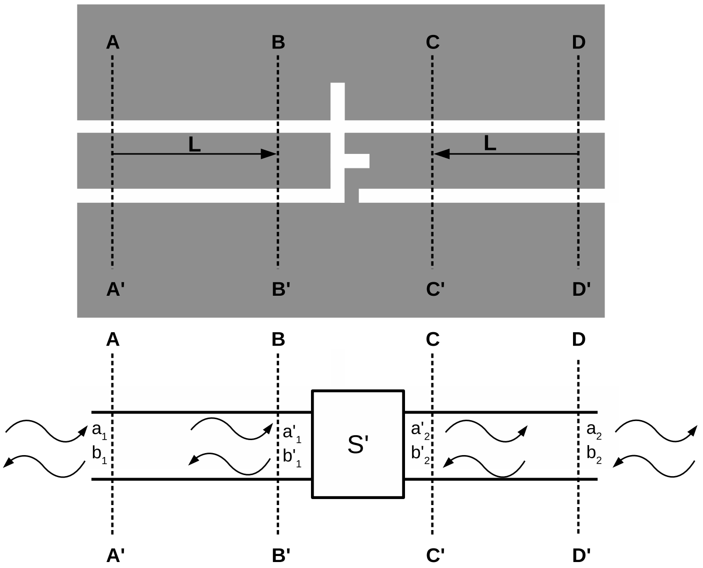

**Fig. 2.8:** Discontinuity characterization. The discontinuity can be analyzed as a dimensionless bi-port accessed by transmission lines.

# 2 Characterization of CPW Discontinuities

Historically, micropstrip technology has attired more attention than CPW. There is an extensive bibliography of microstrip circuits, filters and discontinuities. Although the literature is not devoid of CPW based publications, this technology lacks the wide coverage of microstrip. Due to the advatages of CPW over microstrip —treated in chapter 1— during the past few decades, a considerable number of studies on CPW have been indeed published [86, 95, 77, 78, 79, 75, 90, 113, 76]. Nevertheless, the behavior of complex CPW discontinuities is difficult to model and most of the literature primarily addresses the simplest discontinuities, such as the step discontinuity in fig 2.10a [82], one-port discontinuities [90] (figs 2.10e and in fig 2.10f) or the series gap in fig 2.10d [86, 95].

In order to model the behavior of discontinuities in CPW —or any other transmission line— a full analytic solution of CPW discontinuities is cumbersome and, oftentimes nearly impossible to derive. Fortunately, under certain conditions,the analysis of discontinuities can be greatly simplified. If the discontinuity is flanked by transmission lines that are long enough to exhaust higher order modes —this is typically the case for lines longer than $\lambda_g/8$ to $\lambda_g/10$—, the discontinuity can be modeled as a dimensionless circuit with two accessing transmission lines. The side transmission lines run down to a reference plane that can be set arbitrarily (fig 2.8) as long as the same dimensions are kept once the discontinuity is placed into the circuit.

There, the S parameters of the whole structure can be determined with full-wave simulation or measurements and the S parameters of the inner circuit, $S$ in fig 2.8, can be easily de-embedded with a transmission line model [72, 114]:

$$[S] = \begin{matrix} e^{-j\beta_w L} & 0 \\ 0 & e^{-j\beta_w L} \end{matrix} \; [S\ ] \; \begin{matrix} e^{-j\beta_w L} & 0 \\ 0 & e^{-j\beta_w L} \end{matrix} \qquad (2.28)$$

The discontinuity $S$ matrix can then be transformed into a  or $T$ network to simplify its use within a circuit. The choice between  and $T$ is somewhat arbitrary; however, some geometries are better suited for one or the other. For instance, a discontinuity like a plate connecting the central strip to the ground presents a strong concentrated shunt phenomenon and can be modeled more accurately over a larger bandwidth with a $T$ network than a  network [115]. On the other hand, a discontinuity like the series gap (fig 2.10d) has a strong series coupling and smaller fringe coupling with the ground plane, what makes it more suitable for a  network.

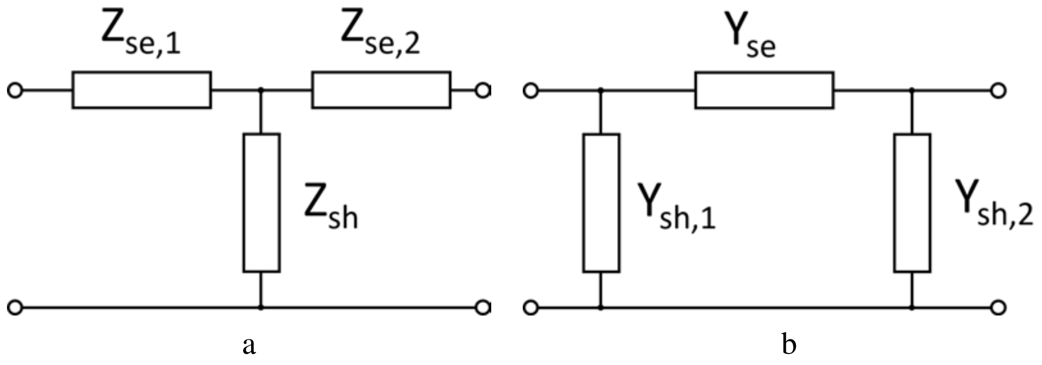

**Fig. 2.9:** a)  network b) T network

More precisely, from the de-embedded $S$ matrix, the corresponding $Z$ matrix can be computed and the series and shunt impedances of the $T$ model (fig 2.9a) would be calculated as

$$Z_{sh} = Z_{21} \qquad (2.29)$$

$$Z_{se,1} = Z_{11} - Z_{21} \qquad (2.30)$$

$$Z_{se,2} = Z_{22} - Z_{21} \qquad (2.31)$$

.

Analogously, with the de-embedded $Y$ matrix, the shunt and series admittances of the model (fig 2.9b) are computed in the following manner

$$Y_{se} = -Y_{21} \tag{2.32}$$

$$Y_{sh,1} = Y_{11} + Y_{21} \tag{2.33}$$

$$Y_{sh,2} = Y_{22} + Y_{21} \tag{2.34}$$

.

In a circuit, discontinuities may be clumped together to create a complex behavior (fig 2.8). If the overall discontinuity is large, the dimensionless description described above can no longer be true. In that case, a rigorous characterization requires to analyze them all together as a single, larger discontinuity and models may have a narrower bandwidth, but the methodology remains the same as for the small discontinuity.

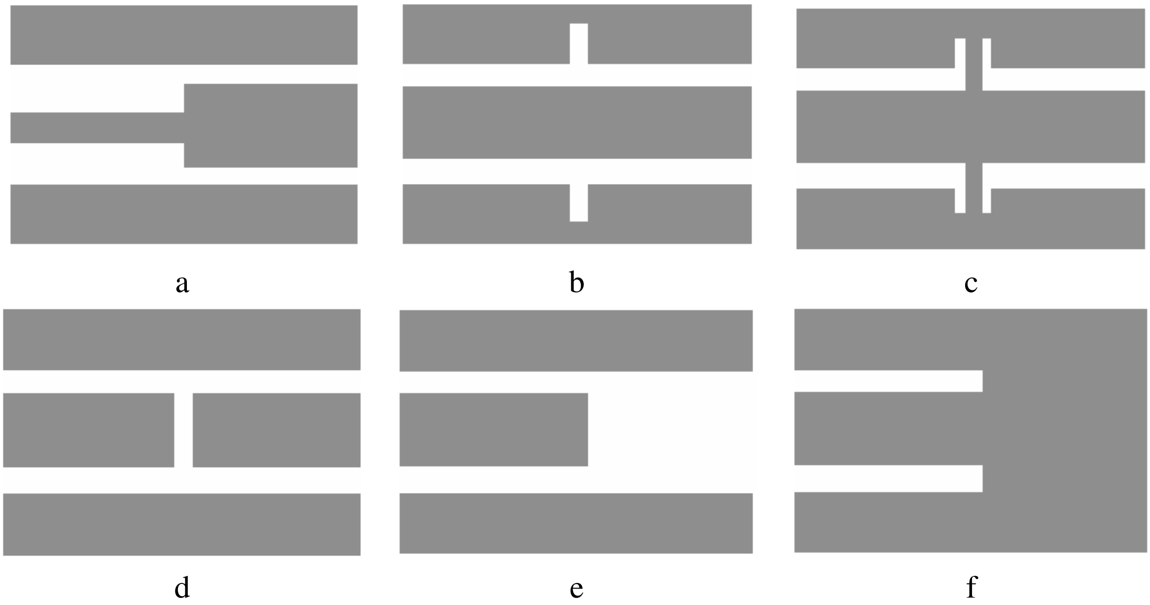
a b c
d e f

**Fig. 2.10:** Coplanar waveguide discontinuities.(a) Step discontinuity,(b) slot antenna,(c) shorted stub,(d) series gap,(e) open end line,(f) short end line.

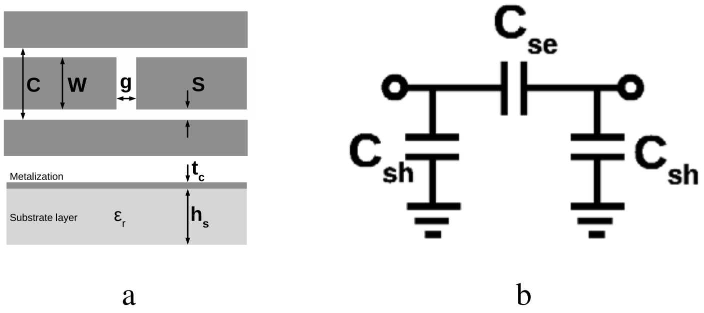

a b

**Fig. 2.11:** Series gap. (a) Layout: A gap is etched in the signal strip. (b) equivalent circuit

## 2.1 Semi-statistical Model: The Series Gap

The simpler discontinuities in CPW can be analyzed with a theoretical approach. Some discontinuities, like the step discontinuity (Fig 2.10a) have been analyzed with mode-matching techniques [83], others, like the gap, (Fig 2.10c) have been studied using conformal mapping [95] or Babinet's duality principle [86]. Nevertheless, the initial assumptions of uniform distribution of charge throughout the discontinuity are challenged in [116, 117], where it is shown that the existing theoretical models are accurate over a wide range of geometries but loose validity for certain $W/C$ and $g/C$ ratios (see fig 2.11).

The most basic series capacitor consists of a transverse gap in the central strip of the CPW. In its equivalent circuit, $C_{se}$ models the coupling between both ends of the gap and $C_{sh}$ models the coupling between the corners of the gap and the ground plane. The value of the series capacitance is determined mainly by its geometry. This is an useful trait, since the capacity can be easily designed. Still, the fine value of the capacity is also affected by frequency and the propagating mode of the line. In the case of the fundamental quasi-TEM odd mode of the CPW line, the capacity can be related to the static capacitance of the geometry.

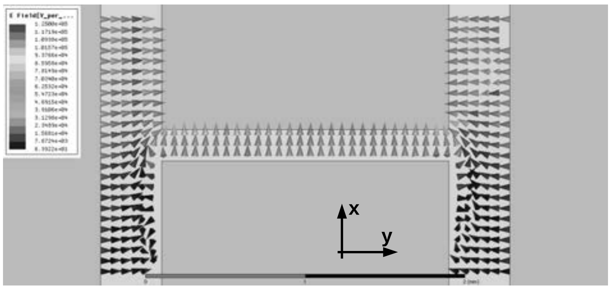

**Fig. 2.12:** Electric field in the gap. The electrical coupling between both ends of the gap in the central strip create a capacitance that can be modeled with a series capacitor

A first inspection of the electric field in the gap (Fig 2.12) shows that most of the field lines go over the gap between the two conductors of the central strip. For wide enough strips, there is a clear translation symmetry along the y-axis. In addition to the uniformly distributed electric field in the center of the gap there is an extra component in the corners that add a fringe contribution to the capacitor which is independent from the width of the strip $W$. Both contributions create a series capacitor between the ends connected to the central strips of the access lines, $C_{se}$, which can be expressed as:

$$C_{se} = C_{se,u} \quad g,\epsilon_{eff} \quad \cdot W + C_{se,f} \quad g,\epsilon_{eff},S \tag{2.35}$$

where $C_{se,u}(F/m)$ is the per-unit-length capacitance of the uniform contribution, $\epsilon_{eff}$ is the effective electrical permittivity of the medium and $C_{se,f}(F)$ is the fringe capacitance contribution to which a dependence with $S$ has been implied. There are accurate equations to determine the value of $\epsilon_{eff}$ but, for a substrate of relative permittivity $\epsilon_r$, a good approximation is:

$$\epsilon_{eff} = \epsilon_0 \frac{1+\epsilon_r}{2} \tag{2.36}$$

In fig 2.12 can be seen that there is an electrical coupling between both sides of the central strip and the ground plane, which forms a shunt capacitor $C_{sh}$, between the signal line and the ground. Both $C_{se}$ and $C_{sh}$ are represented in the circuit in fig 2.11b. As discussed above, a $T$ circuit could have been used to model the discontinuity but is apparent that a network naturally flows from the structure and can potentially model the gap over a wider bandwidth. The values of $C_{se,u}$ and $C_{se,f}$ that compose the series capacitance $C_{se}$ can be determined through full-wave simulation, from the de-embedded network in eq. (2.34):

$$C_{se} = \frac{Im\{Y_{se}\}}{} \tag{2.37}$$

$$C_{sh} = \frac{Im\{Y_{sh,1} + Y_{sh,2}\}}{2} \tag{2.38}$$

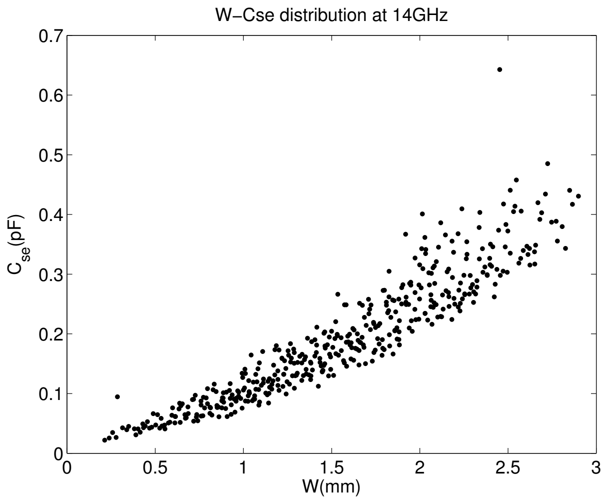

**Fig. 2.13:** Plot of the series capacitor $C_{se}$ against the strip width $W$. Each point represents one simulation with different $g$ and $C$ values.

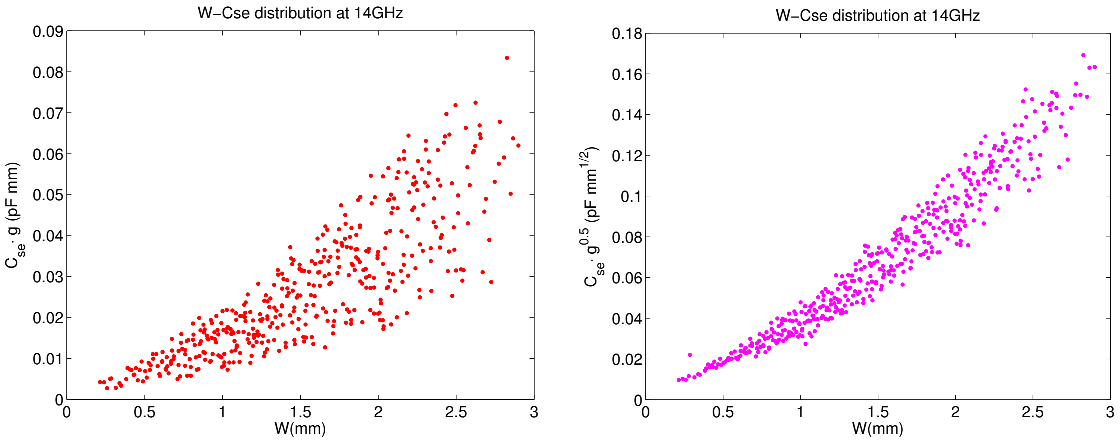

a b

**Fig. 2.14:** Plot of $C_{se} \cdot g$ and $C_{se} \cdot \sqrt{g}$ against the strip width $W$. Each point represents one simulation with different $g$ and $C$ values. The dispersion of the points shows a tighter correlation of $C_{se}$ with $W/\sqrt{g}$ than with $W/g$

For fixed values of $g$, a minimum square error (MSE) curve fitting procedure allows the extraction of the $a, b$ parameters in $C_{se} = a \cdot W + b$, then the variation with $g$ can be deduced. Limiting the value of $g$ to $50\mu m < g < 200\mu m$,the following dependence has been identified in [116]

$$a \quad g^{-1/2} \tag{2.39}$$

$$b \quad g^{-1/2} \tag{2.40}$$

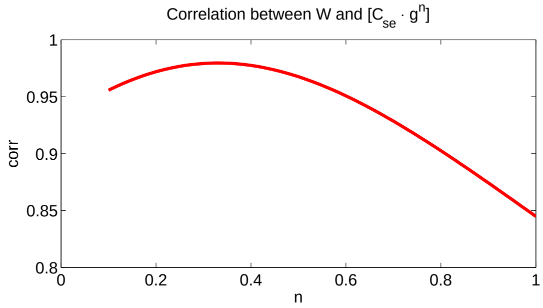

**Fig. 2.15:** Correlation between $C_{se} \cdot g^n$ and $W$ for different values of $n$. There is a clear maximum around $n = 0.34$.

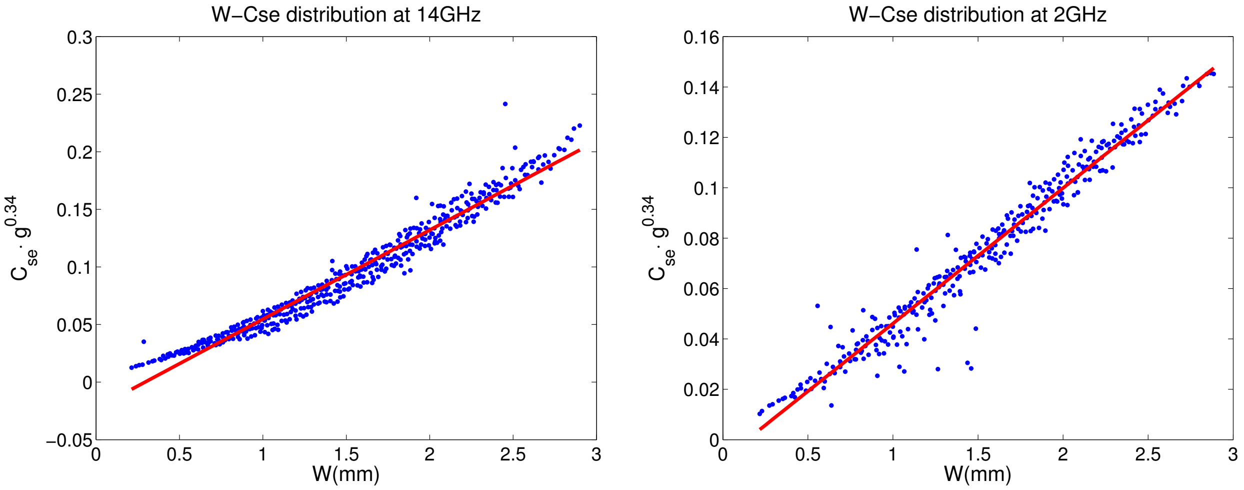

a b

**Fig. 2.16:** Plot $C_{se} \cdot g^{0.34}$ vs $W$ for 2GHz and 14GHz. There is a much lower dispersion than those appreciated in fig 2.14.

Fig 2.14 shows such dependency, which can be translated into the following equation

$$C_{se} = \frac{k_u \cdot W + k_f}{\sqrt{g}} \tag{2.41}$$

Contrary to a parallel plate capacitor, the series gap has a dependence closer to $g^{-0.5}$ than to $g^{-1}$. Actually, there might be a factor n, that minimizes the dispersion in the data in $C_{se} \cdot g^n$. To study that problem, two approaches can be taken. Either study the dispersion of the data or the correlation between $W$ and $C_{se} \cdot g^n$, as seen in Fig 2.15. A maximum of correlation —which minimizes the error of the model— is found for n=0.34. For this value, $k_u$ and $k_f$ are

$$C_{se}(pF) = \frac{0.0789 \cdot W(mm) - 0.0231}{g(mm)^{0.34}} \quad at\ 14GHz \tag{2.42}$$

$$C_{se}(pF) = \frac{0.0538 \cdot W(mm) - 0.0077}{g(mm)^{0.34}} \quad at\ 2GHz \tag{2.43}$$

$$\tag{2.44}$$

Fig 2.14 shows how the correlation between $W$ and $C_{se} \cdot g^n$ for $n = 0.34$ is smaller than for $n = 1$ or $n = 1/2$ (fig 2.15). The model can also be compared to the theoretical predictions of the duality principle [86] and the conformal mapping [95] techniques.

Fig 2.17 shows that the duality principle is consistently less accurate than the conformal mapping and the semi-statistical model. While the semi-statistical model is only slightly better than the conformal mapping for this population, it gives easy, intuitive design formulas and its accuracy can be greatly improved by reducing the domain of prediction or increasing the simulation population.

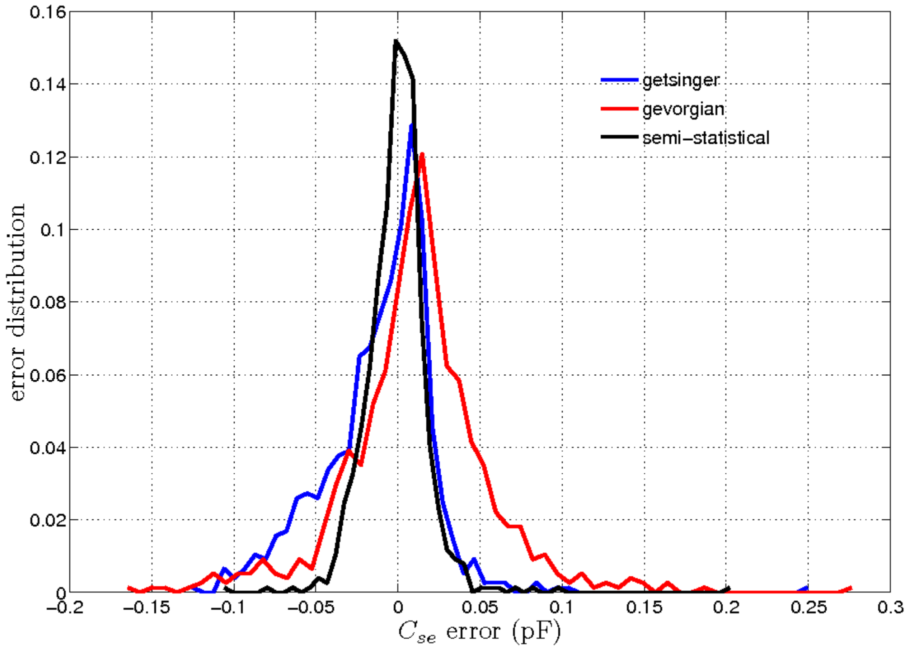

**Fig. 2.17:** Histogram representing the errors for the proposed characterization method, and the ones proposed by Gevorgian *et al.* [95] and Getsinger *et al.* [86].

Although no precise relation has been found to predict the value of $C_{sh}$ (fig 2.18), its value is very small and can often be neglected from the model altogether. For the purpose of this thesis, an average $C_{sh}/C_{se}$ ration will suffice.

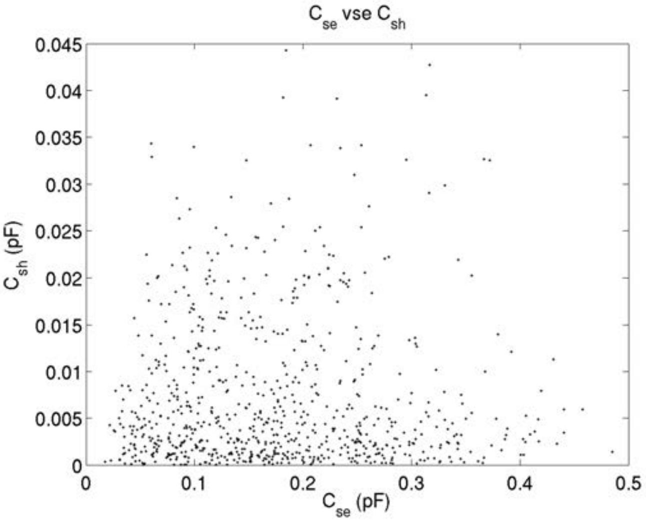

**Fig. 2.18:** Plot of $C_{sh}$ versus $C_{se}$ for different values of $C$ and $g$. The values are fairly independent from each other when a large number of simulations are included.

*Applicability of the Model*

One of the assumptions of the model is the use of thin metal sheets. When the value of $g$ is comparable to the metal thickness $t_c$, that approximation is no longer valid and the $g^{-1/2}$ variation will predictably migrate towards something resembling $g^{-1}$ as the geometry approaches that of a parallel plate. Similarly, for values of $g$ too large, the coupling between the two ends of the central strip weakens and the circuit begins to behave like two open ended circuits, where the open-ended capacitance is the dominant behavior, for which an estimation of its value can be found in [90]. For small $W$, the uniform component $C_{se,u}$ is inexistent, hence the model should not be applied for $S$ much larger than $W$ since the model does not describe such geometry.

The variation with the permittivity of the medium is presumed linear, and the model extracted for a certain value of permittivity $\epsilon_1$ can be extended to a target permittivity $\epsilon_2$ with the following formula

$$C_{se}(\epsilon_2) = \frac{\epsilon_2}{\epsilon_1} C_{se}(\epsilon_1) \tag{2.45}$$

However, this is only valid if the substrate is thick enough to contain most of the $E$ field lines. For thin substrates, the effective permittivity needs to be calculated accurately; however, the model does not contemplate this possibility *a priori*.

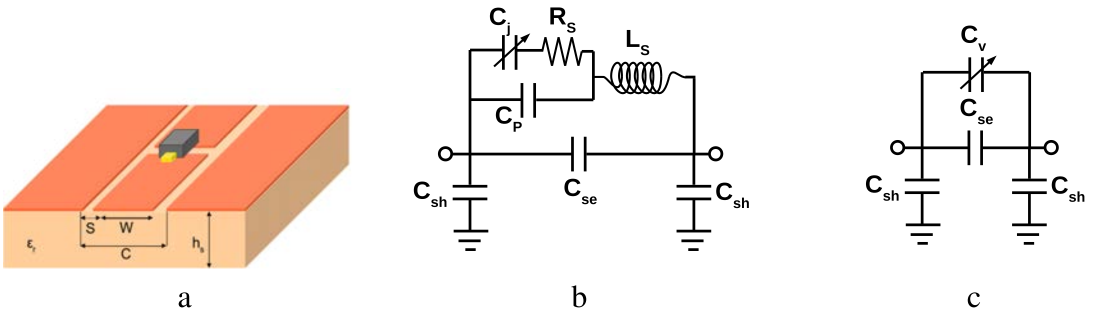

**Fig. 2.19:** Model of the varactor loaded series gap. a) 3D model of the set-up. b) Circuit including the SMD packaging. c)Simplified circuit including only the effects of the diode, valid when the diode is integrated into the series gap without packaging.

*Loaded Series Gap*

The series gap has a small but stable capacitance value but, more importantly, it can be used as the support for a SMD capacitor. The SMD can add its capacitance to that of the gap in a parallel configuration. If the extra SMD capacitor is implemented with a varactor diode, the series capacitance can be electrically tuned in real time and, consequently, the overall phase shift of the CRLH cell in which the capacitor is inserted will be controlled as well.

A varactor diode creates a variable capacitance in its depletion zone when it is polarized with reversed bias. The main RF behavior of the varactor can be well modeled by a capacitor between its anode and cathode yet, parasitic effects also take place. The most important effects to study can be seen in Fig 2.19b and are the series resistance of the diode and the packaging series inductance and parallel capacitance. For the abrupt diodes considered in this thesis, the series resistance will be neglected. The series inductance and packaging capacitance depend on the encapsulation and may be nonexistent in integrated configurations. Since only narrow band functions are considered, the model of the varactor can be greatly simplified to a single capacitor of value:

$$C_V = \frac{C}{1-\ {}^2L_{se}C} \tag{2.46}$$

$$C\ \ = C_j + C_P \tag{2.47}$$

can predict the behavior of the circuit in the presence of a varactor, its final value should be corrected in the manufacturing process by taking into account the extra parasitic effects. Appendix D includes a more complete description of the varactor diodes considered for this thesis and chapter 4 discusses the validation and manufacturing process.

| Diode | $RSs(\ )$ | $L_S(nH)$ | $C_P(pF)$ | Dynamic Range (pF) |
|---|---|---|---|---|
| SMV1405-079LF | 0.8 | 0.7 | 0.29 | 0.63-2.67 |
| SMV1408-079LF | 0.6 | 0.7 | 0.21 | 0.95-4.08 |
| SMV1413-079LF | 0.35 | 0.7 | 0.3 | 1.77-9.24 |
| SMV1430-079LF | 3.15 | 0.7 | 0.13 | 0.31-1.24 |
| SMV1493-240 | 0.5 | 0.5 | 0 | 7.1-28.7 |
| SMV1494-240 | 0.5 | 0.5 | 0 | 14.7-57.8 |

**Table 2.1:** Summary of diode characteristics

## 2.2 Shunt Inductor

The shunt inductor necessary to create the $L_L$ component in fig 2.2 can be created by connecting the central strip with the ground plane. This, however, yields too weak values of inductance to create the required CLRH line. A way to increase the value of the inductor is to create a shorted stub. A shorted stub of length smaller than $\lambda/4$ behaves like an inductor with much larger values than the mere plate connection between strip and ground.

The CPW line has two fundamental modes: the odd and even mode (see appendix C). The line proposed here is fed to excite solely the odd mode yet, the even mode has its cutoff at DC and the geometry of the discontinuity can excite it, transferring useful power into this undesired mode. Although the use of wire bounding can prevent the excitation of the even mode. However, keeping a symmetrical layout is also a good practice for protection against the even mode (fig 2.20).

As discussed at the beginning of the chapter, to control both the phase and the characteristic impedance of the CRLH line, in addition to a controlled series capacitor, it may be necessary to have an inductance that can be controlled as well. This can be achieved with a stub loaded with a varactor diode. Both the shorted and loaded stub will be presented in this section.

*Varactor loaded stub*

Fig 2.20 shows a CPW discontinuity that, to an extent, can be equated to a loaded stub. In order to ensure stub-like behavior, the connection with the baseline CPW should excite a CPW mode in the stub. The configuration of the stub creates a discontinuity that jeopardizes the correct excitation of the stub. The slots at the sides of the CPW that creates the stub will not be equally excited due to the electrical separation of the sides of the ground plane. This can be solved by adding air bond-wires [118] that force equipotential between separated regions of the ground plane.

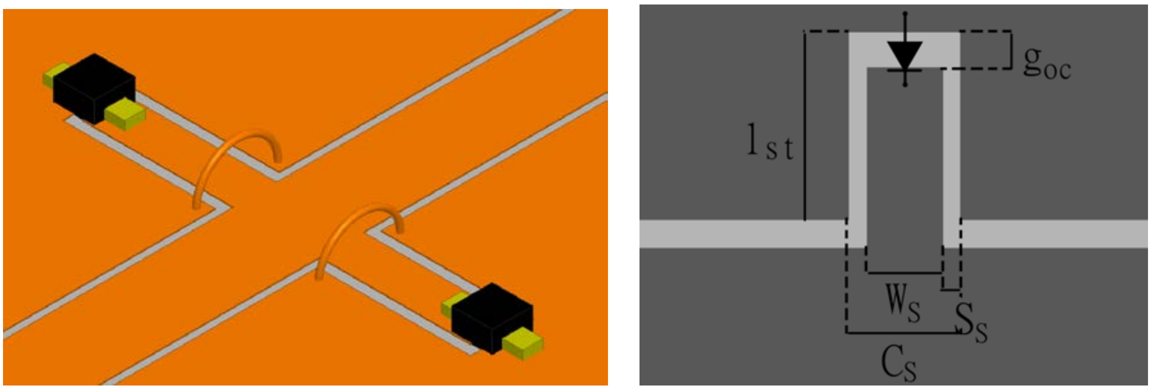

a b

**Fig. 2.20:** Loaded stub.(a) 3D representation of the loaded stub with air bond-wires. (b) Layout of the same structure with nomenclature.

The stub presented here differs from those found in the literature in the fact that it includes a capacitor at the end of the stub. This capacitor — a varactor diode — allows to modify the load of the stub acting, at the same time, in the inductance value seen by the baseline CPW at the beginning of the stub. Needless to say, this is very interesting in tunable or reconfigurable applications. This type of configuration, which is a direct translation of the very well know transmission line theory has been proposed for microstrip configuration [34] but not for CPW.

For the proper stub working conditions is of paramount importance to use air bond-wires at the base of the stub to the CPW line (fig 2.21a,b), otherwise, a CPW mode will not be excited in the stub. Fig 2.21c shows the transversal **E** field in the stub when no air bond-wire is placed, the result is that the potential at both ends of the stub is not forced to be the same and excitation is asymmetric, some combination of even and odd modes.

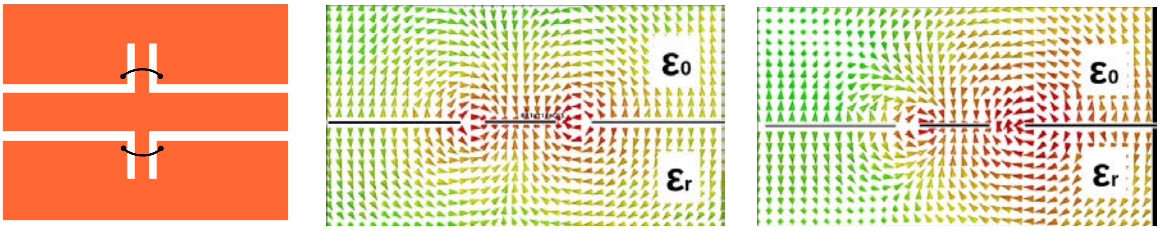

a b c

**Fig. 2.21:** E field propagating through a shorted stub at 2GHz, b) with an air bond-wire at the connection to the CPW line and c) without air bond-wire

The characterization of the cross created in the connection of stub and line is not an easy problem. The equivalent circuit of the stub is affected by the dimensions of the appended line, the biasing of the load varactor and the dimensions of the cross that fix the stub to the line. Since the main effect of the stub is to create an impedance between the signal and ground conductors, a $T$ network is the most suitable equivalent circuit. The length of the stub line and the value of the loading varactor will determine the nature of the shunt impedance —inductive or capacitive—. The objective of the stub is to create a tunable shunt inductor, it can be assumed that the shunt impedance is indeed an inductor, the stub length can be later designed to meet this hypothesis. The series impedances in fig 2.23 account for higher order interactions between the stub and the main line and will be assumed to be inductive as well (Fig 2.23b).

An accurate theoretical model of the stub may not be simple, hence a characterization of its behavior will be done prior to its use in the design of CRLH cells. The layout of the shunt stub can be consulted in Fig 2.20; for simplicity, the dimensions of the baseline CPW and the two values Cs and Ws are fixed. Only a variation in the $(l_{st}, C_L)$ space is considered, where $C_L$ is the value of the equivalent capacitance of the loading varactor.

The T network can easily be measured or simulated with standard deembedding techniques in the same way previously done for the series gap in section 2.1. In particular, the series and shunt inductors in fig 2.23b can be computed from the equivalent $T$ model (eq. 2.34) as:

$$L_{sh} = \frac{Im\{Y_{sh}\}}{} \tag{2.48}$$

$$L_{se} = \frac{Im\{Y_{se,1} + Y_{se,2}\}}{2} \tag{2.49}$$

Although the inductance $L_{sh}$ (fig 2.23b) does not correspond exactly to a mere capacitance loaded stub, it presents a frequency evolution similar to that of a loaded stub. As seen before, the fields within the stub far from the extremities are those expected in a CPW line; however, the end of the stub and the connection to the baseline CPW are not easy to analyze in a way that allows the prediction of the behavior of the stub for any given dimensions.

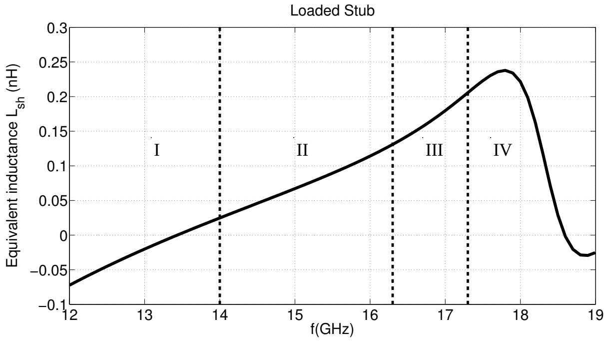

**Fig. 2.22:** Working modes of a Loaded stub : (I) capacitive-resonant region ; (II) linear region ; (III) exponential region ; (IV) resonant region

The simplest way to analyze the stub is to focus on a small portion of the spectrum and assume a simplified model. To do that, a preliminary wide-range analysis of the shunt inductance using full-wave simulations is very useful. Fig 2.22 represents a wide band simulation of a test case stub. A frequency variation is analogous to a $l_{st}$ variation since the electrical length of the stub evolves with frequency. Four major regions can be defined out of the frequency variation of the inductance:

I A capacitive region for frequencies smaller than the $L_{sh} = 0$ resonance

II A linear region after the resonance

III An exponentially growing region as we approach the high frequency resonance

IV A resonant region around the high resonance where the inductance value reaches its peak.

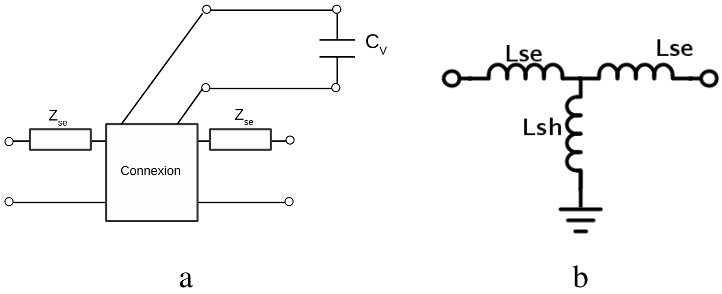

**Fig. 2.23:** T model of the stub. The shunt inductance $L_{sh}$ varies according to a stub-like scheme while the $L_{se}$ is predicted based on simulations

The region in which this study focuses is the linear region. In the linear region, the value of the equivalent shunt inductance are lower than those on the exponential or resonant regions. Yet, the equivalent inductance $L_{sh}$ is predictable and linear, easily modeled with a small number of parameters. The exponentially growing region could be utilized to achieve higher values of inductance, penalizing the bandwidth validity domain. At a first glance, the resonant region could also be an interesting working point due to the high values of inductance. Nevertheless, it is placed in a resonant point, which will be very sensitive to the actual dimensions of the circuit after the fabrication process. In addition, the actual inductance value, closely related to the Q of the resonator, will be strongly influenced by the losses of the actual materials used in the fabrication process.

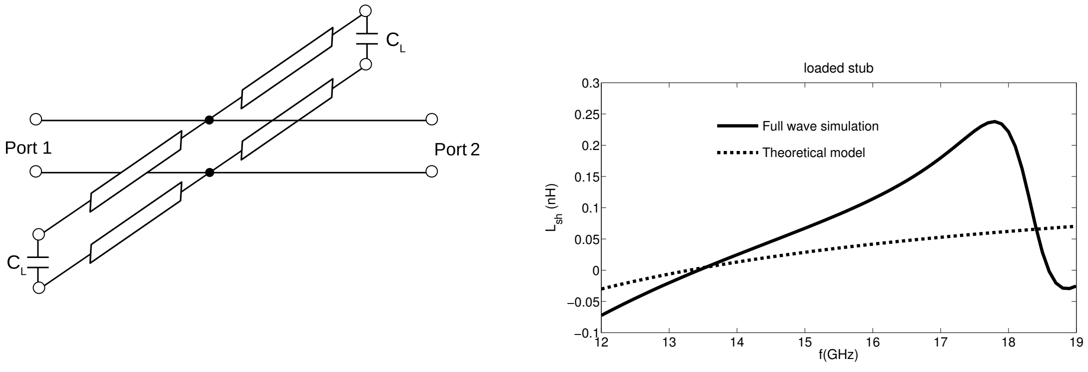

a b

**Fig. 2.24:** a) loaded stub equivalent circuit. b) Simulated stub compared to theoretical model.

A model of the shunt inductor does not need to predict its value over a very large spectrum, since the applications studied here are narrow band. Two models are presented here, a loaded stub —large band— model and a polynomial —narrow band— model that can be used for various applications.

*Loaded Stub Model*

The most straightforward model that can be used is the loaded stub equation. The discontinuity in fig 2.20 is modeled as the circuit in fig 2.24. In that case, the input impedance of the stub can be seen as the parallel of two identical stubs of impedance $Z_0$ and length $l_{st}$ loaded by a capacitor $Z_{load} = \frac{1}{j\ \ C_L}$ :

$$L_{sh} = \frac{Im[Z_i]}{2} = \frac{Z_0}{2}\ \frac{Z_0 \tan\ \ \beta_g l_{st}\ \ -(\ \ C_L)^{-1}}{Z_0 + (\ \ C_L)^{-1} \tan\ \ \beta_g l_{st}} \tag{2.50}$$

where the impedance $Z_0$ and the propagation constant within the line $\beta_g$ are determined by the CPW model [119]. This model, as seen in fig 2.24 is not very accurate since the connection between stub and line introduces higher order effects that are not accounted for in the stub model as well as other non-ideal phenomena like the extension of the stub's length due to the capacity created in the extremity [90].

The stub model can be improved by simulating the stub at various frequencies and minimizing the following equation

$$L_{sh} - \hat{L}_{sh}\,(l_{st}, Z_0, C_L) = 0 \tag{2.51}$$

where

$$\hat{L}_{sh} = \frac{Z_0}{2}\ \frac{Z_0 \tan\ \ \beta_g l_{st}\ \ -\ \ \ \ C_L^{\ \ -1}}{Z_0 +\ \ \ C_L^{\ \ -1} \tan\ \ \beta_g l_{st}} \tag{2.52}$$

In this *statistically determined stub* model, the parameters $l_{st}, Z_0, C_L$ are curve-fitted to accurately model the stub.

*Polynomial model*

Within the linear region, the value of the inductance is somewhat stable, but it is never constant. As long as it is linear enough, a Taylor series can accurately predict the value of the stub over a sufficient band. For that, not only the value of the inductance, but also its first derivative need to be estimated:

$$L_{sh} \approx L_0 + \frac{L_{sh}}{f} \; f - f_0 \tag{2.53}$$

The problem is then reduced to determine the values of $L_0$ and $\frac{L_{sh}}{f}$ in 2.53 for different values of $l_{st}$ and $C_L$.

Except for the theoretical model, all the models are based on the statistically obtained parameters $L_0$ and $\frac{L_{sh}}{f}$ for the polynomial model and $l_{st}$, $Z_0$ and $C_L$ for the loaded stub model.

The small variability of the stub within the linear region reduces the chances of error when choosing which points can be used as input population. It is enough to choose points that are close enough to each other to obtain good accuracy. Nevertheless, to create a representative population, a Latin hypercube distribution can be used as the initial population for the simulations.

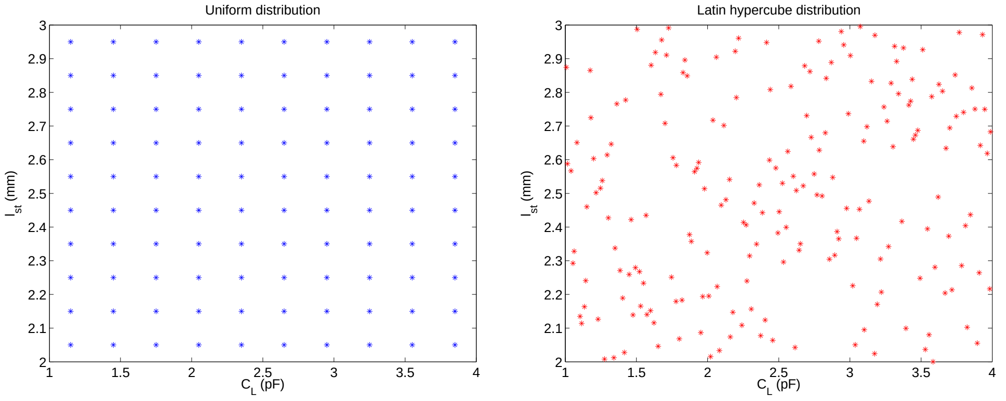

a

b

**Fig. 2.25:** Possible distributions of the simulation points for the loaded stub. a)Uniform distribution. b) Latin hypercube distribution

*The use of kriging interpolation for the efficient characterization of stubs*

Both for the narrow and wide band models, the characterization of the model parameters can be performed by curve fitting a set of samples. Since the models considered in this thesis are narrow band, the narrow band model will be considered (eq. 2.53). The wide band model can be inferred using this same procedure with minor modifications.

The accuracy of the model is related to the size and distribution of the sampling population. For a given stub, it is difficult to decide which population is more convenient. With an uniform distribution of the population (fig 2.25a) it is easy to oversize the sampling space and with more distributed populations (fig 2.25b), an uniform error distribution is not assured.

Kriging interpolation can help with the sampling process. Assuming a gaussian distribution of the error, kriging interpolation estimates the error committed in the interpolation process along with an interpolation of similar accuracy to a spline. Therefore, kriging —or any other error estimation procedure— can be used to reduce the size of the sampling population.

Starting with an initial population, that can be defined based on latin hypercubes, the error throughout a domain can be estimated and the point of maximum error can be defined as the next sample that minimizes the maximum error. This process can be iterated until a desired error is achieved. Fig 2.26 summarizes this process.

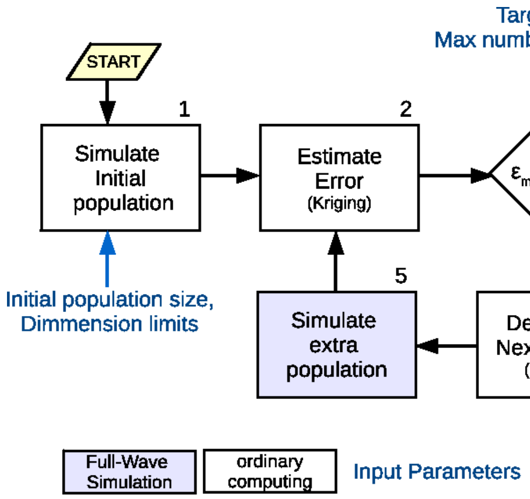

**Fig. 2.26:** Flow chart of the efficient simulation procedure using kriging error estimation.

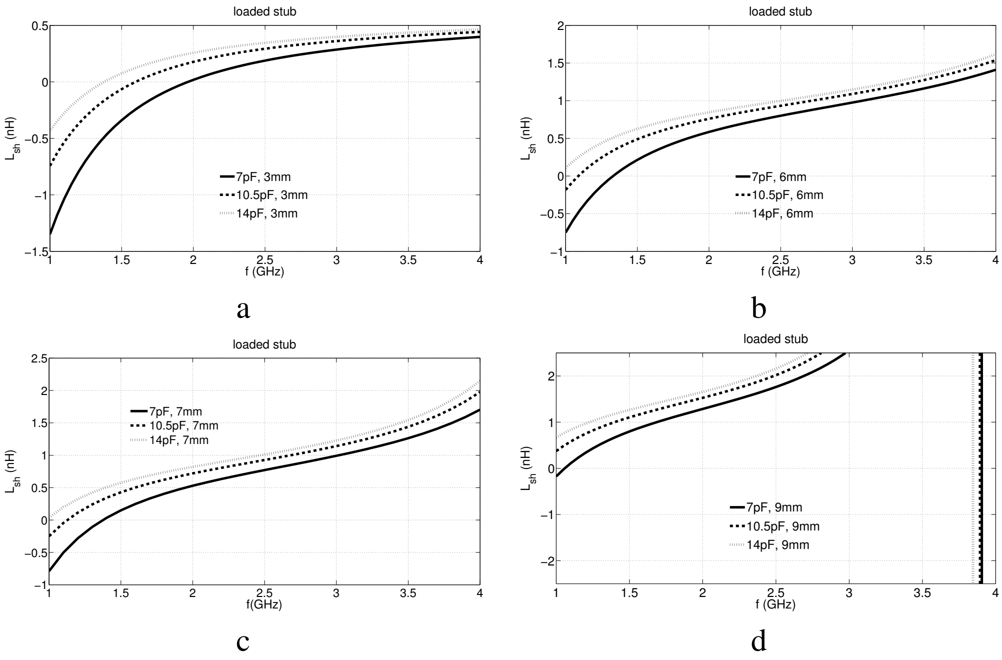

a b

c d

**Fig. 2.27:** Limits of the inductor-like behavior of the loaded stub

As an example, a loaded stub like the one in Fig 2.20b can be characterized. The first step is to find the domain in the $(C_L, l_{st})$ space for which the stub behaves like an inductor, for that, Fig 2.27 shows some initial simulations that can help define the limits of the population space.

Between about 4mm to 7mm of length combined with a 7pF to 14pF loading varactor span, the stub should reasonably behave like an inductor.

Following the graph in fig 2.26, the steps towards the modeling of a parameter $L_0$, using the kriging base method are the following:

### *Step 1: Simulate Initial Population*

The method begins by simulating a representative population. For low variation parameters, like $L_0$, somewhere between 10 to 20 elements suffices. A Latin hypercubes distribution can help create a more spread representation of the inductance function.

The initial population could be taken to be one element. From one element, the method will still fill the space in the subsequent iterations, however, the estimation of the error through kriging will not be adequate at the beginning of the algorithm because of lack of samples.

### *Step 2: Estimate Error*

In order to estimate the error, a thin uniform mesh is defined in the $(C_L, l_{st})$ space. For each point of the mesh, the variance of the kriging error $\;_\epsilon$ is computed. This yields maps like those seen in fig 2.28.

A precise description of the operation of kringing can be found in the appendix E. For now it is enough to know that kriging can estimate the variance of a gaussian like distribution of the error perpetrated in interpolation at a given point. From the variance, a 3 bound —>99% of errors contained— or a 5 bound —>99.99% of errors contained— can be defined as the *kriging generated error bound* $\;^i_k$ of the $i-th$ iteration:

$$\;^i_k = 3 \cdot max\{\quad_{,i}(C_L, l_{st})\} \tag{2.54}$$

### *Step 3: Check Error*

In this step, a condition is defined to ensure that the desired error level is met. Since the bound $\;^i_k$ represents the absolute error in $nH$, a tolerance represents the maximum absolute error desired for the model. More details on different estimations of the error and convergence of the method are detailed in the appendix F.

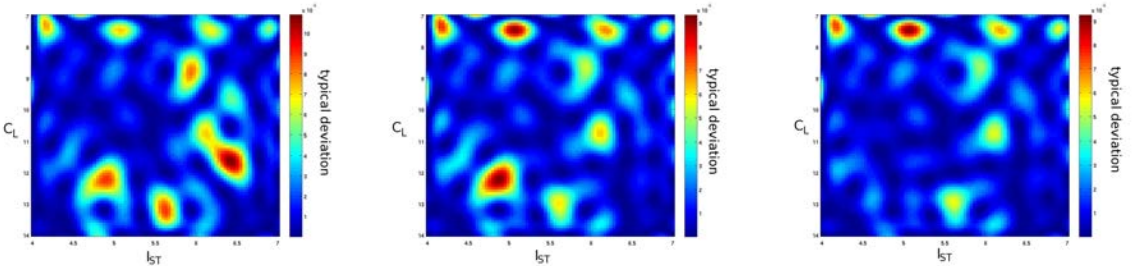

a
68 elements

b
69 elements

c
70 elements

**Fig. 2.28:** Loaded Stub. Evolution of the variance of the error. Error estimated with simple kriging

### *Steps 4 and 5: Determine Next Sample and Simulate New Population*

While the exit condition is not met, step 4 tries to find the next sample that minimizes the error. To do that, the same mesh used to compute the kriging error variance map can be used to pinpoint the coordinates of the maximum error. This can be seen in fig 2.28. In the first 68-th iteration, the maximum estimated error is around $l_{st} \approx 6.4mm$, $C_L \approx 11.8pF$.

Once the point of maximum error is found, the next step is to simulate the stub right in that point. This will decrease the average length between sample points and eliminate the maximum error region of the stub model. The algorithm now loops back to *step 2* and, in the following iteration, the position of the maximum of error migrates to $l_{st} \approx 4.8mm$, $C_L \approx 12.9pF$.

### *Step 6: Store Simulated Samples*

Once the error condition is met, the information need to be stored, *i.e.* the simulation points and the value of the function to interpolate. For a final population of size $N$, the number of *words* to be stored is $(2N+N)$: $N$ function evaluations plus 2 words for each of the $N$ values of the sample space $(C_L, l_{st})$.

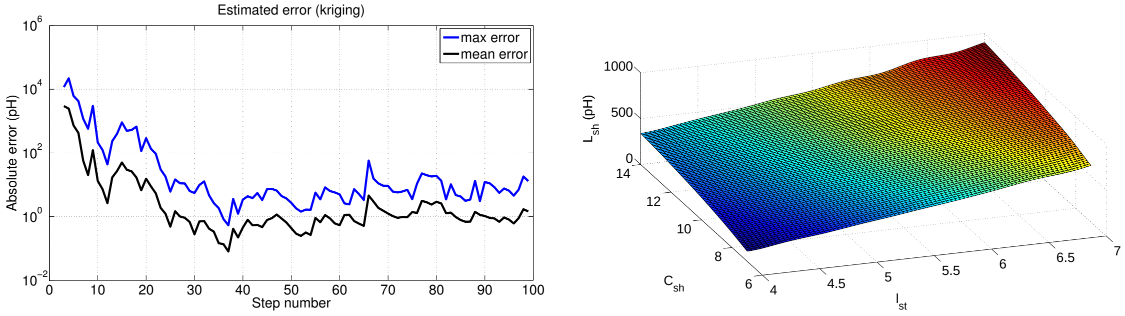

a b

**Fig. 2.29:** Loaded Stub (2GHz). a)Maximum and mean error as estimated by kriging interpolation. b) Estimation of the shunt inductance

The method described here can effectively model the parameter $L_0$ of eq. (2.53). Yet, eq. (2.53) also includes a dispersion parameter $L_{sh}$ and the model of the stub contains a series inductor $L_{se}$ as well (fig 2.23). The kriging based methodology can be easily extended to include these three parameters or any other model equation —*e.g.* the wide-band model—. Since it does not add more relevant information for the design of CRLH lines, that extension and some other relevant results can be found in appendices E-G.

### *Shorted Stub*

The characterization process used in the previous section can be applied to any type of discontinuity. For instance, the shorted stub could be characterized by means of the error prediction methodology. The shorted stub is a non-reconfigurable discontinuity that can synthesize relatively large shunt inductances. As opposed to the loaded stub, the shorted stub has a more reliable behavior and simplifies the biasing circuit of the line. It can be useful for circuits in which only the series capacitor is reconfigured.

The shorted stub follows the behavior described by the input impedance of a shorted stub,

$$Z_{in} = \frac{1}{2} Z_0 \tan\ \beta_{st} l_{st} \tag{2.55}$$

Similarly to the loaded stub, in CPW the parameters $Z_0$, $\beta_{st}$ and $l_{st}$ do not correspond in general to the physical dimensions of the stub. Fig 2.20b shows the design parameters in a shorted stub. Longer and thinner stubs provide larger inductance. Larger side slots also increase the stub impedance, creating larger inductances. Unfortunately, as discussed before there are high order effects that play a role in the behavior of the stub and the application of the formula does not give an accurate prediction of the inductance. Similarly to the loaded stub, the shorted stub can be developed into a Taylor series as in eq. (2.53). Fig 2.30 summarizes the convergence and error characteristics of the $L_0$ parameter for the shorted stub.

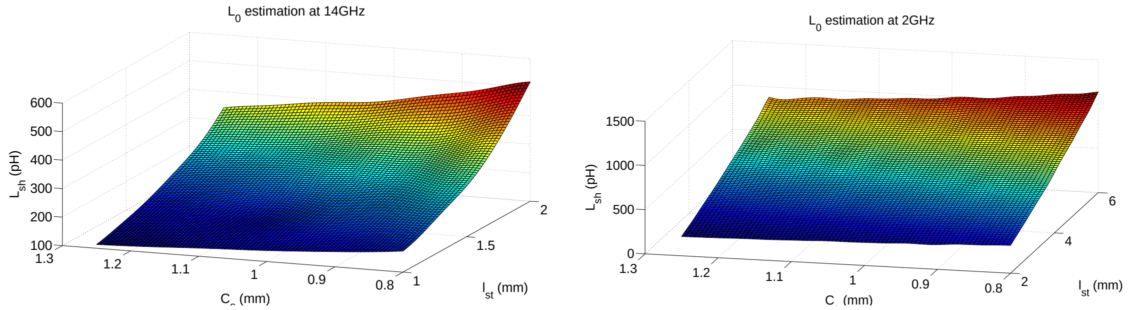

a

b

**Fig. 2.30:** Shorted Stub. a)Ku band surface. b)L band surface

Fig 2.30 shows some values calculated for a loaded stub at 14GHz ($\epsilon_r = 6.15$) and at 2GHz ($\epsilon_r = 10.7$). It can be seen that there is a non negligible variation of the inductance $L_0$ with the value of the varactor (up to 1.4:1) and that the range can be chosen with the length of the stub.

Another conclussion that can be drawn is that the inductance has a greater variation ratio as the stub works closer to the resonance ($\lambda/8$). Nevertheless, this reduces the useful band and increases the derivative of the inductance with frequency because of the non linear function of the stub.

The variability may seem limited but it is not an issue since the large variation of the CRLH cell parameters can be made with the series capacitor while the stub can be used for fine tuning.

# 3 CRLH Line Design

The theory behind the *CRLH* line have been reviewed and some tools for the synthesis of lumped elements in CPW have been introduced. The remainder of this chapter is dedicated to the design process of a reconfigurable *CRLH* line. This is important because, there is an extensive literature on the design of *static CRLH* but, to the knowledge of the author, this is the first design procedure proposed for reconfigurable CPW CRLH lines.

Two different design methods are proposed hereafter, each for a different type of cell. The first one specifies how to design a line that has tunable series capacitors but non tunable inductors. This case will be known as the *one-way* reconfiguration circuit and will use the varactor loaded series gap and the shorted stub, its layout can be seen in fig 2.31a.

The second method presented, *two-way* reconfiguration circuit is depicted in fig 2.31b and makes use of the shunt loaded stub instead of the shorted stub in addition to the varactor loaded series gap. This method gives extra degrees of freedom for impedance matching or extra steering angle in case the *one-way* reconfiguration circuit does not suffice for the requirements.

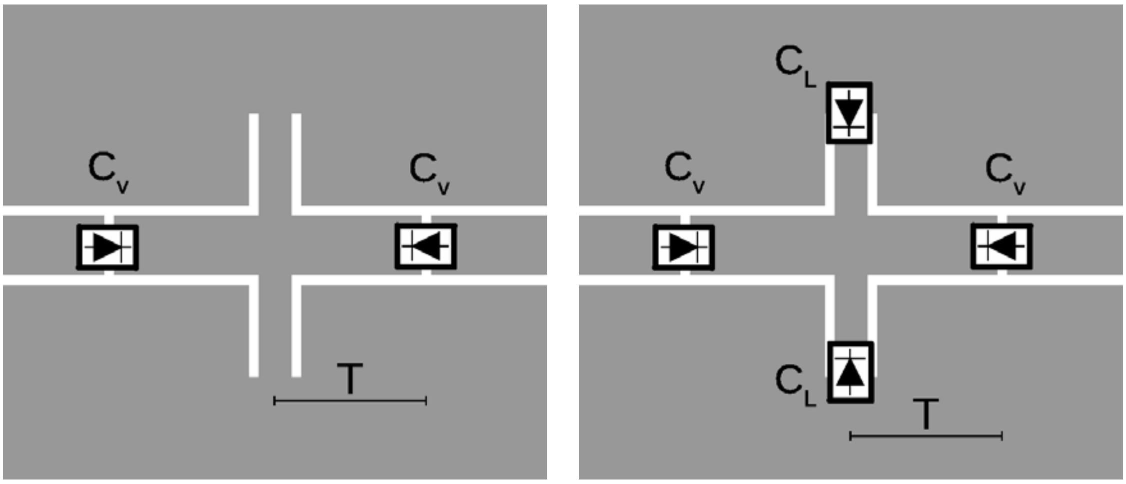

a b

**Fig. 2.31:** Proposed cells. a) One-way reconfiguration cell. b)Two-way reconfiguration cell.

## 3.1 *One-Way* Reconfiguration Circuit Design Methodology

For many applications, merely reconfigurating the series capacitor may prove enough to achieve the phase reconfiguration required for beam steering with an acceptable impedance matching. Moreover, single-C reconfiguration is easier to understand than LC reconfiguration, which makes it ideal for a first introduction into the methodology.

Whenever single-C reconfiguration is acceptable, it is also desirable since the complexity is greatly reduced with respect to the LC reconfiguration since it halves the number of varactor diodes in the structure. As a starting point, some arbitrary requirements could be the ones listed below:

- Input impedance of 50 .
- Broadside radiation.
- Beam steerable from −30° to +30°.

### *Step 1*

The first step is to define the host CPW line. The CPW could be 50 but the impedance of the line is somewhat irrelevant since the true input impedance of the full line will be the Bloch impedance, as discussed in section 1.1. For this example, a $2mm$ wide CPW line with characteristic impedance of 33 is chosen. Lines with low characteristic impedance have the advantage of having small side slots, this reduces the radiation and fosters the odd mode excitation of the CPW.

*Step 2*

The next step is to choose the varactor diode and the stub. In order to achieve the broadside radiation condition, the series capacitor and shunt inductor should fulfill the following condition [120]:

$$Z_w = \sqrt{\frac{L_{sh}}{C_{se}}} \tag{2.56}$$

*Step 2.1* Depending on the line impedance chosen, the varactor or the inductor will be the limiting factor. In this case, the $C_{se}$ can be chosen to be in the range of $0.6pF$ to $2pF$, which corresponds to the varactor SMV1405-079LF (see annex D).

*Step 2.2* The inductor should have a value, somewhere in the range of

$$Z_w^2 \cdot C_{se,min}^{(eq)} < L_{sh} < Z_w^2 \cdot C_{se,max}^{(eq)} \tag{2.57}$$

where

$$C_{se}^{(eq)} \approx \frac{C_{se}}{2} \tag{2.58}$$

In a 2C+1L cell. For $Z_w = 33$ , $C_{se,central} \approx 1.2pF$, the inductor can be approximately of $0.6nH$.

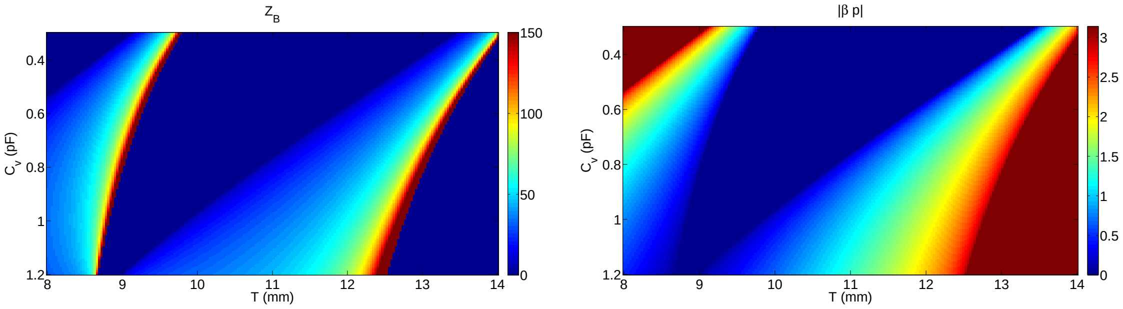

a b

**Fig. 2.32:** First guess for the design of a cell. a) Bloch impedance and b) T-C diagram of the $\beta p$ for a $600pH$ shunt inductor loaded cell

*Step 3*

Fig 2.31a depicts the layout of a cell. From eq. (2.13) and (2.24) the effective propagation constant $\beta_{eff}$ and Bloch impedances $Z_B$ can be calculated.

To determine the separation between discontinuities $T$ the diagram in fig 2.32a can be created. In fig 2.32a,b the ordinate represents the value of the series gap $C_{se}$, which represents the reconfigurability span. The abscissa describes different values for $T$. Once $T$ is fixed, the circuit's $\beta_{eff}$ and $Z_B$ vary with the varactor's capacitor along a fixed horizontal line in the diagram.

As explained in chapter 1, the value of the propagation constant in the line $\beta_{eff}$ is decisive to calculate the steering. Similarly to a leaky wave antenna, the steering in a linear array $\theta$ can be calculated through the following equation:

$$\theta = asin\ \frac{\beta_{eff}}{k_0} \tag{2.59}$$

where $k_0$ is the propagation constant in vacuum and the steering has been taken as the angle between the broadside and boresight directions.

Since the diagram does not present a large variation in $\beta_{eff}$, the inductor can be modified until a convenient $C-T$ diagram is generated. This is done through numerical circuit models, whose low computation time allows for optimization schemes. Fig 2.33 shows the $C-T$ diagram for $L_{sh} = 202.9pH$ —corresponding to a stub $1.25mm$ wide and $1.4mm$ long—. In the diagram, it is easy to notice that, for a $T$ around $12.61mm$, a large beam steering is possible with a non-imaginary Bloch impedance.

*Step 4*

Choose the T that gives the best performance in Beam Steering or Impedance adaptation. In this case, a $T = 12.61mmm$ seems to cancel the band gap around $\beta = 0$. Fig 2.33c shows a continuous Bloch impedance and fig 2.33d represents the absolute value of the beam steering that could be achieved with this line in addition to the VSWR for a reference impedance of 50 .

It is worth noting that the specifications may not be met for the *one-way* reconfiguration circuit because of the limited values in varicap impedances and the reconfigurability of only one of the two elements. In that case, a different stub can be used or a *two-way* reconfiguration scheme can be used.

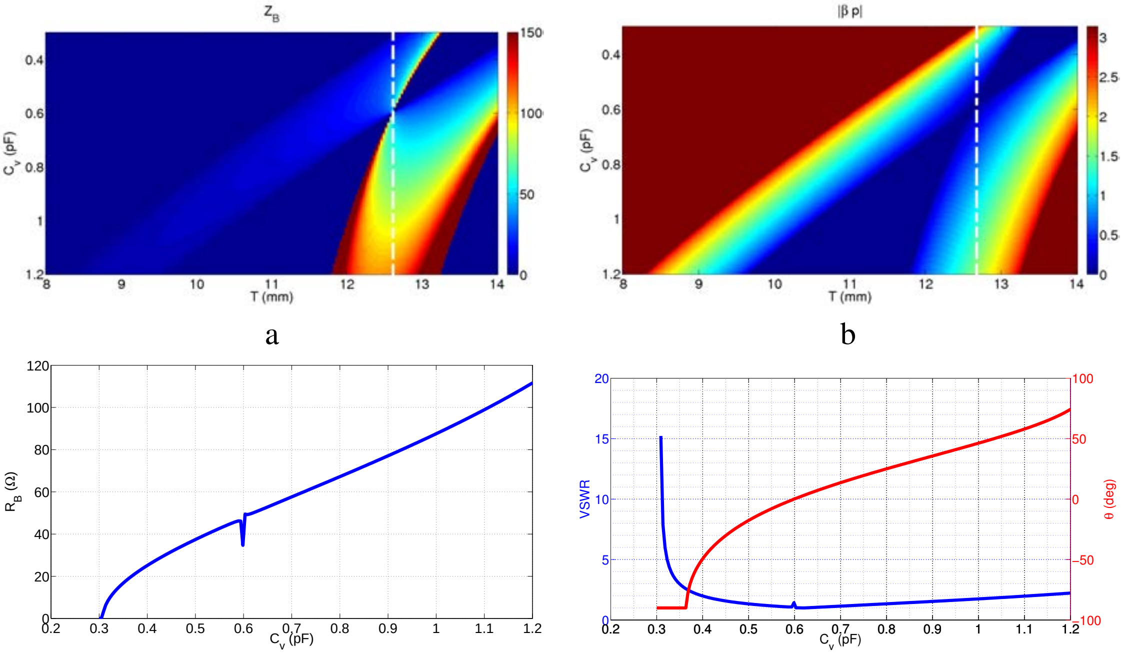

a

b

c

d

**Fig. 2.33:** a)T-C diagram of the Bloch impedance of a shorted stub of length 1.4mm and a double series gap loaded with varactors. b) T-C $\beta p$ diagram c) Bloch impedance of the central point ($T = 12.61mm$) d) steering angle and VSWR for a reference 50 impedance at the central point ($T = 12.61mm$)

*Step 5*

There may be a slight difference between the circuit model and the full-wave simulation. In fig 2.34 a small shift can be appreciated, this shifts comes from the calculation of the effective permittivity of the CPW line. As a last step, in order to make sure the design is robust, a final optimization process can be done with a full-wave simulator to ensure a minimum VSWR all over the dynamic range of the capacitor (fig 2.35).

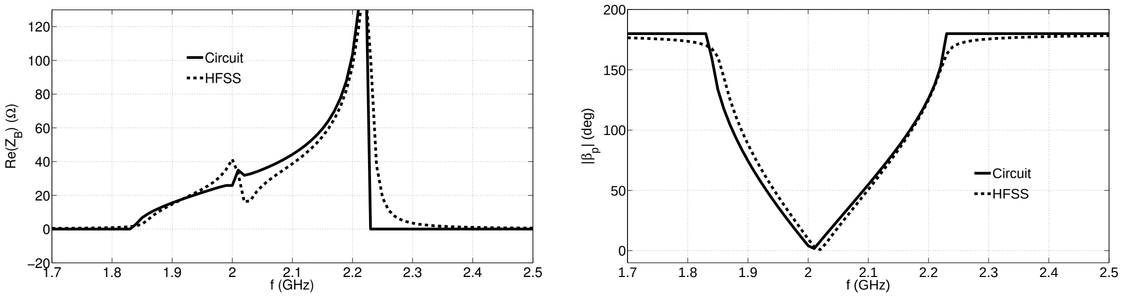

a b

**Fig. 2.34:** a) Bloch impedance comparison circuit-HFSS simulation b) $\beta p$ circuit-simulation comparison

Once the cell is simulated and optimized, a three-cell simulation can be done to make sure that there is no important intercell coupling effect. The results of the three-cell simulation is presented in 2.36.

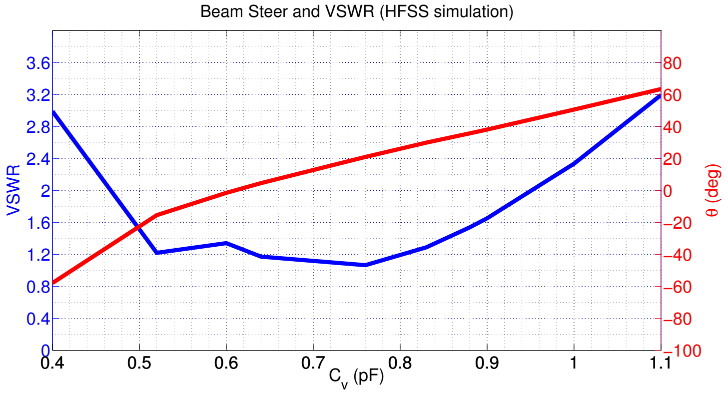

**Fig. 2.35:** Simulation after optimization (T=12.55mm, $L_s$=1.4mm)

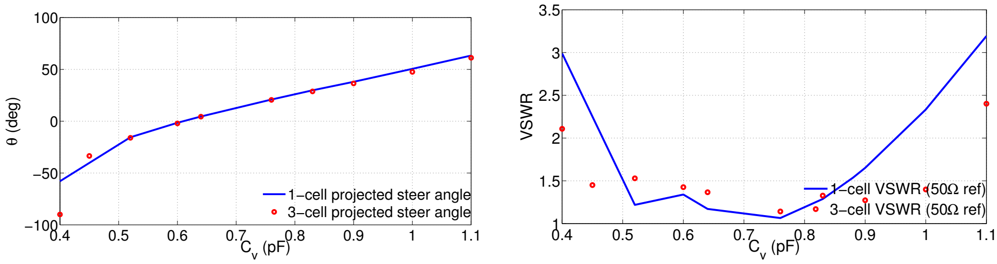

a b

**Fig. 2.36:** Simulation of 3 cells (one cell with two neighbors to simulate the coupling effects)

## 3.2 *Two-Way* Reconfiguration Design Methodology

The procedure is similar to the one-way reconfiguration design, except that there are two dynamic variables, $C_{v,gap}$ and $C_{v,stub}$, as opposed to one dynamic $C_{v,se}$ and one static variable $T$.

After the host CPW has been chosen, the stub can be determined regarding the span of values the shunt inductor can take. For this example, the stub characterized in appendix G will be used, therefore its host configuration will be used as well. A summary of the initial configuration can be seen in table 2.2.

| Param | Value | Param | Value |
|---|---|---|---|
| $C$ | $0.28mm$ | $W$ | $0.24mm$ |
| $h_s$ | $0.508mm$ | $\epsilon_r$ | 6.15 |
| $Z_w$ | 40 | $\epsilon_{r,eff}$ | 3.18 |

**Table 2.2:** Initial configuration for the *two-way* reconfiguration methodology example

Once that the host CPW is defined, the $T - C_{v,gap}$ graph can be traced for different values of $C_{v,stub}$ to define the T that gives broadside for the central $C_{v,gap}$ value as seen in fig 2.37.

Following the information in appendix G we can see that for $l_{st} = 2mm$ and SMV1430 $L_{sh}$ can span from $110pH$ to $330pH$ approximately. Fig G.1 shows a few different values within that range.

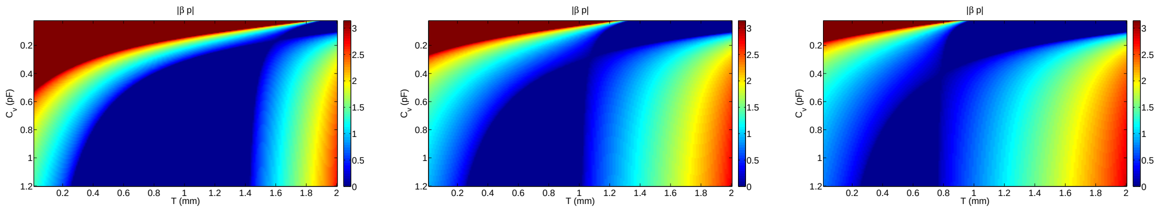

$L_{sh} = 110pH$ $L_{sh} = 220pH$ $L_{sh} = 330pH$

**Fig. 2.37:** Two-way reconfiguration design example. $C_{v,gap} - T$ diagram representing $|\beta p|(rad)$ for different values of $L_{sh}$

Different values of $T$ in the $0.8mm$ to $1.6mm$ range can be tried, $T = 1.2mm$ shows a good variability within the $C_v, L_{sh}$ domain, as seen in fig 2.38. Fig 2.38 represents the Bloch impedance and the steer angle $\theta$ as in eq. (2.59) for different values of $C_{v,gap}$ and $L_{sh,stub}$. This chart can be used as a design tool and also as a operation tool, to calibrate the antenna and define what working point generates which beam steer.

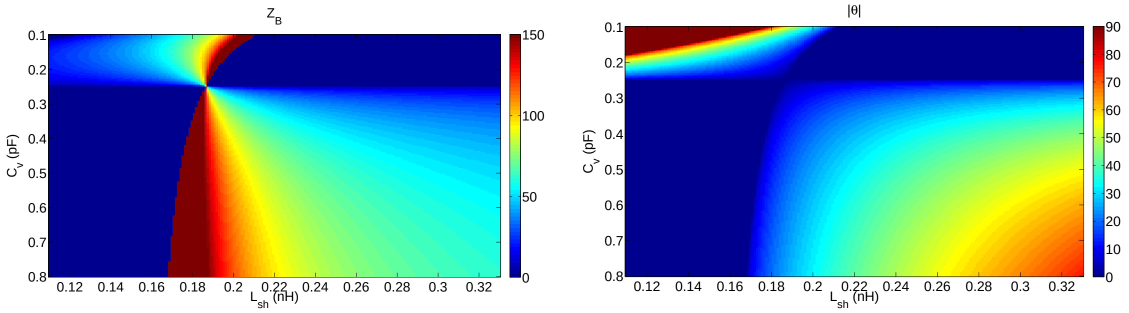

$Z_B$ $|\theta|(°)$

**Fig. 2.38:** Two-way reconfiguration design example for $T = 1.2mm$

Fig 2.38 shows how the *two-way* reconfiguration circuit gives a much larger capability of reconfiguration than the *one-way* reconfiguration counterpart at the cost of increased complexity. This chart can also be recalibrated for a manufactured circuit and be used as a chart to determine the biasing needed for the diodes to achieve a certain steer.

Additionally, the *two-way* reconfigurable circuit gives an extra degree of freedom that can be exploited to extend the circuit in another dimension. Indeed, the extra control can be used to tune in the frequency of operation as seen in fig 2.39.

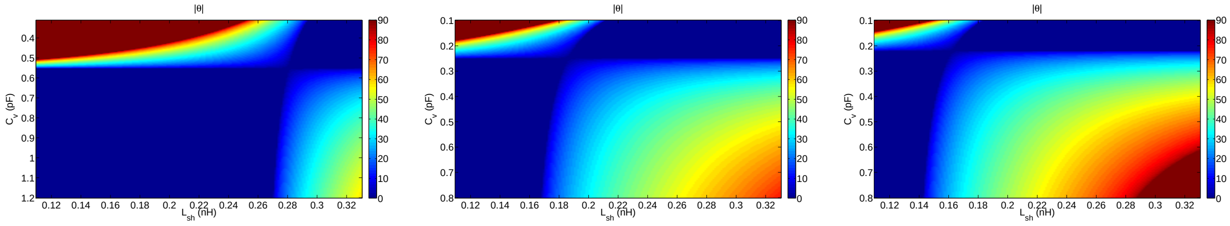

13.5GHz 14GHz 14.75GHz

**Fig. 2.39:** Steer angle $|\theta|(°)$ for different frequencies ($T = 1.2mm$)

This last feature is very important since it can allow the antenna to choose a reception channel, provided that the radiative element has a large enough bandwidth to receive in multiple channels.

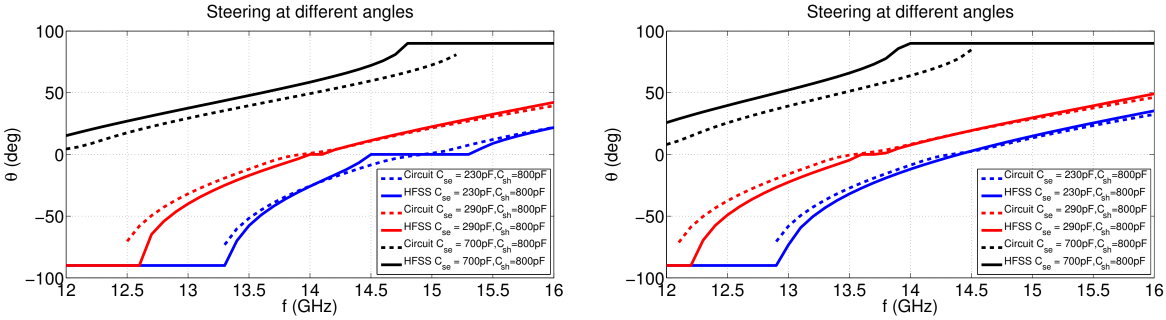

a b

**Fig. 2.40:** Comparison between circuit and HFSS simulations. (CPW model $\epsilon_{eff} = 3.5$, $Z_0 = 32$ )

Even though some differences can be noticed in fig 2.40 between the simulation and the circuit prediction, it worth noting that the cell is able to achieve a large range of phase variations that can be post-calibrated. Also, the model of the CPW line can be optimized to account for the parasitic effects and have a more accurate circuit prediction.

## 4 Experimental Validation

With the objective of validating the circuit model, a set of mock-ups have been manufactured: An *active* CRLH cell with two reconfigurable capacitors and a shorted stub and a *passive* CRLH cell with two shorted stubs and a non-reconfigurable series capacitor (fig 2.41).

The stubs were chosen to be shorted because they are easier to manufacture and allow to validate the model without increasing complexity. Equally, the reconfigurable series gaps are tested by repeating the cell multiple times and using fix SMD capacitors of known values at its place (fig 2.42a). To suppress the apparition of undesired modes and the ensure the correct excitation of the stub, air bond-wires connect the four sides of the ground plane at the base of the stub (fig 2.42b).

The mock-ups have been etched on a 1.5mm AD1000 substrate with relative permittivity of 10.7. The dimensions of the reconfigurable and non-reconfigurable cells are summarized in table 2.43.

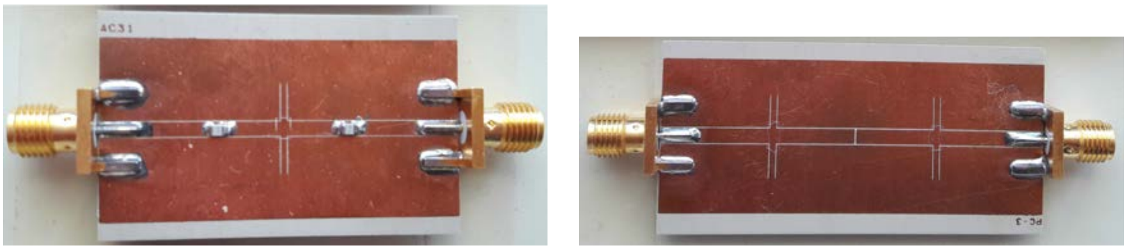

a b

**Fig. 2.41:** a) Active *One-way* reconfigurable CRLH cell b) Non-reconfigurable (passive) CRLH cell

a b

**Fig. 2.42:** a) SMD capacitor mounted on the series gap. b) Air bond-wires connecting the ground planes at the base of the stub to the central CPW line

| Reconfigurable Cell | | Non Reconfigurable Cell | |
|---|---|---|---|
| C | 2mm | C | 2.5mm |
| W | 1.7mm | W | 2.1mm |
| g | 0.15mm | g | 0.2mm |
| $C_s$ | 1mm | $C_s$ | 1.13mm |
| $W_s$ | 0.7mm | $W_s$ | 0.83mm |
| $L_s$ | 4.665mm | $L_s$ | 4.8mm |
| T | 8.05mm | T | 12mm |

a

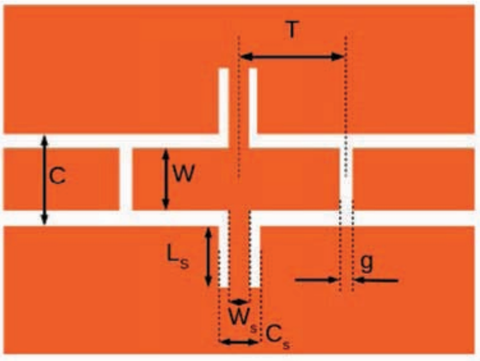

b

**Fig. 2.43:** Mock-up dimensions. b) Cell layout

To validate the circuit model, the $S$ parameters are compared between the model and the measurement. Since the main function of the cell is as a phase shifter, the phase of the $S_{21}$ is compared separately. The reconfigurable cell has beeb tested for the following series capacitors: $0.7pF$, $1.5pF$ and $3pF$.

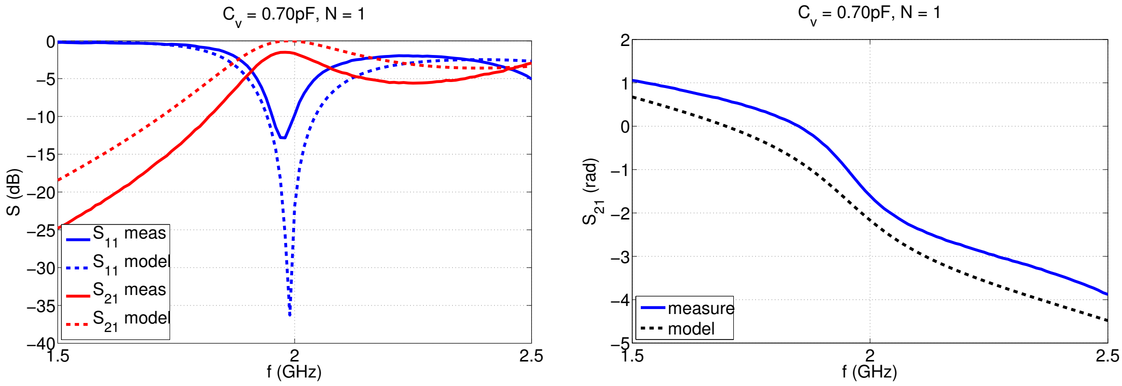

a b

**Fig. 2.44:** Reconfigurable CRLH cell with series SMD capacitor of $0.7pF$. a)$|S_{ij}|$ (dB) b) phase of $S_{21}$

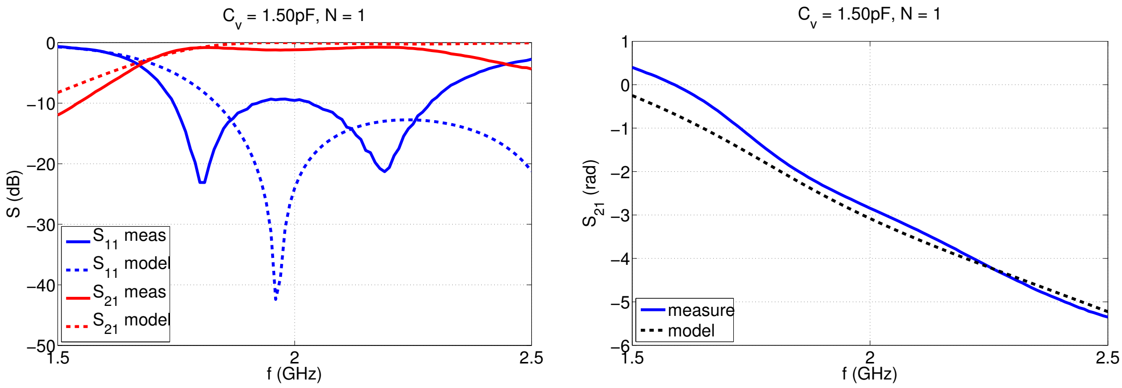

a b

**Fig. 2.45:** Reconfigurable CRLH cell with series SMD capacitor of $1.5pF$. a)$|S_{ij}|$ (dB) b) phase of $S_{21}$

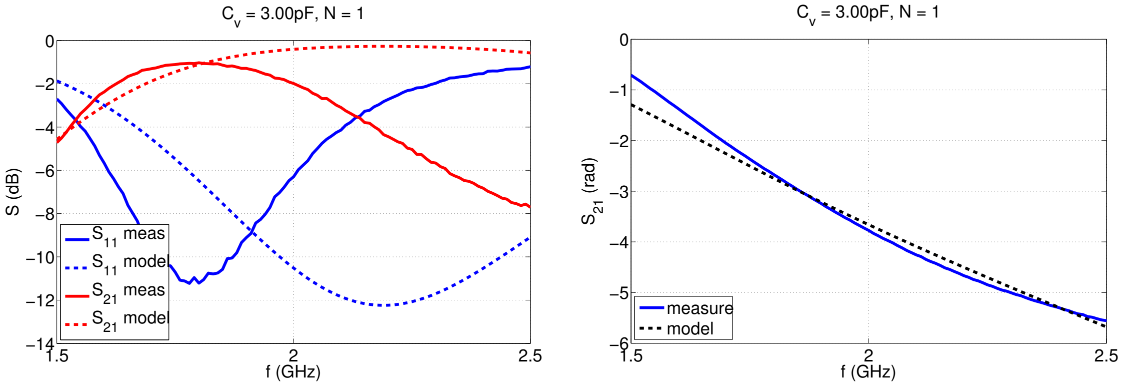

a b

**Fig. 2.46:** Reconfigurable CRLH cell with series SMD capacitor of $3.0pF$. a)$|S_{ij}|$ (dB) b) phase of $S_{21}$

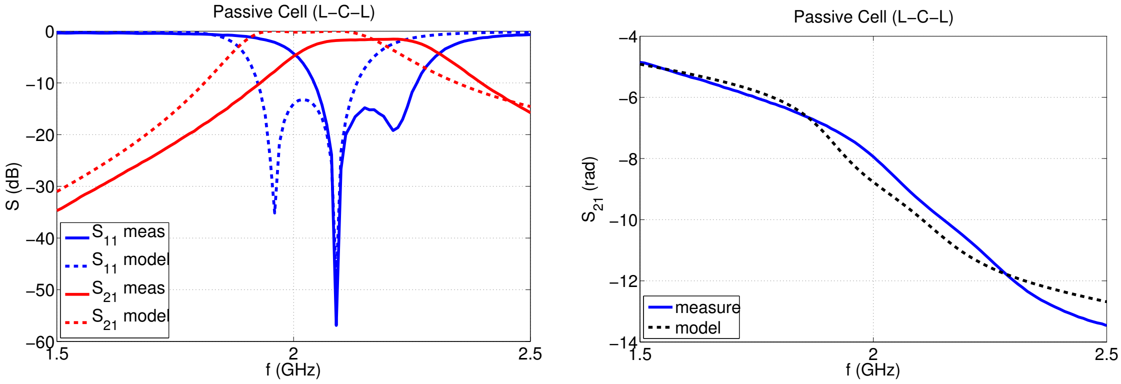

a b

**Fig. 2.47:** Non reconfigurable CRLH cell. a)$|S_{ij}|$ (dB) b) phase of $S_{21}$

Fig 2.44 to 2.47 show a good agreement between the model and the measurement. The model is more accurate for smaller values of the series capacitance. The prediction of the phase is however very accurate, which is a principal parameter for beam steering as a feed of a linear array.

One key aspect that was sought to validate with the mock-up circuits is the capability of modifying the phase evolution of the line with the modification of the series capacitor. This effect is evident in fig 2.48 where the phase of the three cells is compared to an arbitrary reference —in this case, the phase of the cell with capacitor $3pF$—.

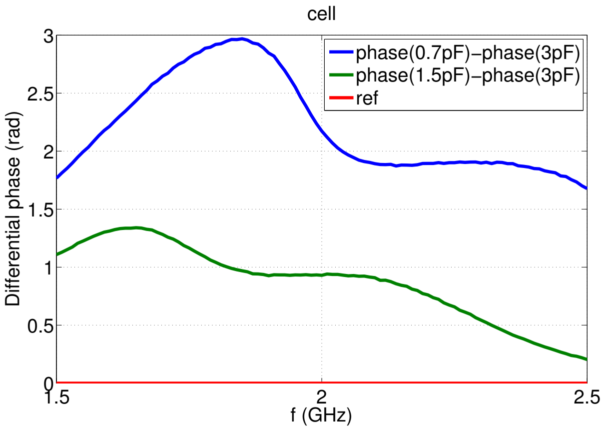

**Fig. 2.48:** Differential phase measurements

A three cell line has also been tested for the reconfigurable circuit with the same dimensions as the single cell. Fig 2.49 shows a photograph of the cell and fig 2.50 to 2.52 show the comparison of $S$ parameters between cell and circuit.

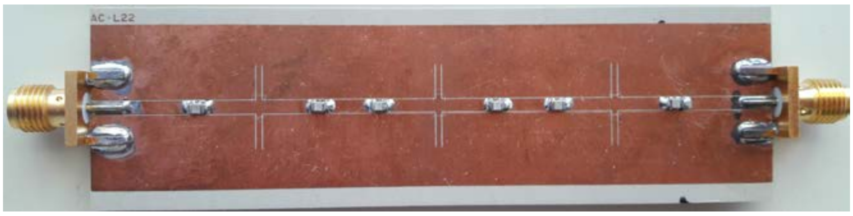

**Fig. 2.49:** CLRH reconfigurable line with 3 cells

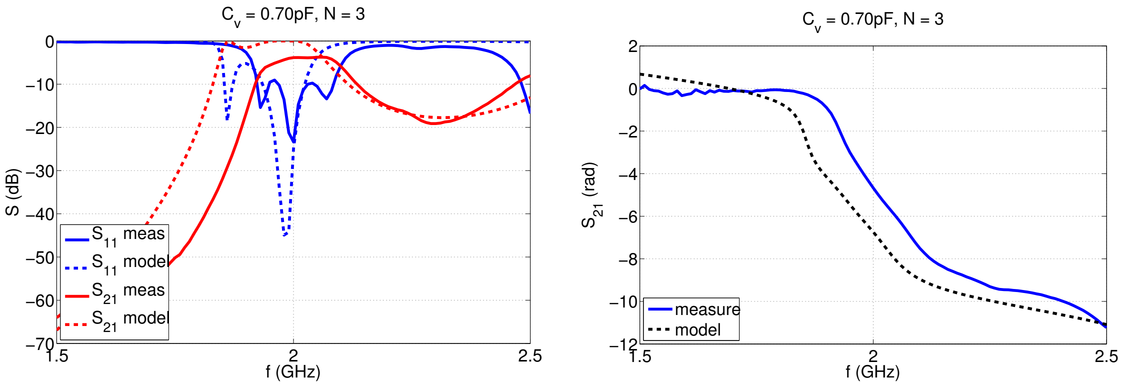

a b

**Fig. 2.50:** Reconfigurable CRLH line with 3 cells with series SMD capacitor of $0.7pF$. a)$|S_{ij}|$ (dB) b) phase of $S_{21}$

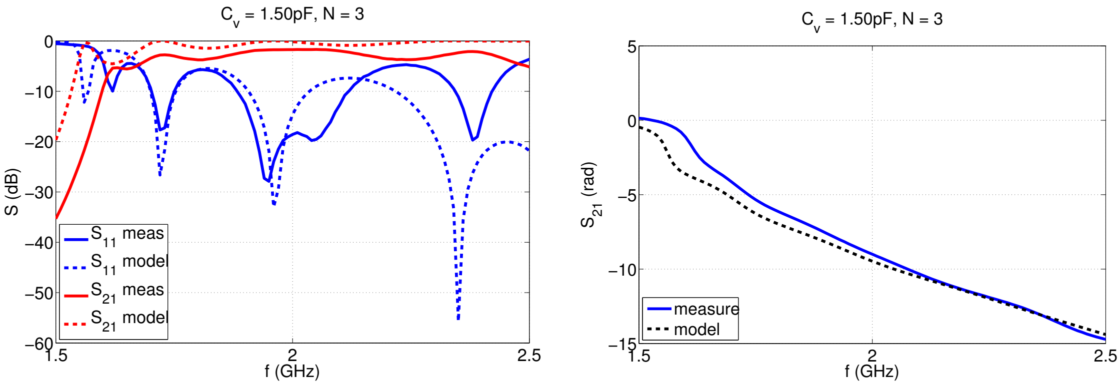

a b

**Fig. 2.51:** Reconfigurable CRLH line with 3 cells with series SMD capacitor of $1.5pF$. a)$|S_{ij}|$ (dB) b) phase of $S_{21}$

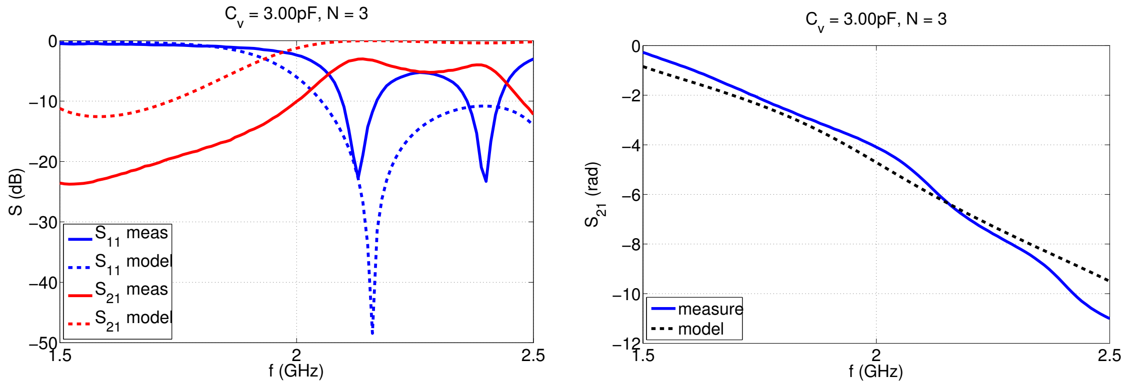

a b

**Fig. 2.52:** Reconfigurable CRLH line with 3 cells with series SMD capacitor of $3.0pF$. a)$|S_{ij}|$ (dB) b) phase of $S_{21}$

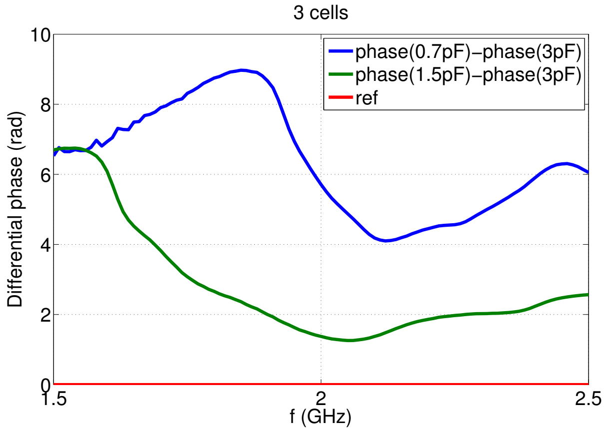

**Fig. 2.53:** Differential phase measurements for 3 cells

Similarly as for the single cell, the relative phase of the three circuits is shown in fig 2.53. There it can be seen that the phase shift of three cells does not corresponds to 3 times the shift of one cell. This may be due to the fact that the reference, the $3pF$ line, differs from the model, probably due to parasitic effects in the etching or the soldering of the connector.

The mock-ups have been realized at 2GHz instead of 14GHz because of the highly demanding etching required by the Ku band circuit. Indeed, the Ku band circuit typically required slots at least ten times smaller than the precision limit of standard manufacturing technology. Nevertheless, the 2GHz mock-up circuits were very close to the limit of the manufacturer, which resulted in some non-ideal effects (fig 2.54) for that reason the 6 cell passive CRLH line was manufactured but could not be tested. Variations from the original design can result in differences in line impedance or equivalent circuit of the discontinuity and that could explain the variation between circuit and model. Some radiation losses that were not included in the model were indeed present in the mock-up which further decreases the accuracy of the model.

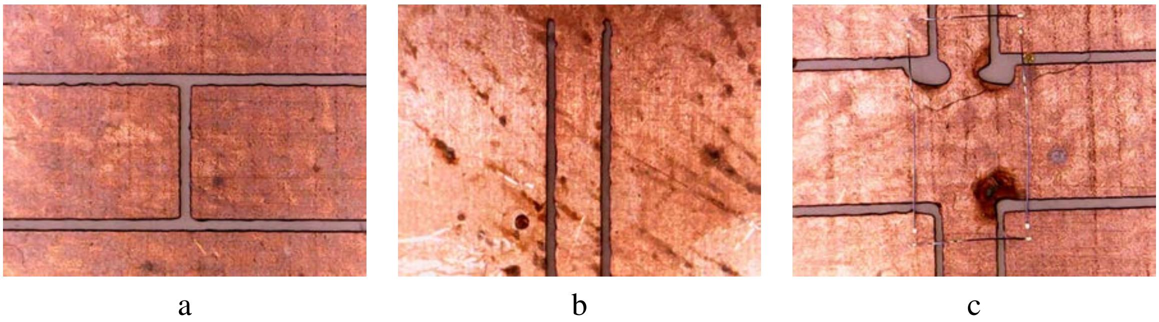

**Fig. 2.54:** Photographs of details of the circuit. a) Series gap b) Shorted end of stub c) Non-ideal stub connection

Finally, the bandwidth of three cell circuits have been calculated. The line is narrow band by design but this calculation sheds some light on what is the order of magnitude to expect from the CRLH based antenna. Table 2.3 summarizes the bandwidth of this three circuits.

| $C_v$ | $f_{min}$ | $f_{max}$ | bandwidth |
|---|---|---|---|
| 0.7pF | 1.97GHz | 2.03GHz | 3% |
| 1.5pF | 1.88GHz | 2.12GHz | 12% |
| 3.0pF | 2.09GHz | 2.17GHz | 3.76% |

**Table 2.3:** Bandwidth of the reconfigurable circuit for different values of the capacitor

In conclusion, the model has proven accurate for phase prediction and variably accurate for the module of the S parameters. The radiation losses that affect the behavior of the circuit will not be present in the final design, as will be explained in the next two chapters.

The model has proven to be a powerful tool for the design of CLRH reconfigurable lines. It allows much more rapidly than full-wave optimization to find a cell layout that creates the required phase profile. While the final design may require full-wave/prototype optimization, the circuit model greatly reduces the overall design time.

## Conclusion

This chapter has described the tools required for the design of a CPW CRLH reconfigurable line that can be used as the phased feed for a linear array. The theory behind periodic CRLH structures have been described and the discontinuities that can implement it have been successfully characterized. Finally, two design methods have been introduced that focus on the reconfigurability of the line and have been validated experimentally, this model greatly reduces the design time for CRLH lines.

The CRLH line introduced in this chapter represents the phasing of the series array, the heart of the beam forming subsystem. Next chapter deals with the shielding of the line and its interface with the radiating elements.

# Radiating element for the series array

## Contents

## Objectives

This chapter is devoted to the radiation of the line. In the last chapter, the CRLH line was designed so a certain phase profile can be chosen. Now the attention turns to how the CRLH line can be used as a beam forming network and lead to the radiation of a directive beam. First, the line is shielded to avoid undesired radiation. The first section of this chapter deals with how to shield the line without compromising the CRLH behavior.

Once the line is shielded, a probing mechanism to divert energy from the CPW line to a potential radiating element is introduced. This probing mechanism needs to have a minimal impact in the CPW CRLH line. A second condition imposed to the probing mechanism is that the percentage of energy drained needs to be controllable as well, this will help designing excitation profiles and create longer lines without radiating most of the power in the first few cells.

The chapter continues with the design of a radiating element connected to the probing mechanism and acts as array element. The independence of the radiating element from the probing mechanism allows the design of a large range of antennas with different polarization characteristics. This element will also need to present a wide beamwidth in order to efficiently radiate at angles away from broadside.

Finally, the full radiating system will be characterized in terms of circuit elements which can be included in the design of the CRLH line. The integration of the CRLH line and the radiating elements will be done in the following chapter.

# 1 CPW CRLH Line Shielding

The tunable CPW CRLH used in chapter 2 as a feed line for the series array has all the characteristics of a leaky wave line. Whenever the phase velocity reaches the *fast wave* condition $v_p > c$, the unshielded line radiates through the discontinuities.

The radiation of the line comes primarily from the series gap, since it is the only element that present asymmetric magnetic currents in the cell structure. As seen in [121] the radiation of the series gap is linearly polarized, in the $\theta$ direction. A polarizer might be enough to have a circularly polarized antenna but dual linear polarization might prove impossible. Additionally, the radiation of the gap is defined by its geometry. Moreover, as described in [121], the addition of the tuning varactor may reduce the radiation to lower levels than required.

Although the direction of the radiated beam follows the phase profile of the line, other characteristics such as polarization and field intensity cannot be controlled easily. For these reasons, this thesis proposes to shield the line and find other means of radiation using periodically energy extraction devices and radiating elements which are separated from the CPW line. Thereby, the radiating element can be more easily designed to create a better illumination of the array with a controlled polarization —circular, linear or dual linear—.

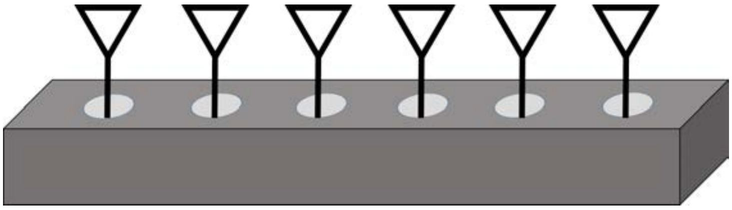

**Fig. 3.1:** Shielded CPW line probed periodically

The shielding in a CPW should be designed not to interfere with the functioning of the unshielded line. This can be achieved by separating the shielding from the CPW line. To study the optimal dimensions of the shielding a square shielding as in Fig 3.2 is considered. Keeping the shielding far from the CPW line should guarantee a behavior close to that of an unshielded line. Fig 3.2a shows how a narrow shielding modifies the line impedance. On the other hand, when the dimensions $D$ and $H$ are too large, a rectangular waveguide mode is supported in the structure and energy can potentially be transferred between modes. Indeed, in fig 3.2c unwanted resonances appear when the dimension $D$ gets electrically large. To ensure that only a CPW mode travels through the shielded line, the rectangular waveguide fundamental mode needs to be suppressed [114]:

$$h_1, D < \frac{\lambda}{2} \tag{3.1}$$

$$D < \frac{\lambda}{2\sqrt{\epsilon_r}} \tag{3.2}$$

$$h_s \cdot \sqrt{\epsilon_r} + h_2 < \frac{\lambda_0}{2} \tag{3.3}$$

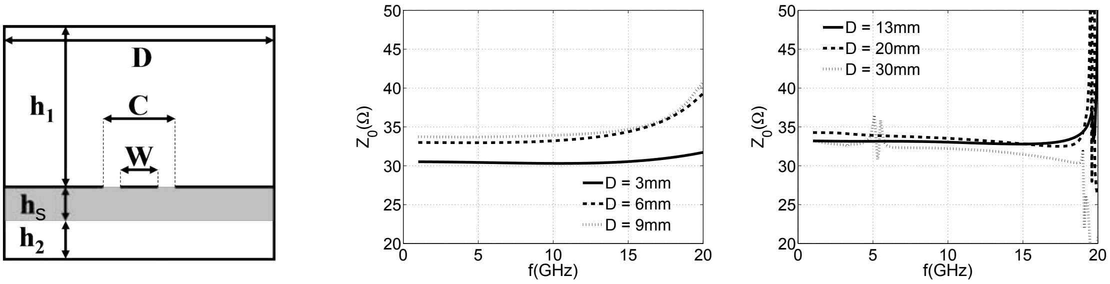

a b c

**Fig. 3.2:** a) Shielding geometry b)c) Wideband full-wave simulation of the characteristic impedance of the shielded line for different shielding widths. ($C = 2mm$, $W = 1.7mm$, $h_s = 1.54mm$, $\epsilon_r = 10.7$)

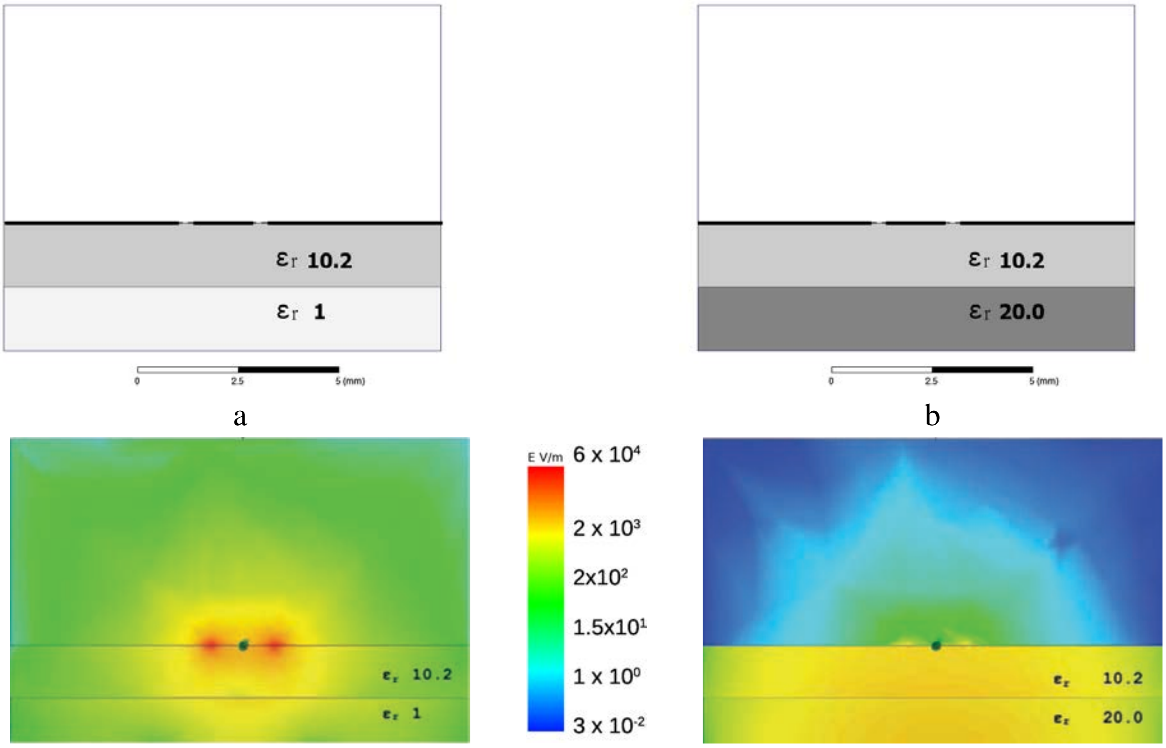

a b

c d

**Fig. 3.3:** a) Shielded CPW line with two dielectric slabs where $\epsilon_{r,1} > \epsilon_{r,2}$ b) Shielded CPW line with two dielectric slabs where $\epsilon_{r,1} < \epsilon_{r,2}$. c) E field intensity of the fundamental mode of (a) as solved with HFSS (logaritmhic scale). d) E field intensity of the fundamental mode of (b) as solved with HFSS (logaritmhic scale)

If the shielding is directly in contact with the substrate, the CPW becomes a Ground Backed CPW (GBCPW) with different propagating modes than CPW. To prevent GBCPW from propagating, there should be a spacing between the substrate and the shielding. In fact, any other substrate with permittivity lower than that of the CPW substrate helps insulating the CPW from the back conductor.

For any spacer set between the line and the shielding, as long as $\epsilon_{r1}>\epsilon_{r2}$, the fields remain akin to those of a CPW. This is demonstrated in fig 3.3, where the intensity of the electric field is represented.

For the line with $\epsilon_{r1}>\epsilon_{r2}$, the **E** field is concentrated around the slots like a regular CPW mode. For the line with $\epsilon_{r1}<\epsilon_{r2}$ on the other hand, the coupling with the lower shield is intensified and the CPW modes are dimmed or absent.

# 2 Study of coupling mechanisms for energy probing

## 2.1 State of the Art in CPW Couplers

In this chapter, a coupling mechanism is developed for draining the energy out of the CPW line. For that, a transition between a CPW line and a microstrip line will be implemented. Therefore a brief *state of the art* on the type of multilayer transition is presented here.

In the type of transitions here presented, the transmission of energy is chiefly performed by direct connection of the two layers through a via hole. In [122], a quadrature coupler is created by connecting two parallel CPW lines through two microstrip lines etched in the back of the substrate. Fig 3.4 shows how the connection between CPW and microstrip is done directly through a via hole that connects both signal strips.

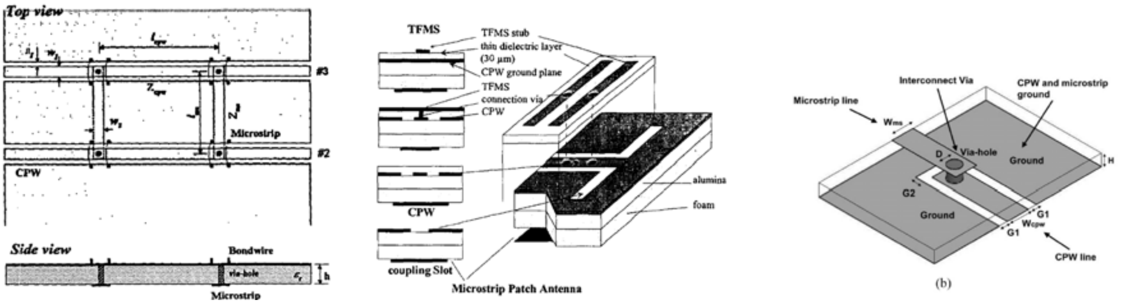

a b c

**Fig. 3.4:** CPW multi-layer coupling through via holes. a)[122] b)[56] c)[57]

This type of connection is also presented in [56], where a CPW line is connected to two stripes in a different level through via holes. Also in [57], a multilevel transition is made by directly connecting the central strip of a CPW line to a microstrip line.

Coupling is also possible without direct contact by placing the two lines co-axially in different levels. This is the case of [123] or [124], where the extension of a microstrip in the back of a CPW line create a broadband coupling (fig 3.5).

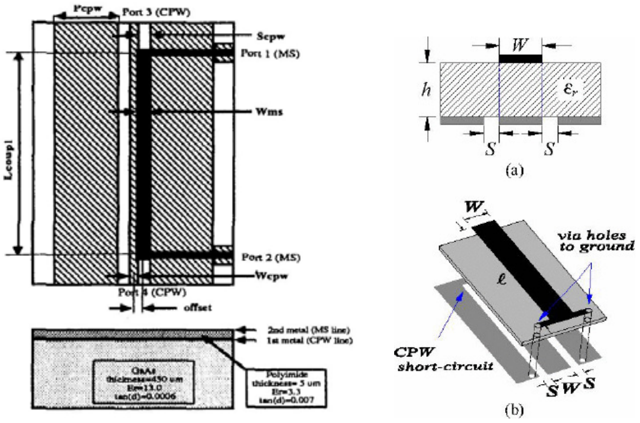

a b

**Fig. 3.5:** CPW multi-layer coupling. a)[123] b)[124]

## 2.2 Extraction of energy from the shielded line

To achieve a series array, extraction of energy must be carried out periodically along the line. The extraction can be done by opening a window in the shield to provide access to the line (fig 3.1). The smaller the extraction aperture is, the more the line will be protected from undesired leakage and external interference.

Theoretically, an aperture much smaller than the wavelength should not affect the shielding. Since the unit cell is already much smaller than the wavelength, an aperture width the size of a fraction of a cell will be small enough.

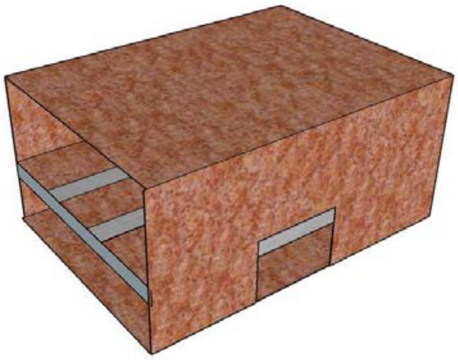

**Fig. 3.6:** An electrically small aperture is carved in the side of the shielding to extract the energy

A port can be defined on the side of the shielding, therefore the design of the coupling mechanism can be dissociated from the access to the line. Fig 3.7 shows a scheme of this concept. A transverse access line is created to define a clear port as independent as possible from the coupling mechanism. For the access, the ground plane of the CPW can be utilized as the ground plane of a microstrip line that runs in the opposite side of the substrate, this way, it can reach an opening of the shielding where it transforms into a stripline port, as seen in fig 3.7.

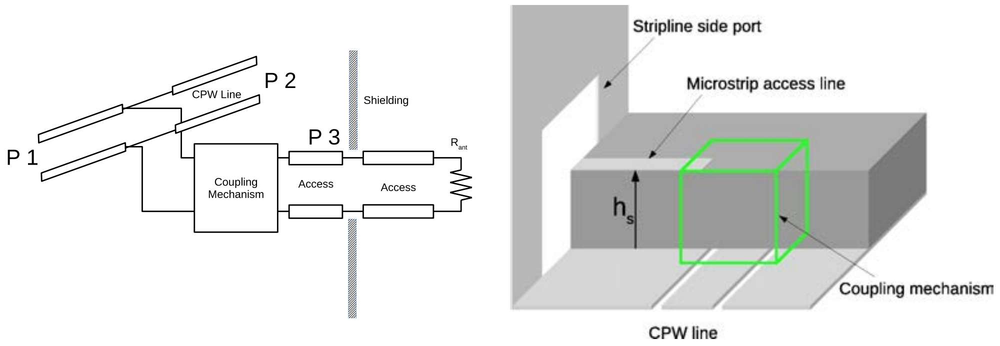

a b

**Fig. 3.7:** a)Scheme of the coupling system. b)Design of the microstrip access line an stripline port

Separating the antenna from the coupling the study the coupling level easier. A simulation can be done where a CPW line is excited in both ends through the ports 1 and 2 in fig 3.7 and a third port can be defined on the shielding. This way, the $S_{ij}$ parameters with $i = 1,2$ can be used to study the effect of the coupling system in the CLRH line as if it was another discontinuity and the $S_{31}$ parameter gives an idea of the amount energy coupled,

$$P_3 = \frac{P_1}{1-|S_{11}|^2}|S_{31}|^2 \tag{3.4}$$

For a negligible $S_{11}$, the coupling efficiency $\eta_C$ can be defined as

$$\eta_C = \frac{P_3}{P_1} = |S_{31}|^2 \tag{3.5}$$

The characterization of the coupling mechanism need to be done thoughtfully. It is well known that a lossless 3-port circuit cannot have its three ports matched [114]. However, the study of this 3-port device is only an intermediate step and, as described in appendix H, once the radiating element is connected, it will act as a 2-port device delivering power to the antenna.

This does not mean that the impedance of the antenna is irrelevant, the study of the coupling through $S_{31}$ is only meaningful if the antenna impedance is close to the reference impedance used for the simulation as load. Larger impedances have a smaller impact in the normal transmission of energy through the CRLH line but also drain a smaller portion of energy.

## 2.3 Coupling Mechanism

To feed an arbitrary number of radiating elements, the amount of energy drained from the CPW line has to be controllable. Long lines should drain a very small percentage per cell, otherwise, most of the radiation will come from the beginning of the line and extra cells would be irrelevant, not contributing to the gain of the array.

In order to tackle the coupling problem, the attention is shifted towards the domain of electromagnetic compatibility (EMC). In EMC the coupling between circuits is thoroughly studied with the intention of preventing it, for this report the concepts will be applied in the other direction. Any basic text of electromagnetic compatibility [125] gives an account of the types of *undesired* coupling mechanisms in a given circuit. The most important ones are:

— Electric coupling
— Magnetic coupling
— Radiation coupling
— Common impedance coupling

Since the common impedance coupling has a greater impact at lower frequencies, and the radiative coupling occurs when two elements are in their respective far field regions, only the electric and magnetic coupling are worth considering.

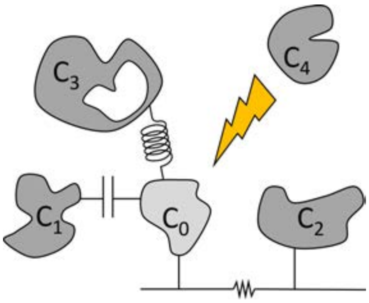

**Fig. 3.8:** Different ways of coupling between circuits. 0-1:electric coupling, 0-2: common impedance coupling, 0-3: magnetic coupling, 0-4: radiation coupling

To create a magnetic coupling, a loop could be etched at the back of the substrate as seen in fig 3.9a. By virtue of Faraday's law, the magnetic field created by the CPW line will induce a current on the loop that can be later re-directed towards a port on the side of the shielded CPW line. The size of the loop can control the amount of energy coupled out of the system. Fig 3.9b shows how different loops couple as a function of their area and distance from the line. This type of coupling, although promising, have proven to be hard to control and susceptible to parasitic electric coupling between the access line and the shielding of the CPW line and will be discarded.

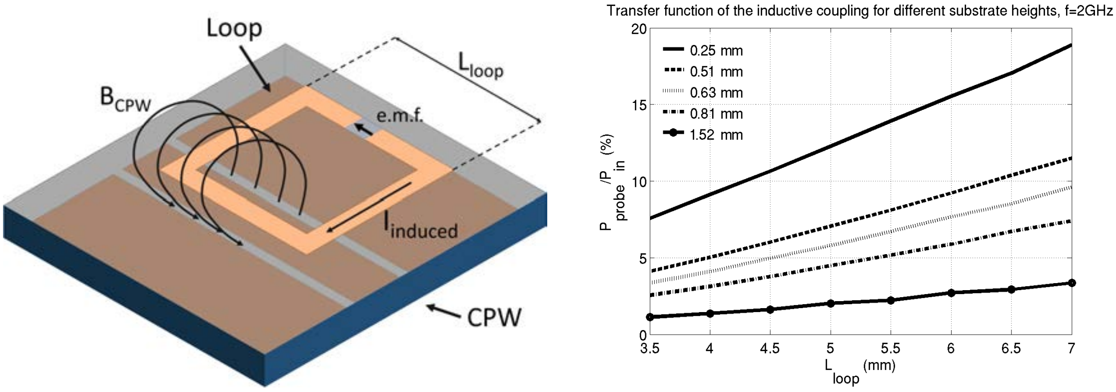

a b

**Fig. 3.9:** Magnetic coupling

The second option, the electric coupling consists of a controlled capacitor between the signal strip of the CPW line and a microstrip line that accesses the side port (fig 3.10a,b). Analogously to the circuits seen in section 2.1, a via hole needs to be made in the substrate but the result is a system where the phasing signal travels through a side of the circuit and, on the other side, the energy is coupled out of the system progressively in a direction orthogonal to propagation.

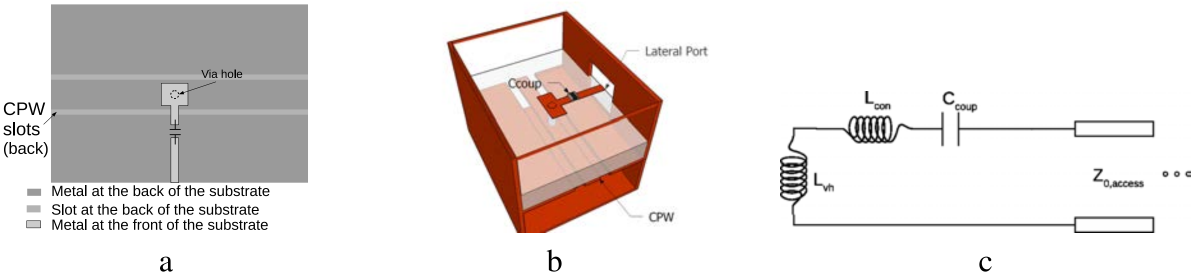

a b c

**Fig. 3.10:** Electrical coupling. a) layout b) scheme of the electric probing system c)equivalent circuit

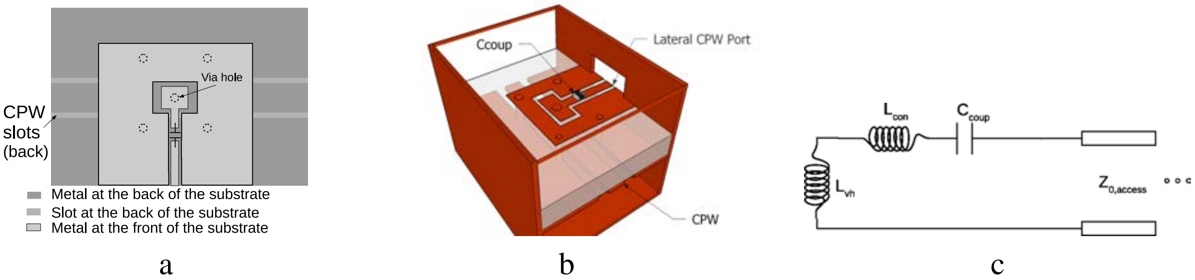

a b c

**Fig. 3.11:** Electrical coupling. a) layout b) scheme of the electric probing system c)equivalent circuit

A similar concept can be applied to a CPW coupling port, as seen in fig 3.11a,b. In that case, the ground planes of both the CRLH plane and coupling plane are connected and the control capacitance is inserted in the central strip of the coupling CPW, resulting in a circuit similar to the previous *stripline* one.

The circuit that represents both systems can be seen in fig 3.10c. Here the effects of the via $L_{vh}$, the coupling capacitor $C_{coup}$ and the connection between them $L_{con}$ are represented by reactive circuit elements. The resistor $R_c$ represents the energy coupled out of the circuit, considering that the antenna has a purely resistive load. This circuit has series resonance at

$$f_r = \frac{1}{2 \quad \overline{(L_{vh}+L_{con})\,C_{coup}}} \tag{3.6}$$

For instance, a substrate of 1.5mm, a 0.7mm diameter via-hole and a 0.5mm separation between the coupling capacitor and the center of the circuit, lead to a total inductance in the neighborhood of $0.5nH$. That sets a resonance frequency in the tens of GHz for coupling capacitors in the $pF$. This can be used to draw energy, setting the resonance closer or further from the working frequency to control the amount of energy extracted from the CPW line.

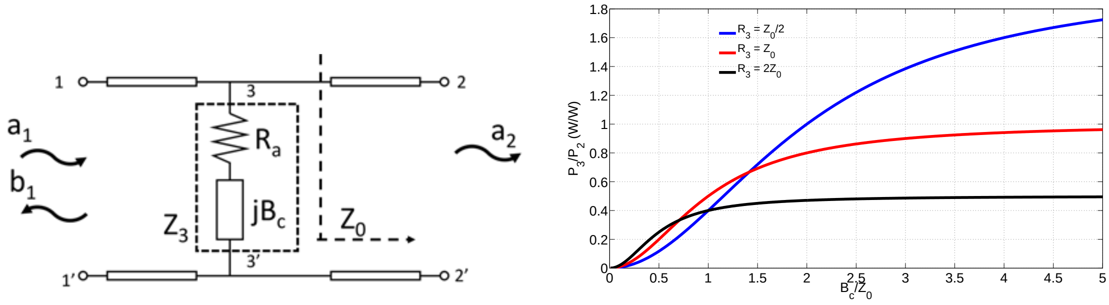

a b

**Fig. 3.12:** Coupling mechanism, a)equivalent circuit and b)port 3 to port 2 coupling ratio as a function of the susceptance $B$

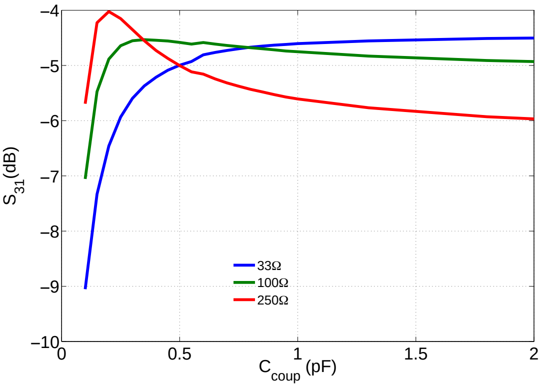

**Fig. 3.13:** $S_{31}$ for different reference impedances in port 3 ($h_s = 0.508mm, \epsilon_r = 6.15, W = 240\mu m, C = 280\mu m, h_1 = 1.5mm, h_2 = 1mm, D = 3mm$)

When the coupling mechanism is implemented, it can be seen as load connected in parallel to the transmission line (fig 3.12). The shunt impedance $Z_3$ in fig 3.12 represents the coupling mechanism plus the antenna. The power lost to radiation is represented by $R_a$ while the reactive elements, including the coupling capacitor, by susceptance $B_c$. Modifying the coupling capacitor modifies the susceptance $B_c$, hence controlling the ratio of power drained (port 3) to transmitted (port 2), as seen in fig 3.12b. Appendix H includes a reflection to this respect. Fig 3.13 shows that, for different reference impedances $Z_3$ in port 3, different kinds of coupling can be achieved.

The peak in the curve for $Z_3 = 33$ highlights that some extra parasitic elements that were not considered in 3.12 are in place, as the reference impedance increases, these effects become less relevant. The effect remains that the transmission parameter $S_{31}$ can be easily controlled with the coupling capacitance $C_{coup}$.

The coupling capacitor can be an etched capacitor or a SMD capacitor. Fig 3.14 shows different coupling levels for different values of $C_{coup}$ in L and Ku bands for the circuit in fig 3.10b.

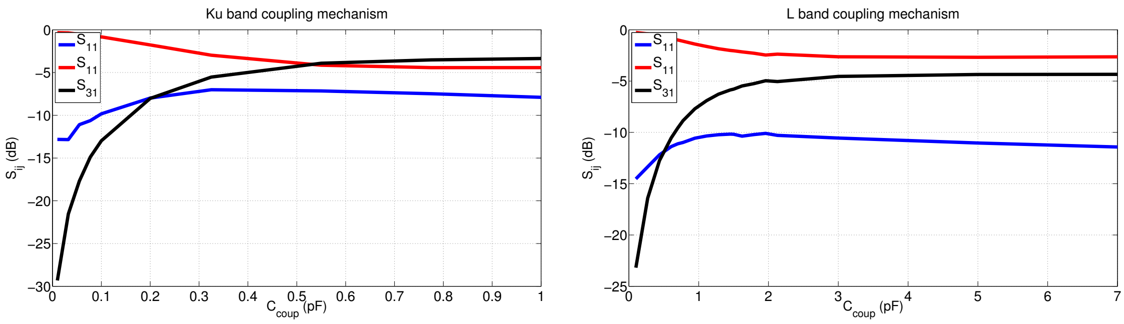

a b

**Fig. 3.14:** Coupling level between the CPW line and the side port ($h_s = 1.49mm, \epsilon_r = 10.7$)

One drawback of this draining circuit is the phase shift introduced by the capacitance. Fig 3.15 shows the phase shift between ports 1 and 3 for different values of $C_{coup}$. The beam steering of the final antenna is based on the phase difference between radiating elements, which needs to be controlled by the CRLH line and not by $C_{coup}$.

The phase to $C_{coup}$ variability is not a problem if all the probing points are set to the same coupling efficiency $\eta_C$. A constant $\eta_C$ structure can create fully illuminated arrays by setting the efficiency very low; however, an uniformly illuminated antenna needs to have ever increasing coupling efficiencies and that can only be achieved if the access line to the radiating element compensates for the phase difference introduced by the different values of $C_{coup}$. Means of phase compensation can be envisioned for the full antenna and will be discussed in the next chapter.

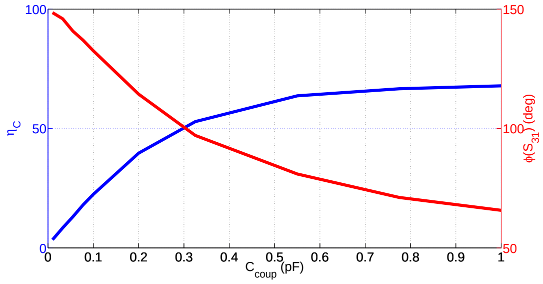

**Fig. 3.15:** Coupling level (%) and phase difference between CPW input and side port

In the first half of the chapter, the CPW line has been shielded to insulate the CRLH from the radiation. A system to drain energy from the line have been designed and characterized for an arbitrary reference impedance. In the rest of the chapter, a radiating element will be designed and connected to the energy draining circuit. Finally, the full radiating subsystem will be characterized as a circuit element ready to be insert it in the design of the CRLH line.

## 2.4 Experimental Validation

A three port circuit with a CPW ended energy extraction device (fig 3.16) has been manufactured to corroborate the simulations of the energy extraction device. Ports 1 and 2 feed a CPW line of impedance 32 . In the center of the line, an energy extraction device diverts some energy towards a transverse CPW port of impedance 50 .

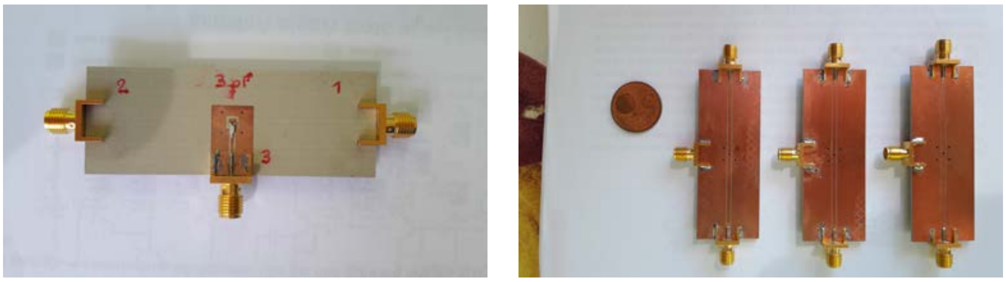

a b

**Fig. 3.16:** Energy extraction device prototype

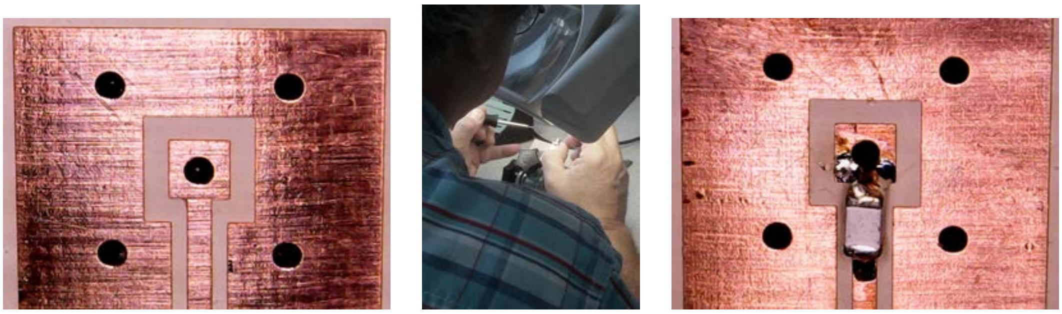

a b c

**Fig. 3.17:** Energy extraction device prototype. Details

Because of the available manufacturing etching precision, the prototype has been done in L band. The measurement has been performed with 50 connectors and the S parameters have been renormalized to a reference impedance equal to that of the CPW line.

Three prototypes have been manufactured. One with a $1.5pF$ coupling capacitor $C_{coup}$, another one with a $3pF$ coupling capacitor and one last circuit with a straight line without connector which represents an infinite capacitance.

The power transmitted to the third port to a fictitious impedance of value $Z_3$ is calculated through the value of $|S_{31}|^2$. The magnitude does not represent the power in absolute values but gives a measurement of power ratios:

$$\frac{P_{3,Z_3=Z_a}}{P_{3,Z_3=Z_b}} = \frac{|S_{31,Z_3=Z_a}|^2}{|S_{31,Z_3=Z_b}|^2} \tag{3.7}$$

As explained before, both the coupling capacitor and the impedance of the load in the third port controls the power coupled. Designing the load impedance to have a certain amount of power coupling gives an extra degree of freedom to choose the value of the coupling capacitor and vice-versa. Fig 3.19 shows the power coupled into port 3 for different load impedances in the three prototypes.

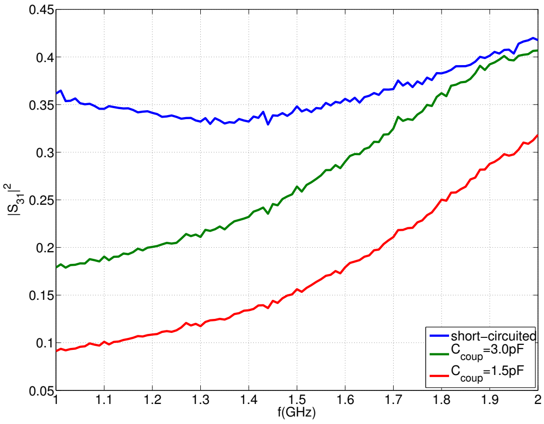

**Fig. 3.18:** $|S_{31}|^2$ for the three prototypes at different frequencies

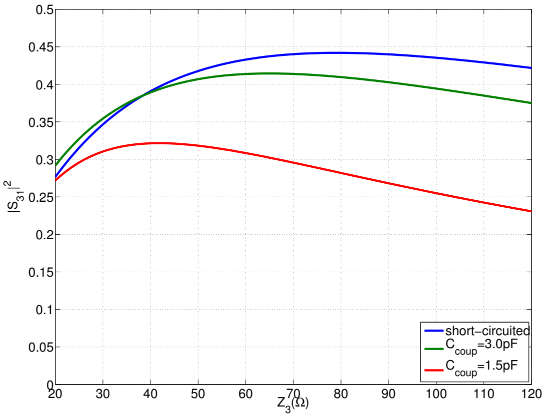

**Fig. 3.19:** $|S_{31}|^2$ for the three prototypes for different load impedance $Z_3$

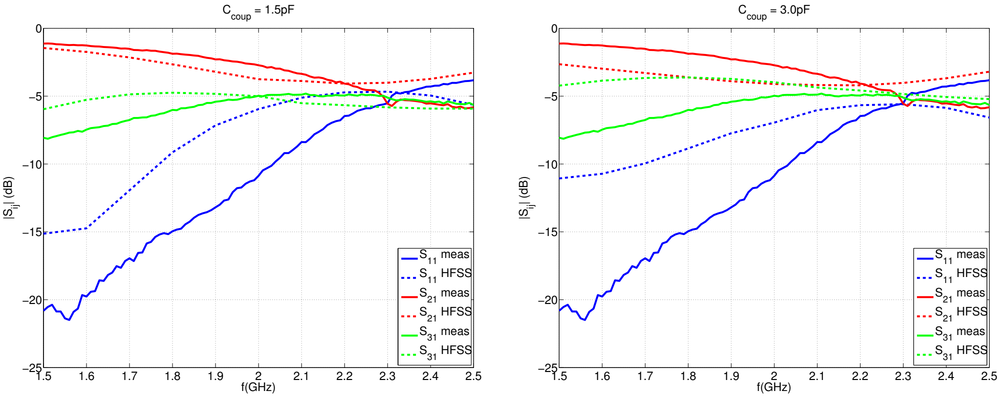

a b

**Fig. 3.20:** Simulation and measurement comparison of the overall S parameters

For completion, fig 3.20 shows a comparison between simulation and measurement. Some disparities are probably due to the effect of the connector. Indeed, the impedance of the CPW line 32 does not match the impedance of the connector 50 and a proper calibration kit was not used.

Moreover, no air bond-wires are introduced in the CPW line. The bond-wires help suppressing undesired modes. In this structure the via connection to the probing side of the circuit should have the same effect but, ideally, the air bond-wires should be as electrically small as possible.

Despite these small discrepancies, the measurements validate the concept used. The loading impedance as well as the coupling capacitor $C_{coup}$ clearly control the power coupled to the port 3 and serve as an energy extraction device. This can be used as a connection point for radiators to create CPW fed linear arrays or leaky wave antennas.

# 3 Radiating element

The probing mechanism described in this chapter can be used to feed any type of antenna that could be adapted to a stripline or a CPW port, preferably backed with a ground plane to force radiation into a single semispace. This feature allows the control of the polarization and the beamwidth to be designed independently from the illumination.

## 3.1 Patch antenna

The microstrip patch antenna is chosen to be the radiative element of the line. As a first proof of concept, the patch antenna is ideal since it is easy to design and can be used as validation. The most basic patch antenna is linearly polarized and narrow band but it offers options for expanding both of these features. For example, the patch antenna can not only be designed to radiate circular polarization, it can also be adapted for dual excitation, offering dual polarization capabilities. Although it will not be treated in this report, topology modifications for band widening exist.

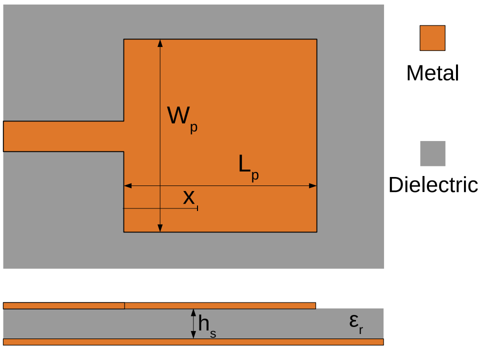

**Fig. 3.21:** Microstrip or patch antenna

*Antenna Design*

A layout of the patch antenna fed by a microstrip line is depicted in fig 3.21. Typically, the height of the substrate should be much smaller than the wavelength and the permittivity as low as possible. The equations for the design of the patch antenna can be found in [126].

If the permittivity of the substrate is high, it can have a negative effect in the characteristics of the antenna in terms of impedance and gain. Nevertheless, a low gain antenna can still be useful in an array since the array factor boosts the final gain of the complete antenna. The size of the patch is roughly $\lambda_g/2x\lambda_g/2$, with a high permittivity substrate, these dimensions will be considerably smaller than $\lambda_0/2x\lambda_0/2$, a typical size of an antenna array.

The width of the antenna $W_p$, relates to the input impedance and the bandwidth. Larger widths have larger bandwidth and smaller impedance. A good starting point for optimization is to fix $W_p = L_p$, in which case the impedance is somewhere in the neighborhood of 300 .

*Feed Design*

To feed the antenna, the coupling mechanism explained in the previous section can be seen as a voltage generator with a source impedance $Z_s$. The objective is to match that impedance as much as possible to the input of the antenna $Z_a$ (fig 3.22a). Traditionally there are two main techniques for matching a patch antenna. The first technique consists of inserting a quarter wavelength adapter between the source and the patch, i.e. a line of length $\lambda_g/4$ and impedance $Z_w = \sqrt{Z_a Z_s}$.

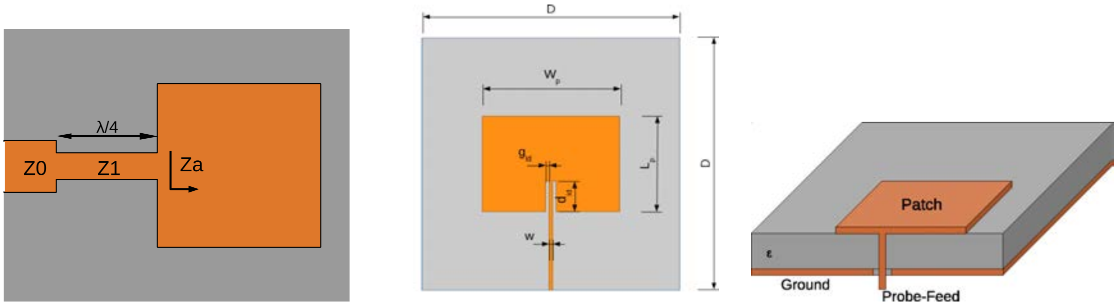

a b c

**Fig. 3.22:** a)Quarter wavelength transformer fed patch antenna, b) inset fed patch antenna c) backfed patch

The other technique moves the feed point of the antenna to a spot of lower impedance. To better understand that, the profile of current along the antenna can be analyzed. The current will basically be zero at the radiating ends of the antenna, since they are equivalent to an open circuit.

Because the length $L_p$ is set to be one half wavelength, the current increases as $I \approx \cos \frac{x}{L_p}$ . The voltage is maximum in the ends and decreases with the same profile of $I$, yielding an impedance as a function of the distance from the border $Z(x)$ of

$$Z(x) = Z(0) \cdot \cos^2 \frac{x}{L_p} \tag{3.8}$$

In order to reach the point of the desired antenna impedance, there are different feeding techniques. An inset (fig 3.22b) etches a groove in the antenna for the feed to connect to the patch at the desired $x$ distance. Another option is to excite it through the substrate. A hole can be pierced in the ground plane through which a probe feed can be inserted (fig 3.22c) through the back. In this back-fed structure, the point of antenna impedance desired can be reached without adding complexity to the shape of the patch.

A patch antenna have been designed to test the probing mechanism. The layout can be seen in fig 3.22, the substrate is a Rogers Duroid 6006 with a relative permittivity or 6.15 and a height of $0.508mm$ ($20mil$). The choice of substrate is to have high permittivity for miniaturization purposes but not so high to overcomplicate the design of the antenna. In order to simulate array conditions, the antenna has been simulated with PMC walls. The $S_{11}$ and gain of the antenna are represented in fig 3.24, a bandwidth of 2.3% can be appreciated.

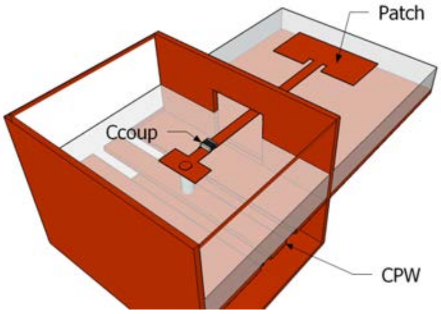

**Fig. 3.23:** Patch antenna connected to the CPW line

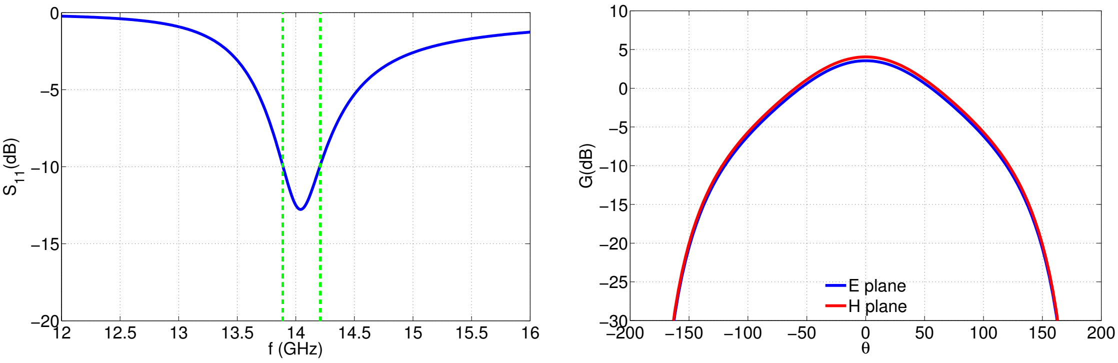

a

b

**Fig. 3.24:** $S_{11}$ and gain of the patch antenna in fig 3.22. Characteristics in table 3.1

The patch can be easily connected to the microstrip port on the side of the CRLH line created by the coupling mechanism (fig 3.22). In the image it can be seen the continuity in the substrate and how the level of the CPW serves as the ground plane for the patch antenna. In chapter 4, possible realizations will be discussed, for now, it is only necessary to know that the CPW line is fully shielded except for the stripline hole on its side that serves as feed for the patch antenna.

In order to emulate a network condition, the patch antenna is placed in a box filled with air of size $\lambda_0/2x\lambda_0/2$ with periodic boundaries on the sides. This imitates the conditions of an infinitely periodic array. A real array will have some edge effects in the extremities but the infinite line condition will suffice for now for the design of the patch antenna. After an optimization process, the final dimensions of the patch antenna can be seen in table 3.1. The radiation pattern, represented in fig 3.25, remains similar to that of a patch antenna. Finally, fig 3.26 shows how the choice of the coupling capacitor $C_{coup}$ can control the percentage of power radiated by the antenna.

Single Patch

| Param | Value |
|---|---|
| $W_p$ | 5.07mm |
| $L_p$ | 3.9mm |
| $g_{id}$ | W/40 |
| $d_{id}$ | 1.3mm |
| w | 0.15mm |

Connected Patch

| Param | Value |
|---|---|
| $W_p$ | 5mm |
| $L_p$ | 4mm |
| $g_{id}$ | W/40 |
| $d_{id}$ | 0.8mm |
| w | 0.15mm |

CPW line

| Param | Value |
|---|---|
| $C$ | 0.28mm |
| $W$ | 0.24mm |
| $h_s$ | 0.508mm |
| $D$ | 5mm |
| $C_{coup}$ | 0.2pF |

**Table 3.1:** Patch antenna connected to the CPW line. Table with dimensions

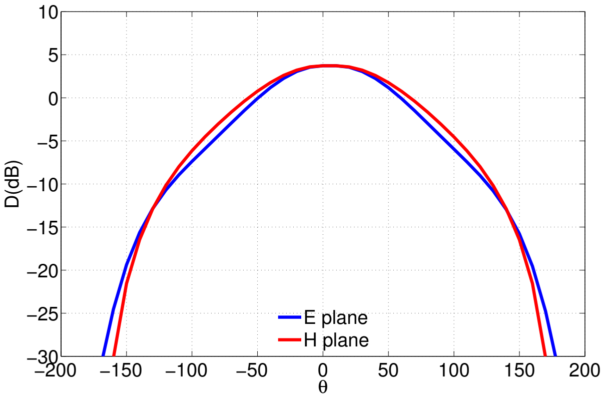

**Fig. 3.25:** Directivity of the patch antenna connected to the CPW line. Characteristics in table 3.1

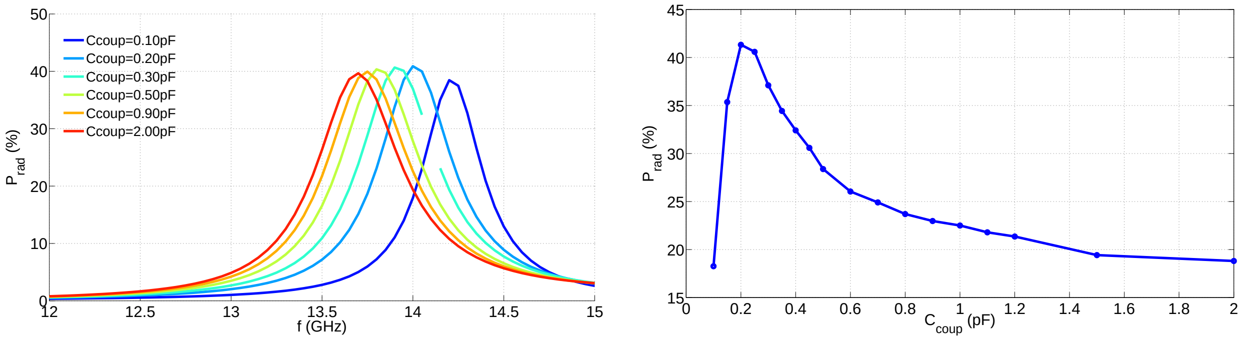

a b

**Fig. 3.26:** Patch antenna connected to the CPW line. Percentage of the power injected in the CPW line that is radiated by the patch antenna.Characteristics in table 3.1. a) Representation in frequency for different $C_{coup}$. b) $P_{rad}$ vs $C_{coup}$ at 14GHz

## 3.2 Dual Polarized Patch

A circular patch can be designed to be fed, for instance, with a CPW energy extraction port like the one in fig 3.11. The probe can be connected through a vias like the one created for the energy extraction device. Fig 3.27 shows the design of such a patch.

The patch is supported by two layers of dielectric separated by a metal layer. It is in that metal layer (layer 2) that the CPW feed is etched. The whole stack composed of metal layer 1 (patch), substrate 1 (with via), metal layer 2 (CPW feed) and substrate 2 rest on a ground plane that prevents radiation to the back.

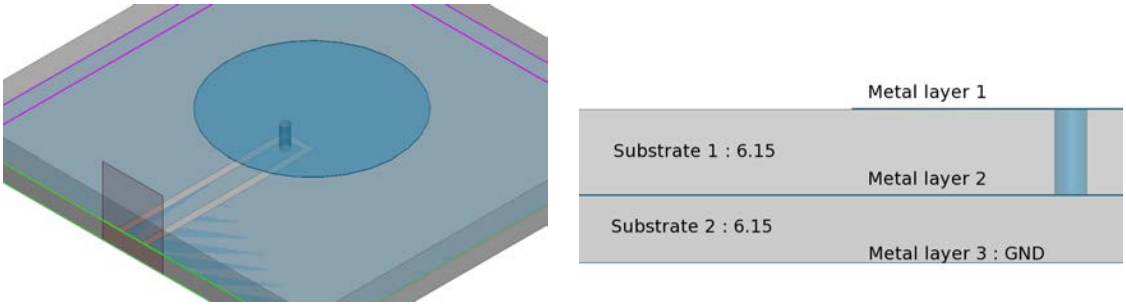

a b

**Fig. 3.27:** Single Circular patch

The point of access is selected so the patch antenna is matched to the port impedance of the CPW line — 40 in this case—. This simplifies the connection to the energy extraction device. Since the patch is completely circular, another access point can be added creating a right angle between the points *VOH* (fig 3.28). The two access can now feed the antenna two orthogonal modes that can generate dual linearly polarized radiation. The antenna needs to be design to radiate the energy input by each of the ports, here named V and H for vertical and horizontal. As important as the impedance matching is to ensure that the energy does not couple from one feed to the other and gets coupled between the V and H ports. The simulations of the developed antenna can be seen in fig 3.28 and the dimensions of the patch are compiled in table 3.2.

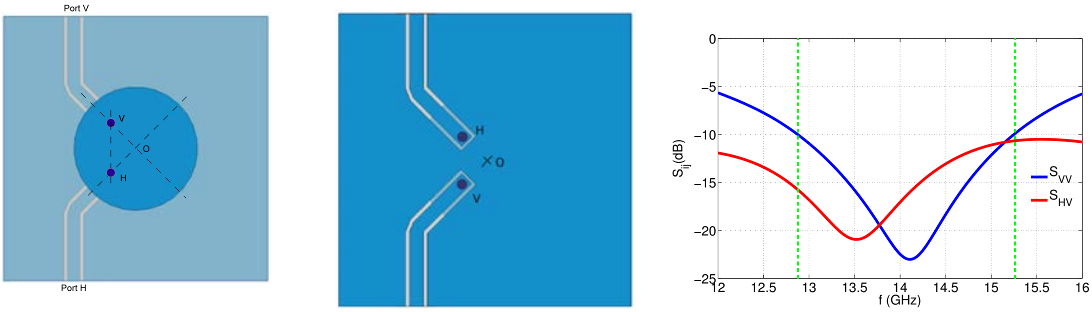

a (metal layer 1) b (metal layer 2) c

**Fig. 3.28:** Dual fed circular patch a) Top view and b) Bottom view c) isolation and insertion loss, a bandwidth of 16.9% is appreciated

| **Param** | **Value** | **Param** | **Value** |
|---|---|---|---|
| Radius | 2.5mm | $\overline{VO}$ | 1.2mm |
| Radius (single fed) | 2.5mm | center-to-feed (single fed) | 0.8mm |
| $h_{s1}$ | 0.508mm | $h_{s2}$ | 0.508mm |
| $\epsilon_{r1}$ | 6.15 | $\epsilon_{r2}$ | 6.15 |
| $C_{CPW}$ | 0.9mm | $W_{CPW}$ | 0.5mm |

**Table 3.2:** Dimensions of patches in fig 3.27 and 3.28

The use of two ports requires the connection to two different lines (fig 3.29). Each of the lines will have the same configuration —*i.e.* it will have the diodes biased similarly— but with a phase shift in its input. This way, the antenna can choose whether to receive in linear or circular polarization in different directions and senses of rotation. The dual polarized antenna have been simulated for different configurations (fig 3.30).

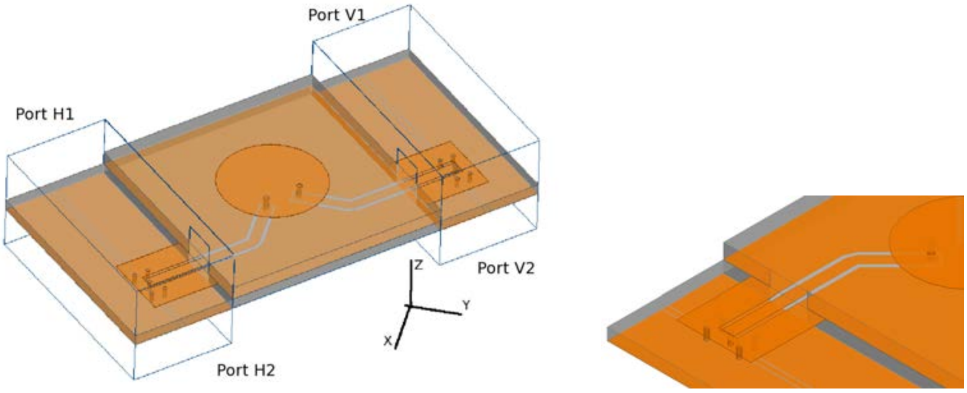

**Fig. 3.29:** Dual fed circular patch connected to two side CPW lines

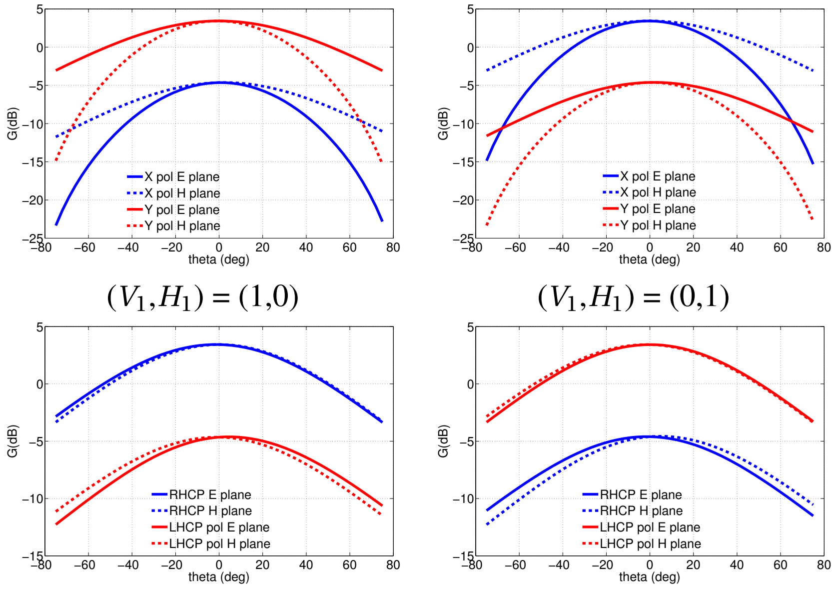

$(V_1, H_1) = (1{,}0)$ $(V_1, H_1) = (0{,}1)$

$(V_1, H_1) = (1{,}i)$ $(V_1, H_1) = (i{,}1)$

**Fig. 3.30:** Dual fed circular patch connected to CPW lines

# Conclusion

In this chapter, the radiation of the array has been studied. It was concluded that the CRLH line radiation is not versatile enough to generate the illumination required for high gain and the demanding polarization constraints of GEO satcom. Therefore, a shielding for the CRLH line have been studied and a mean of draining energy out of the CRLH have been developed to create the linear array designed in chapter 1.

The separation of phase and radiation allows to design a wide variety of radiating elements, as an example, a patch antenna have been developed and upon connection to a generic CPW line it has been proved that its radiation efficiency can be controlled.

The patch connected to the line radiates in the expected way; nevertheless, some steps remain toward the development of the line. First of all, the patch has not been tested yet within a line, the design methodology need to be slightly altered to include the effects of the patch.

The patch is linearly polarized, a full antenna need to be able to generate dual polarization. The dual polarization reception can be achieved by doubling the number of lines. A circular patch has been with dual feed has been developed. This patch can be fed by two parallel lines, controlling the relative phase between those lines allows the reception in multiple types of polarization.

Both the line and the radiating element have been discussed in chapters 2 and 3 respectively.Their integration and assessment remains to be studied. These topics and the path to follow for the validation of the antenna will be addressed in chapter 4.

# Integration of the Series Array Components

# 4

## Contents

## Objectives

In the first chapter the concept of the double series array was presented. The proposed antenna is composed of a series of linear arrays which, in turn, are based on a phased CRLH line and a series of radiating elements. Chapter 2 dealt with the CRLH phasing line and chapter 3 with the energy extraction and radiation. This chapter is devoted to the integration of the antenna components created in chapters 2 and 3.

Some general design rules will be presented to adapt the architecture of chapter 1 to the satcom specifications, thus setting the basis for the final design. In order to have an integrated system, the design methodologies of chapter 2 will be augmented to include the radiating element. Consequently, the antennas proposed in chapter 3 will be characterized as circuits. To fulfill the design of the antenna, a method to model the radiation of the full antenna based on the characterization of the cell will be presented.

For completion, the proposed biasing circuit of the diode will be explained and the roadmap for the full validation of the antenna will be explained.

# 1 Integration of Elements and Design of a Single Line

## 1.1 The Proposed Macrocell

In chapter 2, a design methodology was presented for a CRLH traditional cell. That methodology is differentiated from other design rules by the fact that it is focused on the reconfiguration of the line. Yet, the CRLH cell of chapter 2 does not include the effects of the radiation element.

The energy extraction device plus radiating element constitute a load to the CPW line that can be viewed as a discontinuity. In the same way, the series gap and the stub were characterized as circuit elements, the radiation mechanism can also be represented by a circuit. Most of the circuitry is concentrated between the line and the ground, hence a $T$ circuit seems most suitable.

However, even if the patch appears not to have any series contribution to the $T$ network, the behavior of the energy extraction mechanism plus the antenna is rather complex. Non negligible series and shunt contributions cannot be ruled out without previous verification (fig 4.1).

The shunt and series impedances have a resistive and a reactive parts. The resistive parts $R_{se}, R_{sh}$ represent the radiation of the antenna. Any losses of the system are also included in $R$, but in this text are considered to be negligible. The reactive part $X_{se}, X_{sh}$ accounts for the coupling capacitor and all the parasitic elements in the energy extraction circuitry.

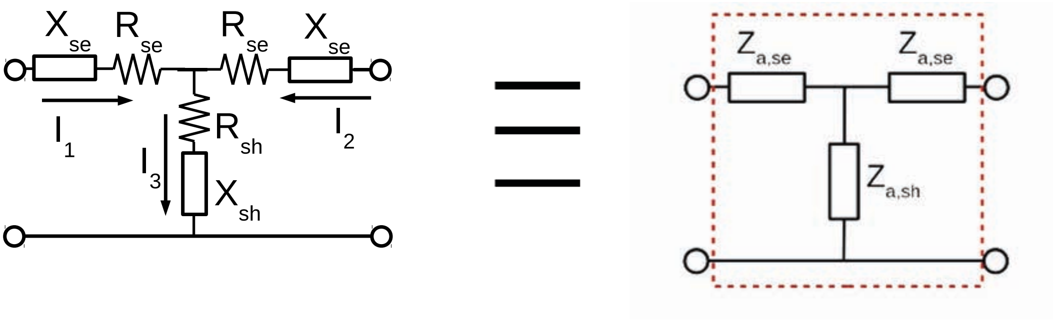

**Fig. 4.1:** Equivalent circuit of the energy extraction device

As explained in chapter 2, a typical CRLH cell is very small with respect to the wavelength, typically smaller than $\lambda_g/4$. This means that, if the radiating patches are to be separated by $\lambda_0/2$, two consecutive patches need to be separated by at least two CRLH cells. The size of the cell imposes the separation between radiating elements; nevertheless, some maneuverability remains in the connection to the patch, which can be lengthened by a distance $t$ as long as its included in the final design of the line.

With these elements, a new cell can be defined that compiles all the CLRH cells and radiating elements. This new cell will be referred as *macrocell* and is composed of $N_c$ CRLH cells of size $3T$ each and the energy extraction device plus radiating element connected by two transmission lines of size $t$, giving a total cell length of $p_m = 3T \cdot N_c + t$. Fig 4.2 shows the representation of a macrocell that with $N_c = 2$. The total macrocell size is imposed to be approximately one half wavelength $p_m \approx \lambda_0/2$.

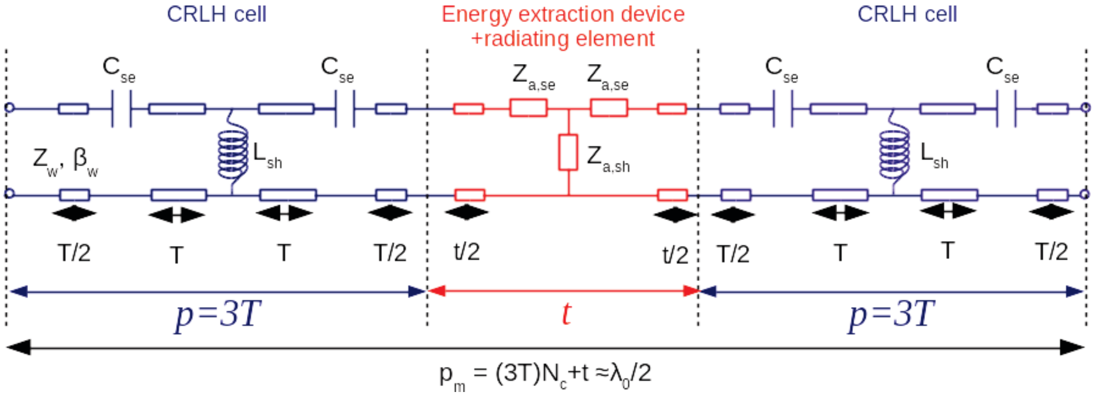

**Fig. 4.2:** Equivalent circuit of a macrocell with $N_c = 2$

This new cell is too big to be considered a metamaterial cell but it remains a periodic cell to which all the periodic cell theory in chapter 2 section 1.1 applies. As long as the radiation mechanism drains small portions of energy, the CRLH function remains unaffected.

The rest of this section will study the modeling of the energy extraction device and the design of the macrocell.

## 1.2 Equivalent T Circuit of the Energy Extraction Device

In the previous section it was explained that the energy extraction device can be modeled as a T circuit. Since the antenna is a large discontinuity in the CPW line, the series and shunt impedances do not necessarily have a one on one correspondence with the radiative and reactive elements that form the antenna. Large discontinuities like the one formed by the energy extraction device plus the radiating element can be described as lumped circuits but the circuits may fail to represent clear isolated electromagnetic phenomena.

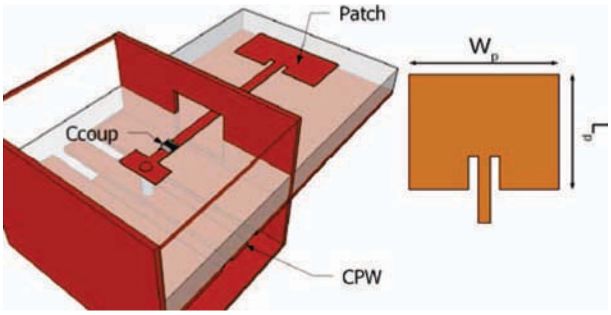

**Fig. 4.3:** Patch antenna connected to the CPW line

The modeling can be performed the same way it was done for the other CPW discontinuities. Based on full-wave simulations, the series and shunt impedance are derived from the deembedded Z matrix. Upon characterization, the results at 14GHz for different values of $C_{coup}$ can be seen in fig 4.4.

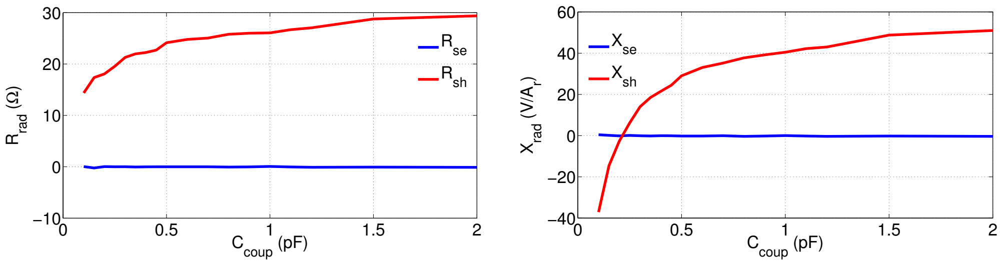

a b

**Fig. 4.4:** Real (a) and imaginary (b) parts of the components of the equivalent circuit of the energy extraction device and the radiating element. ($L_p = 4mm, W_p = 5mm$)

Fig 4.4 shows that most of the radiation resistance is concentrated in the real part of $Z_{sh}$. Equally, the reactance $X_{se}$ is negligible with respect to $X_{sh}$ which means that the patch can be represented merely by a shunt impedance.

There is a correlation between the magnitude of the shunt equivalent impedance and the impact of the energy extraction device plus radiating element in the behavior of the macrocell. Large shunt impedances resemble an open circuit and have little effect in the CRLH functions of the macrocell; whereas small equivalent $Z_{sh}$ drain large currents and may perturb the initial CRLH design. The latter case typically corresponds to big macrocell radiation efficiency $\eta_C$.

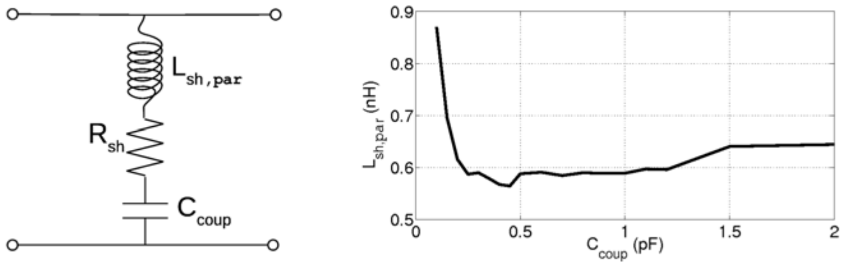

a b

**Fig. 4.5:** Circuit characterization of the energy extraction device as a $T$ circuit ($L_p = 4mm, W_p = 5mm$). a) T network for the patch b) $L_{sh,par}$

Lastly, since the shunt reactance is resonant, an equivalent inductor and capacitor can be defined. The coupling capacitor $C_{coup}$ serves as the capacitive part of the reactance and a fictitious parasitic inductance $L_{sh,par}$ can be used to account for the rest of the reactance. These may not correspond exactly to the actual capacitor and inductance in the patch, but gives an easy characterization of the loading effect of the patch. The simulated values of the circuit elements can be seen in fig 4.5 to fig 4.7.

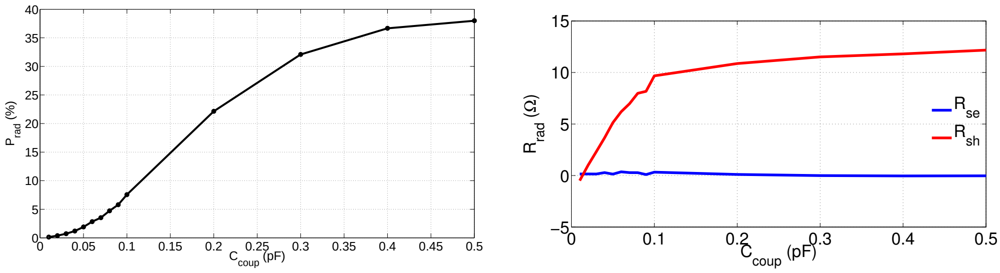

a

b

**Fig. 4.6:** Circuit characterization of the energy extraction device with $L_p = 3.9mm$ and $W_p = 5mm$. a) Radiated power b) Real part of the shunt and series impedances

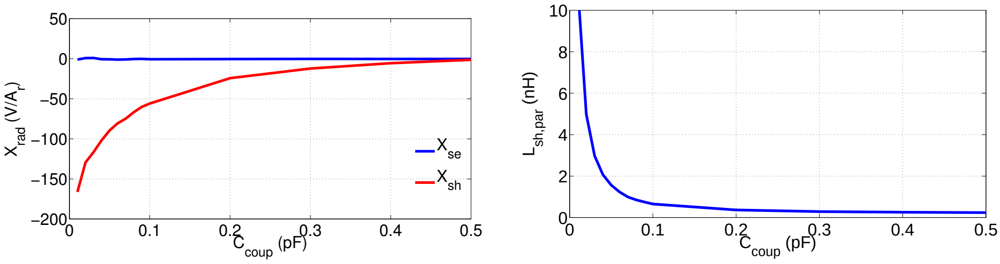

a

b

**Fig. 4.7:** Circuit characterization of the energy extraction device with $L_p = 3.9mm$ and $W_p = 5mm$. a) Imaginary part of the shunt and series impedances b) Parasitic inductance

The size of the shielding also affects the radiation and equivalent circuit of the patch. To avoid grating lobes [126], the patch and shielding share a $\lambda_0/2x\lambda_0/2$ cell in the array. The larger the shielding, the less room is left for the patch. In fig 4.8, the curves for radiated power, radiation resistance and parasitic inductance are shown for a $5mm$ shielding instead of the $3mm$ of fig 4.7 to be able to accommodate longer stubs.

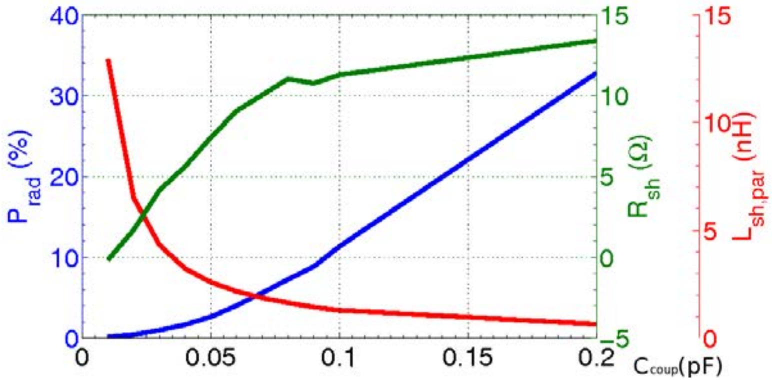

**Fig. 4.8:** Circuit characterization of the energy extraction device with lower $C_{coup}$ ($L_p = 3.9mm, W_p = 5mm$) and shielding of size $5mm$ instead of $3mm$

| **Parameter** | | **Units** |
|---|---|---|
| Distance between discontinuities | $T$ | m |
| Access line to the radiating element | t | m |
| Number of CRLH cells in macrocell | Nc | |
| Number of macrocells in series array | N | |
| CRLH cell size | p | m |
| Macrocell size | $p_m$ | m |
| Steering/scanning angle | $\theta$ | degrees |
| Coupling capacitor of the energy extrac. device | $C_{coup}$ | F |
| Parasitic inductor of the energy extrac. device | $L_{sh,par}$ | H |
| Radiation resistance of the energy extrac. device | $R_{sh}$ | |
| Equivalent series capacitor of the CRLH line | $C_{se}$ | F |
| Equivalent series capacitor of the varactor diode | $C_{v,se}$ | F |
| Equivalent shunt inductor of the CRLH line | $L_{sh}$ | H |
| Loading capacitor of the CRLH stub | $C_{v,sh}$ | F |

**Table 4.1:** Summary of design parameters of the macrocell

## 1.3 Design Procedure for Reconfigurable Macrocells

The *one-way* and *two-way* reconfigurable cell design introduced in chapter 2 need to be adapted to include the radiating element. As seen in the previous sections, the macrocell incorporates the radiating element as a $T$ network represented by circuits and its presence may disrupt the intended CRLH behavior of the cells if the cell is not modified. To counteract the effects of the energy extraction device and the radiating element, the design procedure presented in chapter 2 is here augmented for the macrocell.

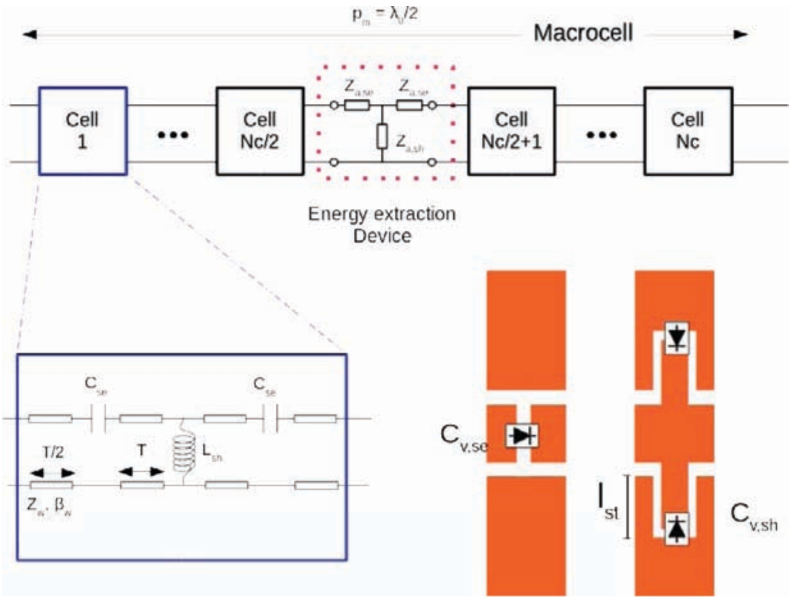

**Fig. 4.9:** Summary of the composition of a Macrocell

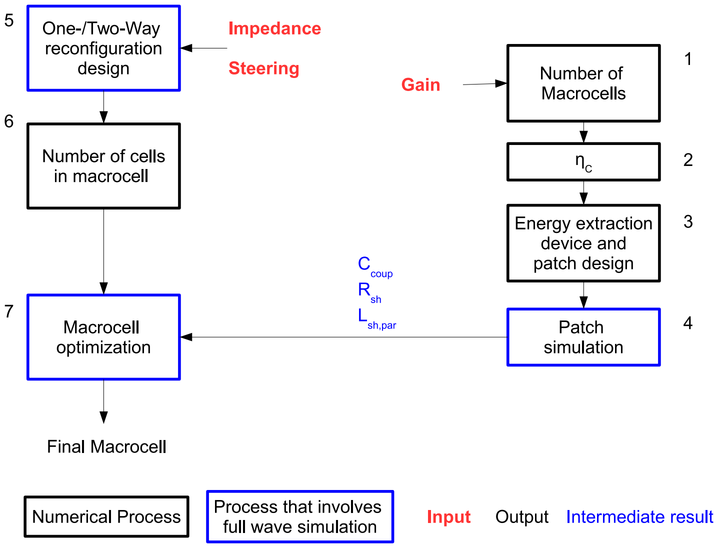

**Fig. 4.10:** Design flow chart for the macrocell

The process begins by creating an initial CRLH cell as the ones shown in chapter two and work the macrocell up from there. It aims at reducing the number of full-wave simulations required for the final cell. The process is described in the following and its corresponding flow chart can be seen in fig 4.10.

*Step 1-2: Number of elements and efficiency*

As it will be explained later in this chapter, the number of macrocells in an array can be determined by the target gain. From the theory of uniform arrays [126], a first approximation to the gain could be $g \approx number\ of\ cells$.

While the final number of cells $N$ will certainly be modified in the end to adjust for the intended gain, this approximation can be used as a first dimensioning of the line to determine the required radiation efficiency of a macrocell $\eta_C$ with equation 4.14.

If the final $N$ required differs greatly from the initial one, the design should be restarted with a different $N$. Further discussion on the gain and number of cells will be presented later in this chapter.

*Step 3-4: Patch design*

With $\eta_C$ as an input, the energy extraction device and patch can be designed. As previously mentioned, if the shunt impedance is designed to be large, the effect in the CRLH line will be minimal.

When simulating the patch, it is important to use periodic boundaries in a $\lambda_0/2x\lambda_0/2$ and to include the CRLH shielding as a metallic box. The close surrounding of the patch affects its input impedance and its radiation. For small lines, the periodic boundary condition is not an accurate approach; yet for long lines, *i.e.* large gain, the effect of the patches in the extremities is not relevant in the behavior of the array as a whole.

Full wave simulations help optimizing the radiating element and extracting the equivalent $T$ network, *i.e.* the values of $R_{sh}$, $C_{coup}$ and $L_{sh,par}$ and the electric field $E$ of the single element. The axial ratio can be directly extracted from the single element and the electric field of the single patch can be used in combination with the array factor to predict the behavior of the linear array.

*Step 5-6: Initial macrocell design*

A macrocell is composed of a radiating element and a number of reconfigurable CRLH cells. Since the size of a CRLH cell is not known a priori, an initial design of a CRLH cell —*one-* or *two-way* reconfigurable— is realized to fit the steering and impedance specifications. From the size of the cell $p$ the number of cells in a macrocell is determined:

$$N_c \approx \frac{\lambda_0/2}{p} \tag{4.1}$$

Ideally, the number of cells in a macrocell is such that the macrocell length is as close to $\lambda_0/2$ as possible. This is a dimension set arbitrarily in this thesis to ensure that no grating lobes appear in the radiation pattern but, theoretically it could be as large as

$$p_m < \frac{\lambda_0}{(1+|cos(\theta_{max})|)}.$$

At this point, an initial macrocell composed of a number of CRLH cells and an energy extraction device is completed. Nevertheless, the correct function of this macrocell cannot yet be ensured. Consequently, an optimization process is required.

*Step 7: Macrocell optimization*

With a final number of cells per macrocell already determined, an optimization process can be applied. For that, design graphs analogous to those generated for the cell in chapter 2 can be used here (fig 4.11).

As done for the single CRLH cell, the $T$ vs $C_{v,se}$ graph can be used as a first step to find an optimal $T$. Afterwards, the $C_{v,se}$ vs $L_{sh}$ graph can be used to predict the behavior of the macrocell and optimize its length and diode range. Full wave simulation can be used to verify the results of this process and further optimize the dimensions of the cell.

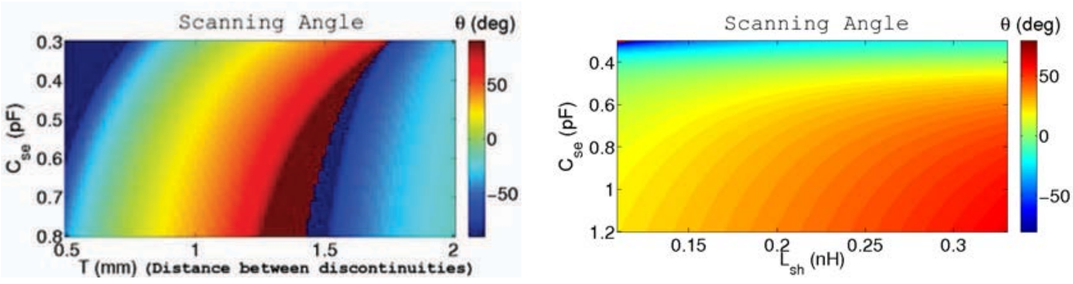

a b

**Fig. 4.11:** Scanning angle charts for a) choosing $T$ ($T$ vs $C_{v,se}$ diagram) b) steering design ($L_{sh}$ vs $C_{v,se}$ diagram). (Step 7 of the macrocell design)

## 2 Characterization of the Radiation and Design of the Line

In order to achieve the high gain required for a full satcom antenna, a large number of macrocells is to be expected for the series array. This presents a problem for simulations since the calculation time and memory requirements can be very large for such a structure. Fortunately, the structure is an array and some shortcuts can be made to have a first estimation of the full radiation pattern based on the knowledge of a single cell.

It is well known that the field of an array with equal radiating elements can be expressed as a function of the field of one of the elements $E_u$ and an array factor $AF$:

$$E_T = E_u \cdot AF = \sum_{i=1}^{N} a_i W^i E_u \tag{4.2}$$

where $W^i = e^{jk_0 \cos\phi \sin\theta p_m i}$ for a linear array that lies on the $\hat{x}$ axis. This term depends only on the position of the elements and the wavelength and can be thus calculated based only on the macrocell size $p_m$.

The field of a single radiating element $E_u$ can be extracted through full-wave simulation. A periodic boundary condition can be established in the walls of the simulated cell to emulate an infinite array. This can be precise enough for large arrays where the effects of the extremities is not relevant. However, for a more rigorous treatment, the elements in the borders can be simulated with only periodic boundaries where they interface with other cells.

Finally, the complex term $a_i$ represents the excitation. Its magnitude is related to the relative power radiated by the single antenna and its phase is related to the relative phase of the feed of the radiating elements. The next sections study how can $a_i$ be defined from the characteristics of the macrocell.

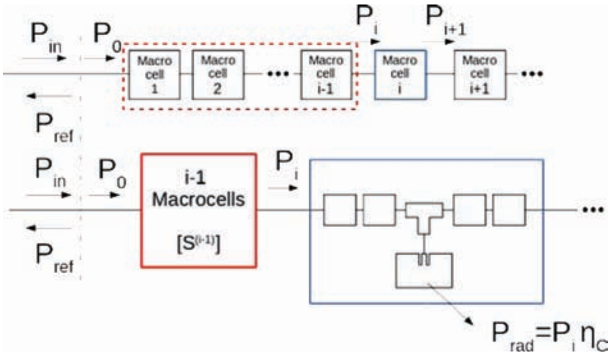

**Fig. 4.12:** Determination of the magnitude of $a_i$

| **Parameter** | **Notation** |
|---|---|
| Input power to the line | $P_{in}$ |
| Power accepted by the line | $P_0$ |
| Reflected power at the input of the line | $P_{ref}$ |
| Input power to the $i-th$ macrocell | $P_{i-1}$ |
| Output power to the $i-th$ macrocell | $P_i$ |
| Power radiated by the $i-th$ macrocell | $P_{rad,i}$ |
| Power delivered to the load | $P_N$ |
| S matrix of the cascaded cells 1-to-$(i-1)$ | $\left[S^{(i-1)}\right]$ |
| Excitation of the $i-th$ radiating element | $a_i$ |
| Radiation efficiency of the $i-th$ macrocell (custom illumination) | $\eta_{C,i}$ |
| Radiation efficiency of any macrocell (decreasing illumination) | $\eta_C$ |
| Number of CRLH cells in a macrocell | $N_c$ |
| Phase shift introduced by a macrocell | $\Phi_M$ |
| Phase shift introduced by a CRLH cell (decreasing illumination) | $\Phi_c$ |
| Phase shift introduced by the CRLH cell *before* the energy extraction device (custom illumination) | $\Phi_{c,b}$ |
| Phase shift introduced by the CRLH cell *after* the energy extraction device (custom illumination) | $\Phi_{c,a}$ |
| Phase difference between the input of the energy extraction device and the input of the radiating element | $\varphi$ |
| Phase difference between the input and the output of the energy extraction device | $\alpha$ |

**Table 4.2:** Summary of relevant parameters

## 2.1 Magnitude of $a_i$

The magnitude of $a_i$ is a measure of how much power is transmitted through the $i-th$ element with respect to a reference that can be taken to be a fictitious zeroth element $a_0$. Since $a_i$ multiplies fields, the actual power ratio $P_i/P_0$ is proportional to the square of $a_i$:

$$P_i = \frac{1}{2}Re\{E_i x H_i^*\} = \frac{1}{2}Re\{(a_i E_0)x(a_i H_0)^*\} = |a_i|^2 P_0 \tag{4.3}$$

Further in this chapter, some considerations on the design of $|a_i|$ will be presented. Here the value of $|a_i|$ is merely determined based on the macrocell analysis.

Fig 4.12 shows how all the macrocells up to the $i-th$ one can be substituted by a bi-port with scattering matrix $\left[S^{(i-1)}\right]$. Considering $P_0$ as the admitted power to the line:

$$P_0 = P_{in}(1-|S_{11}^{(i-1)}|^2), \tag{4.4}$$

any matching problem can be disregarded at this point.

Under those conditions, the power radiated by the $i-th$ macrocell can be described as:

$$P_{rad,i} = P_0|S_{21}^{(i-1)}|^2\eta_C \tag{4.5}$$

and the corresponding magnitude of $a_i$ would be:

$$|a_i| = |S_{21}^{(i-1)}|\sqrt{\eta_C} \tag{4.6}$$

## 2.2 Phase of $a_i$

The phase of $a_i$ represents the relative phase between the center of phase of the different radiating elements. This parameter is very important for this thesis since it is the one that carries the information for beam steering. Fig 4.13 represents a macrocell that introduces an arbitrary phase shift $\Phi_M$. Each macrocell has a phase shift approximately equal to the sum of the CRLH cells it contains:

$$\Phi_M \approx N_c\Phi_c \tag{4.7}$$

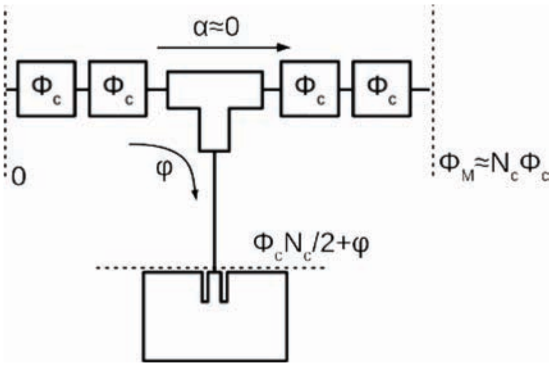

**Fig. 4.13:** Determination of the phase of $a_i$

For the steering of the beam, only the relative phase between the $a_i$ coefficients is important. Thus, the first element $a_1$ can be taken to have phase 0, *i.e.*, to be purely real.

The phase between an element $a_i$ and $a_0$ will then be a whole number of macrocells. This yields, for the $i-th$ element, a total phase of

$$phase(a_i) = (i-1)\cdot\Phi_M \tag{4.8}$$

## 2.3 Line Design Procedure

A method to characterize the radiation of the full line has been explained in section 1.3 of this chapter. Additionally, a method to design the macrocell has been explained in the previous section. With these elements, a full line design procedure can be already defined.

*steps 1-7*

The first seven steps remain similar to those explained for the macrocell in page 103. Nevertheless, since a full line needs to be designed, a set of different energy extraction devices may be required in order to create an uniform profile of illumination and thus a line optimization process is included.

Making use of the array factor and the range of $\eta_C, R_{sh}, C_{coup}, L_{sh,par}$ the line can be optimized in impedance and phasing. Each macrocell may have a different efficiency and a different optimal size. The use of metamaterial allows a variation from cell to cell, as long as each cell remains much smaller than the wavelength. If a compensation scheme is used to counteract the phasing effects of different cell efficiencies, it should also be included in the line optimization process.

To reduce the overall optimization time, the cells can be simulated independently and a circuit model can be used to predict the behavior of the full heterogeneous line. A final full simulation of the whole line —or subsections of it— can be performed at the end of the optimization process.

*step 8*

Once the phase delay and efficiency of each cell are optimized, it can be used as an input to the array factor to determine the expected final radiation pattern of the full array for different biasing voltages.

A summary of the process is presented in fig 4.14 where distinctions are made between processes that require full wave simulation and processes that can be done solely with mathematical software like matlab.

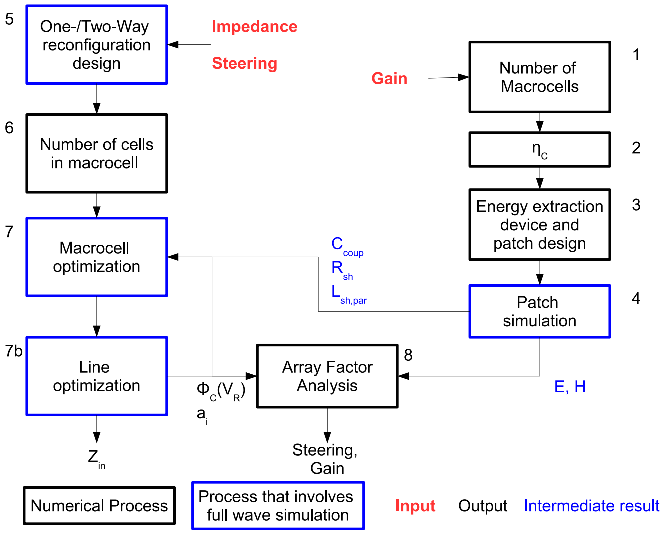

**Fig. 4.14:** Design flowchart for the linear array design

# 3 Beam Steerable Series Array Design Considerations

So far, the development of the elements that compose the antenna has followed a *Bottom-up* approach, developing separately the building blocks of the steerable antenna. For the final design of the antenna, a *Top-down* methodology can be followed instead.

Starting from the specifications of a full antenna, the requirements of each cell can be worked out downwards so the final gain, steering and polarization are achieved. The four main points that need to be considered in the design of the system are

- Radiation Pattern
- Bandwidth
- Polarization

each of them will be illustrated in the following.

## 3.1 Radiation Pattern Considerations

Recalling table 1.4 (page 33), an elevation steering of 60° and a gain larger than $30dB$ are set as objectives. Ohmic and dielectric losses have not been considered in this thesis, however, real materials have been used in the examples. To have a rough account of the losses and have a conservative approach, the design considerations from now on will be done for a target directivity of $33dB$.

In a scanning array, steering the beam reduces unavoidably the gain and SLL of the full array. This comes from the fact that the directivity of an array [126] depends mainly on two factors, the array factor and the radiation pattern of the single element.

When the array is configured to scan away from broadside, the array factor merely experiences a rotation, as shown in fig 4.15. While the maximum of the AF might point at an arbitrary angle, its shape and SLL remain unchanged. This is not true for the radiation pattern of the radiating element.

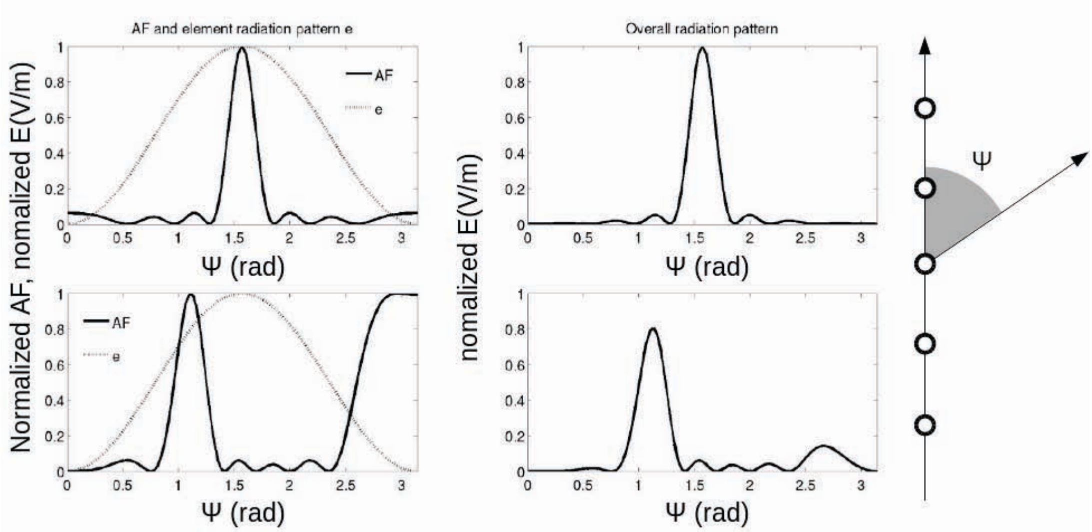

**Fig. 4.15:** Array factor and radiation pattern of an array

The radiation pattern of the radiating element acts as a weighting function, typically strengthening the broadside angle over other steering angles $\theta$. Fig 4.15 makes explicit how the main lobe of the overall directivity is reduced as the array factor pivots away from broadside and how the secondary lobe gains weight as it approaches the broadside direction, reducing both the maximum directivity and the SLL.

When the beam steered an angle $\theta$ from broadside in a square planar array, the directivity is reduced by and amount of $\cos(\theta)$ [127]. This can be used in the well known equation of the effective area:

$$\frac{A}{\lambda_0^2} = \frac{1}{4} d \frac{1}{e_a \cos(\theta)} \tag{4.9}$$

where $e_a$ is the aperture efficiency of the antenna, $d$ is the target directivity and $A$ is the physical area of the radiating surface.

A realistic value for $e_a$ of a decreasing illumination like the one presented here is around 75%. For a 60° beam steer and $33dB$ of target directivity, the radiating surface should be at least

$$\frac{A}{\lambda_0^2} = 424.41$$

This hypothesis serves as an initial design, later in this chapter it will be revisited and the number of cells can be ultimately modified without major design changes, thanks to the cellular structure of the array. Incidentally, the same procedure can be used for any other target directivity.

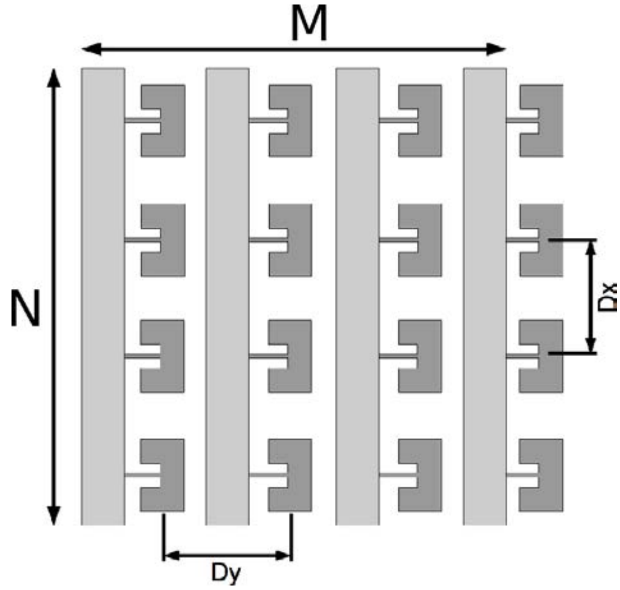

**Fig. 4.16:** Beam steerable patch array

In order to avoid grating lobes [127], the elements need to be separated at most by

$$D_x, D_y < \frac{\lambda}{1 + cos(\theta_{max})} = \frac{\lambda}{1.5} \tag{4.10}$$

A more constraint limit commonly used is $D_x, D_y < \lambda/2$ and will be adopted in this text. The values $D_x$ and $D_y$ correspond in this particular case to the macrocell size $p_m$ and the distance between lines respectively.

Finally, the physical area A can be written as

$$A = N \cdot D_x \cdot M \cdot D_y \tag{4.11}$$

using $D_x = D_y = \lambda_0/2$ and substituting in eq 4.9, the total number of cells for this example can be computed as $N \cdot M \approx 1700$.

For a beam as symmetrical as possible in every direction the array should be somewhat square. In particular, a patch like the one in fig 4.3, presents a directivity slightly smaller in the transverse direction to the CRLH line —E plane—, then, the number of lines should be slightly larger than the number of radiating elements in a line. Yielding a total of 42 lines of 41 elements. In consequence, the array will be approximately $21\lambda x 21\lambda$.

One last element to consider for the radiation pattern is the illumination of the antenna. Different illumination profiles —uniform, triangular, binomial, exponential— result in different values of directivity or SLL [126]. The illumination profile is determined by the radiation efficiency of the energy extraction device $\eta_C$. Since $\eta_C$ can be easily controlled with the energy extraction device, the efficiency can be fine tuned to radiate as much power as desired and to have an arbitrary illumination of the array elements.

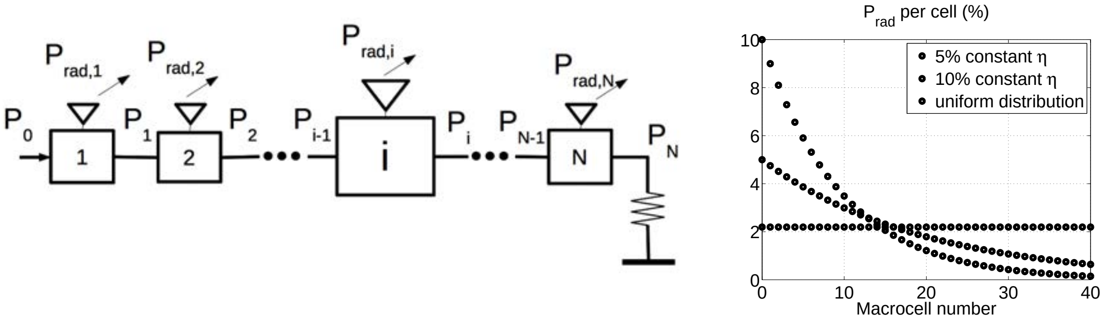

a b

**Fig. 4.17:** Series linear array a) Cell diagram b) Illumination profiles

Two different strategies for the illumination of the antenna will be here considered:

a A constant $\eta_c$ illumination. Which results in an geometric decay of the relative radiated power as the position of the radiation element in the line increases.

b A constant radiation power, or uniform illumination, where each cell radiates the same amount of power.

### *a. Decreasing Illumination (Constant $\eta_C$)*

Firstly, a constant $\eta_C$ is studied. In this case, all macrocells are identical to each other. In consequence, every patch radiates the same percentage of its input available energy (fig 4.17). Using the definition of $\eta_C$ from eq 3.5:

$$P_{i+1} = P_i(1-\eta_C) = P_0 \;\; 1-\eta_C^{\;\;i+1} \tag{4.12}$$

$$P_{rad,i} = P_{i-1}\eta_C \tag{4.13}$$

In this case, in order to radiate *e.g.* 90% of the energy at the end of the line, the power transmitted by the final cell to the load must be $P_{N=41} = P_0 \cdot 0.1$ and each element needs to radiate with an efficiency of

$$\eta_c = 1 - \sqrt[N]{\frac{P_N}{P_0}} \tag{4.14}$$

or $\eta_c = 5.46\%$ for 90% antenna efficiency and 41 elements. As mentioned before, this method yields a decreasing illumination (fig 4.17b) since every cell radiates 5.46% of an ever smaller amount of power. This analysis is akin to that of a leaky wave antenna.

Based on eqs 4.12, 4.13 and 4.3, the magnitude of the $a_i$ in eq 4.2 can be redefined as:

$$|a_i| = \sqrt{\eta_C \left(1-\eta_C\right)^{i-1}} \tag{4.15}$$

where it has been considered that all the power non radiated is transmitted to the following macrocell.

### *b. Uniform Illumination (Constant $P_{rad,i}$)*

To have a constant illumination (fig 4.17b), the radiation efficiency $\eta_C$ per element has to increase slightly at each cell. Forcing $P_{rad,i} = P_{rad,i+1}$, the value of the $i-th$ radiation efficiency can be defined as:

$$\eta_{C,i+1} = \frac{\eta_{C,i}}{1-\eta_{C,i}} \tag{4.16}$$

where the value of the efficiency for the first element is:

$$\eta_{C,0} = \frac{P_N - P_0}{N \cdot P_0} \tag{4.17}$$

Unfortunately, the energy extraction device developed in chapter 3 does not guarantee equal phase for different coupling values. Fig 4.18a shows a macrocell without phase compensation. The energy extraction device inserts a phase shift $\varphi$ in the port of the patch that depends on the coupling capacitor. If all the patches are set to radiate with the same radiation efficiency $\eta_C$, all the energy extraction devices introduce the same $\varphi$ and the relative phase between radiating elements is independent from $\varphi$.

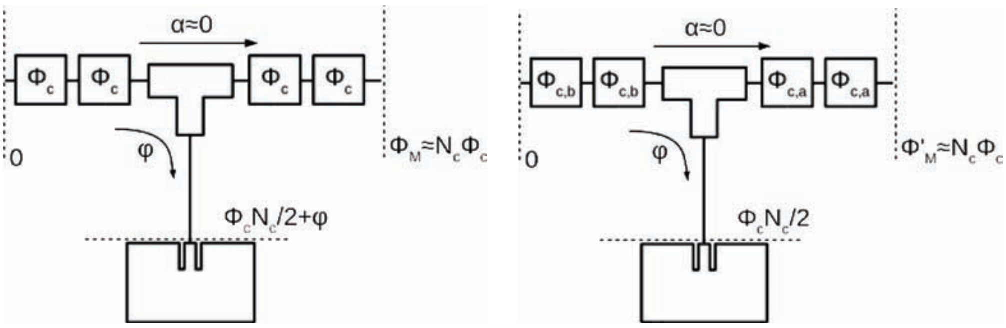

a b

**Fig. 4.18:** Phase compensation. a) Non compensated structure (decreasing illumination) b) Compensated structure (uniform illumination)

For an uniform illumination, each macrocell introduces a different $\varphi$ thus, in order to preserve the phase profile designed for beam steering, $\varphi$ needs to be compensated. However, the structure of the macrocell introduces enough degrees of freedom for such compensation. The macrocells *before* the energy extraction device can be set to a phase shift $\Phi_{c,b}$ that compensates the varying $\varphi$. For the $i-th$ macrocell of $N_c$ CRLH cells:

$$\frac{N_c}{2}\Phi_{c,b}+\varphi=\Phi_M/2 \tag{4.18}$$

Within the same macrocell, the variation of the phase shift introduced by the CRLH cells locate *before* the energy extraction device can be compensated with the CRLH cells located after the energy extraction device so the overall phase shift of the macrocell is similar to that of the *decreasing illumination* scheme $\Phi_M$.

The CRLH cells located *after* the energy extraction $\Phi_{c,a}$ device of the macrocell can now compensate the variation in phase introduced by those CRLH cells located *before*:

$$\frac{N_c}{2}\Phi_{c,a}=\Phi_M-\frac{N_c}{2}\Phi_{c,b} \tag{4.19}$$

This systems allows to create any desired illumination profile, not only uniform. But it comes at the cost of an increased complexity. Each macrocell requires two independent biasing circuit for its cells, whereas the *decreasing illumination* scheme can use one single biasing system for all the cells in the antenna.

Table 4.3 summarizes the design equations for the beam steerable linear array.

| Parameter | Value |
|---|---|
| Macrocell Size | $p_m \approx \frac{\lambda}{2}$ |
| Distance between lines | $D_y \approx \frac{\lambda}{2}$ |
| Macrocell Phase[1] | $-156^\circ < \Phi_M < 156^\circ$ |

| | Decreasing Illumination | Uniform Illumination |
|---|---|---|
| Radiation Efficiency | $\eta_C = \sqrt[N]{\frac{P_N}{P_0}}$ | $\eta_{C,i+1} = \frac{\eta_{C,i}}{1-\eta_{C,i}}$,<br>$\eta_{C,0} = \frac{P_N - P_0}{N \cdot P_0}$ |
| Feed Coefficient (Magnitude) | $\lvert a_i \rvert = \sqrt{\eta_C (1-\eta_C)^{i-1}}$ | $\lvert a_i \rvert = 1$ |
| Feed Coefficient (Phase) | $phase(a_i) = (i-1)\Phi_M$ | $phase(a_i) = (i-1)\Phi_M$ |

**Table 4.3:** Design Equations.[1] Calculated as $\Phi_M = k_0 p_m sin(\theta)$

## 3.2 Bandwidth and Impedance Matching Considerations

As seen in table B.1 (page 150), most of the satcom satellites for GEO communications have around 25 channels of 36MHz. These channels are typically multiplexed in polarization, which means that the full bandwidth in reception rounds the 12x36MHz, or 432MHz. At 14GHz, this represents a 3% bandwidth. This may be a larger bandwidth than the one achievable by the antenna proposed here.

However, the antenna does not need to receive a 432MHz wide signal. It is sufficient to receive 36MHz channels as long as the central frequency of reception can be tuned as well as the direction of reception. In chapter 2 it was explained how the CRLH line can be readily exploited to choose a receiving channel within a band, as long as the radiating element has a large enough bandwidth.

For the antenna, two types of bandwidth need to be considered: impedance bandwidth and pattern bandwidth. For the impedance bandwidth, a value of $|S_{11}|$ smaller than -10dB can be considered as a good matching.

The Bloch impedance of the CRLH line, as was seen in chapter 2, tends to either increase or decrease from the near-broadside value as the steering of the antenna changes. This is a consequence of the nature of metamaterials.

In the CRLH line, the Bloch impedance either raises to infinity or goes down to zero when it gets close to the limits of its pass band [59, 31]. Fortunately, this corresponds to a 90° steering, whereas for 60°, the impedance has been observed to raise to around 120 to 150 for the studied cases.

A similar phenomenon happens at broadside, where the metamaterial bandgap [31] cancels the real part of the Bloch impedance. While the broadside case can be worked around by carefully choosing the biasing of the diodes to create a balanced structure, the high impedances achieved at 60° need to be matched with reconfigurable matching networks in the extremities of the line. The works towards the large spectrum matching network are not included in this text; nevertheless, the use of the CRLH line structure as a matching network is proposed in the *Way-Forward* part of this text.

In terms of steering bandwidth, assuming that no other satellite transmits with the same polarization and frequency in the close vicinity of the target satellite, the gain in the direction of the satellite needs to be greater than the minimum required $g_{array}$ at all frequencies (see appendix J).

## 3.3 Polarization considerations

Table B.1 (page 150) summarizes some of the main GEO communication satellites. In most of satcom cases linear polarization dominates, whereas for broadcast satellites circular polarization is more common. The problem with linear polarization comes when the transmitted wave passes through the ionosphere. The ionosphere introduces rotation in the polarization; moreover, the relative position of the antenna with respect to the satellite as the receiver travels through the Earth also changes the polarization alignment between transmitter and receiver. The difference between the polarization of the antenna and that of the received wave, commonly known as skew, needs to be corrected in the antenna.

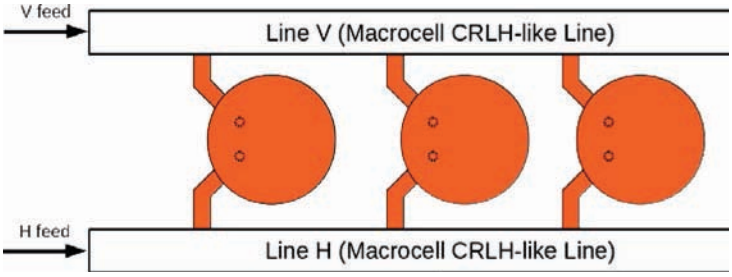

**Fig. 4.19:** Dual polarized line

The polarization tracking can be easily done with dual polarized antennas. To do that, a patch could be fed from two independent lines, as shown in fig 3.29 (page 94). Maintaining a good decoupling between ports H and V, the desired polarization can be received by controlling the relative phase difference between the feeds of the lines H and V.

## 3.4 Example of a Linear Series Array

Using the procedure described in section 1.3 (page 103), and the dimensioning considerations explained in section 3.1 (page 109) a macrocell has been created to exemplify how can the the gain and steering requirements set in table 1.4 (page 33) be achieved. The $L_{sh}$ vs $C_{v,se}$ graph can be seen in fig 4.11 and the final dimensions in table 4.4.

| **Specification** | | **Value** |
|---|---|---|
| Minimum directivity | $D_{min}$ | 33dB |
| Maximum steering angle | $\theta_{max}$ | 60° |
| Central frequency | $f_0$ | 14GHz |

| **Parameter** | | **Value** |
|---|---|---|
| Distance between discontinuities | $T$ | 0.9mm |
| Energy extraction device connection length | $t$ | 0mm |
| Number of cells in a macrocell | $N_c$ | 4 |
| Radiation resistance of the energy extraction device | $R_{sh}$ | 7.98 |
| Coupling capacitor of the energy extraction device | $C_{coup}$ | $80fF$ |
| Parasitic inductor of the energy extraction device | $L_{sh,par}$ | $0.85nH$ |
| Stub equivalent inductor span ($C_{v,sh}SMV1430$) | $L_{sh}$ | $0.11nH-0.33nH$ |
| Series varactor (SMV1430) | $C_{se}$ | $0.3pF-1.2pF$ |
| Macrocell size | $p_m$ | $10.8mm$ |
| Relative permittivity of the substrate | $\epsilon_r$ | 6.15 |
| Thickness of the substrate | $h_s$ | 0.508mm |
| Gap size | $g$ | 0.150mm |
| Inter-ground distance | $C$ | 0.200mm |
| Central strip width | $W$ | 0.170mm |
| Stub's length | $l_{st}$ | 2mm |
| Stub's Inter-ground distance | $C_s$ | 0.080mm |
| Stub's strip width | $W_s$ | 0.040mm |
| Number of cells per linear array (initial estimation) | N | 41 |
| Number of lines in the antenna (initial estimation) | M | 42 |

**Table 4.4:** Exemple of Ku-band macrocell : summary of parameters.

This design will be used in the next section to validate the steering requirements through full-wave simulations and to discuss the determination of the directivity. The simulations are all carried out at 14GHz and the *decreasing illumination* scheme has been chosen for simplicity.

# 4 Proof of Concept through Simulations

## 4.1 Demonstration of the Steering

With the purpose of validating the steering capabilities of the macrocell, some simulations have been conducted. A four element array is shown in fig 4.20. To reduce the simulation time, only the cells between the patches are included, since the cells in the extremities do not contribute to the steering. The different series and shunt varactor configurations create backwards and forward steering. All the simulations are conducted at 14GHz.

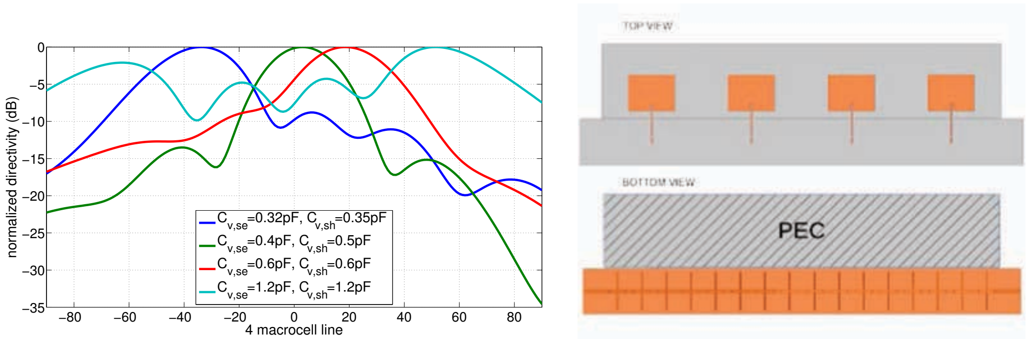

**Fig. 4.20:** Directivity radiation patterns of a four macrocell array, full wave simulation (HFSS)

However, four elements is not representative of a long or infinite line. In fig 4.21 a set of arrays of patches with the same dimensions and environment of the macrocell line are simulated. For a 160° phasing between elements, which corresponds to a −61.8° steer from broadside, the normalized directivity is calculated for a two to nine elements array.

Fig 4.21 shows how the steering angle of a linear series array approaches the theoretical value of an infinite line as the number of elements in the array increases. In particular, the nine element array has a 6% variation of the scanning angle with respect to the infinite array while a two element array has a variation closer to a 40%. Nevertheless, simulating longer lines has higher memory requirements, which creates a trade-off between simulation time/capabilities and steering prediction accuracy.

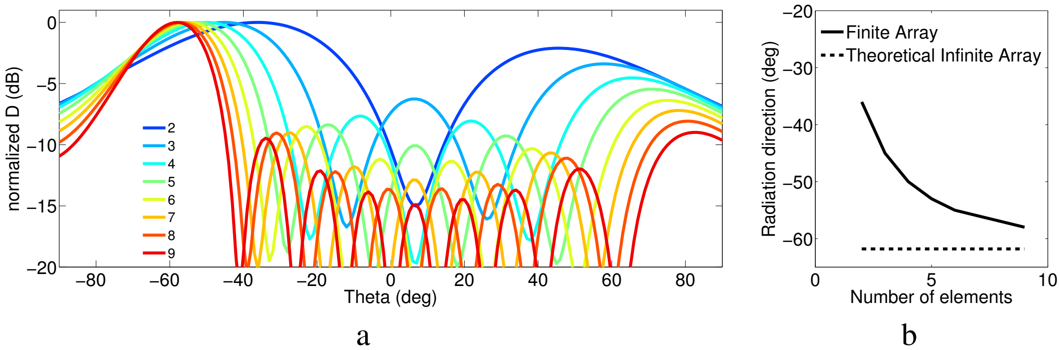

a b

**Fig. 4.21:** Directivity radiation patterns of patch arrays with different number of elements (HFSS). The array is set to a 160° phasing between elements, which yields a −61.8° steer from broadside

An array larger than ten elements can give a good idea of the behavior of the 41 cell line. However, the simulation time can be very long and the memory required for a full wave simulation is too large for personal computers.

At this stage of development of the technology, the steering of the line can be proved in other way by simulating the patches without the CRLH line. To do that, the patches are simulated in an air box along with the shielding. To estimate the steering of the line, the realtive phase shift $\Phi_M$ is applied to the patch elements. The value of $\Phi_M$ is determined through the simulation of a single macrocell.

The N element array can then be used to validate the numerical array factor approach, which can easily predict the directivity of an arbitrary large number of cells (fig 4.22).

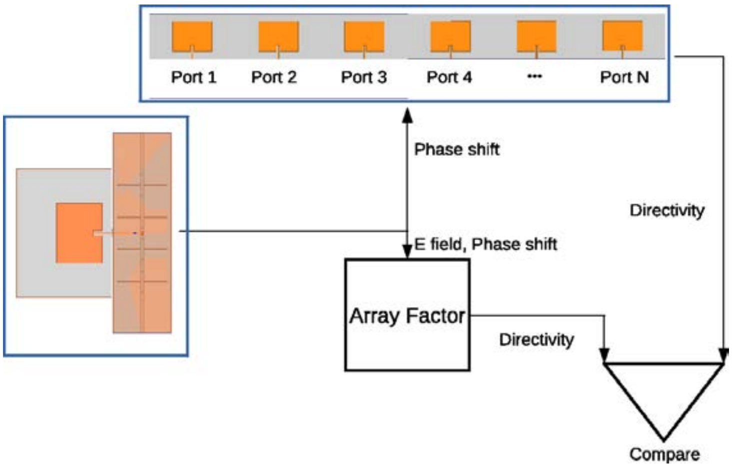

**Fig. 4.22:** Procedure for pattern simulation and array factor verification using a periodic macrocells

It should be noted that there are other problems that may arise from the development of a macrocell line. Namely, the matching at higher steering angles and close to broadside may be challenging since the Bloch impedance tends to approach zero or infinity for certain configurations. However, as long as the impedance is real, reconfigurable matching networks could be envisaged to match the line to the extremities. This thesis will deal with the steering requirement and discuss the mismatch considerations in the *Way Forward*.

## 4.2 Steering for a single radiating line

To validate the effectiveness of the array factor method depicted in fig 4.22 a single macrocell has been employed (fig 4.23). A simulation of the single macrocell (fig 4.23) serves as the baseline for the phasing that can be achieved and also for the unitary element of the full array.

To have a representative measure of the radiation, the macrocell is inserted into a box of size $\lambda/2x\lambda/2$ with periodic boundary condition. Also, the effects of the shielding of the CRLH feeding line and an adjacent line are included. This gives a better approximation to the behavior of the macrocell in the full 2D steering antenna.

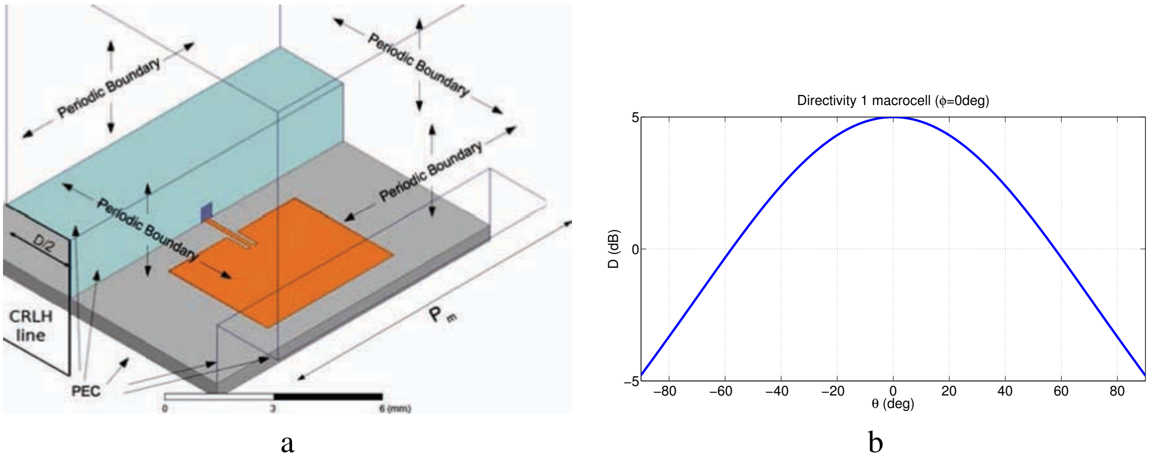

a b

**Fig. 4.23:** a) A macrocell simulated under periodic boundary conditions. b) Directivity of the macrocell

| | $C_{v,se}$ | $C_{v,sh}$ | $\Delta\Phi$ | $\theta_\infty$ |
|---|---|---|---|---|
| Case a | $0.3pF$ | $0.3pF$ | 167.8° | 67.6° |
| Case b | $0.32pF$ | $0.35pF$ | 124.9° | 43.5° |
| Case c | $0.32pF$ | $0.4pF$ | 93.2° | 30.9° |
| Case d | $0.4pF$ | $0.5pF$ | 12.7° | 4.0° |
| Case e | $0.5pF$ | $0.4pF$ | 4.4° | 1.4° |
| Case f | $0.6pF$ | $0.6pF$ | −60.3° | −19.4° |
| Case g | $1.2pF$ | $1.2pF$ | −163.0° | −63.9° |

**Table 4.5:** Phase of some configurations of the macrocell of fig 4.23

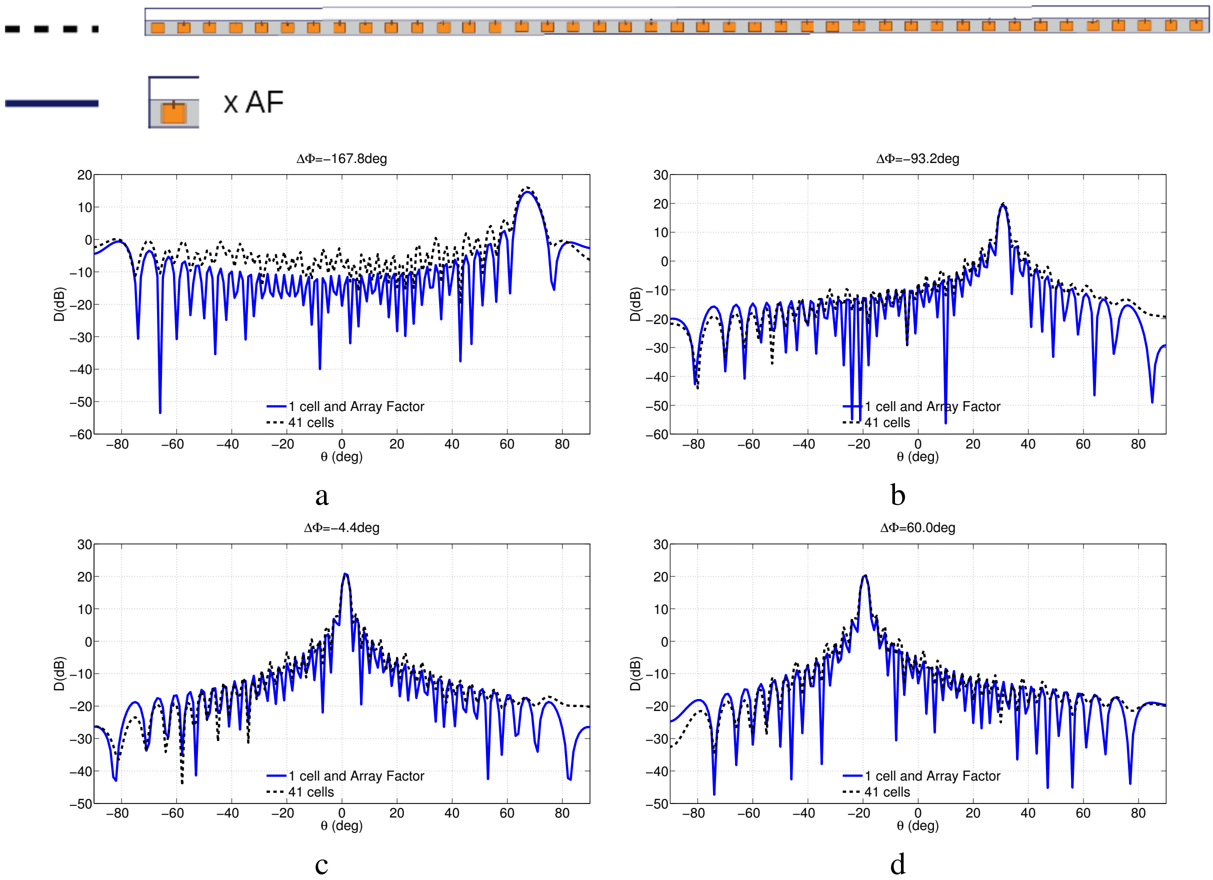

a b

c d

**Fig. 4.24:** Directivity comparison between a simulation of one macrocell and the array factor and a simulation of 41 patches

A 41 element array of patches has been simulated separated from the CRLH line, as explained before. The phasing obtained from the simulation of the single macrocell in fig 4.23 is used as an input to determine the relative phase of the ports in the full wave simulation of 41 elements.

The phase of the macrocell can be taken to be the argument of the $S_{21}$ parameter (or the $\beta_{eff}p_m$) as calculated from the cell with periodic boundary condition (eq 2.13). The difference is small in general and can often be taken to be equal. In general, for CRLH cells, the $\beta p$ parameter yields an accurate approximation of the effective propagation constant of the line.

For the macrocell however, the total phase shift corresponds to that of a few cells —four in this case— and the determination of $\beta$ is more complex.

Because of the periodicity of the phase, cell phase shifts of more than 45° will be wrapped back to $-180°$ $(45° x4)$ and the correct determination of $\beta_{eff}$ is more delicate. From now on, the text only deals with macrocells and full phase shifts, the term $-phase(S_{21})$ will be utilized as the phase shift $\Delta\Phi$ for simplicity, bearing in mind that for angles near broadside, in the final design of the antenna, the parameter $\beta_{eff} p_m$ should be verified in order to find the correct $(C_{v,se}, C_{v,sh})$ pair that generates a balanced CRLH configuration.

The following graphs show good accordance between the array factor approach and the 41 cell simulated array. The interest of this decoupling of patches and macrocell is evident here since it would have been impossible to simulate a full 41 macrocell line.

## 4.3 Steering for an Array of Lines

Finally, the directivity of the full array should be tested to confirm the hypothesis that the 41-cell x42-line antenna yields a sufficient directivity. Fig 4.25 shows the full steering at broadside and 60°. For validation purposes, a 41 element array lying in the $\hat{x}$ direction has been simulated and an array factor has been applied in the $\hat{y}$ direction.

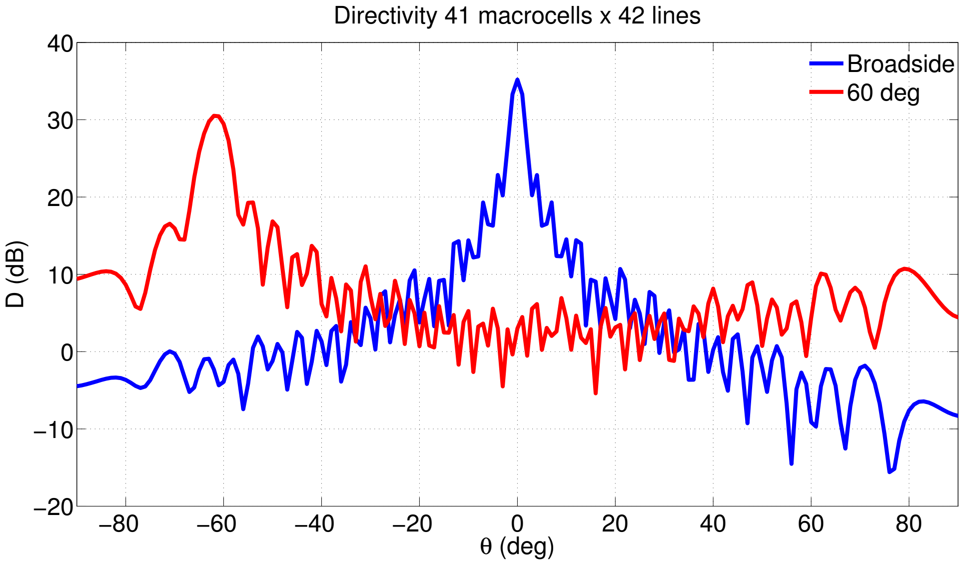

b

**Fig. 4.25:** Directivity of an antenna of 41 macrocells and 42 lines. Maximum directivity at Broadside : 35.19dB, at 60° : 30.05dB

The maximum directivity at 60° for the 41 macrocell x 42 lines antenna is not enough to meet the requirements of table 1.4 (page 33). The number of macrocells or lines can then be increased to meet the requirements. For a 45 macrocell x 45 lines antenna, the requirements in terms of directivity are well met (fig 4.26). Fig 4.27 shows different steering corresponding to the phasing determined in simulation for a macrocell in a 45 macrocell linear array (single line). Data for the macrocell and line is summarized in table 4.6.

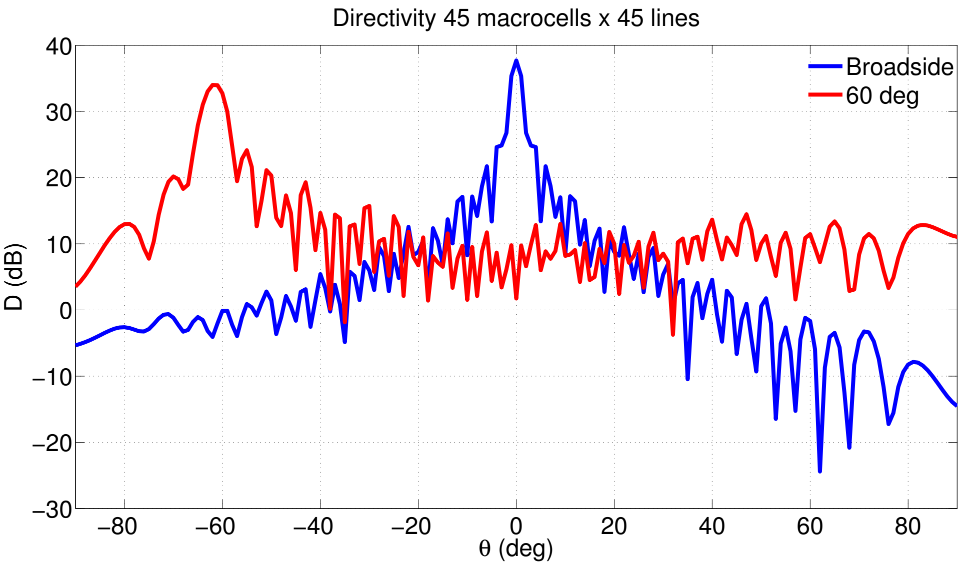

**Fig. 4.26:** Directivity of an antenna of 45 macrocells and 45 lines. Maximum directivity at Broadside : 37.69dB, at 60° : 34.00dB

| | $C_{v,se}$ | $C_{v,sh}$ | $\Delta\Phi$ | $\theta_\infty$ | $\theta_{N=45}$ | $D_{max}$ |
|---|---|---|---|---|---|---|
| Case a | $0.3pF$ | $0.3pF$ | −167.8° | 67.6° | +67° | 32.76dB |
| Case b | $0.32pF$ | $0.35pF$ | −124.9° | 43.5° | +43° | 36.13dB |
| Case c | $0.32pF$ | $0.4pF$ | −93.2° | 30.9° | +31° | 37.02dB |
| Case d | $0.4pF$ | $0.5pF$ | −12.7° | 4.0° | +4° | 37.68dB |
| Case e | $0.5pF$ | $0.4pF$ | −4.4° | 1.4° | +1° | 37.37dB |
| Case f | $0.6pF$ | $0.6pF$ | +60.3° | −19.4° | −19° | 37.14dB |
| Case g | $1.2pF$ | $1.2pF$ | +163.0° | −63.9° | −64° | 33.63dB |

**Table 4.6:** Different phasing configurations of the macrocell (HFSS simulations)

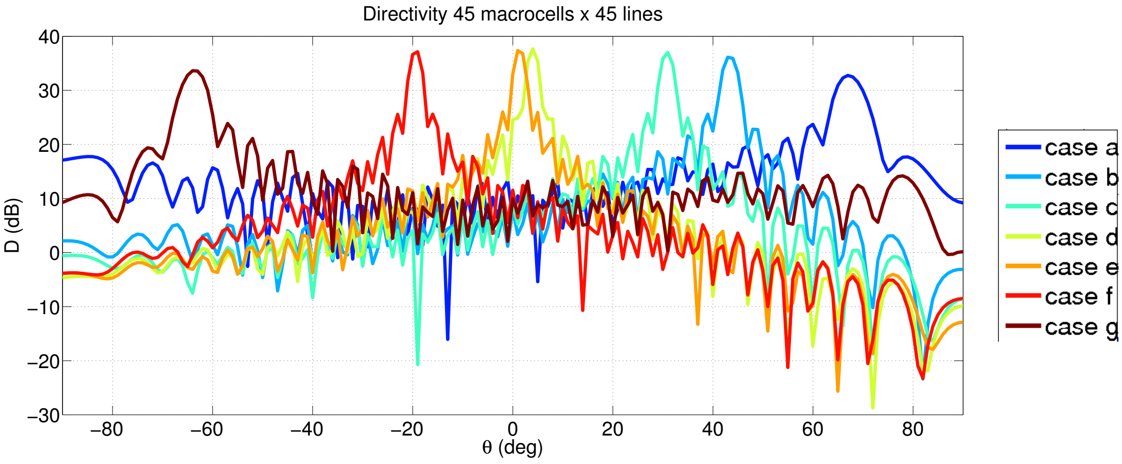

**Fig. 4.27:** Directivity of an antenna of 45 macrocells and 45 lines at different angles as calculated by the macrocell

## 5 Diode Biasing

It was shown in chapter 1 section 4 that varactor diodes need to be reverse polarized to act as variable capacitor. Moreover, the magnitude of the reverse voltage $V_R$ controls the value of the capacitor. Consequently, the anode and cathode of the diode need to be accessible at every time.

From the structure of the line, two considerations need to be addressed:

On the one hand, the DC and RF power need to cohabit in the same circuit, making sure at every time that the anode and cathode of a diode are not in DC contact.

On the other hand, the anode and cathode of the diodes need to be accessed by the biasing circuit, despite the fact that the lines are several wavelengths long and that they are shielded all along the structure.

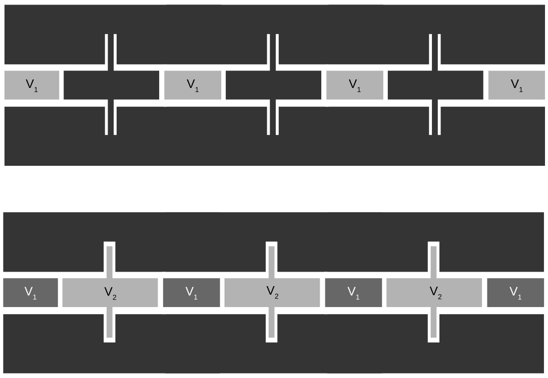

**Fig. 4.28:** DC insulation of subsections of the circuit

Regarding the anode-cathode insulation, the chosen cell structure with two capacitors and one stub allows the insulation of biasing of diodes. Focusing on the *one-way* reconfiguration structure first, it is clear that a structure with only one capacitor per cell and a shorted stub has one single DC conductor and the diodes could not be properly biased. Yet, the two capacitor plus shorted stub creates islands —light grey in fig 4.28—, that can be set to the right voltage with respect to ground —black in fig 4.28—.

Fig 4.28 also represents the *two-way* reconfigurable structure. In this case, the ground plane serves as zero voltage and $V_1$ and $V_2$ as the biasing voltages. Following the disposition of fig 4.29, diode DA requires $V_1 < 0$, diode DX $V_2 > 0$ and diode DY $V_2 > V_1$.

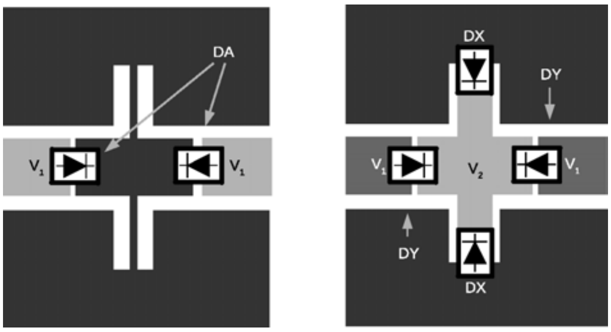

**Fig. 4.29:** Biasing of the diodes

In order to access the diodes, since all the diodes that occupy similar positions are biased with the same voltage, it can be convenient to polarize all the diodes with the same biasing line and to access such line at one of the extremities of the line to avoid piercing the shielding.

Such a biasing line needs to run parallel to the CPW line somewhere within the shield, for instance in the back of the substrate. However, a parallel line connected to the back of the substrate may perturb the fundamental CPW mode.

However, in order to bias the diodes to a particular reverse voltage, a certain amount of charge need to be extracted or inserted into the depletion layer, making the diode behave like a capacitor to the biasing circuit. It is worth noting that the capacitor seen by the biasing circuit may not be the same as the RF capacitor created by the PN junction. This structure has an equivalent circuit like the one shown in fig 4.30a, where $C_d$ is a generic equivalent capacitor, $R_c$ is the charging resistance, that comes from the biasing copper line and $r_d$ is the diode resistance, typically very small.

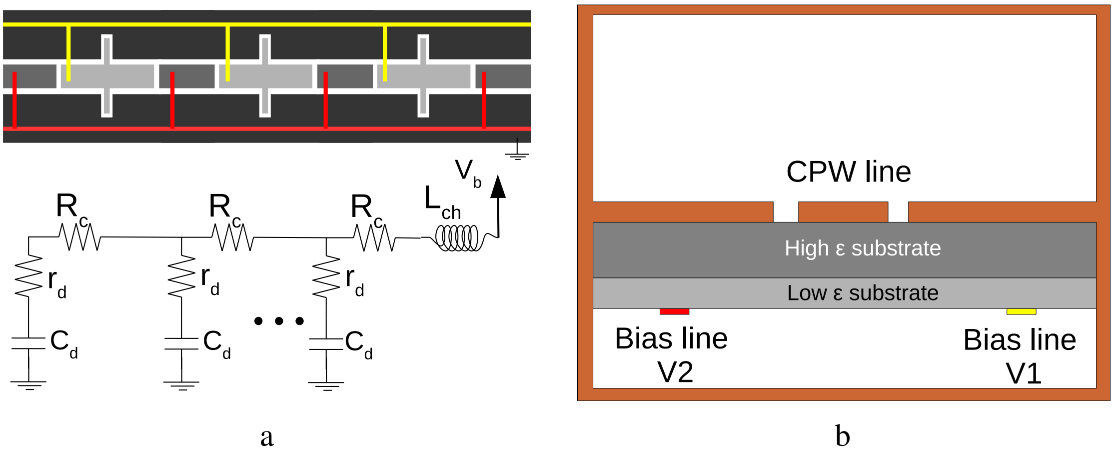

**Fig. 4.30:** Series biasing circuit, the biasing line of a diode is connected to that of the previous one. b) Cross section of the biased CPW line

The charge flux in the diode will be able to stabilize much faster if the charge resistance viewed by the capacitors is small. However, in this structure, the last diode will charge through all the charge resistance from the first one until its position, what reduces considerably the time required to switch the bias of the varactor.

Another way to bias the diodes can be seen in fig 4.33, where each of the diodes is biased with a different access to a low impedance biasing network that runs outside of the shielding. The line would need to be pierced but since it is DC power, the aperture in the shielding can be small which should not affect much the CRLH line.

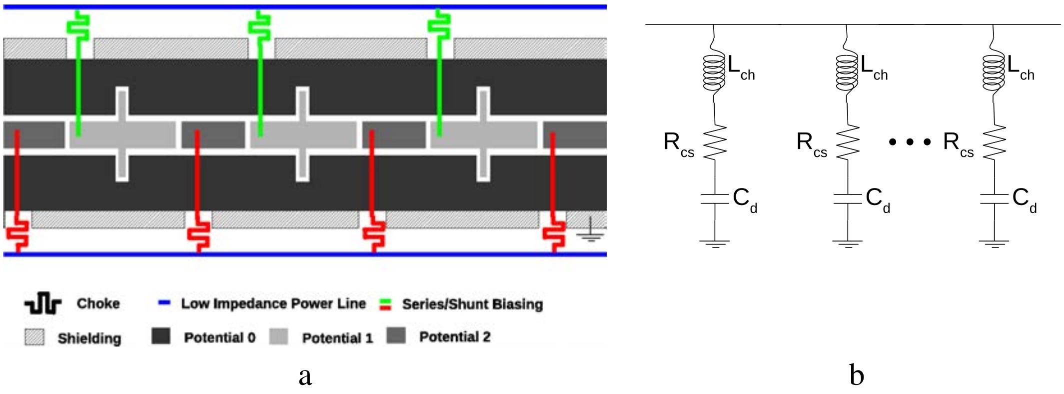

**Fig. 4.31:** Parallel biasing network. Each of the diodes is charged or discharged through a small copper access from a low impedance distribution network

The access to the anode and the cathode of the diode can be done through the back of the dielectric (fig 4.32a) or on the top of the ground plane with bond wire connections (fig 4.32b). In any of these cases, the beam can be switched much faster than in fig 4.30 and the biasing circuit can be designed independently from the antenna.

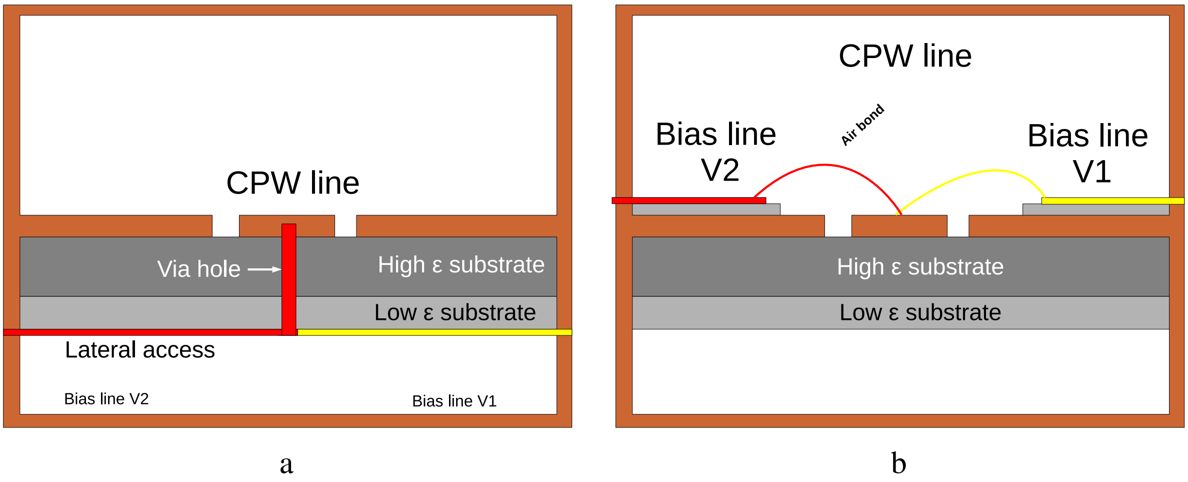

**Fig. 4.32:** a) Back biased circuit and b) Top biased circuit

The lateral access is less intrusive than biasing lines running parallel to the CPW —which may modify the CPW impedance—; however, it does affect the circuit slightly. To show the order of the perturbation, fig 4.33 shows a simulation of a CRLH cell without biasing line and the same line with the side lower (fig 4.32a) and upper (fig 4.32b) biasing. To correct for the effect of the lines, the cell size had to be lengthened by 2% from its original length.

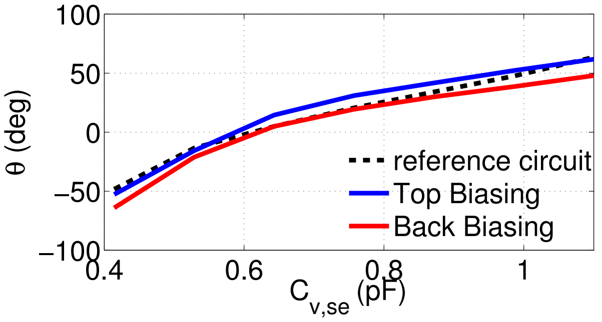

**Fig. 4.33:** Comparison of the expected steering in Lband for a cell without biasing circuit, one with biasing circuit on the top of the ground and another with the biasing in the back of the substrate

# 6 Considerations for the Validation of the Design

The full linear array is a complex system and thus should be validated progressively. In its full Ku band validation two major difficulties may be encountered, namely the etching precision and the diode integration.

First, standard etching precision, can be seen in appendix I is close to $100\mu m$, while the required slots in Ku band can be as small as a few tens of microns. Also in appendix I are presented examples of advanced etching technologies of a few microns, which demonstrates the feasibility of the layouts proposed in this thesis.

The second challenge is the integration of the diodes in the CPW line. Ideally the diodes should be integrated in the substrate, as will be explained in the *Way-Forward* chapter, but this is a very complex process unnecessary for validation. SMD packaged diodes, nevertheless are not suitable for Ku band because of the parasitic components of the package, as was explained in chapter 1. For the validation process, the diodes need to be mounted as a bondable die. For this process, precision soldering is required.

The key steps and considerations to a full validation of the steering linear array are described in this section.

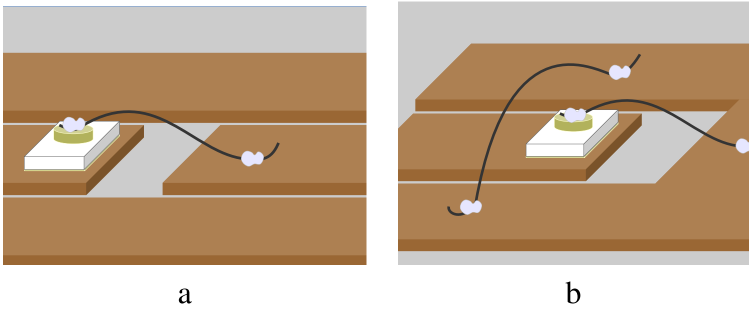
a b

**Fig. 4.34:** Representation of bondable die varactor soldered to the CPW discontinuity

## *Discontinuity and Varactor Validation*

The first step in the validation should be the model for the discontinuity. Some steps have already been made in that direction in this report and the basic model has been validated for L band. The two reconfigurable discontinuities —loaded gap and loaded stub— are more sensitive than the shorted stub or the single series gap. As explained before, the varactor as a bondable die should be mounted directly on the CPW line and the series inductance introduced by the bondable wire may introduce some parasitic effects nonetheless (fig 4.34).

For measuring a single discontinuity, the biasing circuit can be done in the extremities of the circuit, as seen in fig 4.35. A TRL calibration kit can be used to deembed the value of equivalent $T$ and networks. These measurements also give a tension-to-capacitance and tension-to-inductance calibration curves that can be subsequently used to predict the behavior of a cell as a function of the biasing tensions. The kriging methodology for characterization presented in chapter 2 can be used to create a precise map of the inductance/capacitance to biasing voltage relation.

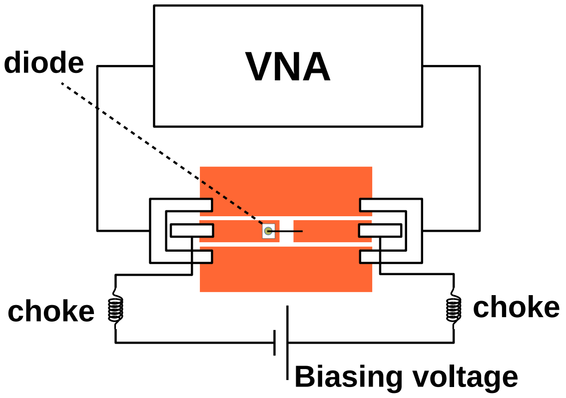

**Fig. 4.35:** Reconfigurable discontinuity as a DUT in a typical measurement set up

*Cell Validation*

The next level of complexity is the cell. The design of the cell can be supported by the measurements of the single discontinuity. For the *one-way* reconfigurable cell, a similar setup as for the discontinuities can be used since only one biasing voltage needs to be used and there is an easy access to both the anode and cathode of the diode (fig 4.36).

The *two-way* reconfigurable cell has a more difficult access and since the purpose is to validate the behavior of the discontinuity within a cell, a classical CRLH can be used to validate the double biasing without need of the biasing circuit. Nevertheless, as seen in this chapter the strips inserted for biasing may change slightly the behavior of the cell and some adjustments may be required. For that reason, it is interesting to test the cell with the biasing. One single cell can already help validate the distance between discontinuities. The use of varactors provides the cell with some versatility. If the whole biasing range of the diode is not exploited, a recalibration of the biasing voltage can give similar results in terms of shunt inductor and series capacitor even if the characteristics of the line vary slightly.

If the biasing circuit is included in the validation of the cell, the *two-way* reconfigurable cell can be easily tested with a vector analyzer independent from the biasing circuit, in conditions similar to the final line (fig 4.37).

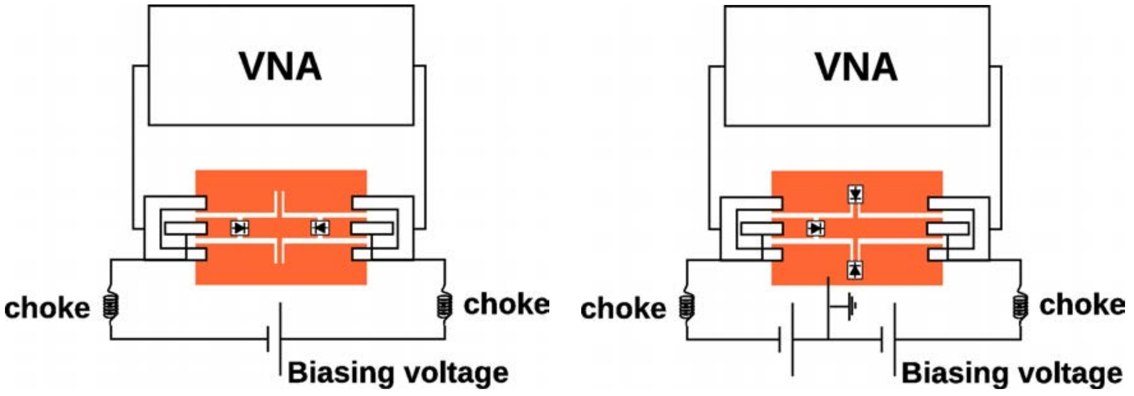

a b

**Fig. 4.36:** Reconfigurable cell as a DUT in a typical measurement set up. a) *one-way* and b) *two-way* reconfigurable cell

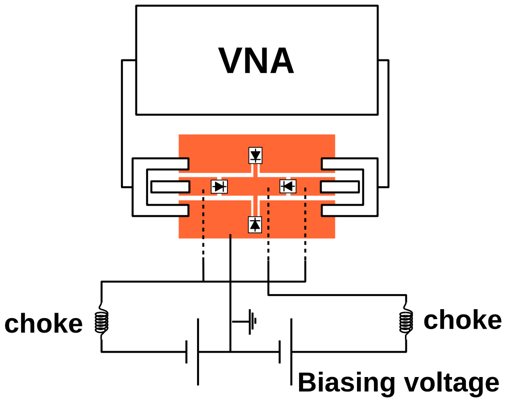

**Fig. 4.37:** Reconfigurable discontinuity as a DUT in a typical measurement set up

*Considerations on the Shielding*

The SIW shielding can be created with three layers, as seen in fig 4.38. the superior and inferior layer, in blue in fig 4.38, have one layer metallized and are there to provide rigidity to the top and bottom of the shielding. These structures are supported by dielectric rods that maintain, periodically, a certain distance between the dielectric of the CPW (green) and the upper and lower dielectrics.

Also periodically and with a period much smaller than the wavelength, metallic rods connect the metallization layers in the rigid dielectrics to the ground plane in the CPW line. If the separation between rods is small enough, it should behave like a full shielded structure.

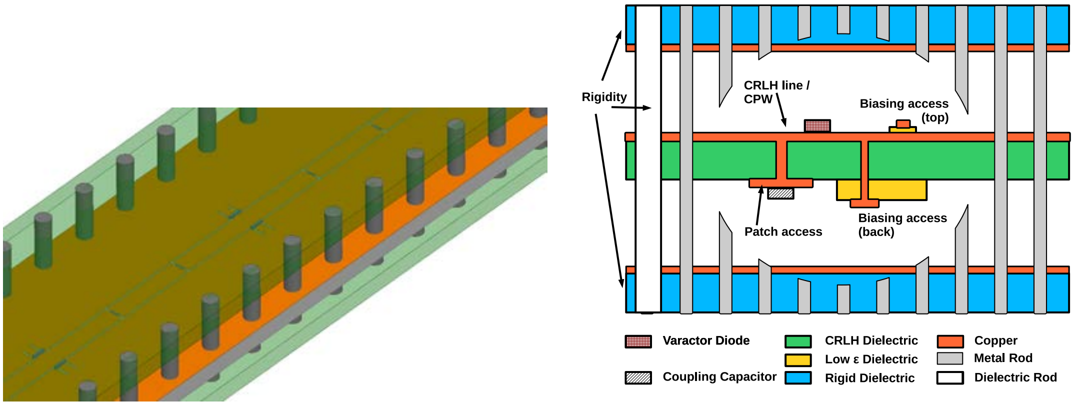

a b

**Fig. 4.38:** SIW shielding

With the SIW shielding is very easy to create accesses for the patch and the biasing circuit since the whole side of the shield can be easily penetrated between the metallic rods. However its rigidity relies chiefly in the dielectric and metallic rods and it may not be robust against vibration or more mechanically demanding applications. For that reason a rigid shielding is also proposed.

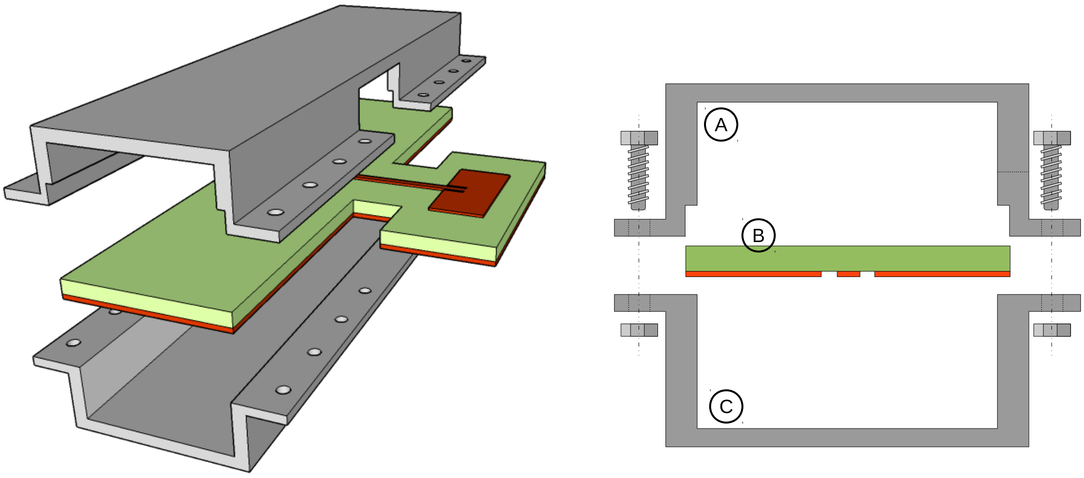

a b

**Fig. 4.39:** Rigid shielding. The shielded line can be built in three pieces.

A metallic case can be placed around the line. To create the shielding case so it is easy to manufacture and assemble, the full shielded line can be done in three pieces (fig 4.39). The piece A is a U-shaped metallic structure which serves as the lower half of the shielding. This part of the shielding is placed against the side of the substrate where the line that feeds the patch in the energy extraction device is etched. The U is ended with two wings that will ensure a good electric connection with the higher half of the shielding. On the side walls, a small groove can be cut with a milling machine for the CPW line to rest. The cut should be the same height as the substrate so the CPW ground makes contact with the upper part of the shielding.

The piece B is the CRLH line with the patches etched in the back and the piece C is the upper part of the shielding, which is the mirror image of the lower shielding except for the groove. The side walls of the lower shielding have apertures (fig 4.39, part A) for the energy extraction device to connect to the patch, outside of the shielding. The three piece structure of the shielding allows to etch both the CRLH line and the patches in a monolithic block of substrate.

## Conclusion

A step towards the design of the full antenna has been taken with the integration of the radiating element into the CRLH line. A modified design procedure models the radiation device as a discontinuity and includes it into the CRLH line. This new procedure makes use of a new periodicity unit, the macrocell, that includes one antenna and several cells. This new definition allows the re-use of the periodic circuit theory. For large steering angles, the Bloch impedance of the line tends to deviate from the nominal impedance. This problem can be resolved with a matching network, as will be explained in the way forward part of this report.

The antenna array theory is combined with the periodic structure theory to extend the characterization of a macrocell to a full antenna. Although all the array theory can be readily used for a two dimensional array, the repartition tree for the array of CRLH lines has not been developed and the simulations used for validation are restricted to one dimensional linear array.

Finally a roadmap toward the validation of the full array has been presented making emphasis on the critical points.

# Part III

# Conclusion and Way Forward

# Conclusion

The requirements for a satellite communications beam steerable antenna have been analyzed. Through the study of the *state of the art* of the relevant technology, those requirements have been translated into clear specifications and a structure that fulfills them have been proposed. The structure is based on two transverse linear arrays where the phasing between elements is electrically controlled.

The phased line that controls the phasing between elements have been adapted from a CRLH structure and made reconfigurable through the integration of varactor diodes. The CRLH structure allows, in a single line to create phase advancement and phase lag, which can create backfire to endfire radiation.

The use of CRLH brings another major advantage. The CRLH/linear array approach is intrinsically narrowband; however, the tuning of the line with two tuning elements —a capacitor and an inductor— can be exploited to perform channel selection. Since satcom systems are usually divided into 36MHz channels, the CRLH approach can select a scanning direction, at a given frequency —within a band—, extending the useful bandwidth far beyond the central frequency of operation.

There are precedents of varactor tunable CRLH lines, however, they are typically built in microstrip. In this thesis, the suitability of CPW for SMD integration is exploited. Varactors can be soldered onto the line without the need for via holes or even can be integrated in the substrate. This is a very powerful feature since it leaves free to use other levels —the back of the substrate— for other purposes like the energy extraction and diode biasing.

In order to design a CRLH line, the discontinuities that generate the series capacitor and shunt inductor were modified for reconfigurability through varactor. For the geometries required in this thesis, the theoretical models proved less accurate than desired. Hence, statistical models for the CPW discontinuities have been developed. These models are efficient and make use of the intelligent choice of parameters to predict the values of the circuit elements in the $T$ and equivalent networks of the discontinuities with a reduce number of pre-simulations.

The theory behind CRLH lines and periodic structures have been condensed into two design methodologies for reconfigurable CLRH lines. These methodologies, unlike the traditional CRLH design, focus on the reconfiguration of the line and gives a support for the creation and calibration of the linear array beamforming network. This same procedure has been proved to be an useful tool for multi-channel design of the CRLH line.

Traditional leaky wave CRLH structures have little control over the radiation of the line in terms of uniformity and polarization. The structure here proposed evolved the CRLH line into a linear array by shielding the CPW line to prevent undesired leakage and protect it from external radiation. In the process, a study has been performed about the substrate layers that can be used and the dimensions of the shielding. This study resulted in some design guidelines that can be applied to the shielding of CPW out of the context of this thesis.

The shielding of the line forced the creation of a means of extracting energy. The energy extraction device drains energy out of the CPW line in a direction orthogonal to the propagation and redirects it towards a radiating element. The extraction device can tune the illumination of the linear array within some limits thanks to its ability to control the percentage of power diverted to the radiating element.

The energy extraction device separates the CRLH line from the radiating element of a given macrocell by an aperture in the shielding of the line. Such aperture defines a port on the side of the shielding that has the geometry of a standard CPW or a standard stripline port, these are geometries often used as feeds for printed antennas. Consequently, the great range of antennas that can be found in the literature stripline or CPW fed can be readily adapted to be the radiating element of the linear array. As an example, a simple patch antenna has been proposed for proof of concept.

In addition to the simple rectangular patch, a dual polarized circular patch has been designed. This patch is fed through the substrate and needs two parallel lines to create the dual polarization. However, in addition to being able to generate any arbitrary polarization, it has a much larger bandwidth than the first patch, which allows for multiple channels.

The patch used as radiating element has been characterized as a discontinuity. This allows to incorporate it into the line design using design procedures similar to those developed for the CRLH line. All the theory developed for the CRLH line has been adapted to the radiating line by defining a new periodic unit, the macrocell, that incorporates phasing and radiation. This new unit helps designing long lines based on a periodic cellular structure, which greatly simplifies the process.

For the design and validation process, some methods for the simulation of large arrays have been discussed. The shielding of the line allows to simulate the patches independently, which makes possible the simulation of a large number of cells. The validation of the steering through CRLH has been performed as well for the full line with a small number of macrocells.

The roadmap for the validation of the line is presented. Considerations on the shielding and the biasing have been presented and detailed solutions of how to proceed for the design of a full line are included in this text.

The measurement of partial mock-up circuits on the CRLH reconfiguration line and the energy extraction device, corroborate some key hypothesis made in this text and serve as proof of concept.

While the technology here developed is not band specific, the design is focused on L and Ku bands, while making it readily extendable to S, C, and X band. In theory, it could also be used in Ka-band if the manufacturing technology allows it, covering then the whole spectrum of standard satellite communications.

Finally, the objectives of the thesis have been fulfilled. A theory have been developed behind the creation of radiating lines that can be used as building blocks of a beam steerable radiating metasurface.

The steer of the beam is achieved through the electrical reconfiguration of varactor diodes and the polarization of the line can be chosen to fit that of the satellite —circular, linear, dual-linear or dual-circular—.

The achievable gain is sufficient for satcom applications; moreover, the cellular structure of the antenna makes possible the design of radiating lines and metasurfaces of much larger gain than the one presented in this thesis.

# Way Forward

In the previous chapter, the main contributions of this work were explained. Although the objectives of defining a low profile technology for beam steering that could support GEO satellite communications were attained, there is still part of the road to be completed towards the full validation of the antenna. Additionally, the very nature of the technology opens new fields that could be explored to increase the performance and versatility of the antenna. The principal ways forward towards the integration and improvement of the antenna are listed in this chapter.

## Matching Network

As explained in chapters 2 and 4, the CRLH line may show some important mismatching at steering angles close to zero or to 60°. This comes from the very nature of metamaterials. Close to the stop bands —low and high propagation constant—, the Bloch impedance tends to either zero or infinity. While at $\beta_{eff} = 0$ a configuration of varactors can be found to balance the line and avoid the mismatch, for high $\beta_{eff}$ configurations this is not possible.

A reconfigurable matching network should be designed to keep up with the variations in Bloch impedance. During the thesis, the focus was on the steering and a reconfigurable matching network was not fully developed.

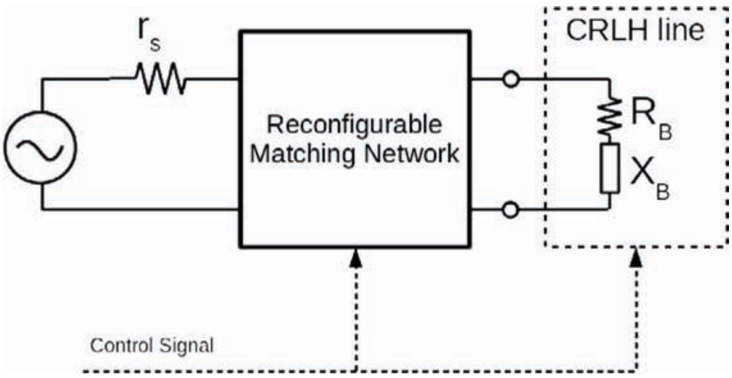

**Fig. WF.1:** CRLH taper

Assuming no reflection in the exit end of the CRLH, this reconfigurable matching network should be able to mimic a semi-infinite CRLH line of similar characteristics than the CRLH line of the antenna.

The matching network sees the Bloch impedance at the input of the antenna and needs to adapt to this value. The Bloch impedance will always have a real part when the CRLH transmits but there is a possibility that it also has a reactive component. Both components need to be matched.

On the input side of the matching network, it needs to match to an arbitrary impedance, typically a real 50 resistance.

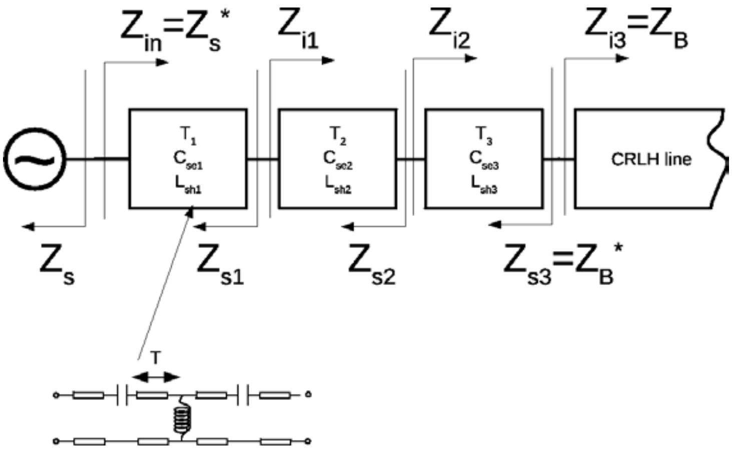

**Fig. WF.2:** CRLH taper

One way of achieving the reconfigurable matching network is by extending the CRLH line a few cells at the extremities. The extra cells can be used as a taper where their characteristic —Bloch— impedance slowly shifts from 50 to the required Bloch impedance of the line (fig **WF**.3).

The cells of the taper introduce various phase shifts that may not be in line with the steering requirements, but that is not important since they are placed at the beginning of the line and do not affect the relative phase of the radiating elements.

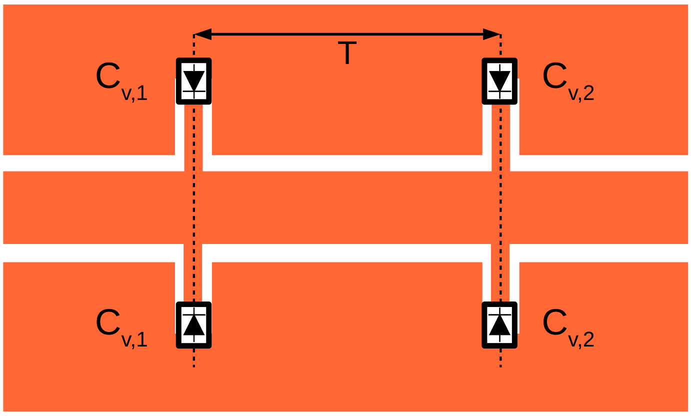

**Fig. WF.3:** CPW reconfigurable adapter

The modeling of the discontinuities can also be used to create a reconfigurable matching network based on the stub-line-stub structure. Making use of two independent loaded stubs, a large number of impedances real and complex can be matched to the input by changing the bias of the diodes. This solution is more compact than the CRLH taper.

It is worth noting that, by carefully choosing the stub lengths, the equivalent reactance of the stub can go from inductor-like to capacitor-like with the same diode.

## Diode Monolithic Integration

The varactor diode can be integrated into the substrate of the line. As seen in fig **WF**.4, through deposition techniques a high doped well of acceptors $P^+$ and a well of donors $N$ can recreate the varactor diode required for the CRLH line.

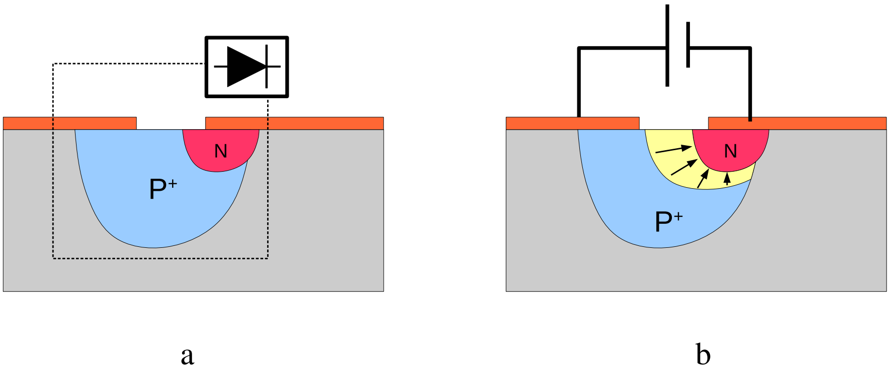

**Fig. WF.4:** Integration of the diode in the substrate

Depending on the geometry of the diode, the depletion zone will have different dimensions. The value of its junction capacity will depend on its geometry and the material with which the diode is manufactured, *i.e.* the substrate of the CRLH line.

## Full 2D Steering

As explained in chapter 1, the full 2D steerable metasurface can be seen as a linear array where each of the radiating elements is one of the radiating lines studied in this thesis. The 2D steering capability is then reduced to the design of a reconfigurable 1D steerable feed for the array of lines.

One option could be to create a reconfigurable corporate beamforming network. The beamforming network could be a tree of Wilkinson dividers where a CRLH cell is connected at the end of its branches to control the relative phase between the two outputs. The Wilkinson would be perfectly balanced if two cells are used at each exit. One with 0rad phase shift and a another that will generate the phased feed for all the lines (fig **WF**.5).

**Fig. WF.5:** Wilkinson divider with phase control, top and bottom layers

Having each level of the beamforming network phase each left arm a shift half of the previous level, an uniform phasing between lines can be achieved (fig **WF**.6).

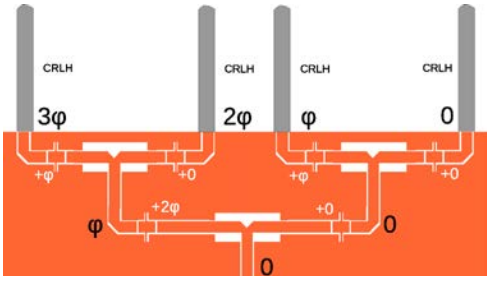

**Fig. WF.6:** Wilkinson divider with phase control within a corporate beamforming network

Another option to create a very compact beanforming network is to reutilize the technology developed for the linear array and use one extra line to excite the array of lines (fig **WF**.7)

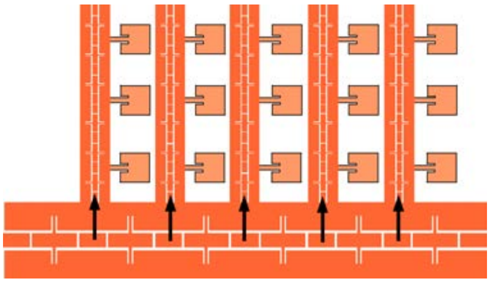

**Fig. WF.7:** CRLH line used as an excitation for the array of linear arrays

This structure is preferable to the Wilkinson-like tree for several reasons. For instance, this structure is more compact than the Wilkinson, merely requiring an extra line width to complete the surface of the antenna. The Wilkinson, on the other hand, requires extra surface for each distribution level.

Another strength of the CRLH feed is that the design of the feed is independent from the number of lines. There is no added complexity to a number of lines in the antenna that is not a power of two. Whereas, the Wilkinson distribution tree is most suited for $2^n$ lines and any other number of lines would require a dedicated design of the feed. Fig **WF**.8 shows a projection of what would the full 2D steerable antenna would look like with either feed.

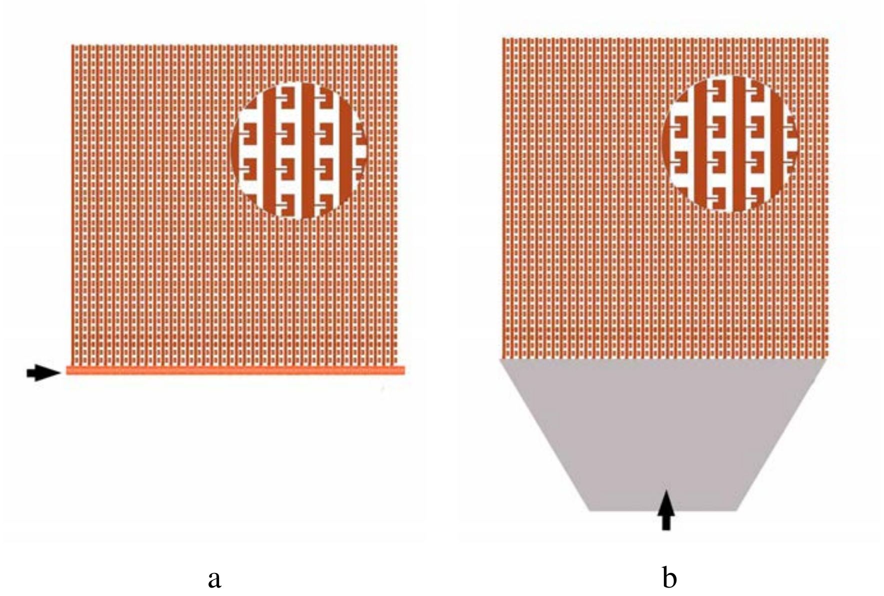

**Fig. WF.8:** a) CRLH fed line array b) Wilkinson-like distribution tree fed antenna

One last possibility is to feed the array of lines with a non-reconfigurable corporate beamforming network and electrically steer in the plane of the line (elevation) while the azimutal steering is done mechanically.

## Polarization

In chapter 3, a dual polarized patch antenna is developed. Such an antenna can implement any direction of linear polarization as well as dual circular polarization. However, it needs to be excited by two independent and equal CRLH lines that are excited with a very precise phase and power ratio.

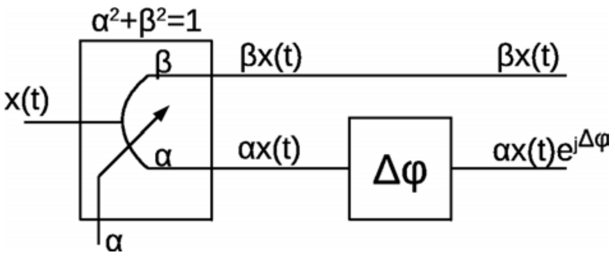

**Fig. WF.9:** Power divider with control of phase and power ration between outputs

A power divider akin to the one shown in fig **WF**.5 should be inserted at the feed of every line (fig **WF**.9). That controller should be modify to be able to select the ratio $P_V/P_H$ from 0 to $\infty$. An extra CRLH cell at the beginning of the line with independent biasing can create the phase different required for CRLH polarization.

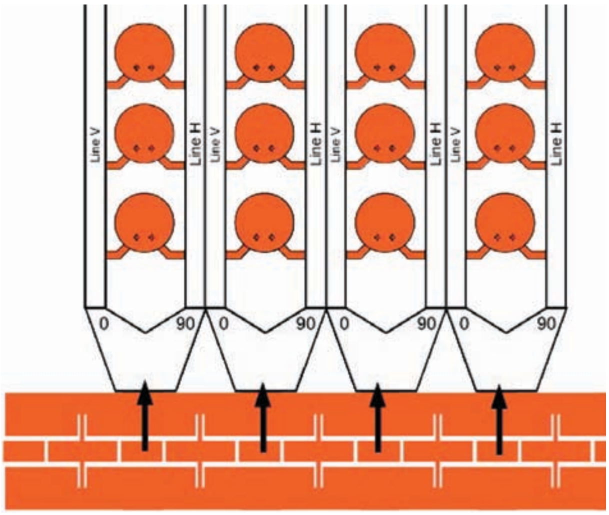

**Fig. WF.10:** Power divider with control of phase in the feed of every line

## Bandwidth

Because of the dispersion of CRLH lines, the steering angle of the linear array studied in this thesis depends directly on the frequency. It has been shown that there is no real need to make the antenna wide band since it can be used to select the channel of operation merely by changing the biasing of the diodes. The square patch antenna used as an example does not have a sufficient wide band to allow channel selection, however, the configuration employed for the dual polarized version has a much larger bandwidth.

There are also some strategies that could be explored to widen the band. For instance, the use of non-Foster reactances. A controllable non foster capacitor and inductor can recreate a CRLH like the one presented in this report and create the phase profile required for a certain steer constant for a whole bandwidth [128, 129]. This introduces two BJT transistors per non-Foster reactance and requires a configuration circuit fig **WF**.11.

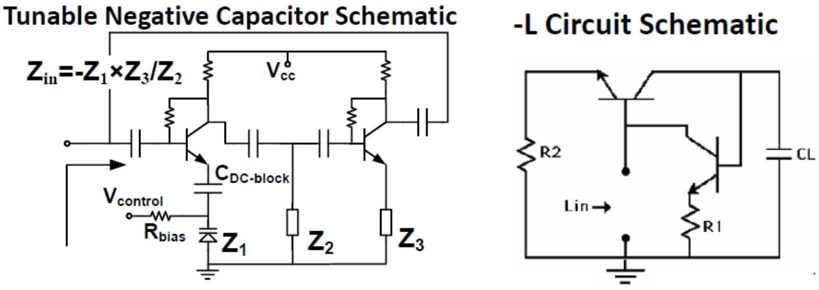

a b

**Fig. WF.11:** Implementation of a negative a) C and b) L [128]

# Part IV

# Appendix

# Some Useful Definitions

## 1 Coordinate System

Throughout the report, the spherical and cartesian coordinate systems will be used with the following definitions:

1. **Theta** $\theta$. Angle between Z and the line OP
2. **Phi** $\phi$. Angle between X and the line between O and the projection of P on the plane XY.

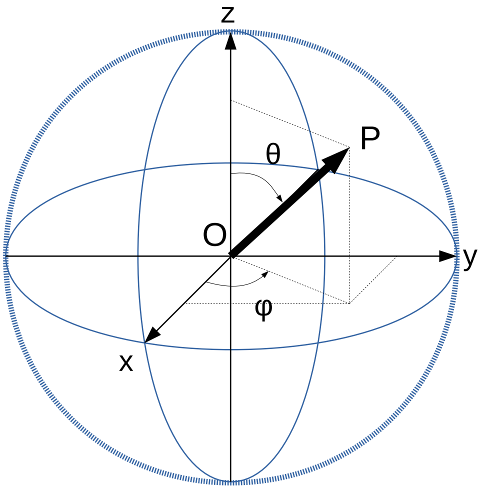

**Fig. A.1:** Boresight of an antenna

## 2 Direction of radiation and steering

1. **Boresight**. The *boresight* of the antenna is the direction of maximum gain.

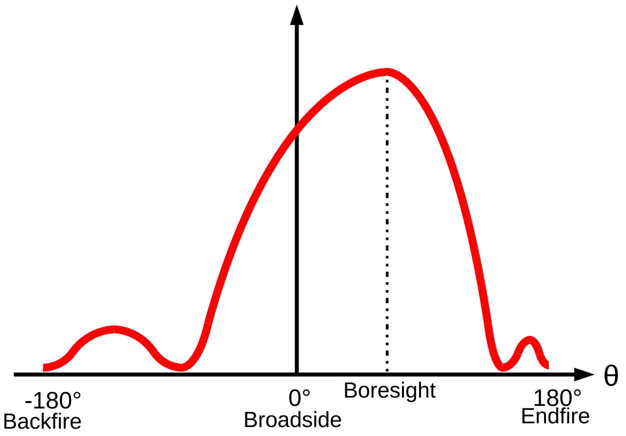

**Fig. A.2:** Boresight of an antenna

2. **Endfire**. A linear array or antenna is said to be *Endfire* when the maximum of radiation, *i.e.* its boresight, occurs in the axis on which the antenna lies. It can be extended to two dimensions whenever the boresight occurs orthogonal to the normal vector of the plane the antenna lies on. It the antenna is a leaky wave, there is a direction of propagation within the line, in that case, *Enfire* will be understood as the direction of propagation within the line.
3. **Backfire**. For leaky wave antennas, the *Backfire* direction is that opposite to the direction of propagation *i.e.* to the *Endfire* direction.
4. **Broadside**.A linear or planar array or antenna is said to be *Broadside* when the maximum of radiation occurs in a direction normal to the line or plane on which the antenna lies.

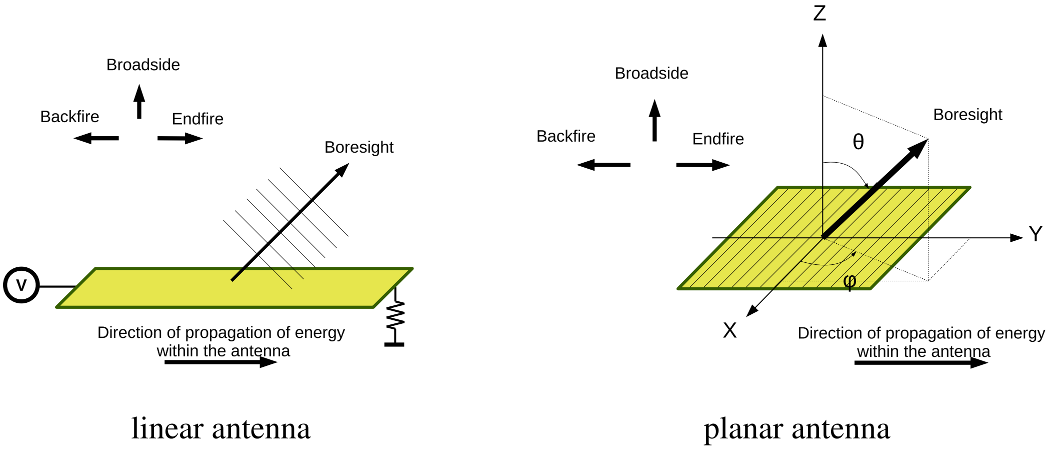

linear antenna planar antenna

**Fig. A.3:** Definitions for linear and planar antennas/antenna arrays

Regarding the steering, there can be one- and two-dimensional steering:

1. **One-dimensional steering**. The steering in this report is said to be *one-dimensional* whenever the beam scans in one single dimension, *i.e.*, the boresight travels within a plane.

   For example, if the beam scans solely in the plane XZ, the steer can be described by a single angle, $\theta$ in this case.

2. **Two-dimensional steering**. The steering in this report is said to be *two-dimensional* whenever the beam scans in two dimensions, *i.e.*, the boresight travels within a space or a semispace.

   For example, in the semispace $Z^+$, the steer can be described by a two angles, $\theta, \phi$ in this case, *i.e.* two dimensions.

# B

# GEO Communications Satellites

| **Satellite** | **Operator** | **Band** | **Channels** | **EIRP**[1] | **Purpose** | **Pol.** | **Ref** |
|---|---|---|---|---|---|---|---|
| Yamal 300K | Gazprom | C | 11x72MHz | 45dBW | | Linear | [4] |
| | | Ku | 11x72MHz | 44dBW | | Linear | |
| Yamal 202 | | C | 18x72MHz | 36dBW | | Circular | [4] |
| Yamal 401 | | C | 17x72MHz | 45dBW | | Circular | [4] |
| | | Ku | 18x36MHz<br>18x72MHz | 44dBW | | Linear | |
| Yamal 402 | | Ku | 18x36MHz<br>16x72MHz | 43dBW | | Linear | [4] |
| Galaxy 11 | Intelsat | C | 24x36MHz | 42dBW | | Linear | [5] |
| Intelsat 1R | | C | 36x36MHz | 30dBW | | Linear | [5] |
| | | Ku | 36x36MHz | 40dBW | | Linear | |
| Intelsat 9 | | C | 24x36MHz | 36dBW | | Linear | [5] |
| | | Ku | 24x36MHz | 43dBW | | Linear | |
| Intelsat 1W | | C | 10x33MHz | 38dBW | | Linear | [5] |
| Intelsat 701 | | C | 42x36MHz | 26dBW | | Circular | [5] |
| | | Ku | 20x36MHz | 41dBW | | Linear | |
| Intelsat 14 | | C | 48x36MHz | 36dBW | | Circular | [5] |
| | | Ku | 24x36MHz | 43.7dBW | | Linear | |
| Intelsat 11 | | C | 12x54MHz<br>4x64MHz | 36dBW | | Linear | [5] |
| Intelsat 903 | | C | 76x36MHz | 31dBW | | Circular | [5] |
| | | Ku | 22x36MHz | 47dBW | | Linear | |
| AMC-1 | SES | Ku | 16channels | 38dBW | Broadband services | Linear | [6] |
| ASTRA-5B | | Ku | 40 BSS | 46dBW | Satcom | Linear | [6] |
| | | Ka | 6x600MHz | | TV | Circular | |
| NSS-7 | | C | 50 channels | 39dBW | | Circular | [6] |
| | | Ku | 40 channels | 44dBW | | Linear | |
| SES-4 | | C | 52 channels | 35dBW | | Circular | [6] |
| | | Ku | 72 channels | 43dBW | | Linear | |
| ASTRA-2E | | Ku | 62 | 43dBW | | Linear | [6] |
| | | Ka | 600MHz | 53dBW | TV | Circular | |

| | | | | | | |
|---|---|---|---|---|---|---|
| SES-14 | 28 channels | C | | 37dBW | circular | [6] |
| | | Ku | 20 channels | 43dBW | linear | |
| Star One D1 | Star One | C | 28x36MHz | 36.7dBW | Linear | [7] |
| Star One C2 | | C | 28x36MHz | 37dBW | Linear | |
| | | Ku | 12x36MHz<br>2x72MHz | 46dBW | Linear | |
| Star One C12 | | C | 11x36MHz | 40dBW | Linear | |
| Brasilsat B2 | | C | 28x36MHz | 36.7dBW | Linear | |

**Table B.1:** Summary of key characteristics of relevant GEO satellites. [1]End of coverage, approximate values

# C

# The Coplanar Waveguide

Introduced by C. P. Wen in 1969 [130] the coplanar waveguide (CPW) is composed of a conductor strip printed on a substrate and two semi-infinite coplanar ground planes flanking it (fig C.1). Because the ground plane and the central strip share the same level, no via holes are required to connect them, through printed patterns or SMD components. Cross talk effects between adjacent lines —as is the case of an array of CRLH lines— are reduced with respect to microstrip because of the presence of a ground plane between them.

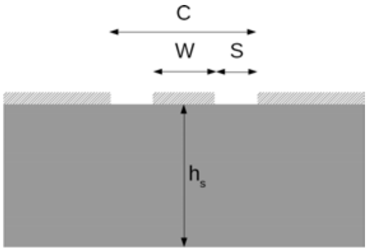

**Fig. C.1:** CPW line, transverse cut

As seen in fig C.2, two modes are supported by CPW lines. The odd mode has the electric field in opposition on the slots, making it non radiative. This is commonly the desired mode in the CPW line. The even mode, sometimes called the *coupled slotlines* mode, has the two ground planes at different potentials and is usually undesired.

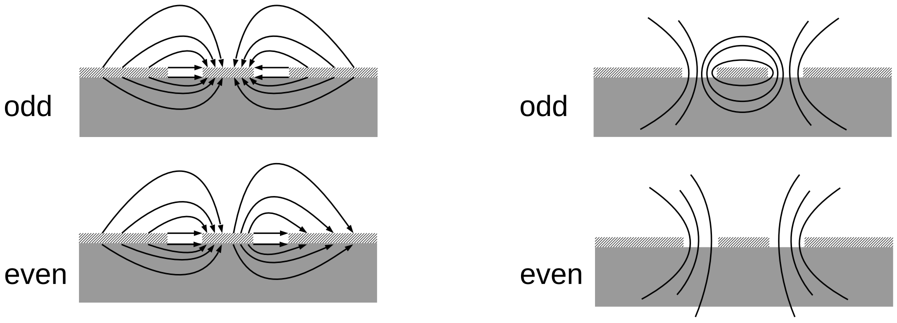

a

b

**Fig. C.2:** a)E field, b)H field

Even when solely the odd mode is excited, the presence of discontinuities and asymmetries can transfer energy from the odd mode to the even mode. To prevent this from happening, bond wires can be placed over the strip, connecting both sides of the ground plane. The bond wires —also known as air bridges— force equipotential conditions at both sides of the strip. This condition reinforces the odd mode and goes against the excitation of the even mode.

When the side slots in the CPW are small compared to the central strip width, the **E** and **H** fields remain concentrated near the slots. This makes the CPW line independent from the substrate thickness, which does not affect the effective propagation constant except for very thin substrate layers.

The symmetric configuration of the fields prevents the CPW from radiating. As the frequency augments, the electrical separation of the side slots augments in turn and the radiation losses increase. This radiation is related to the generation of surface waves [90], consequently, for high frequency design, the suppression of such waves must be taken into consideration. A rigorous analysis of the CPW line and design equations can be found in [119] or [131].

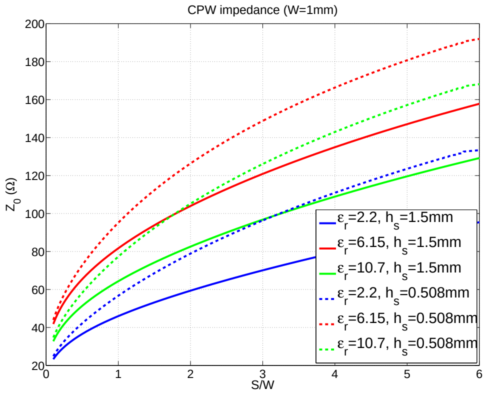

**Fig. C.3:** Line impedance $Z_0$ of different CPW lines

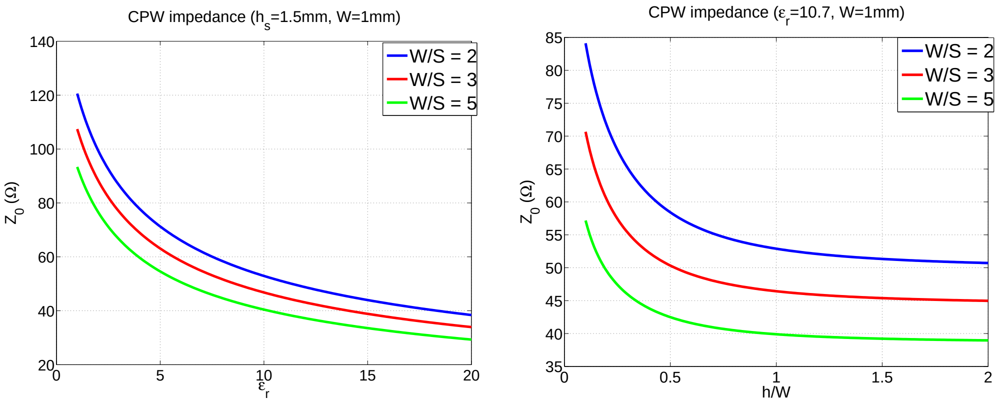

a b

**Fig. C.4:** Line impedance $Z_0$ of different CPW lines. a)variation with $\epsilon_r$ b)variation with $h_s$

# D

# Varactor Diodes

## 1 Silicon Abrupt Junction Diodes

A basic PN diode is composed of a N layer doped with donors and a P layer doped with acceptors. Although the net charge in both P and N layers is zero, the N layer has free electrons that can move over to the P layer and recombine with its holes when there is physical contact between the layers.

The recombination in the neighborhood of the junction creates a region depleted of free electrons or holes. This depletion region separates two charged regions, the P and N with excess and lack of electrons, respectively. Therefore, an electric field is created within the depletion region between the regions of the P and N layers with net charge. Applying an external biasing voltage to the diode changes the size of the depletion region.

Once the depletion region is formed, two regions with free charges are separated by the depletion region that acts as a dielectric. Therefore, a capacitor is formed inside of the diode. If the diode is constructed as a cylinder, which is often the case, the capacity created in the junction follows the well known formula

$$C_J = \frac{\epsilon_D A_d}{d_D(V_b)} \tag{D.1}$$

where $\epsilon_D$ is the permittivity of the depletion region, $A_d$ is the area of the section of the diode and $d_D$ is the length of the depletion region which depends on the bias voltage $V_b$.

Regarding the doping profile, there are two main types of diodes : the abrupt and the hyper-abrupt diode. In an abrupt diode, the doping concentration of the cathode is constant all along

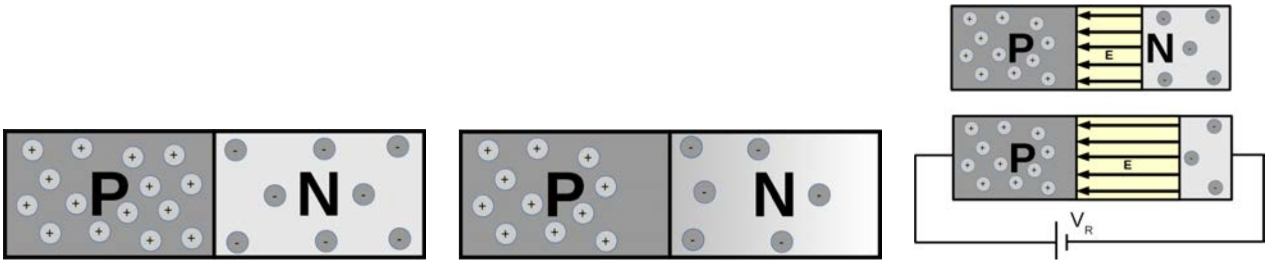

a b c

**Fig. D.1:** a)PN Junction. b) Hyperabrupt PN Junction. c) Depletion region in a unbiased and a biased PN junction the layer. This magnitude is a few orders of magnitude lower than that of the P layer. Since the P is much more doped than the N layer, the depletion region is mainly contained in the N layer, changing its length with the bias voltage while the part that lays on the P layer remains practically constant.

In a hyperabrupt diode, the doping concentration in the cathode is not constant, it decreases rapidly with the distance from the junction. This means that the depletion region will extend also rapidly with the reverse bias voltage. Creating a capacitor that is more sensitive to the reverse bias than an abrupt diode.

| Diode | $R_s(\ )$ | $L_S(nH)$ | $C_P(pF)$ | Dynamic Range (pF) |
|---|---|---|---|---|
| SMV1405-079LF | 0.8 | 0.7 | 0.29 | 0.63-2.67 |
| SMV1408-079LF | 0.6 | 0.7 | 0.21 | 0.95-4.08 |
| SMV1413-079LF | 0.35 | 0.7 | 0.3 | 1.77-9.24 |
| SMV1430-079LF | 3.15 | 0.7 | 0.13 | 0.31-1.24 |
| SMV1493-240 | 0.5 | 0.5 | 0 | 7.1-28.7 |
| SMV1494-240 | 0.5 | 0.5 | 0 | 14.7-57.8 |

**Table D.1:** Summary of diode characteristics

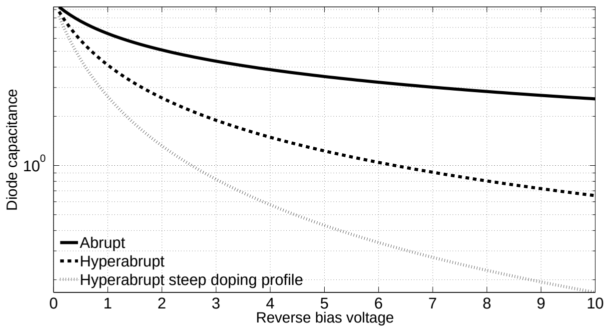

**Fig. D.2:** a)Capacitance profile for different types of diodes

## 2 Packaging

A very convenient way to integrate diodes in CPW circuits is by soldering them in a SMD package as seen in fig D.3a; however, the packaging introduces a non negligible effect in the overall equivalent. Bondable die chips can also be mounted in the circuit, thus avoiding the effect of packaging. Nevertheless, the characterization of the connections between the die and the circuit will have variable effects and is the responsibility of the designer to characterize them.

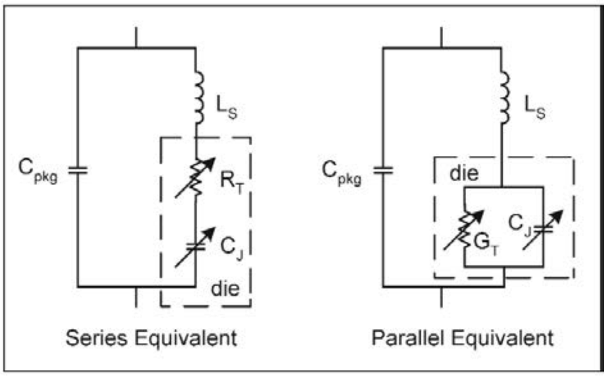

**Fig. D.3:** Equivalent circuits of diode (single bondable die) inside of a generic packaging [132]

The two main parasitic effects can be seen in fig D.3. The packaging capacitance $C_p$ or $C_{pkg}$ actually adds to the junction capacitance, but decreases the maximum to minimum capacitance ratio of the diode [132]. The series inductance $L_s$ is more problematic, it introduces a resonance that decreases the value of the overall capacitance and can even cancel it at higher frequencies. Some diodes are advertised as high frequency diodes because of their high $Q$ —energy stored to dissipated ratio— that allows them to operate at high frequencies as a single diode but they become useless when mounted in a package.

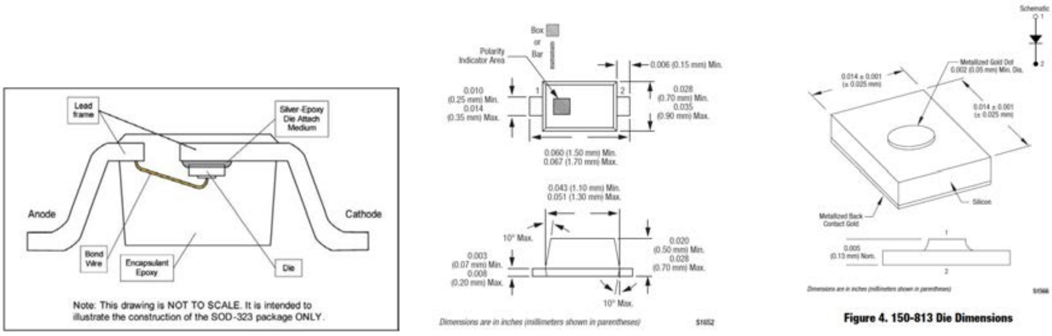

a b

**Fig. D.4:** a) Cross-section of a packaged diode (SOD-323) [132] b)SC-79 packaging [133] c)Varactor in a bondable chip [134]

For narrow band applications, the equivalent circuit's real and imaginary parts can be equated to an equivalent overall resistor $R_d$, and an overall susceptance $B_d$ which ideally is the junction capacitor $C_j$. In general, $B_d$ includes the effects of the series inductor and packaging capacitor, that is why certain packages are not suitable for high frequencies. In order to achieve lower series inductances chip varactors can be soldered or welded directly into the circuit, this is a more complex procedure but may be necessary for higher frequency applications.

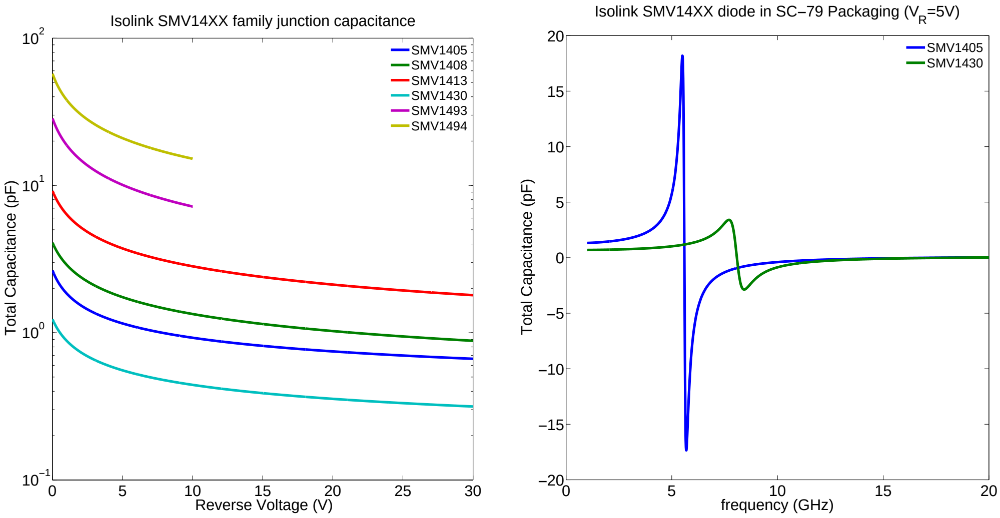

a b

**Fig. D.5:** SMV family junction capacitances and self resonance

# E

# Kriging interpolation

## 1 Definition and advantages

Kriging interpolation was conceived by G. Matheron based on D. G. Krige's works —hence the name— as an interpolation method where the estimated values are based on the covariance of the interpolated function. Each estimation is a weighted linear combination of the sample points.

The weights are assigned according to the sample data, its position and an estimation of the covariance of the original function. The kriging algorithm has the typical characteristics of an interpolation algorithm:

1. If the sample population uniformly covers the interpolation domain, the estimation is fairly good.
2. If the sampling points are close enough to each other to be able to sample faster than the variability of the function, the estimation is fairly good.
3. If the estimation is far from the sampling points, the estimation is degraded.
4. Almost all interpolation algorithms underestimate heights and overestimate lows. A function without local maxima/minima can be interpolated more accurately.

In addition to these common characteristics, kriging has the following advantages:

5. Kriging compensates for data clustering by reducing the weight of clustered samples.
6. Along with the interpolation of the function, kriging can calculate an estimation of the variance of the error of the estimation.

It will be later shown that is the last property of kriging that will be utilized to implement the discontinuity characterization method introduced in this report.

## 2 Simple kriging

There are different approaches to the kriging algorithm but all of them are variations of the following formulation:

$$\hat{f}(\mathbf{r}) - m(\mathbf{r}) = \sum_{i=1}^{N} \lambda_i \left[ f(\mathbf{r}_i) - m(\mathbf{r}_i) \right] \tag{E.1}$$

where the interpolated function is $f(\mathbf{r})$, the weights are $\lambda_i$, the sample population is $\mathbf{r}_i, i = 1..N$ and $m$ is a function called the *trend*.$\mathbf{r}$ can belong to a n-th dimensional domain. The trend is chosen so the residual component $\hat{R}(\mathbf{r}) = \hat{f}(\mathbf{r}) - m(\mathbf{r})$ can be assumed to have zero mean.

The difference between the various kriging algorithms comes from the treatment of the trend function. In this appendix, simple kriging will be explained as an example. In simple kriging, the trend function is assumed to be constant

$$m(\mathbf{r}) = m \tag{E.2}$$

but other types of kriging may assume that the trend is locally constant $m(\mathbf{r} \quad \mathbf{r}_i) = m_i$ —ordinary kriging— or that the trend varies linearly $m(x, y) = ax+by+c$ —kriging with a trend—.

Assuming no bias $E\left[\hat{f}(\mathbf{r}) - f(\mathbf{r})\right] = 0$, the variance of the estimator is defined as

$$ {}^{2}_{error}(\mathbf{r}) = Var\left[\hat{f}(\mathbf{r}) - f(\mathbf{r})\right] \tag{E.3}$$

since the residual component has zero mean, the covariance of the interpolated function, and that of the residual component is

$$Cov\left[f(\mathbf{r}), f(\mathbf{r}+\mathbf{h})\right] = Cov\left[R(\mathbf{r}), R(\mathbf{r}+\mathbf{h})\right] + m^2 \tag{E.4}$$

where the covariance of the residual component depends only on the distance between points and not the positions

$$Cov\left[R(\mathbf{r}), R(\mathbf{r}+\mathbf{h})\right] = C_R(\mathbf{h}) \tag{E.5}$$

kriging calculates the weights $\lambda_i$ so the error variance in eq E.3 is minimal. To do that, eq E.3 can be expanded with eq E.1 adapted to simple kriging and the optimization condition can be set

$$\frac{{}^{2}_{error}}{\lambda_i} = 0 \tag{E.6}$$

which leads to the following system

$$\underline{\underline{K}}\overline{\lambda}(\mathbf{r}) = \overline{k}(\mathbf{r}) \tag{E.7}$$

where

$$K_{i,j} = C_R(\mathbf{r}_i - \mathbf{r}_j) \tag{E.8}$$

$$k_i(\mathbf{r}) = C_R(\mathbf{r}_i - \mathbf{r}) \tag{E.9}$$

$$\lambda(\mathbf{r}) = [\lambda_1\ \lambda_2\ ..\ \lambda_N] \tag{E.10}$$

the resolution of this system for a give point $\mathbf{r}$ results in the weights that interpolate the function in $\mathbf{r}$ (eq E.1) and also in the estimation of the variance of the error of interpolation as

$$ {}^{2}_{error}(\mathbf{r}) = C_R(0) - \sum_{i=1}^{N} \lambda_i(\mathbf{r}) C_R(\mathbf{r}_i - \mathbf{r}) \tag{E.11}$$

# Kriging applied to multi-parameter discontinuity modeling

In chapter 2, a kriging based algorithm is developed to create a surrogate model for the shunt inductor $L_{sh}$ in fig 2.23 (page 56). However, the polynomial characterization included both a value at the central frequency $L_0$ and a sensitivity parameter $\frac{L_{sh}}{f}$. Additionally, it may be useful as well to estimate the series value $L_{se}$. This all can be estimated in the same process using the kriging based methodology extended for multi-parameter.

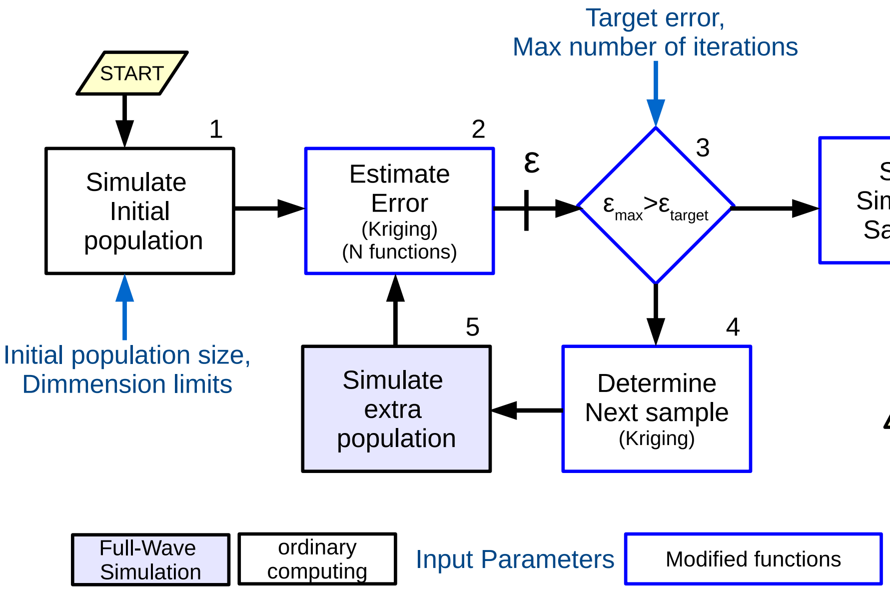

**Fig. F.1:** Multi-parameter kriging based discontinuity modeling

The basic algorithm is represented in fig F.1, where the boxes in blue represent those sub-algorithms that differ from the single-parameter method explained in chapter 2. The algorithm will be reminded here, pointing out the differences that arise in the multi-parameter extension, using the three parameter set $(L_0,\ \ L_{sh}, L_{se})$ as an example:

*Step 1: Simulate Initial Population*

In the same way as the single-parameter method, the multi-parameter method should begin with a large enough population to be representative, otherwise the first estimations of the error will not be accurate. In this step it can be useful to begin with a Latin hypercubes distribution, as explained in chapter 2.

*Step 2: Estimate Error*

The estimation of the error is performed for each of the parameters in the same way as the single-parameter method. Using the kriging estimation of the error, an error vector can be computed where each of the elements is the error estimation of each of the parameters. For a 3 bound, the error can be defined as $e = 3 \cdot max\{\ \ \}$ and the error vector as:

$$\overline{e}_i = [\ \ {}_{k,L_0}, e_{k,\ L_{sh}},\ \ {}_{k,L_{se}}] \tag{F.1}$$

*Step 3: Check Error*

In this step the variation from the single-parameter is more pronounced. Different strategies can be followed depending of the need for precision in each of the parameters.

The decision to stop the algorithm can be made based on a *hard* condition, like having a vector of error tolerances $\overline{\ }_{tol}$ and having the error vector meet each of the single tolerances:

$$\overline{\ }_{k,L_0,i} < \overline{\ }_{L_0,tol} \tag{F.2}$$

$$\overline{\ }_{k,\ L_{sh},i} < \overline{\ }\ _{L_{sh},tol} \tag{F.3}$$

$$\overline{\ }_{k,L_{se},i} < \overline{\ }_{L_{se},tol} \tag{F.4}$$

or it can be made meet a *soft* condition, in which a weighted error ${}_W$ needs to be smaller than a certain tolerance

$${}^{(i)}_{W} < \ \ {}_{tol} \tag{F.5}$$

where the weighted error is a linear combination of the different partial errors

$${}_W = \sum_j w_j\ \ {}_{k,j}\ \ \ withj = \{L_0,\ \ L_{sh}, L_{se}\} \tag{F.6}$$

the choice of the weights may give relevance to the first parameter only, and do *best effort* for the rest

$$w_{L_0} = 1\ \ and\ 0\ otherwise \tag{F.7}$$

or give more weight to bigger errors

$$w_j = \frac{max\{\ \ {}_j\}}{{}_k\, max\{\ \ {}_j\}} \tag{F.8}$$

*Step 4: Determine Next Sample*

While the exit condition is not met, step 4 tries to find the next sample that minimizes the error. This step is tightly related to the previous one. If the *soft* condition F.7 is applied, then the point of maximum error in *step 3* for the first parameter will be the next point of simulation. For a *hard* error condition, a good choice would be to select the point of maximum error for the parameter that presents the maximum error.

*Step 6: Store Simulated Samples*

In this case the storage need is increased. The simulation points vector will be the same for all variables but their respective values need to be stored separately *i.e.*, for a sample population of $N$ a two variable —$C_L, l_{st}$— model of three parameters —$L_0$, $L_{sh}, L_{se}$— will increase the storage space with respect to the single parameter in:

$$(2N+N)words \qquad (2N+3N)words$$

.

# 1 Error and Convergence

In order to estimate the error, different paths can be taken. Kriging offers a good *a priori* estimation that can be used to estimate the following point to analyze but, once the simulations are run the new information can be used to evaluate the methodology. As discussed in chapter 2, a 99% bound to the absolute error can be done by multiplying the maximum typical deviation by 3:

$$^{(i)}_{k} = 3max\{\ _{i}\} \tag{F.9}$$

In simulation time, an *a posteriori* error can be calculated on the new simulated point. This *true error* $_i$ can be defined as the difference between the simulated inductance at a point $(C_{L,i}, l_{st,i})$ $L_{sh}(C_{L,i}, l_{st,i})$ compared to the estimation of that inductance using all the previously simulated points $\hat{L}_{sh}^{(i-1)}(C_{L,i}, l_{st,i})$.

$$_{i}(\%) = \frac{|\hat{L}_{sh}^{(i-1)}(C_{L,i}, l_{st,i}) - L_{sh}(C_{L,i}, l_{st,i})|}{|L_{sh}(C_{L,i}, l_{st,i})|} \cdot 100 \tag{F.10}$$

Once the simulation is finished, the last value of the interpolated function $L_{sh}^{(end)}$ can be used as the most accurate approximation of the real function to calculate the relative error. In those conditions, the relative error in the $i-th$ step can be calculated *backwards* as

$$x^{(i)}(\%) = \frac{||L_{sh}^{(end)} - L_{sh}^{(i)}||_F}{||L_{sh}^{(end)}||_F} \cdot 100 \tag{F.11}$$

where $||\cdot||_F$ is the Frobenius norm applied over all the points of the error grid

$$||f||_F = \overline{\sum_i \sum_j f(i,j)\ ^2} \tag{F.12}$$

While the *true error* shows accurately how the method performs at a particular point of interest, the *backwards* relative error gives a better idea of how the method performs over the domain.

# G

# Some results of kriging characterization

This appendix compiles the results of the characterization of some useful stubs. These stubs are characterized at 14GHz as an example frequency of Ku band. They are also characterized at 2GHz because it was the frequency chosen to build the demonstrators at. The length and dimensions of the stubs is chosen so their behavior is inductive but also so their dimensions are suitable for the intended shielded CRLH line and their equivalent shunt inductance $L_{sh}$ fulfill the CRLH requirements for this thesis.

## 1 Ku-band Loaded Stub

| Parameter | Value | Parameter | Value |
|---|---|---|---|
| $C$ | $280\mu m$ | $W$ | $240\mu m$ |
| $C_s$ | $80\mu m$ | $W_s$ | $40\mu m$ |
| $C_{L,min}$ | $1pF$ | $C_{L,max}$ | $15pF$ |
| $l_{st,min}$ | $0.5mm$ | $l_{st,max}$ | $2mm$ |

| Parameter | Value | Parameter | Value |
|---|---|---|---|
| $h_s$ | $508\mu m$ | $\epsilon_r$ | 6.15 |
| $f_0$ | 14GHz | | |

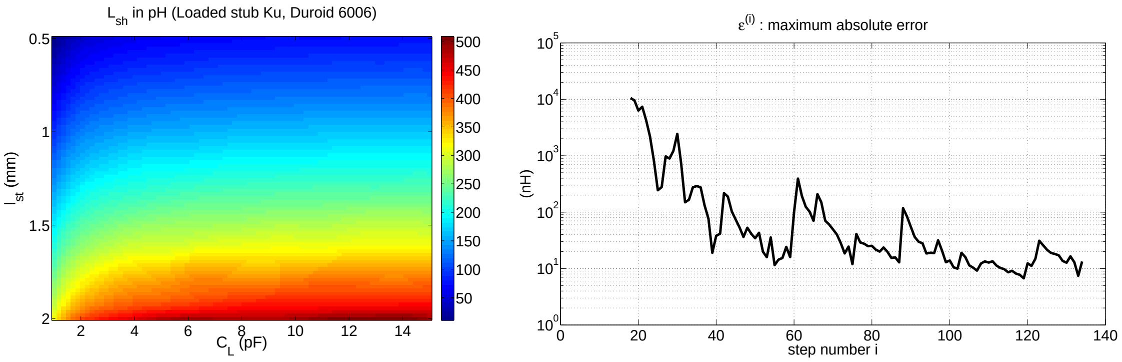

a

b

**Fig. G.1:** Ku band loaded stub with substrate Rogers Duroid RT 6006 $\epsilon_r = 6.15, h_s = 0.508mm$ a)$L_{sh}$ b) $^{(i)}_{k}$

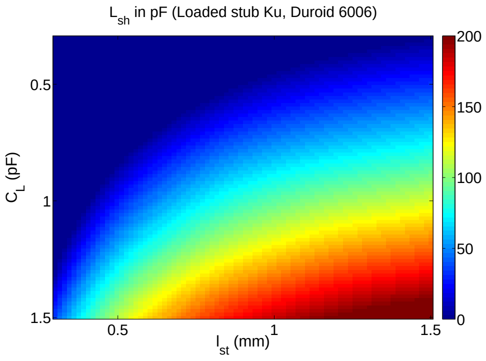

**Fig. G.2:** Ku band loaded stub with substrate Rogers Duroid RT 6006 $\epsilon_r = 6.15, h_s = 0.508mm$ a)$L_{sh}$ b) $^{(i)}_{k}$

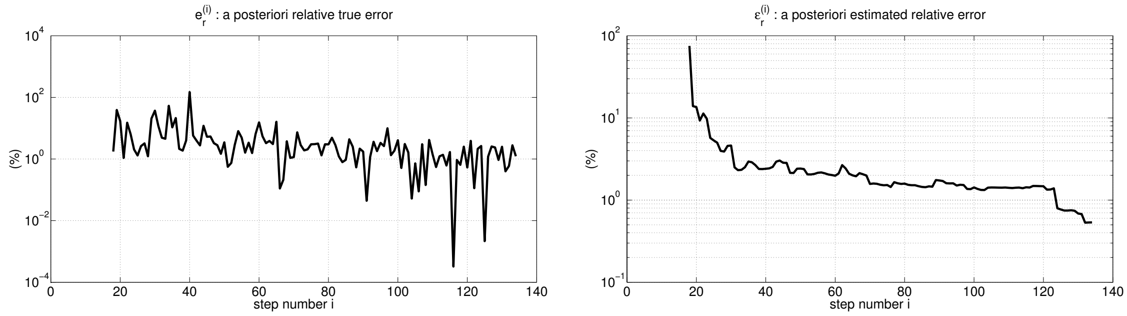

a b

**Fig. G.3:** Ku band loaded stub with substrate Rogers Duroid RT 6006 $\epsilon_r = 6.15, h_s = 0.508mm$ a) $_r$ b) $_{r,bw}$

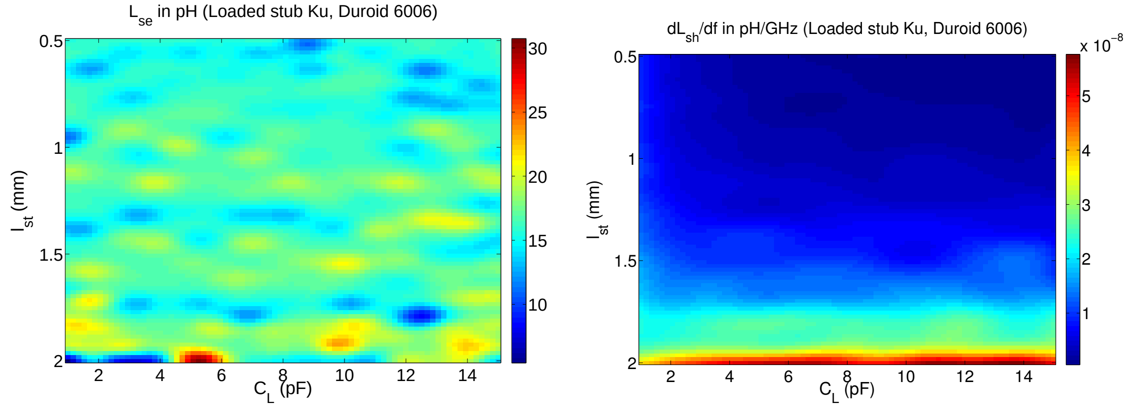

a b

**Fig. G.4:** Ku band loaded stub with substrate Rogers Duroid RT 6006.$L_{se}$ and $\frac{dL_{sh}}{df}$. $\epsilon_r = 6.15, h_s = 0.508mm$ a)$L_{sh}$ b) $^{(i)}_{k}$ c) $_r$ d) $_{r,bw}$

## 2 Ku-band Shorted Stub

| Parameter | Value | Parameter | Value |
|---|---|---|---|
| $C$ | $2000\mu m$ | $W$ | $1700\mu m$ |
| $S_s$ | $200\mu m$ | | |
| $C_{s,min}$ | $0.8mm$ | $C_{s,max}$ | $1.25mm$ |
| $l_{st,min}$ | $1mm$ | $l_{st,max}$ | $2mm$ |

| Parameter | Value | Parameter | Value |
|---|---|---|---|
| $h_s$ | $1499\mu m$ | $\epsilon_r$ | 10.7 |
| $f_0$ | 14GHz | | |

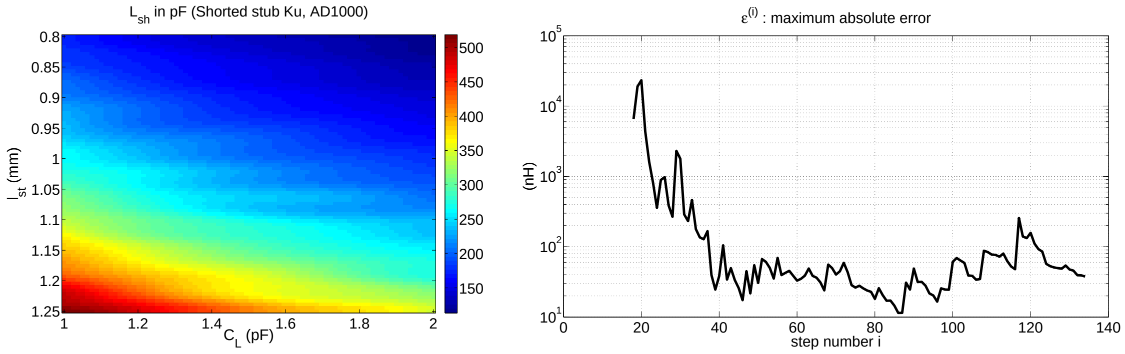

a b

**Fig. G.5:** Ku band shorted stub with substrate AD2000 $\epsilon_r = 10.7, h_s = 1.49mm$a)$L_s h$b)$\epsilon$

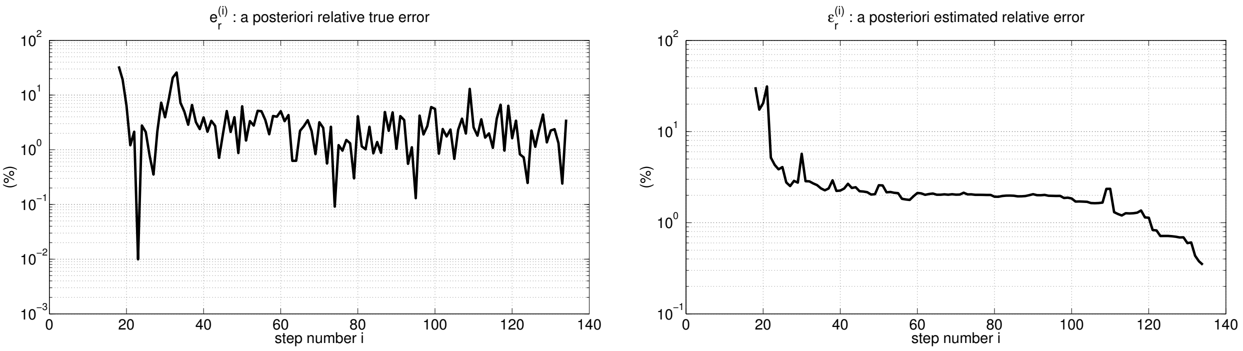

a b

**Fig. G.6:** Ku band shorted stub with substrate AD2000 $\epsilon_r = 10.7, h_s = 1.49mm$a)$e_r$b)$\epsilon_r$

## 3 L-band Loaded Stub

| Parameter | Value | Parameter | Value |
|---|---|---|---|
| $C$ | $280\mu m$ | $W$ | $240\mu m$ |
| $C_s$ | $80\mu m$ | $W_s$ | $40\mu m$ |
| $C_{L,min}$ | $7pF$ | $C_{L,max}$ | $14pF$ |
| $l_{st,min}$ | $4mm$ | $l_{st,max}$ | $7mm$ |

| Parameter | Value | Parameter | Value |
|---|---|---|---|
| $h_s$ | $1499\mu m$ | $\epsilon_r$ | 10.7 |
| $f_0$ | 2GHz | | |

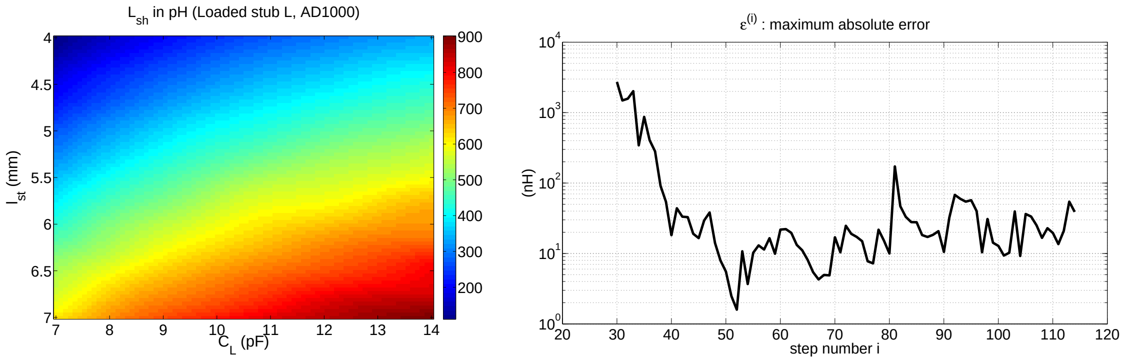

a b

**Fig. G.7:** L band Loaded stub with substrate AD2000 $\epsilon_r = 10.7, h_s = 1.49mm$a)$L_{sh}$b)$\epsilon$

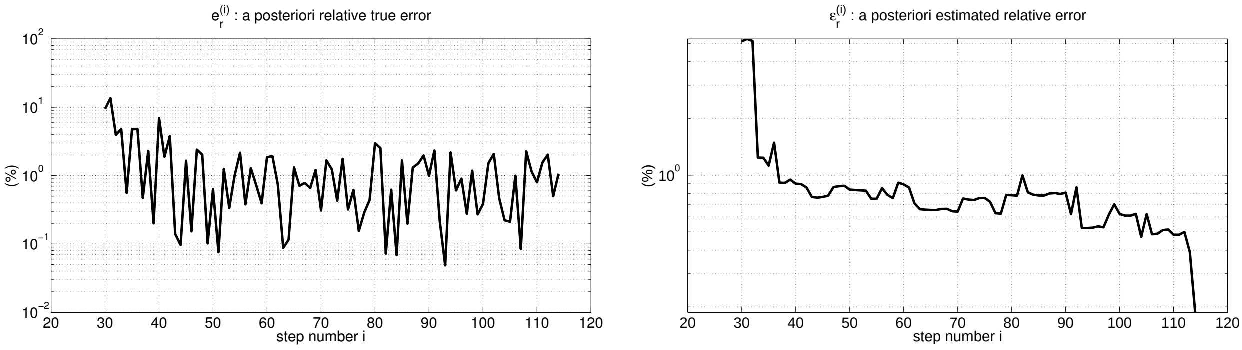

a b

**Fig. G.8:** L band Loaded stub with substrate AD2000 $\epsilon_r = 10.7, h_s = 1.49mm$a)$e_r$b)$\epsilon_r$

# 4 L-band Shorted Stub

| Parameter | Value | Parameter | Value |
|---|---|---|---|
| $C$ | $2000\mu m$ | $W$ | $1700\mu m$ |
| $S_s$ | $200\mu m$ | | |
| $C_{s,min}$ | $0.8mm$ | $C_{s,max}$ | $1.25mm$ |
| $l_{st,min}$ | $1mm$ | $l_{st,max}$ | $2mm$ |

| Parameter | Value | Parameter | Value |
|---|---|---|---|
| $h_s$ | $1499\mu m$ | $\epsilon_r$ | 10.7 |
| $f_0$ | 2GHz | | |

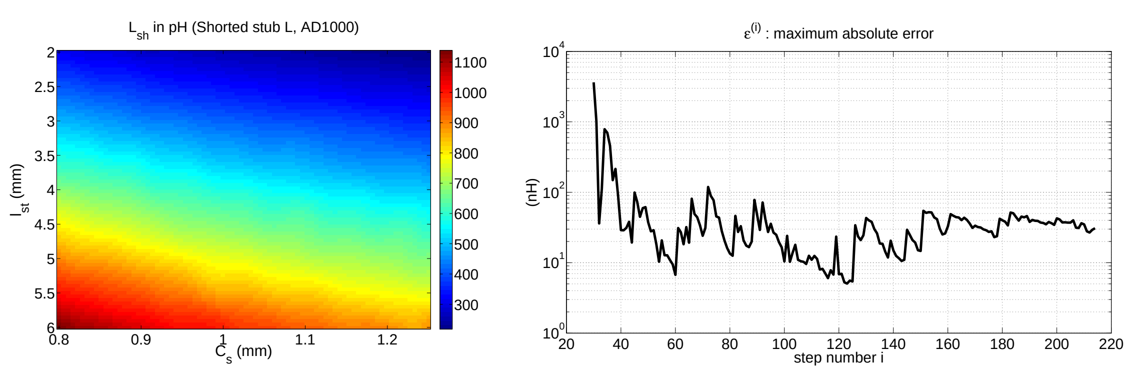

a b

**Fig. G.9:** L band shorted stub with substrate AD2000 $\epsilon_r = 10.7, h_s = 1.49mm$a)$L_{sh}$b)

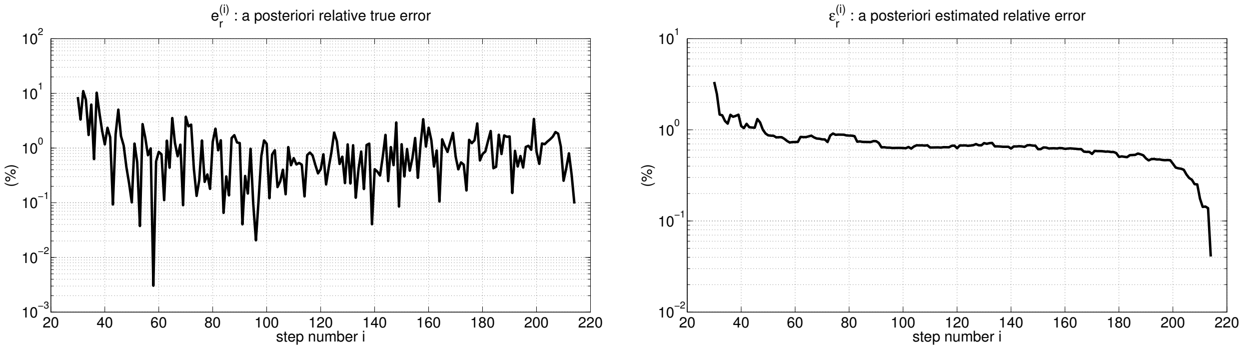

a b

**Fig. G.10:** L band shorted stub with substrate AD2000 $\epsilon_r = 10.7, h_s = 1.49 mm$a) ${}_r$ b) ${}_r$

# Power Coupling in a Lossless 3-port Circuit

H

## 1 Desadaptation in a Lossless 3-port Circuit

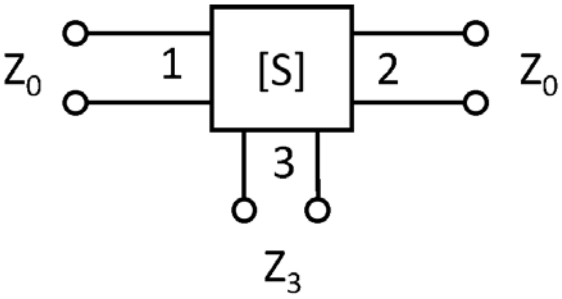

**Fig. H.1:** Simple 3-port network

In the study of three port networks —such as the Wilkinson divider— it is often explained [114] that a 3-port network that is

— lossless :

$$\sum_{k=1}^{3} S_{ki}S_{kj}^{*} = \quad {}_{ij}$$

— passive (reciprocal) : $S_{ij} = S_{ji}$

cannot be matched in all three ports. If the network is reciprocal and its ports are adapted ($S_{ii} = 0$), the scattering matrix is

$$S = \begin{matrix} 0 & S_{12} & S_{13} \\ S_{12} & 0 & S_{23} \\ S_{13} & S_{23} & 0 \end{matrix} \tag{H.1}$$

and, applying the lossless condition to this matrix

$$|S_{12}|^2+|S_{13}|^2=1 \tag{H.2}$$

$$|S_{12}|^2+|S_{23}|^2=1 \tag{H.3}$$

$$|S_{13}|^2+|S_{23}|^2=1 \tag{H.4}$$

$$S_{13}S_{23}^*=0 \tag{H.5}$$

$$S_{23}S_{12}^*=0 \tag{H.6}$$

$$S_{12}S_{13}^*=0 \tag{H.7}$$

it can be seen that these equations are inconsistent since the last three equations force at least 2 of the parameters to be zero, which is not compatible with at least two of the first three equations.

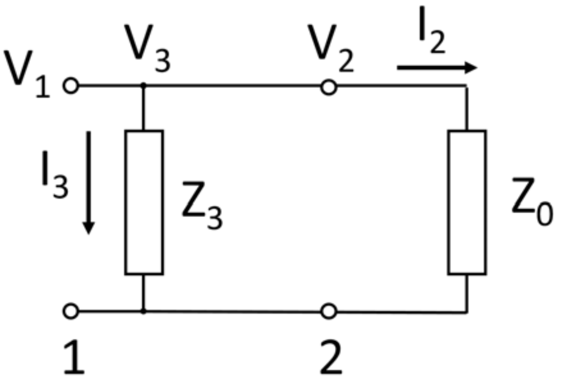

**Fig. H.2:** Simple connection seen as a 3-port with its third port loaded

## 2 Power Transmission in a 3-port Where the Third Port is Loaded

When a 3-port has its third port loaded with a complex impedance it can be seen as a bi-port like the one seen in fig H.2. This charge $Z_3$ can have a real part $R_3$ that represents the radiation of an antenna and an imaginary part $X_3$ that represents the connection circuitry. Under those conditions, the power delivered to port 3 is

$$P_3=\frac{1}{2}Re\{V_3I_3^*\}==\frac{|V_1|^2}{2}Re\{\frac{1}{Z_3^*}\} \tag{H.8}$$

whereas the power delivered to port 2 is

$$P_2=\frac{1}{2}Re\{V_2I_2^*\}==\frac{|V_1|^2}{2Z_0}\} \tag{H.9}$$

where it has been considered that $Z_0$ has only real part. The power ratio between ports 3 and 2 can be computed as

$$\frac{P_3}{P_2}=Z_0Re\{\frac{1}{R_3-jX_3}\}=\frac{r_3}{r_3^2+x_3^2} \tag{H.10}$$

with $r_3 = R_3/Z_0$ and $x_3 = X_3/Z_0$. This means that the power delivered to the port 3 can be controlled with the reactance $X_3$, as seen in fig H.3.

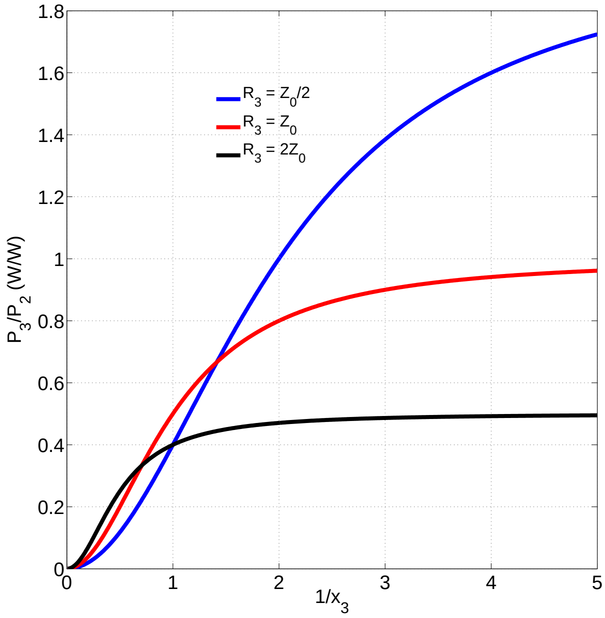

**Fig. H.3:** $P_3/P_2$ power ratio

# I

# Technology Limitations

## 1 Etching Capabilities

One of the difficulties in high frequency printed circuit manufacturing is the etching precision capabilities. While in L band, $\lambda_0/100$ is larger than $1.5mm$, in Ku band it can be as small as $160\mu m$. This reduction of the scale pushes the limits of the circuits a certain technology can manufacture.

In standard procedures, Elvia [135] offers $100\mu m$ of etching precision and down to $70\mu m$ in high quality standards. A sample of specifications of some PCB manufacturers is presented in table I.1.

More advanced procedure also exist, like high precision laser etching is utilized in [136], where slots of a few microns are etched.

## 2 Drilling

In terms of drilling, standard manufacturing procedures can make aspect ratios ($h_s/d_{via}$ of 10:1 approximately. In the technical catalogs sometimes larger ratios are presented but usually a correct metal contact is not ensured. Laser drilling can often create very small diameter holes but the aspect ratio that can be achieved through laser drilling is much smaller than mechanical drilling.

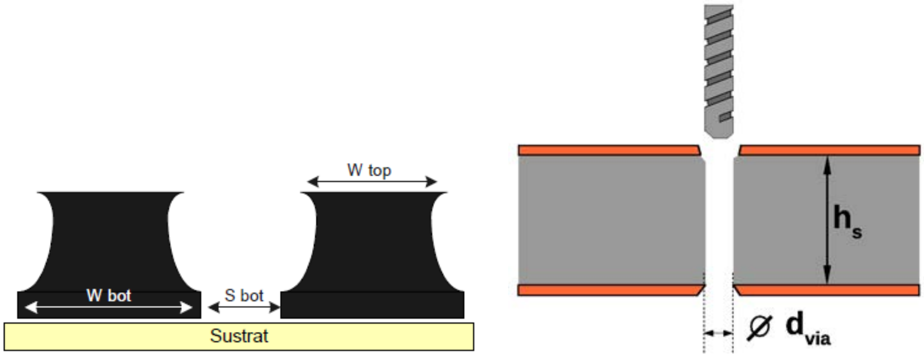

a

b

**Fig. I.1:** a) Etching precision [135] b) Via drilling scheme

| | [135] | [137] | [138] | [139] | [140] |
|---|---|---|---|---|---|
| Drilling | | | | | |
| Via min diameter | $80\mu m$ | $75\mu m$ | $200\mu m$ | $370\mu m$ | $50\mu m$ |
| Via aspect ratio | 8:1 | 12:1 | | | 10:1 |
| Etching | | | | | |
| Width/Separation | $70\mu m$ | $75\mu m$ | $75\mu m$ | $150\mu m$ | $50\mu m$ |

**Table I.1:** Summary of PCB technical capabilities

# Steering Bandwidth

In the CRLH approach to beam steering defined in this thesis, there can be defined a steering bandwidth in addition to the VSWR bandwidth. To better understand it, a minimal system with two satellites can be considered as seen in fig J.1.

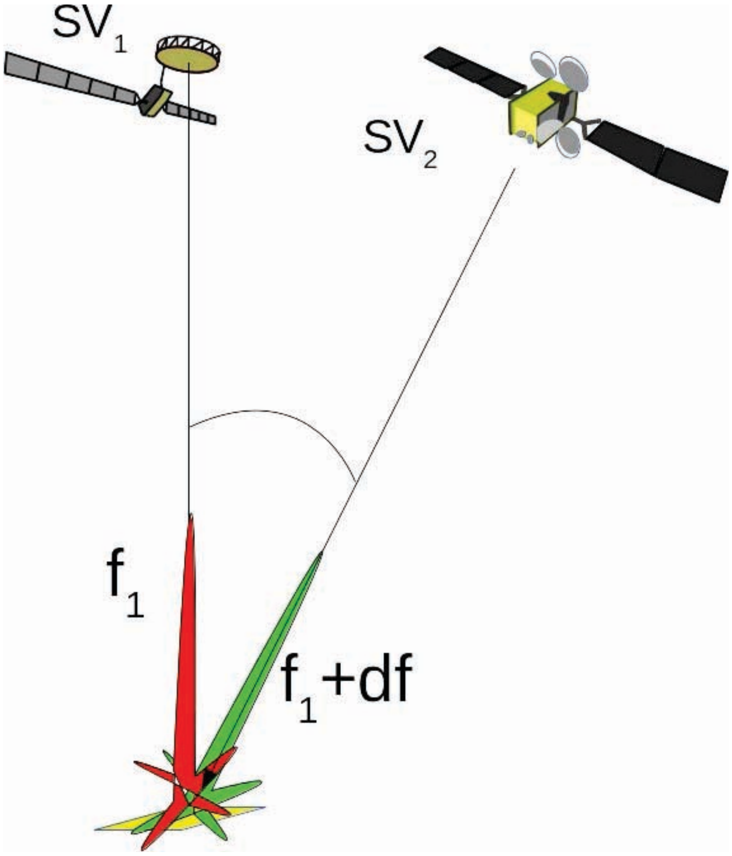

**Fig. J.1:** While the antenna aims at one satellite $SV_1$ at frequency $f_1$, it may receive signal from a neighboring satellite $SV_2$ at frequency $f_1 + df$

Supposing that the line aims at satellite SV1 for the frequency $f_1$, because of the nature of CRLH, the steering angle depends on the frequency. Assuming that for a frequency $f + df$, the antenna points at the satellite SV2, there is a frequency between $f$ and $f + df$ at which the power received from the SV2 is larger than that of SV1. Fig J.2 depicts the power density illuminating the antenna from both satellites and the gain at $f$ and $f + df$.

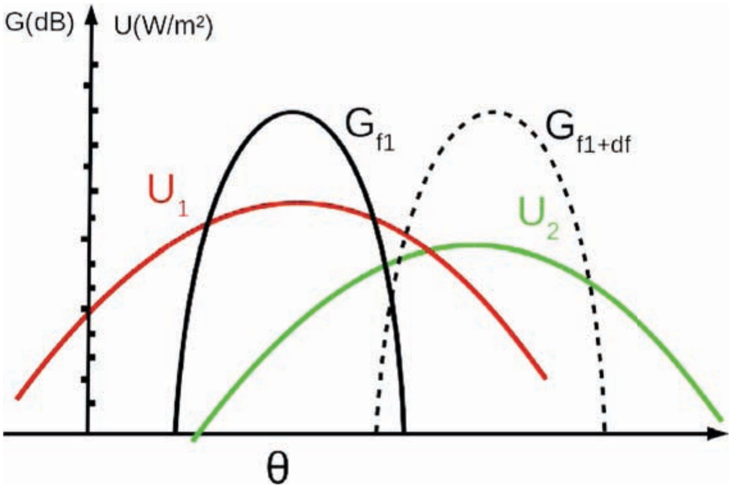

**Fig. J.2:** The ratio of power densities $U$ illuminating the antenna from each satellite depends on the angle of reception

For each frequency, a different amount of total received power at the output of the antenna can be seen in fig J.3. The steering bandwidth could be define as *the size of the region of the spectrum at which the power received by a neighboring satellite is larger than that of the target satellite*. Nevertheless, this definition depends on the position of the satellites relative to the receiver, which is not known *a priori* and is particular of each system. Moreover, it only applies when both the target and interfering satellite transmit at the same channel, with the same polarization. Even in that case, if different modulations are utilized by each satellite, advanced filtering can sort out the target signal and the interfering one.

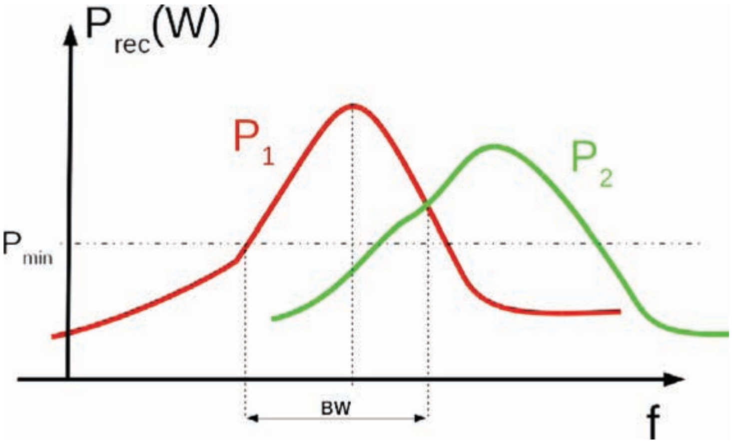

**Fig. J.3:** The combination of power density coming from the satellite and gain determines the power received from each of the satellites at any particular frequency

Another definition of the steering bandwidth can be established by assuming that no neighboring satellite is present. In this case, a minimal gain in a particular direction can be defined as the limit of the bandwidth. As the antenna points away from the satellite, the gain in the direction of the satellite relative to the maximum decreases, but the antenna is still able to receive signal from that direction. A $-3dB$ limit is a common value to choose and can be used as well here to define the steering angle bandwidth.

It is worth noting that the steering bandwidth depends on the steering angle. Firstly, the value of the maximum gain depends on the steering angle. As the antenna steers the beam, the $-3dB$ value also varies. Additionally, the frequency derivative of the phase shift in the CRLH line also depends on the steering angle, thus making it complex to readily determine the steering bandwidth of a given antenna.

# Part V

# References

# References

[1] News : Space bus neo. `http://www.esa.int/Our_Activities/Telecommunications_Integrated_Applications/Next_Generation_Platform_Neosat`.

[2] Kymeta beam steerable antenna. `https://www.kymetacorp.com/`.

[3] Jast beam steerable antenna. `https://artes.esa.int/projects/planar-array-active-antennas-mobile-terminals`.

[4] Gazprom website. `http://www.gazprom-spacesystems.ru/en/infrastructure/`.

[5] Intelsat website. `www.intelsat.com/global-network/satellites/fleet/`.

[6] S.e.s. website. `http://www.ses.com`.

[7] Embratel: Star one website. `http://www.starone.com.br/en/`.

[8] Ligado satellite communications. `http://ligado.com/our-network/satellite/`.

[9] J. I. Herranz-Herruzo, M. Ferrando-Rocher, A. Valero-Nogueira, R. Lenormand, A. Hirsch, J. L. Almeida, M. Arnaud, and L. Barthe. Locomo satcom terminal: A switchable rhcp/lhcp array antenna for on-the-move applications in ka-band. In *2015 IEEE International Symposium on Antennas and Propagation USNC/URSI National Radio Science Meeting*, pages 210–211, July 2015.

[10] M. Ettorre, F. F. Manzillo, M. Casaletti, R. Sauleau, L. Le Coq, and N. Capet. Continuous transverse stub array for ka-band applications. *IEEE Transactions on Antennas and Propagation*, 63(11):4792–4800, Nov 2015.

[11] M. Ettorre, R. Sauleau, and L. Le Coq. Multi-beam multi-layer leaky-wave siw pillbox antenna for millimeter-wave applications. *IEEE Transactions on Antennas and Propagation*, 59(4):1093–1100, April 2011.

[12] Viasat aero mobile terminal 5230. `https://www.viasat.com/sites/default/files/media/documents/aero_mobile_terminal_5230_datasheet_010_web.pdf`.

[13] Viasat aero mobile terminal 5320. `https://www.viasat.com/sites/default/files/media/documents/global_aero_terminal_5320_datasheet_011_web_0.pdf`.

[14] F Tiezzi. Overview of automotive antennas for satellite mobile communications. In *ARTIC WorkShop*, Apr 2010.

[15] Airbus a320 sky service. `http://aviationweek.com/awin/boulliounaviationdeliversnewairbusa320skyservice02200SB`.

[16] Cma2200sb array antenna datasheet. `https://www.esterline.com/Portals/17/Documents/enus/CMA2200SB_SpecSheet.pdf`.

[17] M. C. Vigano; G. Toso; G. Caille; C. Mangenot; I. E. Lager. Sunflower array antenna with adjustable density taper. *International Journal of Antennas and Propagation*, 2009.

[18] G. Toso ; P. Angeletti. Workshop on multibeam antennas and beamforming networks. In *EuCAP*, Apr 2014.

[19] G. Toso; C. Mangenot; A.G. Roeder. Sparse and thinned arrays for multiple beam satellite applications. In *29th ESA Antenna Workshop on Multiple Beams and Reconfigurable Antennas*, Apr 2007.

[20] C. Mangenot; G. Toso; C. Tienda Herrero. Array antenna having a radiation pattern with a contolled envelope, and method of manufacturing it. In *International Patent Application No PCT/IB2011/051583*.

[21] T. Tamir and A. A. Oliner. Guided complex waves. part 2: Relation to radiation patterns. *Electrical Engineers, Proceedings of the Institution of*, 110(2):325–334, February 1963.

[22] T. Tamir and A. A. Oliner. Guided complex waves. part 1: Fields at an interface. *Electrical Engineers, Proceedings of the Institution of*, 110(2):310–324, February 1963.

[23] Mauro Ettorre. *Analysis and design of efficient planar leaky-wave antennas*. PhD thesis, Universita degli Studi di Siena, 2008.

[24] Richard C Johnson. *Antenna Engineering Handbook*. McGrawHill, 3rd edition, •.

[25] G. V. Trentini. Partially reflecting sheet arrays. *IRE Transactions on Antennas and Propagation*, 4(4):666–671, October 1956.

[26] A. Ourir, S. N. Burokur, and A. de Lustrac. Electronic beam steering of an active metamaterial-based directive subwavelength cavity. In *Antennas and Propagation, 2007. EuCAP 2007. The Second European Conference on*, pages 1–4, Nov 2007.

[27] D. Sievenpiper, Lijun Zhang, R. F. J. Broas, N. G. Alexopolous, and E. Yablonovitch. High-impedance electromagnetic surfaces with a forbidden frequency band. *IEEE Transactions on Microwave Theory and Techniques*, 47(11):2059–2074, Nov 1999.

[28] R. Guzman-Quiros, J. L. Gomez-Tornero, A. R. Weily, and Y. J. Guo. Electronically steerable 1-d fabry-perot leaky-wave antenna employing a tunable high impedance surface. *IEEE Transactions on Antennas and Propagation*, 60(11):5046–5055, Nov 2012.

[29] Y. J. Guo and J. L. Gomez-Tornero. Reconfigurable fabry-perot leaky-wave antennas. In *Antenna Technology (iWAT), 2013 International Workshop on*, pages 390–393, March 2013.

[30] R. Guzman-Quiros, J. L. Gomez-Tornero, M. Garcia-Vigueras, A. R. Weily, and Y. J. Guo. Advances in electronically reconfigurable lwas in fabry-perot and siw technologies. In *Antennas and Propagation (EuCAP), 2013 7th European Conference on*, pages 2001–2005, April 2013.

[31] Christophe Caloz and Tatsuo Itoh. *Electromagnetic Metamaterials:Transmission Line Theory and Microwave Applications*. Wiley-IEEE Press, 2006.

[32] C. Caloz and T. Itoh. Transmission line approach of left-handed (lh) materials and microstrip implementation of an artificial lh transmission line. *IEEE Transactions on Antennas and Propagation*, 52(5):1159–1166, May 2004.

[33] Sungjoon Lim, C. Caloz, and T. Itoh. Metamaterial-based electronically controlled transmission-line structure as a novel leaky-wave antenna with tunable radiation angle and beamwidth. *IEEE Transactions on Microwave Theory and Techniques*, 53(1):161–173, Jan 2005.

[34] Romain Siragusa. *Étude de nouvelles fonctions radiofréquences à base d'antennes à onde de fuite composite main droite/gauche*. PhD thesis, LCIS Grenoble, 2009.

[35] R. E. Horn, H. Jacobs, E. Freibergs, and K. L. Klohn. Electronic modulated beam-steerable silicon waveguide array antenna. *IEEE Transactions on Microwave Theory and Techniques*, 28(6):647–653, Jun 1980.

[36] Limin Huang, Jung-Chih Chiao, and M. P. De Lisio. An electronically switchable leaky wave antenna. *IEEE Transactions on Antennas and Propagation*, 48(11):1769–1772, Nov 2000.

[37] Sungjoon Lim, C. Caloz, and T. Itoh. Electronically scanned composite right/left handed microstrip leaky-wave antenna. *IEEE Microwave and Wireless Components Letters*, 14(6):277–279, June 2004.

[38] Sungjoon Lim, C. Caloz, and T. Itoh. Electronically-controlled metamaterial-based transmission line as a continuous-scanning leaky-wave antenna. In *Microwave Symposium Digest, 2004 IEEE MTT-S International*, volume 1, pages 313–316 Vol.1, June 2004.

[39] N. Wiwatcharagoses and P. Chahal. A novel reconfigurable metamaterial unit cell based composite right/left handed microstrip design. In *Antennas and Propagation (APSURSI), 2011 IEEE International Symposium on*, pages 2954–2957, July 2011.

[40] K. J. Nicholson, W. S. T. Rowe, P. J. Callus, and K. Ghorbani. Electronically tunable composite right/left handed transmission line for the slotted waveguide antenna stiffened structure. In *Advanced Electromagnetic Materials in Microwaves and Optics (METAMATERIALS), 2013 7th International Congress on*, pages 109–111, Sept 2013.

[41] K. J. Nicholson, J. Clough, and K. Ghorbani. Electronically tunable coaxial right / left handed transmission line for carbon fibre reinforced polymer waveguides. In *Microwave Conference (EuMC), 2015 European*, pages 1104–1107, Sept 2015.

[42] H. Lee and T. Itoh. Evolution of circularly polarized composite right/left-handed leaky-wave antenna. In *2014 Asia-Pacific Microwave Conference*, pages 134–136, Nov 2014.

[43] F. A. Ghaffar and A. Shamim. A partially magnetized ferrite ltcc-based siw phase shifter for phased array applications. *IEEE Transactions on Magnetics*, 51(6):1–8, June 2015.

[44] M. F. Iskander, W. Kim, J. Bell, N. Celik, Z. Yun, and H. s. Youn. Antenna arrays technologies for advanced wireless systems. In *Microwaves, Communications, Antennas and Electronics Systems, 2009. COMCAS 2009. IEEE International Conference on*, pages 1–4, Nov 2009.

[45] J. Zafar, A. A. P. Gibson, and H. Zafar. High power ferrite phase shifter for beam steering applications. In *2009 3rd European Conference on Antennas and Propagation*, pages 3029–3033, March 2009.

[46] N. Das and A. K. Ray. Magneto optical technique for beam steering by ferrite based patch arrays. *IEEE Transactions on Antennas and Propagation*, 49(8):1239–1241, Aug 2001.

[47] M. F. Iskander, W. Kim, J. Bell, N. Celik, Z. Yun, and H. s. Youn. Antenna arrays technologies for advanced wireless systems. In *Microwaves, Communications, Antennas and Electronics Systems, 2009. COMCAS 2009. IEEE International Conference on*, pages 1–4, Nov 2009.

[48] H. Mosallaei and K. Sarabandi. Magneto-dielectrics in electromagnetics: concept and applications. *IEEE Transactions on Antennas and Propagation*, 52(6):1558–1567, June 2004.

[49] T. Kodera and C. Caloz. Uniform ferrite-loaded open waveguide structure with crlh response and its application to a novel backfire-to-endfire leaky-wave antenna. *IEEE Transactions on Microwave Theory and Techniques*, 57(4):784–795, April 2009.

[50] A. Kallel, J. Sokoloff, and T. Callegari. Theory and simulations of a beam-scanning plasma antenna. In *Antennas and Propagation (EuCAP), 2013 7th European Conference on*, pages 3457–3461, April 2013.

[51] John W. Goodby et al., editor. *Handbook of Liquid Crystals*, volume 2. Wiley, 2nd edition, Feb 2014.

[52] C. Weickhmann, M. Jost, D. Laemmle, and R. Jakoby. Design and fabrication considerations for a 250 ghz liquid crystal phase shifter. In *2014 39th International Conference on Infrared, Millimeter, and Terahertz waves (IRMMW-THz)*, pages 1–2, Sept 2014.

[53] A. Gaebler et al. Liquid crystal reconfigurable antenna concepts for space applications at microwave and millimeter waves. *Hindawi Publishing Corporation: International Journal of Antennas and Propagation*, 2009.

[54] H. V. Nguyen, S. Abielmona, A. Rennings, and C. Caloz. Pencil-beam full-space scanning 2d crlh leaky-wave antenna array. In *2007 International Symposium on Signals, Systems and Electronics*, pages 139–142, July 2007.

[55] C. Caloz and T. Itoh. Array factor approach of leaky-wave antennas and application to 1-d/2-d composite right/left-handed (crlh) structures. *IEEE Microwave and Wireless Components Letters*, 14(6):274–276, June 2004.

[56] T. Le Nadan, J. P. Coupez, and C. Person. Optimization and miniaturization of a filter/antenna multi-function module using a composite ceramic-foam substrate. In *Microwave Symposium Digest, 1999 IEEE MTT-S International*, volume 1, pages 219–222 vol.1, June 1999.

[57] Jui-Chieh Chiu, Jih-Ming Lin, Mau-Phon Houng, and Yeong-Her Wang. A pcb-compatible 3-db coupler using microstrip-to-cpw via-hole transitions. *IEEE Microwave and Wireless Components Letters*, 16(6):369–371, June 2006.

[58] Ricardo Marques; Ferran Martin; Mario Sorolla. *Metamaterials with Negative Parameters: Theory, Design and Microwave Applications*. Wiley, 2008.

[59] Jing Gao. *Fullwave modeling of coplanar-waveguide discontinuities for filter design and metamaterial characterization*. PhD thesis, National Institute of Information and Communications Technology (NiCT), Japan, 2006.

[60] Jing Gao and Lei Zhu. Guided-wave characteristics of cpw transmission line metamaterials: effective per-unit-length parameters. In *IWAT 2005. IEEE International Workshop on Antenna Technology: Small Antennas and Novel Metamaterials, 2005.*, pages 175–178, March 2005.

[61] N. Amani, M. Kamyab, and A. Jafargholi. Compact, dualband t-junction zeroth-order resonant antenna with extended bandwidth. In *2013 21st Iranian Conference on Electrical Engineering (ICEE)*, pages 1–4, May 2013.

[62] S. Simion, G. Sajin, R. Marcelli, and F. Craciunoiu. Cpw antenna fabricated on silicon substrate, based on transmission line metamaterial approach. In *Electromagnetics in Advanced Applications, 2007. ICEAA 2007. International Conference on*, pages 488–491, Sept 2007.

[63] A. C. Bunea, F. Craciunoiu, M. Zamfirescu, R. Dabu, and G. Sajin. Laser ablated millimeter wave metamaterial antenna. In *CAS 2011 Proceedings (2011 International Semiconductor Conference)*, volume 1, pages 185–188, Oct 2011.

[64] T. Jang, J. Choi, and S. Lim. Compact coplanar waveguide (cpw)-fed zeroth-order resonant antennas with extended bandwidth and high efficiency on vialess single layer. *IEEE Transactions on Antennas and Propagation*, 59(2):363–372, Feb 2011.

[65] M. A. Antoniades and G. V. Eleftheriades. Compact linear lead/lag metamaterial phase shifters for broadband applications. *IEEE Antennas and Wireless Propagation Letters*, 2(1):103–106, 2003.

[66] A. L. Borja, J. Carbonell, V. E. Boria, A. Belenguer, and D. Lippens. A compact coplanar waveguide metamaterial-inspired line and its use in tunable narrow bandpass filters. In *Microwave Conference (EuMC), 2010 European*, pages 922–925, Sept 2010.

[67] A. Velez, F. Aznar, M. Duran-Sindreu, J. Bonache, and F. Martin. Stop-band and band-pass filters in coplanar waveguide technology implemented by means of electrically small metamaterial-inspired open resonators. *IET Microwaves, Antennas Propagation*, 4(6):712–716, June 2010.

[68] A. L. Borja, J. Carbonell, J. Cascon, V. E. Boria, and D. Lippens. Ultra-narrow bandwidth filters based on highly dispersive metamaterial basic cells. In *Proceedings of the Fourth European Conference on Antennas and Propagation*, pages 1–5, April 2010.

[69] A. L. Borja, J. Carbonell, V. E. Boria, J. Cascon, and D. Lippens. Synthesis of compact and highly selective filters via metamaterial-inspired coplanar waveguide line technologies. *IET Microwaves, Antennas Propagation*, 4(8):1098–1104, Aug 2010.

[70] A. L. Borja, A. Belenguer, J. Cascon, H. Esteban, and V. E. Boria. Wideband passband transmission line based on metamaterial-inspired cpw balanced cells. *IEEE Antennas and Wireless Propagation Letters*, 10:1421–1424, 2011.

[71] M. Li, L. Guo, B. Xiao, and H. Yang. Band-pass filter using dual magnetic resonances. In *Antennas, Propagation EM Theory (ISAPE), 2012 10th International Symposium on*, pages 1086–1089, Oct 2012.

[72] Robert E. Collin. *Foundations for Microwave Engineering*. Wiley-IEEE Press, 2001.

[73] M. Houdart. Coplanar lines : Application to broadband microwave integrated circuits. In *Microwave Conference, 1976. 6th European*, pages 49–53, Sept 1976.

[74] R. N. Simons and G. E. Ponchak. Modeling of some coplanar waveguide discontinuities. In *Microwave Symposium Digest, 1988., IEEE MTT-S International*, pages 297–300 vol.1, May 1988.

[75] M. Naghed and I. Wolff. Equivalent capacitances of coplanar waveguide discontinuities and interdigitated capacitors using a three-dimensional finite difference method. *IEEE Transactions on Microwave Theory and Techniques*, 38(12):1808–1815, Dec 1990.

[76] N. Dib R. Simons and L. Katehi. Modeling of coplanar stripline discontinuities,. *IEEE Trans. on Microwave Theory and Techniques*, 44(5):711–716, May 1996.

[77] C. W. Kuo, T. Kitazawa, and T. Itoh. Analysis of shielded coplanar waveguide step discontinuity considering the finite metallization thickness effect. In *Microwave Symposium Digest, 1991., IEEE MTT-S International*, pages 473–475 vol.2, July 1991.

[78] A. M. Tran and T. Itoh. Full-wave modeling of coplanar waveguide discontinuities with finite conductor thickness. *IEEE Transactions on Microwave Theory and Techniques*, 41(9):1611–1615, Sep 1993.

[79] A. M. Tran and T. Itoh. Full wave analysis of short-circuit discontinuities in open coplanar waveguide with finite conductor thickness. In *Antennas and Propagation Society International Symposium, 1992. AP-S. 1992 Digest. Held in Conjuction with: URSI Radio Science Meeting and Nuclear EMP Meeting., IEEE*, pages 1492–1495 vol.3, June 1992.

[80] Fang-Lih Lin and Ruey-Beei Wu. Analysis of coplanar-waveguide discontinuities with finite-metallization thickness and nonrectangular edge profile. *IEEE Transactions on Microwave Theory and Techniques*, 45(12):2131–2138, Dec 1997.

[81] C. Sinclair and S. J. Nightingale. An equivalent circuit model for the coplanar waveguide step discontinuity. In *Microwave Symposium Digest, 1992., IEEE MTT-S International*, pages 1461–1464 vol.3, June 1992.

[82] K. M. Rahman and C. Nguyen. Analysis of cascaded asymmetric coplanar waveguide step discontinuities. In *Antennas and Propagation Society International Symposium, 1997. IEEE., 1997 Digest*, volume 4, pages 2522–2525 vol.4, July 1997.

[83] C. Nguyen and K. M. Rahman. Analysis of coplanar waveguide multiple-step discontinuities. In *Antennas and Propagation Society International Symposium, 1993. AP-S. Digest*, pages 185–188 vol.1, June 1993.

[84] R. Schmidt and P. Russer. Modeling of cascaded coplanar waveguide discontinuities by the mode-matching approach. *IEEE Transactions on Microwave Theory and Techniques*, 43(12):2910–2917, Dec 1995.

[85] A. Wexler. Solution of waveguide discontinuities by modal analysis. *IEEE Transactions on Microwave Theory and Techniques*, 15(9):508–517, September 1967.

[86] W. J. Getsinger. Circuit duals on planar transmission media. In *Microwave Symposium Digest, 1983 IEEE MTT-S International*, pages 154–156, May 1983.

[87] Y. J. Lu and P. Hsu. Metamaterial-inspired circularly polarized slot dipole antenna fed by coplanar waveguide. In *Proceedings of the 2012 IEEE International Symposium on Antennas and Propagation*, pages 1–2, July 2012.

[88] B. Linot, M. F. Wong, O. Picon, V. F. Hanna, and M. Drissi. A rigorous dispersive characterization of radiating coplanar waveguide discontinuities and junctions. In *Microwave Conference, 1994. 24th European*, volume 2, pages 1918–1923, Sept 1994.

[89] Jiang Hu and Lingling Sun. Ec-ann modeling approach for cpw discontinuities. In *Neural Network Applications in Electrical Engineering, 2004. NEUREL 2004. 2004 7th Seminar on*, pages 193–197, Sept 2004.

[90] N. Dib. Comprehensive study of cad models of several coplanar waveguide (cpw) discontinuities. *IEE Proceedings - Microwaves, Antennas and Propagation*, 152(2):69–76, Apr 2005.

[91] R. Bromme and R. H. Jansen. Systematic investigation of coplanar waveguide mic/mmic structures using a unified strip/slot 3d electromagnetic simulator. In *Microwave Symposium Digest, 1991., IEEE MTT-S International*, pages 1081–1084 vol.3, July 1991.

[92] D. Tomic. *Coplanar waveguide discontinuity models and polymer photobleaching characterization*. PhD thesis, University of Colorado at Boulder, 1999.

[93] R. Ming Yu Ke Wu Vahldieck. Analysis of planar circuit discontinuities using the quasi-static space-spectral domain approach. *Microwave Symposium Digest, 1992., IEEE MTTS International*, 2(15):845,848, June 1992.

[94] Lei Zhu and Ke Wu. Unified cad-oriented circuit model of finite-ground coplanar waveguide gap structure for uniplanar m(h)mics. In *Microwave Symposium Digest, 1999 IEEE MTT-S International*, volume 1, pages 39–42 vol.1, June 1999.

[95] Gevorgian S.; Deleniv A.; Martinsson T.; Galchenko S.; Linner P.; Vendik I. Cad model of a gap in a coplanar waveguide. *Int. J. Microw. Mill.Wave Comput. Aided Eng.*, 1996.

[96] B. C. Wadell. *Transmission Line Design Handbook*. Artech House Microwave Library, 1991.

[97] Lei Zhu and Ke Wu. Unified cad-oriented circuit model of finite-ground coplanar waveguide gap structure for uniplanar m(h)mics. In *Microwave Symposium Digest, 1999 IEEE MTT-S International*, volume 1, pages 39–42 vol.1, June 1999.

[98] S M Sze. *Semiconductor Devices Physics and Technology*. John Wiley & Sons, 1985.

[99] J Millman. *Microelectronics*. McGraw-Hill, 1979.

[100] Benedikt A. Munk. *Metamaterials: Critique and Alternatives*. Wiley, 2009.

[101] Anan Fang, Thomas Koschny, and Costas M. Soukoulis. Optical anisotropic metamaterials: Negative refraction and focusing. *Phys. Rev. B*, 79:245127, Jun 2009.

[102] F. Bilotti, S. Tricarico, and L. Vegni. Plasmonic metamaterial cloaking at optical frequencies. *IEEE Transactions on Nanotechnology*, 9(1):55–61, Jan 2010.

[103] A. Lai, T. Itoh, and C. Caloz. Composite right/left-handed transmission line metamaterials. *IEEE Microwave Magazine*, 5(3):34–50, Sept 2004.

[104] M. Duran-Sindreu, P. Vzlez, J. Bonache, and F. Martin. Broadband microwave filters based on metamaterial concepts. In *ICECom, 2010 Conference Proceedings*, pages 1–4, Sept 2010.

[105] G. Minatti, S. Maci, A. Freni, P. De Vita, and M. Sabbadini. Circularly polarized metasurface antennas. In *Proceedings of the 2012 IEEE International Symposium on Antennas and Propagation*, pages 1–2, July 2012.

[106] D. R. Smith; Willie J. Padilla; D. C. Vier; S. C. Nemat-Nasser and S. Schultz. Composite medium with simultaneously negative permeability and permittivity. *Phys. Rev. Lett.*, 84(1), May 2000.

[107] C. Caloz. Novel space, time and space-time processing materials and devices for rf-thz applications. In *Advanced Materials and Processes for RF and THz Applications (IMWS-AMP), 2015 IEEE MTT-S International Microwave Workshop Series on*, pages 1–3, July 2015.

[108] Viktor G. Veselago. The electrodynamics of substances with simultaneously negative values of and $\mu$. *Sov. Phys. Usp*, 10(4):509–514, 1968.

[109] M. Navarro-Tapia, C. Camacho-Peñalosa, and J. Esteban. Beam-scanning performance of a slot array antenna on a composite right/left-handed waveguide. In *Microwave Conference (EuMC), 2011 41st European*, pages 575–578, Oct 2011.

[110] R. M. Foster. A reactance theorem. *The Bell System Technical Journal*, 3(2):259–267, April 1924.

[111] A. Papoulis. Foster's reactance theorem. *Transactions of the IRE Professional Group on Circuit Theory*, PGCT-2:106–106, December 1953.

[112] A. Mehdipour and G. V. Eleftheriades. Leaky-wave antennas using negative-refractive-index transmission-line metamaterial supercells. *IEEE Transactions on Antennas and Propagation*, 62(8):3929–3942, Aug 2014.

[113] Nihad I. Dib;Linda Katehi. *Theoretical Characterization of Coplanar Waveguide Transmission Lines and Discontinuities.* PhD thesis, University of Michigan, Oct 1992.

[114] David M Pozar. *Microwave engineering; 3rd ed.* Wiley, Hoboken, NJ, 2005.

[115] George L. Matthaei. Techniques for obtaining equivalent circuits for discontinuites in planar microwave circuits. IEEE MTTS Workshop (WSC), 2000.

[116] J. Duran, C. Martel, G. Prigent, and O. Pascal. Efficient characterization of a cpw series capacitor in ku band. In *2015 9th European Conference on Antennas and Propagation (EuCAP)*, pages 1–4, May 2015.

[117] J. Duran, C. Martel, G. Prigent, and O. Pascal. Caractérisation efficace d'une capacité série en ligne coplanaire. In *XIX Journées Nationales des Microondes, Bordeaux*, 2015.

[118] N. I. Dib, G. E. Ponchak, and L. P. B. Katehi. A theoretical and experimental study of coplanar waveguide shunt stubs. *IEEE Transactions on Microwave Theory and Techniques*, 41(1):38–44, Jan 1993.

[119] Rainee N Simons. *Coplanar Waveguide Circuits, Components and Systems*. John Wiley & Sons, Inc, 2001.

[120] A. Grbic and G. V. Eleftheriades. Experimental verification ofbackward-wave radiation from a negative refractive index metamaterial. *J. Appl. Phys.*, 92:5930–5935, 2002.

[121] J. Duran, C. Martel, G. Prigent, and O. Pascal. Radiation characteristics of a coplanar waveguide series gap in ku band. In *IEEE International Symposium on Antennas and Propagation AP-S/USNC-URSI National Radio Science meeting*, Jul 2016.

[122] Joong-Ho Lee and Hai-Young Lee. Novel quadrature branch-line coupler using cpw-to-microstrip transitions. In *Microwave Symposium Digest. 2000 IEEE MTT-S International*, volume 2, pages 621–624 vol.2, June 2000.

[123] F. Mernyei and H. Matsuura. A new broadside-offset coupler using cpw and microstrip lines. In *Microwave Conference, 1993. 23rd European*, pages 617–620, Sept 1993.

[124] J. T. Kuo, Y. C. Chiou, and J. S. Wu. Miniaturized rat race coupler with microstrip-to-cpw broadside-coupled structure and stepped-impedance sections. In *2007 IEEE/MTT-S International Microwave Symposium*, pages 169–172, June 2007.

[125] H W Ott. *Electromagnetic Compatibility Engineering*. Wiley, 2009.

[126] Constantine A Balanis. *Antenna Theory*. Wiley, 2016.

[127] Constantine A Balanis. *Antenna Theory*. Wiley, 2016. chapter 6: "Arrays: Linear, Planar and Circular".

[128] J Long D Sievenpipper, M M Jacob. Materials and components with a negative frequency derivative of reactance. Technical report, UCSD, 2016.

[129] Minu Mariam Jacob. *Non-Foster Circuits for High Performance Antennas: Advantages and Practical Limitations*. PhD thesis, UCSD, 2016.

[130] C. P. Wen. Coplanar waveguide: A surface strip transmission line suitable for nonreciprocal gyromagnetic device applications. *IEEE Transactions on Microwave Theory and Techniques*, 17(12), Dec 1969.

[131] W Heinrich. Quasitem description of mmic coplanar lines including conductor loss effects. *IEEE Transactions on Microwave Theory and Techniques*, 41(1):45–52, Jan 1993.

[132] Inc.) Rick Cory (Skyworks Solutions. The nuts and bolts of tuning varactors. *High Frequency Electronics*, Feb 2009.

[133] Skyworks. Smv1405 to smv1413 series: Plastic packaged abrupt junction tuning varactors. Data Sheet, Apr 2015.

[134] Skyworks. Smv1405 to smv1413 series: Silicon abrupt junction varactor bondable chips. Data Sheet, Sep 2014.

[135] Elvia. `http://www.starone.com.br/en/`.

[136] G. Sajin, F. Craciunoiu, A. Dinescu, I. A. Mocanu, and A. Stefanescu. Laser ablated 48 ghz zor crlh antenna on alumina substrate. In *Microwave Conference (EuMC), 2012 42nd European*, pages 763–766, Oct 2012.

[137] Multi-circuit-boards.eu. `https://www.multi-circuit-boards.eu/en/pcb-design-aid/design-parameters.html`.

[138] Pcb pool. `http://www.pcb-pool.com/ppuk/info_pcbpoolprototype.html`.

[139] Quick teck. `http://www.quick-teck.co.uk/aboutus/capability.php`.

[140] Lab circuits.com. `http://www.lab-circuits.com`.

[141] F. Caminita, A. Mazzinghi, and S. Maci. Surface waves modes on artificial anysotropic boundary conditions. In *Electromagnetic Theory (EMTS), 2010 URSI International Symposium on*, pages 323–326, Aug 2010.

[142] M. R. M. Hashemi and T. Itoh. Composite right/left-handed leaky-wave antenna for concave surfaces. In *Antenna Technology, 2009. iWAT 2009. IEEE International Workshop on*, pages 1–4, March 2009.

[143] Boeing satcom antenna system. `http://boeing.mediaroom.com/20110127BoeingTestsNewKabandSATCOMAntennaSystem`.

[144] R. Pascaud, F. Pizarro, O. Pascal, T. Callegari, and L. Liard. Theoretical and numerical study of a plasma-based frequency tunable microstrip antenna. In *The 8th European Conference on Antennas and Propagation (EuCAP 2014)*, pages 1545–1546, April 2014.

[145] W. Kim and M. F. Iskander. Integrated phased antenna array design using ferroelectric materials and the coplanar waveguide continuous transverse stub technologies. In *2006 IEEE Antennas and Propagation Society International Symposium*, pages 4323–4326, July 2006.

[146] A. Ludwig. The definition of cross polarization. *IEEE Transactions on Antennas and Propagation*, 21(1):116–119, Jan 1973.